

UC Berkeley

UC Berkeley Electronic Theses and Dissertations

Title

Femtosecond Photoelectron Spectroscopy of the Dynamics of Electron Attachment and Photodissociation in Iodide-Nucleobase Clusters

Permalink

<https://escholarship.org/uc/item/68v9z2v8>

Author

Kunin, Alice

Publication Date

2019

Peer reviewed|Thesis/dissertation

Femtosecond Photoelectron Spectroscopy of the Dynamics of Electron Attachment and
Photodissociation in Iodide-Nucleobase Clusters

by

Alice Kunin

A dissertation submitted in partial satisfaction of the

requirements for the degree of

Doctor of Philosophy

in

Chemistry

in the

Graduate Division

of the

University of California, Berkeley

Committee in charge:

Professor Daniel M. Neumark, Chair

Professor Stephen R. Leone

Associate Professor Hartmut Häffner

Fall 2019

Femtosecond Photoelectron Spectroscopy of the Dynamics of Electron Attachment and
Photodissociation in Iodide-Nucleobase Clusters

Copyright 2019

by

Alice Kunin

Abstract

Femtosecond Photoelectron Spectroscopy of the Dynamics of Electron Attachment and Photodissociation in Iodide-Nucleobase Clusters

by

Alice Kunin

Doctor of Philosophy in Chemistry

University of California, Berkeley

Professor Daniel M. Neumark, Chair

DNA and RNA photodamage mechanisms are of significant importance but remain relatively poorly understood. The attachment of low-energy electrons to nucleic acid constituents has been shown to induce single and double strand breaks, although the mechanism of electron attachment and subsequent fragmentation remains debated. Nucleobases have been suggested to be the most likely target for attachment. The transient negative ions (TNIs) that form as a result of attachment have been implicated as important species in the damage mechanism. In addition, nucleobases exhibit strong photoabsorption cross-sections for UV light that may create a photoexcited species vulnerable to electron attachment. *In vivo*, local water molecules may stabilize TNIs and affect dissociation barriers, among other effects.

Time-resolved photoelectron spectroscopy (TRPES) of gas phase iodide-nucleobase clusters is a powerful tool to probe ultrafast reductive damage pathways in nucleic acid constituents. This femtosecond pump-probe technique employs an ultraviolet (UV) pump pulse to either initiate charge transfer from the iodide to the nucleobase or directly photoexcite the nucleobase species. A UV or infrared (IR) probe pulse can photodetach nascent transient negative ions (TNIs) or anionic photofragments to trace the ultrafast dynamics of TNI formation, decay, and cluster dissociation. In this thesis, we employ TRPES in conjunction with excited state calculations and photofragment action spectroscopy to probe the dynamics of electron attachment and photodissociation in a variety of iodide-nucleobase clusters, including iodide-uracil ($I^- \cdot U$), iodide-uracil-water ($I^- \cdot U \cdot H_2O$), and the simpler model system iodide-nitromethane ($I^- \cdot CH_3NO_2$).

Photofragment action spectroscopy and excited state calculations have revealed two distinct regimes of UV photoabsorption in iodide-nucleobase clusters: near the cluster vertical detachment energy (VDE) and near ~ 4.8 eV. Near-VDE photoexcitation corresponds to optical excitation from an $I(5p)$ orbital to form a dipole-bound (DB) anion, in which the

excess electron is bound by the large dipole moment of the base. Photoexcitation from 4.6 – 5.2 eV is expected to correspond to base-centered $\pi - \pi^*$ photoexcitation of the nucleobase. In addition to DB anions, the canonical nucleobases are known to support conventional, valence-bound (VB) anionic states.

Like the canonical nucleobases, nitromethane (CH_3NO_2) also possesses a large dipole moment and is known to support both DB and VB anion states and thus serves as a valuable small molecule model for the dynamics in larger nucleobase species. TRPES of $\text{I}^- \cdot \text{CH}_3\text{NO}_2$ clusters with a near-VDE photon energy UV pump pulse yields instantaneous formation of the $\text{I}^- \cdot \text{CH}_3\text{NO}_2$ DB anion with complete or nearly complete conversion to form a VB state in $\sim 400 - 500$ fs. The VB state exhibits bi-exponential decay in 2 ps and 1200 ps. A UV probe pulse measures the formation of I^- as the major dissociation channel of the cluster, with mono-exponential formation in approximately 20 ps. Rice-Ramsperger-Kassel-Marcus (RRKM) calculations to model the statistical unimolecular dissociation of the cluster predict dissociation to form I^- in only ~ 300 fs. The lack of a charged intermediate decay state suggests that intramolecular vibrational energy redistribution (IVR) in the cluster is the rate-limiting step in the nonstatistical dissociation of the cluster.

TRPES of $\text{I}^- \cdot \text{U}$ binary clusters shows some similarities to $\text{I}^- \cdot \text{CH}_3\text{NO}_2$, with only partial DB to VB anion conversion following near-VDE photoexcitation likely due to the reversed energetic ordering of the two TNI states. In this pump energy regime, bi-exponential formation of I^- in ~ 15 ps and 150 ps is measured and is expected to correspond to internal conversion and dissociation from each of the two relatively long-lived TNIs. Based on our TRPES results for $\text{I}^- \cdot \text{CH}_3\text{NO}_2$, we expect the long dissociation time constant to correspond to decay of the VB anion, with delayed dissociation due to inefficient IVR from vibrationally excited ring modes to the $\text{I}^- \cdots \text{U}$ stretch coordinate.

In the $\pi - \pi^*$ photoexcitation regime, the VB anion of the $\text{I}^- \cdot \text{U}$ complex is found to form instantaneously despite the lack of a direct optical excitation to form this state. No DB anion is detected in this pump regime. We have suggested that VB anion formation occurs by charge transfer from iodide to fill the empty hole in the π orbital following base-centered excitation. Autodetachment decay signal is measured in this photoexcitation regime to be approximately commensurate with the prompt formation and decay of the VB state. Thus, we expect that the decay of the nascent VB state is by autodetachment. I^- formation is measured to occur in 10s of ps, and we expect that cluster dissociation to form I^- likely occurs as a result of internal conversion of the $\pi - \pi^*$ photoexcited base.

The addition of a single water molecule to $\text{I}^- \cdot \text{U}$ is found to have two major effects: near-VDE photoexcitation yields a somewhat more pronounced DB to VB anion conversion in $\text{I}^- \cdot \text{U} \cdot \text{H}_2\text{O}$ than in $\text{I}^- \cdot \text{U}$, and $\pi - \pi^*$ photoexcitation yields bi-exponential formation of I^- . In the near-VDE photoexcitation regime, the nascent DB anion may undergo relatively prompt water binding site reorientation to reach a conformer with a lower DB to VB anion conversion barrier resulting in delayed VB anion formation and thus more prominent conversion. $\pi - \pi^*$

photoexcited $\text{I}^- \cdot \text{U} \cdot \text{H}_2\text{O}$ clusters may have other decay channels that can contribute to the bi-exponential formation of I^- such as the formation of $\text{I}^- \cdot \text{H}_2\text{O}$.

Contents

Contents	i
List of Figures	iv
List of Tables	viii
1 Introduction	1
1.1 Overview	2
1.2 Nucleic Acid Damage	3
1.3 Nucleobase Anions	4
1.4 TRPES of Iodide-Associated Clusters	5
1.5 Time-Resolved Photoelectron Spectroscopy	8
1.6 Dissociation Pathways	15
1.7 Computational Methods	17
1.8 Summary of Systems Studied	18
1.9 References	20
2 Experimental Methods	28
2.1 Overview	29
2.2 Cluster Source	30
2.3 Cluster Selection and Optimization	31
2.4 Detection	32
2.5 Triggering	33
2.6 Femtosecond Laser System	35
2.7 Generation of Pump and Probe Laser Pulses	43
2.8 Experimental Considerations	46
2.9 References	49
3 Photodissociation Dynamics of Iodide-Nitromethane Complexes	53
3.1 Abstract	54
3.2 Introduction	54
3.3 Experimental Methods	56

3.4	Results	58
3.5	Analysis	59
3.6	Discussion	61
3.7	Conclusions	64
3.8	Supplementary Material	65
3.9	References	69
4	Photodissociation Dynamics of Iodide-Uracil Complexes	74
4.1	Abstract	75
4.2	Introduction	75
4.3	Experimental Methods	77
4.4	Results	78
4.5	Analysis	81
4.6	Discussion	85
4.7	Conclusions	88
4.8	Supplementary Material	88
4.9	References	92
5	Dynamics of Electron Attachment and Photodissociation in Iodide-Uracil-Water Clusters	97
5.1	Abstract	98
5.2	Introduction	98
5.3	Experimental and Theoretical Methods	100
5.4	Results	101
5.5	Analysis	105
5.6	Discussion	108
5.7	Conclusions	115
5.8	Supplementary Material	116
5.9	References	122
6	Time-resolved Dynamics in Iodide-Uracil-Water Clusters Upon Excitation of the Nucleobase	126
6.1	Abstract	127
6.2	Introduction	127
6.3	Experimental Methods	129
6.4	Results	130
6.5	Analysis	133
6.6	Discussion	134
6.7	Conclusions	140
6.8	Supplementary Material	140
6.9	References	142

7	Electron Attachment and Photodissociation Dynamics in Iodide-Nucleobase Clusters	147
7.1	Abstract	148
7.2	Introduction	148
7.3	Methodologies	151
7.4	Electron Attachment and Photodissociation Dynamics in $I^- \cdot N$ Clusters . . .	155
7.5	Summary and Outlook	175
7.6	References	176
8	Femtosecond Time-Resolved Photoelectron Spectroscopy of Molecular Anions	186
8.1	Abstract	187
8.2	Introduction	187
8.3	A Brief Overview of Past Anion TRPES Studies	190
8.4	Electron Attachment and Photodissociation Dynamics in $I^- \cdot N$ Clusters . . .	192
8.5	Methodologies for $I^- \cdot N$ Clusters	195
8.6	$I^- \cdot CH_3NO_2$, $I^- \cdot U$, and $I^- \cdot T$ clusters	196
8.7	Summary and Outlook	209
8.8	References	209
9	Experimental Developments Towards TRPES of Larger Biomolecular Anions	227
9.1	Overview	228
9.2	Larger Nucleic Acid Constituents	228
9.3	Laser Desorption Cluster Source	230
9.4	Outlook	237
9.5	References	238
A	Publications from Graduate Work	241

List of Figures

1.1	Structures of uracil and uridine monophosphate.	4
1.2	Calculated orbitals for the VB and DB anions of the $\text{I}^- \cdot \text{U}$ binary cluster.	4
1.3	Example scheme for anion TRPES.	7
2.1	Experimental apparatus for TRPES of iodide-associated clusters.	29
2.2	Example mass spectrum for the production of $\text{I}^- \cdot \text{U} \cdot (\text{H}_2\text{O})_n$ clusters.	32
2.3	Triggering scheme for the experiment.	34
2.4	Mounted amplifier crystal, indium foil, and aperture mask.	38
2.5	Example image from the QuickFrog pulse retrieval software.	41
2.6	KMLabs laser triggering scheme.	42
2.7	Example cross-correlation and Gaussian fit for 260 nm/800 nm.	46
3.1	Photoelectron spectrum of $\text{I}^- \cdot \text{CH}_3\text{NO}_2$ at 3.56 eV pump and 3.14 eV probe.	57
3.2	Time-resolved photoelectron spectrum for the I^- and CH_2NO_2^- features.	58
3.3	Normalized integrated intensity of I^-	59
3.4	Normalized integrated intensity of CH_2NO_2^- for short time delays.	60
3.S1	Normalized integrated intensity of CH_2NO_2^- for long time delays.	66
3.S2	Normalized integrated intensity of the $\text{I}^- \cdot \text{CH}_3\text{NO}_2$ VB anion.	67
3.S3	Normalized integrated intensity of the $\text{I}^- \cdot \text{CH}_3\text{NO}_2$ DB anion.	67
3.S4	Potential energy curve for $\text{I}^- \cdot \text{CH}_3\text{NO}_2$ dissociation.	68
4.1	Photodepletion (absorption) spectrum of $\text{I}^- \cdot \text{U}$ with the corresponding photofragment action spectra of the I^- and deprotonated uracil photofragments.	79
4.2	Photoelectron spectrum of $\text{I}^- \cdot \text{U}$ at 4.03 eV pump and 3.61 eV probe.	80
4.3	Time-resolved photoelectron spectra for I^- from near-VDE photoexcited $\text{I}^- \cdot \text{U}$	80
4.4	Photoelectron spectrum of $\text{I}^- \cdot \text{U}$ with 4.72 eV pump and 3.15 eV probe.	81
4.5	Time-resolved photoelectron spectrum for I^- from $\text{I}^- \cdot \text{U}$ pumped at 4.72 eV.	81
4.6	Integrated intensity of I^- from excitation at 4.03 eV.	83
4.7	Integrated intensity of I^- from excitation at 4.72 eV.	83
4.S1	Negative ion ESI-MS of an iodide/uracil solution.	89
4.S2	Isolation of the $\text{I}^- \cdot \text{U}$ cluster prior to laser irradiation and photofragmentation mass spectrum of $\text{I}^- \cdot \text{U}$ obtained at 260 nm.	90

4.S3	Time-resolved photoelectron spectrum for the $\Gamma^- \cdot \text{U}$ DB anion with an excitation energy of 4.03 eV and probe energy of 3.61 eV.	90
4.S4	Potential energy curve for $\Gamma^- \cdot \text{U}$ dissociation.	91
5.1	Single photon photoelectron spectrum of $\Gamma^- \cdot \text{U} \cdot \text{H}_2\text{O}$	102
5.2	Time-resolved photoelectron spectra for the DB and VB anions of near-VDE pumped $\Gamma^- \cdot \text{U} \cdot \text{H}_2\text{O}$	102
5.3	Time-resolved photoelectron spectra for the autodetachment, I^- , and possible tautomer features of near-VDE pumped $\Gamma^- \cdot \text{U} \cdot \text{H}_2\text{O}$	103
5.4	$\Gamma^- \cdot \text{U} \cdot \text{H}_2\text{O}$ DB anion VDE shifting.	108
5.5	Integrated intensities for the $\Gamma^- \cdot \text{U} \cdot \text{H}_2\text{O}$ DB and VB anions at short time delays.	109
5.6	Integrated intensities for the $\Gamma^- \cdot \text{U} \cdot \text{H}_2\text{O}$ DB and VB anions at longer time delays.	109
5.7	Comparison of the $\Gamma^- \cdot \text{U} \cdot \text{H}_2\text{O}$ DB anion and the $\Gamma^- \cdot \text{U}$ DB anion at different near-VDE pump energies.	110
5.8	Integrated intensity for I^- at 4.38 eV pump excitation energy.	111
5.S1	Time-resolved photoelectron spectra for the DB and VB anions of near-VDE pumped $\Gamma^- \cdot \text{U} \cdot \text{H}_2\text{O}$ as a waterfall plot.	119
5.S2	Time-resolved photoelectron spectra for the autodetachment and I^- features for $\Gamma^- \cdot \text{U} \cdot \text{H}_2\text{O}$ at 4.38 eV pump energy.	119
5.S3	Time-resolved photoelectron spectra for the autodetachment, I^- , and possible tautomer features of near-VDE pumped $\Gamma^- \cdot \text{U} \cdot \text{H}_2\text{O}$ as a waterfall plot.	120
5.S4	EOM-CCSD/aug-cc-pVDZ(-pp) calculated molecular orbital images for the DB and VB states for $\Gamma^- \cdot \text{U} \cdot \text{H}_2\text{O}$	120
5.S5	Comparison of mono- and bi-exponential fits to the near-VDE pumped $\Gamma^- \cdot \text{U}$ I^- feature from Ch. 4.	121
5.S6	Integrated intensities for the possible tautomer features of near-VDE pumped $\Gamma^- \cdot \text{U} \cdot \text{H}_2\text{O}$	121
6.1	Single-photon photoelectron spectrum of $\Gamma^- \cdot \text{U} \cdot \text{H}_2\text{O}$ and calculated ground state structure.	130
6.2	Photoelectron spectra of $\pi - \pi^*$ photoexcited $\Gamma^- \cdot \text{U} \cdot \text{H}_2\text{O}$	131
6.3	Time-resolved photoelectron spectra of the VB anion of $\pi - \pi^*$ photoexcited $\Gamma^- \cdot \text{U} \cdot \text{H}_2\text{O}$	131
6.4	Photoelectron spectra of $\Gamma^- \cdot \text{U} \cdot \text{H}_2\text{O}$ at 4.77 eV pump excitation energy and 3.18 eV probe energy.	132
6.5	Time-resolved photoelectron spectra of the autodetachment and I^- features of $\pi - \pi^*$ photoexcited $\Gamma^- \cdot \text{U} \cdot \text{H}_2\text{O}$	132
6.6	Integrated intensities of the autodetachment and I^- features of $\pi - \pi^*$ photoexcited $\Gamma^- \cdot \text{U} \cdot \text{H}_2\text{O}$	134
6.7	Comparison of the integrated intensities for the VB anion and autodetachment feature of $\Gamma^- \cdot \text{U} \cdot \text{H}_2\text{O}$ and $\Gamma^- \cdot \text{U}$	134
6.8	Integrated intensity of the I^- feature of $\pi - \pi^*$ photoexcited $\Gamma^- \cdot \text{U} \cdot \text{H}_2\text{O}$	135

6.S1	Integrated intensity of the autodetachment feature of near-VDE photoexcited $\Gamma\cdot\text{U}\cdot\text{H}_2\text{O}$	141
6.S2	Integrated intensity of the autodetachment feature of $\pi-\pi^*$ photoexcited $\Gamma\cdot\text{U}\cdot\text{H}_2\text{O}$ with IR and UV probe energies.	141
6.S3	Comparison of $\Gamma\cdot\text{U}\cdot\text{H}_2\text{O}$ autodetachment dynamics resulting from 4.77 eV pump and 1.58 eV probe energy for various probe powers.	142
7.1	Photoelectron spectra of the uracil DB anion and the $\text{U}^-\cdot\text{H}_2\text{O}$ VB anion.	150
7.2	Example scheme for anion photoelectron spectroscopy and time-resolved photoelectron spectroscopy.	152
7.3	Diagram of the TRPES apparatus.	153
7.4	Single photon photoelectron spectra for $\Gamma\cdot\text{CH}_3\text{NO}_2$, $\Gamma\cdot\text{U}$, $\Gamma\cdot\text{T}$, $\Gamma\cdot\text{U}\cdot\text{H}_2\text{O}$, and $\Gamma\cdot\text{A}$	158
7.5	TRPE spectra and DB anion and VB anion integrated intensities at both early times and long delay times for $\Gamma\cdot\text{CH}_3\text{NO}_2$, $\Gamma\cdot\text{U}$, $\Gamma\cdot\text{T}$, $\Gamma\cdot\text{U}\cdot\text{H}_2\text{O}$, and $\Gamma\cdot\text{A}$	160
7.6	Iodide rise times for $\Gamma\cdot\text{CH}_3\text{NO}_2$, near-VDE photoexcited $\Gamma\cdot\text{U}$, $\pi-\pi^*$ photoexcited $\Gamma\cdot\text{U}$, and near-VDE photoexcited $\Gamma\cdot\text{U}\cdot\text{H}_2\text{O}$	162
7.7	TRPE spectra and VB anion and autodetachment integrated intensities at both early times and long delay times for $\pi-\pi^*$ photoexcited $\Gamma\cdot\text{U}$ and $\Gamma\cdot\text{T}$	163
7.8	Overlay of the one color photoelectron spectra with the laser photodissociation spectroscopy results for $\Gamma\cdot\text{U}$ and $\Gamma\cdot\text{T}$	164
7.9	Summary diagram of the approximate energies and ranges for the various excited states of $\Gamma\cdot\text{U}$ accessed in this work, as well as the proposed pathways resulting from near-VDE photoexcitation and higher energy photoexcitation.	170
7.10	Calculated potential energy surfaces corresponding to a DB to VB anion transition for the tautomers of adenine.	174
8.1	Example schemes for anion PES and TRPES.	188
8.2	Photoelectron spectra of the U^- DB anion and the $\text{U}^-\cdot\text{H}_2\text{O}$ VB anion.	194
8.3	Diagram of the TRPES apparatus.	196
8.4	Calculated structures for $\Gamma\cdot\text{CH}_3\text{NO}_2$, $\Gamma\cdot\text{U}$, and $\Gamma\cdot\text{T}$	197
8.5	Single-photon PE spectra for $\Gamma\cdot\text{CH}_3\text{NO}_2$, $\Gamma\cdot\text{U}$, and $\Gamma\cdot\text{T}$	198
8.6	TRPE spectra and integrated intensities at both early times and long delay times for the DB anion and VB anion for near-VDE photoexcited $\Gamma\cdot\text{CH}_3\text{NO}_2$, $\Gamma\cdot\text{U}$, and $\Gamma\cdot\text{T}$	199
8.7	Iodide integrated intensities for $\Gamma\cdot\text{CH}_3\text{NO}_2$, near-VDE photoexcited $\Gamma\cdot\text{U}$, and $\pi-\pi^*$ photoexcited $\Gamma\cdot\text{U}$	200
8.8	TRPE spectra and VB anion and autodetachment integrated intensities at both early times and long delay times for $\pi-\pi^*$ photoexcited $\Gamma\cdot\text{U}$ and $\Gamma\cdot\text{T}$	206
8.9	Overlay of the one color photoelectron spectra with the laser photodissociation spectroscopy results for $\Gamma\cdot\text{U}$ and $\Gamma\cdot\text{T}$	207

8.10	Diagram of the proposed $\text{I}^- \cdot \text{U}$ dynamical pathways resulting from near-VDE photoexcitation and higher energy photoexcitation.	208
9.1	Calculated structures for neutral and anionic uridine.	229
9.2	Calculated structure for iodide-uridine.	229
9.3	Interior of the SRC and 0D vacuum regions and cross-section of the ablation cluster source design.	231
9.4	Homemade pressed uridine targets after irradiation.	232
9.5	Images of the front and rear of the constructed laser ablation cluster source. . .	233
9.6	Mass spectrum of desorbed $\text{I}^- \cdot \text{Ur}$	234
9.7	Proposed experimental apparatus update with ESI source and radio frequency (RF) ion trap, orthogonal VMI detector and in-line reflectron TOF mass spectrometer.	237

List of Tables

3.S1	Beyer-Swinehart calculated densities and sums of states for the $\text{I}^- \cdot \text{CH}_3\text{NO}_2$ ground and transition states.	66
3.S2	$\text{I}^- \cdot \text{CH}_3\text{NO}_2$ calculated vibrational frequencies at the optimized, ground state geometry.	66
4.1	EOM-CCSD calculated transition channels, excitation energies, oscillator strength, and final state configurations for $\text{I}^- \cdot \text{U}$	82
4.S1	Vibrational frequencies of the $\text{I}^- \cdot \text{U}$ ground state, transition state, and bare neutral uracil.	88
4.S2	Beyer-Swinehart calculated densities and sums of states for the $\text{I}^- \cdot \text{U}$ ground and transition states.	89
5.1	The six energetically lowest-lying calculated structures for $\text{I}^- \cdot \text{U} \cdot \text{H}_2\text{O}$ anion complexes.	106
5.2	EOM-CCSD/aug-cc-pVDZ(-pp) calculated electronic transition channels, energies, and corresponding oscillator strengths for the lowest-lying calculated anion conformer of $\text{I}^- \cdot \text{U} \cdot \text{H}_2\text{O}$	107
5.3	Lifetimes and exponential fit coefficients for the DB and VB anions of $\text{I}^- \cdot \text{U} \cdot \text{H}_2\text{O}$ and comparison to $\text{I}^- \cdot \text{U}$	110
5.S1	Structures and dipole moments for neutral iodine-uracil-water in the ground state anion geometry and in the neutral equilibrium geometry, and for neutral uracil-water optimized without iodine.	117
6.1	Lifetimes for the VB anion, autodetachment feature, and I^- feature for 4.77 eV pump $\text{I}^- \cdot \text{U} \cdot \text{H}_2\text{O}$ and comparison to previous $\text{I}^- \cdot \text{U}$ studies.	135
7.1	A summary of calculated anion ground state structures and neutral dipole moments for the $\text{I}^- \cdot \text{N}$ cluster systems examined in this work.	156
8.1	Neutral dipole moments and VDEs for the $\text{I}^- \cdot \text{N}$ cluster systems examined in this work.	197

9.1 Experimentally determined melting points of the canonical DNA and RNA nucleobases and nucleosides.	230
--	-----

Acknowledgments

This thesis would not have been possible without the support of many people. Thank you to Dan for trusting me alone in a room with millions of dollars of equipment, and thank you for being patient and also impatient when everything broke and I had to figure out how to fix it. Thank you for listening to me (including when I was wrong) and for all of your advice and suggestions (including the ones I didn't take). Thank you for purchasing a KM laser 12 years ago and putting me on a build project that ultimately failed – I don't think I could have built all of this character otherwise. Thank you for sending me to places like Monterey (twice), San Diego (twice), Cancún (when morale got low), and Tuscany (when morale got even lower). Without sarcasm – thank you for having me as a part of your group for the past 5.5 years; I am quite proud of the scientist and person I have become in a large part thanks to my experience here at Berkeley.

Thank you to the other Neumarkians both past and present. The biggest thank you to Weili Li for teaching me not only an incredible amount of experimental know-how, but also that there is nothing to be afraid of and that *everything* can be fixed – you were right. Thank you to Holly Williams for taking me in as a junior student, for listening to my frustrations, and for sharing your pets. Thank you to Sarah King and Anne Stephansen for our short but very productive and enjoyable time together while I settled into FPES. Thanks to the other graduates of Neumark past who impressed me and led the way – Marissa Weichman, Mark Shapero, Madeline Elkins, Neil Cole-Filipiak, Jongjin Kim, and Aaron Harrison – I learned something important from all of you. Thank you to Jessalyn DeVine for facing grad school's challenges in solidarity with me, including the less common ones like pushing Dan's car up an icy mountain during a blizzard while he steered. Best of luck to the D-level Neumark graduates yet to come – Isaac Ramphal, Erin Sullivan, Mark Babin, Blake Erickson, Zach Heim, Chin Lee, and Steve Saric. Thank you to Valerie McGraw for the time we shared on FPES and how much I learned from being your senior student. Thank you to Katharine Lunny for the enjoyable time we shared at the end of my PhD and for carrying on the FPES torch - I look forward to seeing the exciting experiments you and Megan Asplund are sure to accomplish.

The support of so many loving friends has helped me through the many ups and downs of grad school – thank you in particular to Kristin Wucherer and Julia Lazzari-Dean for your friendship since Day 1. I could not have been more lucky to have two first-year housemates turn out to be such good friends. Thank you to Elio Champenois for believing in me when I didn't believe in myself, for talking shop, for putting things in perspective, and for making me laugh. Thank you to my family for all of your support and encouragement throughout my never-ending academic career. Your care packages, though excessive, always made me feel loved even from nearly 3,000 miles away.

Chapter 1

Introduction

Either the well was very deep, or she fell very slowly, for she had plenty of time as she went down to look about her, and to wonder what was going to happen next.

Lewis Carroll

1.1 Overview

Ultraviolet (UV) radiation-induced photodamage of DNA triggered by nascent free radicals and low-energy electrons is believed to account for nearly 70% of DNA damage [1]. The attachment of low-energy electrons to DNA has been shown to induce single- and double-strand breaks [2–4], although the mechanism of this damage is not yet well understood. Theoretical calculations and dissociative electron attachment (DEA) experiments generally predict that nucleobases are the initial site of electron attachment, with subsequent bond breakage at the phosphate backbone [3, 5–9]. Additionally, DNA bases have also been shown to have strong photoabsorption cross-sections for the direct absorption of harmful UV radiation [10–12]. *In vivo*, the local solvation environment has been shown to have important effects on the structure, energetics, and stability of DNA and anionic nucleic acid constituents [13–16]. To experimentally probe these DNA damage mechanisms, we have employed femtosecond (fs, 10^{-15} s) time-resolved photoelectron spectroscopy (TRPES) of gas-phase iodide-nucleobase ($\text{I}^- \cdot \text{N}$) and iodide-nucleobase-water ($\text{I}^- \cdot \text{N} \cdot \text{H}_2\text{O}$) microhydrated clusters. A UV pump photon can initiate charge transfer from the iodide to the nucleobase species, or induce a base-centered $\pi - \pi^*$ photoexcitation. An infrared (IR) or UV probe pulse is used to photodetach the excess electron from nascent, photoexcited transient negative ions (TNIs) or anionic dissociation products. In this way, the ultrafast photochemistry of excess electron accommodation in nucleobases is monitored. Gas-phase clusters provide an opportune model system as cluster complexity can be gradually increased to probe larger systems such as $\text{I}^- \cdot \text{N} \cdot (\text{H}_2\text{O})_n$ complexes or larger biomolecule species.

This thesis explores the ultrafast time-resolved dynamics of electron attachment and photodissociation in a variety of $\text{I}^- \cdot \text{N}$ clusters and related species. Chapter 1 provides an overview of reductive DNA damage and how TRPES of $\text{I}^- \cdot \text{N}$ clusters can be used to model the dynamics triggered by electron attachment. Chapter 2 describes the experimental apparatus employed herein to produce the $\text{I}^- \cdot \text{N}$ clusters of interest and monitor the ultrafast dynamics on a femtosecond timescale. Chapters 3 and 4 consider the photodissociation dynamics of iodide-uracil ($\text{I}^- \cdot \text{U}$) and the simpler, model system iodide-nitromethane ($\text{I}^- \cdot \text{CH}_3\text{NO}_2$) following photoexcitation. Chapter 5 discusses the electron attachment and photodissociation dynamics of near-VDE photoexcited iodide-uracil-water ($\text{I}^- \cdot \text{U} \cdot \text{H}_2\text{O}$) clusters to probe the effects of microhydration on $\text{I}^- \cdot \text{N}$ species. Chapter 6 details experiments on $\pi - \pi^*$ photoexcited $\text{I}^- \cdot \text{U} \cdot \text{H}_2\text{O}$ to better understand the similarities and differences in the dynamics induced by electron transfer as compared to initial base-centered photoexcitation. Chapters 7 and 8 reconsider our initial studies of $\text{I}^- \cdot \text{N}$ clusters in the context of the photodissociation results in Chs. 3 and 4 as well as the $\text{I}^- \cdot \text{U} \cdot \text{H}_2\text{O}$ results in Chs. 5 and 6 in an attempt to develop a more unified picture of the dynamics in these systems. Chapter 8 also comments more broadly on the application of TRPES to a wide variety of molecular anions. Finally, Chapter 9 provides an outlook for future experiments focused on larger biomolecule species such as iodide-nucleotide clusters and oligonucleotide polyanions.

1.2 Nucleic Acid Damage

We can generally consider photoinduced nucleic acid damage as arising from one of two pathways: photoabsorption directly by nucleic acid constituents or photoabsorption by the surrounding cellular media (e.g. water, proteins) [17]. The DNA bases thymine, cytosine, adenine, and guanine and the RNA base uracil are all known to have strong photoabsorption cross-sections for UV radiation [10–12]. High energy UV radiation or higher energy cosmic rays may directly photoionize DNA or RNA constituents to create mobile holes linked to strand breakage and fragmentation that may result from Auger decay [18, 19]. However, photoexcited nucleobases have also been shown to undergo efficient relaxation by internal conversion, preventing dissociation and fragmentation [20, 21]. These relaxation mechanisms are responsible for the remarkable photostability of DNA and have been of considerable interest.

Photoionization of the cellular environment is expected to produce free radicals such as the hydroxyl radical (OH^\cdot) or hydrogen radical (H^\cdot) and solvated electrons [17, 22]. Electrons may further ionize the cellular medium by electron impact ionization, or they may lose kinetic energy through collisions [1]. Intermolecular Coulombic decay of photoexcited water has also been suggested to be an important source of low energy secondary electrons involved in DNA damage [23]. As water comprises $\sim 70 - 80\%$ of the cell, DNA damage ultimately ensuing from radicals and solvated electrons produced from the cellular environment has been predicted to account for over 66% of DNA damage [1]. Free radicals and low energy electrons generated from the environment near DNA ($\sim 1 - 10$ nm) [24] are then expected to attach to DNA and ultimately cause single- and double- strand breaks and the loss of genetic information.

It is now most widely accepted from theoretical calculations and DEA experiments that the nucleobase is the most likely site of initial attachment by low energy electrons [3, 5, 7, 8]. Nucleobases have been found to exhibit large DEA cross sections for the resonant capture of low energy electrons ≤ 10 eV. Subsequent to nucleobase attachment, fragmentation is believed to be most likely at the C-O phosphodiester bond linking the phosphate backbone and sugar moieties, although the nucleobase-sugar C-N glycosidic bond may also fragment [8, 9]. The uracil nucleobase and uridine monophosphate nucleotide structures are shown in Fig. 1.1.

Naturally, the role of the local aqueous environment in the stability and relaxation of both photoexcited DNA constituents and reduced DNA constituents is also of considerable interest [20, 21]. For example, solvation of DNA bases has been shown to increase the nucleobase electron affinity (EA) [14] and may decrease excited state lifetimes by increasing the rate of internal conversion [25]. Dissociation barriers in nucleotides and bulk DNA may also be increased in solvated environments [26, 27]. Gas-phase [13, 14] and theoretical studies [28–30] of smaller, microhydrated clusters have shown that the energy ordering of anion states

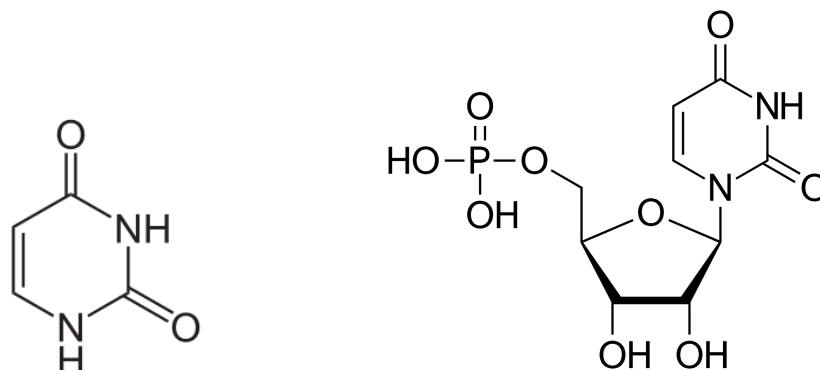


Figure 1.1: Structures of uracil (left) and uridine monophosphate (right).

is significantly affected by the addition of a single water molecule.

1.3 Nucleobase Anions

Nucleobases have been shown to support two types of anion states: valence-bound (VB) anions and dipole-bound (DB) anions [13, 31, 32]. Calculated images of these two types of orbitals for $\Gamma^- \cdot \text{U}$ are shown in Fig. 1.2 [33].

In VB anions, the excess electron occupies a valence orbital of the molecule. In nucleobases, the VB anion corresponds to electron occupation of a π^* orbital [34], which results in distortion in the ring puckering coordinate as compared to the planar, neutral bases [35–37]. The excess electron is bound by approximately 0.2 – 1 eV [14, 34, 38–40].

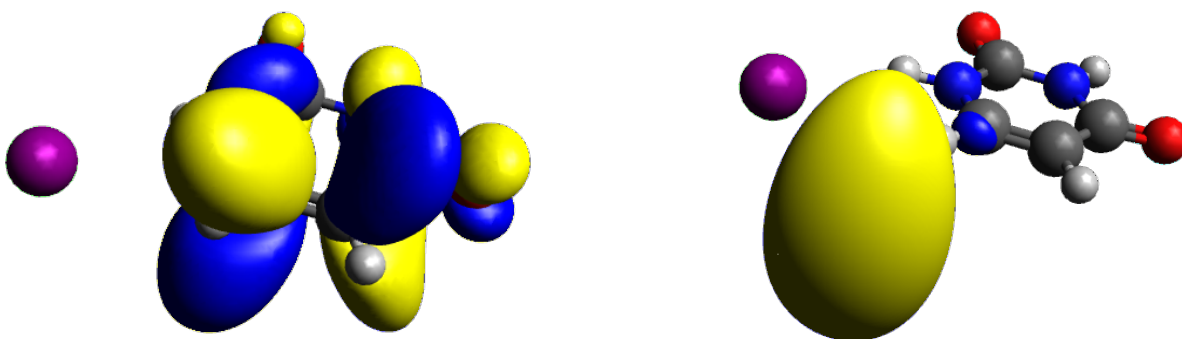


Figure 1.2: Calculated orbitals for the VB (left) and DB (right) anions of the $\Gamma^- \cdot \text{U}$ binary cluster. Calculated with the Gaussian 09 computing package [33] at the equation-of-motion coupled-cluster singles and doubles (EOM-CCSD) aug-cc-pVDZ level of theory.

DB anions correspond to capture of the excess electron by the relatively large dipole moment (μ) of a neutral molecule [32]. To bind an excess electron, a dipolar moment greater than ~ 2 D is required [41]. All of the canonical DNA and RNA nucleobases possess a dipole moment large enough to support a DB state in the gas phase [42–44]. Small nucleobase-water clusters have been shown theoretically [28, 30, 45–47] and recently experimentally (Ch. 5) to support DB states with favorable alignment of the nucleobase and water molecule dipole moments. In solution phase, the nature of the bulk solvent and solvent motion are expected to destabilize the DB anion relative to the VB anion. Note however that bulk water is suggested by calculations to stabilize non-canonical nucleobase tautomers with dipole moments ≥ 10 D [43, 48]. In a Koopmans’ theorem approach [31], where we neglect electron correlation and orbital relaxation effects, the binding energy (E_b) for a DB anion can be estimated as:

$$E_b \sim \frac{\mu}{r^2} \quad (1.1)$$

where $1/r^2$ arises from the long-range electron-dipole attractive interaction potential at a radius r from a point dipole μ [32]. For the nucleobase anions considered here, the binding energy of the excess electron is $\sim 0 - 200$ meV [49]. DB anions are characterized by excess electron density along the dipolar moment in a large ($\geq 10 - 30$ Å), diffuse orbital [49]. Because the excess electron density exists largely outside of the molecular framework, there is little to no geometric distortion between the DB anion and the neutral species [32].

While some nucleobase DB and VB anions have been measured to exist as stable species, others are metastable. Single-photon photoelectron spectroscopy and photofragment action spectroscopy have measured stable nucleobase DB and VB anions as well as stable DB anions for some iodide-associated clusters [13, 50]. Species with positive electron affinity will produce a stable anion, while adiabatically unbound species, i.e. species with negative electron affinity, may have metastable anion states that lie within the neutral continuum and exist with finite lifetimes. These metastable electronic resonances, here referred to as transient negative ions (TNIs), are nonstationary states of the time-dependent Schrödinger equation (see Section 1.5) with lifetimes given by the resonance width [51]. Nonadiabatic coupling between the anionic and neutral states facilitates decay of these resonances, as described in more detail in Section 1.6.

1.4 TRPES of Iodide-Associated Clusters

To model the time-resolved dynamics of nucleobase transient negative ions, we use femtosecond time-resolved photoelectron spectroscopy (TRPES) of $I^- \cdot N$ complexes. As seen in Fig. 1.2, the iodide atom in these complexes has been found to sit near the most acidic hydrogen atom of the nucleobase. Johnson and co-workers reported initial evidence of pho-

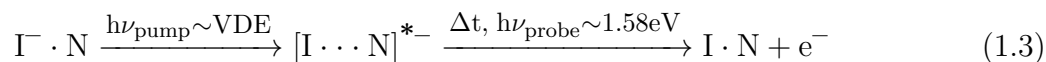
toinduced intracluster charge transfer in iodide-associated clusters [52, 53] with photoelectron and photofragment action spectroscopies. When complexed with polar molecules such as acetonitrile (CH_3CN), acetone ($(\text{CH}_3)_2\text{CO}$), and nitromethane (CH_3NO_2), the iodide-associated complexes were shown to exhibit charge-transfer-to-solvent (CTTS) excitation bands near the vertical detachment energy (VDE) of the complex, which corresponds to the difference in energy between the anion and the neutral at the equilibrium geometry of the anion. Photoexcitation of these CTTS bands was shown to produce DB anionic states [50, 54–56]. Photofragment action spectroscopy and excited state calculations have shown similar phenomena in near-VDE (~ 4 eV) photoexcited iodide-pyrimidine nucleobase complexes [57, 58], as discussed in more detail in this thesis.

To probe the ultrafast time-evolution of these nascent charge transfer states or TNIs, photoelectron spectroscopy is a natural tool of choice. Based on the photoelectric effect, an incident photon of energy greater than or equal to the binding energy of an electron (eBE) to the complex can photodetach the electron. By conservation of energy, the electron will be ejected with kinetic energy (eKE) given by:

$$\text{eKE} = h\nu_{\text{probe}} - \text{eBE} \quad (1.2)$$

where $h\nu_{\text{probe}}$ is the energy of the probe photon. The photodetached electron eKE distributions can be measured with time-of-flight or charged particle imaging techniques (see Ch. 2). Anions are particularly well-suited to study by photoelectron spectroscopy as the relatively low binding energy of the excess electron allows one to employ relatively low energy probe pulses that are easily generated by table-top commercial femtosecond laser systems. The eBE and shape of the photoelectron spectrum allow one to identify the nature of the system at the instant of photodetachment. As noted above, DB and VB TNIs, for example, exhibit differing binding energies and the amount of geometric distortion between the anion and neutral species will affect the breadth of the photodetachment feature (see Section 1.5). By measuring the eKE distribution of photoejected electrons as a function of delay time between the pump and probe photons, we may construct time-resolved photoelectron spectra that reveal the full relaxation and dissociation dynamics of photoexcited species.

By pumping an iodide-associated complex of interest with a femtosecond UV pump photon isoenergetic with the cluster VDE, we can initiate the ultrafast dynamics of TNI formation. The TNIs are easily photodetached by a second, time-delayed femtosecond IR probe photon to track the decay dynamics on femtosecond to picosecond (ps, 10^{-12} s) time scales:



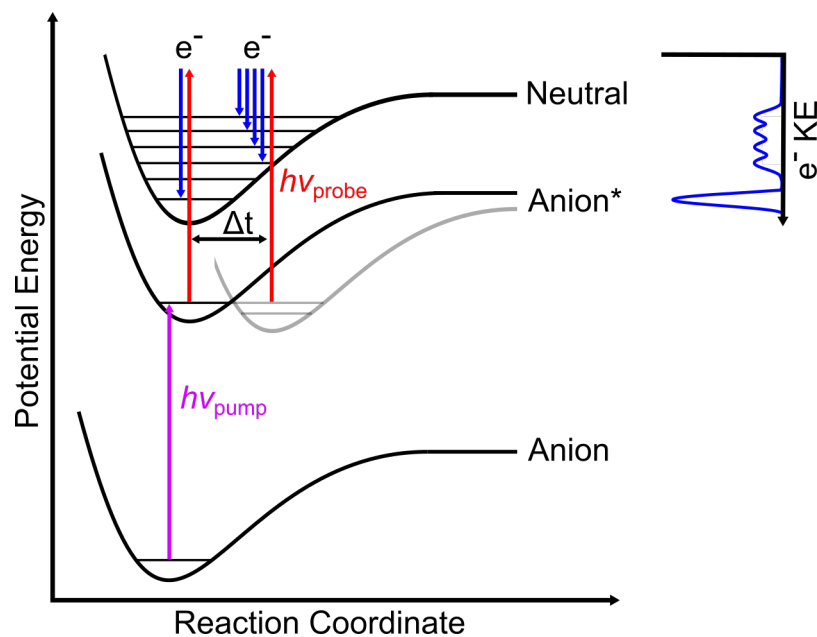
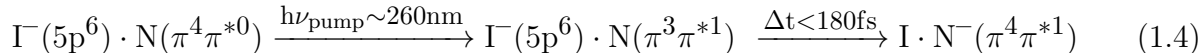


Figure 1.3: Example scheme for anion TRPES. The evolution of the anion state will produce changes in the photoelectron spectrum (right) as a function of time that allow the identity and nature of the excited anionic state to be probed.

This scheme and a schematic photoelectron spectrum are shown in Fig. 1.3. A sufficiently energetic UV probe photon can also be used to photodetach the excess electron from the TNI or from ionic photofragments that form *via* dissociation of the parent complex (see Sec. 1.6). Importantly, we note that the neutral iodine atom that remains following charge transfer is not an “innocent spectator”. Our experimental evidence suggests the motion of the neutral iodine atom after charge transfer can perturb the evolving TNI, particularly for the diffuse DB anion, as the iodine atom sits within the spatial region occupied by the bare uracil DB anion. This perturbative effect has been seen as shifts in the DB anion VDE of as much as 100 meV within the first 1 ps [59–61].

As described earlier, nucleobases also exhibit strong $\pi - \pi^*$ photoabsorption bands from $\sim 4.6 - 5.2$ eV; these bands have been found to be unaffected energetically by the presence of the iodide species [57, 58]. As detailed in later chapters of this thesis, our work indicates that $\pi - \pi^*$ photoexcitation of the nucleobase also yields the VB TNI, but through a different mechanism. Calculations have shown that direct optical excitation to form a TNI is not accessed in this pump energy regime. Accordingly, we have proposed that the VB anion arises from prompt charge transfer from iodide to fill the π hole remaining on the excited nucleobase:



Here, the $\Gamma^-(5p^6) \cdot N(\pi^3\pi^*1)$ species is the $\pi - \pi^*$ photoexcited state and the $\text{I} \cdot N^-(\pi^4\pi^*1)$ species is the iodine-associated VB anion state. This mechanism of VB anion formation is explored in more detail in Chs. 7 – 8.

1.5 Time-Resolved Photoelectron Spectroscopy

Our goal in this section is to describe the time-dependent photoelectron spectrum $P(\epsilon, \Delta t)$ as a function of the photodetached electron eKE (ϵ) and pump-probe delay (Δt).¹ We begin by briefly reviewing basic quantum mechanical descriptions of molecules and light-matter interaction before extending this framework to single photon PES and TRPES.

The time-dependent Schrödinger equation describes the time-evolution of a quantum mechanical state:

$$i\hbar \frac{\partial}{\partial t} |\Psi(t)\rangle = \hat{H} |\Psi(t)\rangle \quad (1.5)$$

Here, $|\Psi(t)\rangle$ refers to the molecular wavefunction that defines the time-dependent state of the molecule, while \hat{H} refers to the time-independent Hamiltonian operator. Recall that $|\Psi(t)\rangle$ can be expressed as:

$$|\Psi(t; t_0)\rangle = e^{-i\hat{H}(t-t_0)/\hbar} |\Psi(t_0)\rangle = \sum_{\mathbf{n}} c_{\mathbf{n}} e^{-iE_{\mathbf{n}}(t-t_0)/\hbar} |\mathbf{n}\rangle \quad (1.6)$$

where $|\mathbf{n}\rangle$ is the set of eigenstates for \hat{H} with energies $E_{\mathbf{n}}$, t_0 is the initial time, and $c_{\mathbf{n}}$ are the complex coefficients. Finally, recall that the probability P for a system to be in a state n is given by $|c_{\mathbf{n}}|^2$. The wavefunction for a molecular state naturally depends upon the coordinates \mathbf{r} and \mathbf{R} of the electrons and nuclei, respectively:

$$|\Psi(t)\rangle = |\Psi(\mathbf{r}, \mathbf{R}; t)\rangle \quad (1.7)$$

¹ Some parts of this section originate from a private communication from W. H. Miller. Note also that Ref. [62] considers a similar, more involved approach to simulate TRPE spectra of I_2^- . The notation here is intended to match as closely as possible to that commonly employed by Miller and co-workers.

The molecular Hamiltonian \hat{H} also depends on both electronic and nuclear interactions, as in Eq. 1.8:

$$\hat{H} = \hat{T}_N + \hat{T}_e + \hat{V}_{NN} + \hat{V}_{ee} + \hat{V}_{eN} \quad (1.8)$$

where \hat{T}_N and \hat{T}_e are the kinetic energy of the nuclei and electrons, respectively, \hat{V}_{NN} and \hat{V}_{ee} are the nuclei-nuclei and electron-electron repulsive Coulomb potential, respectively, and \hat{V}_{eN} is the electron-nuclei attractive Coulomb potential. The Born-Oppenheimer approximation assumes that the electronic and nuclear degrees of freedom of a system may be separated. Since the nuclear motion is expected to be significantly slower than the electron motion due to the much heavier mass of the nuclei, the nuclei can be considered to be essentially stationary from the perspective of the electrons. Within this approximation we may separate the molecular wavefunction into nuclear and electronic components:

$$\Psi(\mathbf{r}, \mathbf{R}) = \psi(\mathbf{r}; \mathbf{R})\chi(\mathbf{R}) \quad (1.9)$$

where $\psi(\mathbf{r}; \mathbf{R})$ is the electronic wavefunction that depends parametrically on the nuclear coordinates and $\chi(\mathbf{R})$ is the nuclear wavefunction.² The Hamiltonian can be similarly separated and simplified.

To describe the time-evolving interaction between the molecular system and electromagnetic radiation, we must define the Hamiltonian to include the time-dependent interaction potential:

$$\hat{H} = \hat{H}_0 + \hat{H}_1(t) \quad (1.10)$$

where \hat{H}_0 is the time-independent initial Hamiltonian for the molecular system and $\hat{H}_1(t)$ is the time-dependent perturbation. Within the electric dipole approximation and the long-wavelength approximation, the potential describing a classical radiation field $\boldsymbol{\varepsilon}(t)$ is given by

$$\hat{H}_1(t) = -\hat{\boldsymbol{\mu}} \cdot \boldsymbol{\varepsilon}(t) \quad (1.11)$$

² We will only consider here the electronic and nuclear (vibrational) components and omit rotational and spin components for brevity. Rotational structure is typically too small in energy to be resolved by photoelectron spectroscopy and spin must be conserved.

where $\boldsymbol{\mu}$ is the electric dipole matrix element.

From time-dependent perturbation theory, we may now write a generic expression for the molecular wavefunction as a function of time t_f as the Dyson series:

$$\begin{aligned}
|\Psi(t_f)\rangle &= \left[\mathbb{I} + \left(\frac{-i}{\hbar}\right) \int_{t_0}^{t_f} dt \hat{H}(t) + \left(\frac{-i}{\hbar}\right)^2 \int_{t_0}^{t_f} dt \int_{t_0}^t dt' \hat{H}(t) \hat{H}(t') + \dots \right] |\Psi(t_0)\rangle \\
&= \left[\mathbb{I} + \left(\frac{-i}{\hbar}\right) \int_{t_0}^{t_f} dt e^{-i\hat{H}_0(t_f-t)/\hbar} \hat{H}_1(t) e^{-i\hat{H}_0(t-t_0)/\hbar} \right. \\
&\quad + \left(\frac{-i}{\hbar}\right)^2 \int_{t_0}^{t_f} dt \int_{t_0}^t dt' e^{-i\hat{H}_0(t_f-t)/\hbar} \hat{H}_1(t) e^{-i\hat{H}_0(t-t')/\hbar} \hat{H}_1(t') e^{-i\hat{H}_0(t'-t_0)/\hbar} \\
&\quad \left. + \dots \right] |\Psi(t_0)\rangle
\end{aligned} \tag{1.12}$$

Let us first consider the case of one-photon photodetachment of an anion M^- :

$$M^-(E_g) + \hbar\omega \rightarrow M(E_F) + e^-(\epsilon) \tag{1.13}$$

Here, $E_g=E_i$ is the initial (ground state) energy and $E_F+\epsilon=E_f$ is the total energy corresponding to the final electronic state M_F with a corresponding photodetached electron eKE of ϵ . We will also denote $|\Psi(t_0)\rangle$ as $|\Phi_i\rangle$, the initial anion state, where $|\Phi_i\rangle = |\phi_g\rangle |\chi_g\rangle$ for the ground electronic (ϕ) and vibrational (nuclear, χ) states, and the final neutral state (eigenfunctions of \hat{H}_0) $|\Phi_f\rangle = |\phi_{F,\epsilon}\rangle |\chi_{E_F}\rangle$, where $|\phi_{F,\epsilon}\rangle$ refers to the neutral electronic wavefunction for the final electronic state F of the photodetached neutral with an outgoing electron eKE of ϵ . For the one-photon transition (first-order perturbation theory),

$$\begin{aligned}
P_{E_f \leftarrow E_i}(t_f) &= |\langle \Phi_f | \Psi(t_f) \rangle|^2 \\
&= \left| \frac{-i}{\hbar} \int_{t_0}^{t_f} dt e^{-iE_f(t_f-t)/\hbar} (\boldsymbol{\mu}_{f,i} \cdot \boldsymbol{\varepsilon}(t)) e^{-iE_i(t-t_0)/\hbar} \right|^2 \\
&= \left(\frac{-i}{\hbar} \right)^2 \left| \int_{t_0}^{t_f} dt e^{i(E_f-E_i)t/\hbar} (\boldsymbol{\mu}_{f,i} \cdot \boldsymbol{\varepsilon}(t)) \right|^2
\end{aligned} \tag{1.14}$$

Before converting from this expression of the transition probability to the photodetachment spectrum, we first note that the derivative of the probability with respect to time will yield the transition rate Γ :

$$\Gamma_{E_f \leftarrow E_i} \equiv \frac{dP_{E_f \leftarrow E_i}}{dt} \quad (1.15)$$

Consider, for example, a perturbing potential given by $\hat{H}_1(t) = \boldsymbol{\varepsilon}_0 e^{-i\omega t}$ where $\boldsymbol{\varepsilon}_0$ is a time-independent vector. We will also denote $(E_f - E_i)/\hbar$ as ω_{fi} . The probability for the transition in a time period t is given by:

$$\begin{aligned} P_{f \leftarrow i}(t) &= \left(\frac{-i}{\hbar} \right)^2 \left| \int_0^t dt' e^{i\omega_{fi}t'} e^{-i\omega t'} \langle \Phi_f | \boldsymbol{\varepsilon}_0 | \Phi_i \rangle \right|^2 \\ &= \left(\frac{-i}{\hbar} \right)^2 |\langle \Phi_f | \boldsymbol{\varepsilon}_0 | \Phi_i \rangle|^2 \left| \frac{e^{i(\omega_{fi} - \omega)t}}{i(\omega_{fi} - \omega)} \right|^2 \end{aligned} \quad (1.16)$$

and the rate of the transition is therefore ultimately given by:

$$\Gamma_{f \leftarrow i} = \frac{2\pi}{\hbar^2} |\langle \Phi_f | \boldsymbol{\varepsilon}_0 | \Phi_i \rangle|^2 \delta(\omega_{fi} - \omega) = \frac{2\pi}{\hbar} |\langle \Phi_f | \boldsymbol{\varepsilon}_0 | \Phi_i \rangle|^2 \delta(E_f - E_i - \hbar\omega) \quad (1.17)$$

This expression is the first-order Fermi's Golden Rule for the case of a harmonic perturbation (e.g. incident photon). If we recall that $E_f - E_i = E_F + \epsilon - E_g$, then $E_F - E_g$ is the electron affinity or eBE and we recover the energy conservation principle given in Eq. 1.2.

Returning to Eq. 1.14, the probability for the one-photon photodetachment transition, we now consider the photoelectron spectrum. We will employ the Condon approximation, which assumes that the electronic transition is vertical i.e. the electron transition occurs much faster than nuclear motion, so the transition dipole moment is independent of the nuclear coordinates:

$$\boldsymbol{\mu}_{f,i} = \langle \chi_{E_F} | \chi_g \rangle \boldsymbol{\mu}_{F,\epsilon,g} \quad (1.18)$$

$\langle \chi_{E_F} | \chi_g \rangle$ is known as the Franck-Condon factor. The presence of this factor in our equation for the probability of the photodetachment electronic transition means that the final and initial nuclear wavefunctions must have nonzero overlap for the transition to be accessible. The extent of the Franck-Condon overlap will ultimately dictate the shape (breadth) of the photoelectron spectrum. We will further assume that the transition dipole moment is independent of the kinetic energy of the outgoing electron (ϵ) so $\boldsymbol{\mu}_{F,\epsilon,g} = \boldsymbol{\mu}_{F,g}$. Therefore:

$$P_{E_f \leftarrow E_i}(t_f) \equiv P(E_F, \epsilon) \propto \left| \langle \chi_{E_F} | \chi_g \rangle \right|^2 \left| \int_{t_0}^{t_f} dt (\boldsymbol{\mu}_{F,g} \cdot \boldsymbol{\epsilon}(t)) e^{i(E_F + \epsilon - E_g)t/\hbar} \right|^2 \quad (1.19)$$

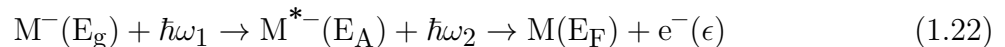
Here we have written that $P_{E_f \leftarrow E_i}(t_f)$, the probability for the photodetachment transition from the ground state to the final detached state, is equivalent to $P(E_F, \epsilon)$, the probability distribution as a function of the final nuclear state and the photodetached eKE. However, measuring $P(E_F, \epsilon)$ in general requires a coincidence experiment, and we measure only ϵ . The probability distribution of eKE, $P(\epsilon)$, corresponds to the sum of the photodetachment transition probability integrated over all final nuclear states:

$$\begin{aligned} P(\epsilon) &\equiv \int dE_F P(E_F, \epsilon) \\ &\propto \int_{t_0}^{t_f} dt \int_{t_0}^{t_f} dt' \boldsymbol{\epsilon}(t) \boldsymbol{\epsilon}(t') e^{-i(E_F + \epsilon - E_g)t/\hbar} e^{i(E_F + \epsilon - E_g)t'/\hbar} \\ &\quad \times \int dE_F \langle \chi_g | \chi_{E_F} \rangle \langle \chi_{E_F} | \chi_g \rangle e^{-iE_F(t-t')/\hbar} \\ &\propto \int_{t_0}^{t_f} dt \int_{t_0}^{t_f} dt' \boldsymbol{\epsilon}(t) \boldsymbol{\epsilon}(t') e^{-i(\epsilon - E_g)t/\hbar} e^{i(\epsilon - E_g)t'/\hbar} \\ &\quad \times \langle \chi_g | e^{-i\hat{H}_F(t-t')/\hbar} | \chi_g \rangle \\ P(\epsilon) &\propto \int_{t_0}^{t_f} dt \int_{t_0}^{t_f} dt' \boldsymbol{\epsilon}(t) \boldsymbol{\epsilon}(t') e^{i(E_g - \epsilon)(t-t')/\hbar} \langle \chi_g | e^{-i\hat{H}_F(t-t')/\hbar} | \chi_g \rangle \end{aligned} \quad (1.20)$$

where \hat{H}_F is the nuclear Hamiltonian for the final state. If we consider $P(\epsilon)$ in the long time limit $t_f \rightarrow \infty$ i.e. the photodetachment spectrum, for a radiation field $\boldsymbol{\epsilon}(t)\boldsymbol{\epsilon}(t') \sim \cos\omega(t-t')$ where $(t-t')=\tau$,

$$P(\epsilon) \sim \int_{-\infty}^{\infty} d\tau e^{i(E_g + \hbar\omega - \epsilon)\tau/\hbar} \langle \chi_g | e^{-i\hat{H}_F\tau/\hbar} | \chi_g \rangle \quad (1.21)$$

Now we consider the two photon case. For an anion M^- with the same ground state g and final state F , we will introduce an intermediate electronic state denoted A , coupled by two photons $\hbar\omega_1$ and $\hbar\omega_2$.



Consider a time-dependent electric field now given by two pulses as $\boldsymbol{\varepsilon}(t) = \boldsymbol{\varepsilon}_1(t) + \boldsymbol{\varepsilon}_2(t) = \boldsymbol{\varepsilon}_{01}\mathbf{E}_1(t)e^{-i\omega_1 t} + \boldsymbol{\varepsilon}_{02}\mathbf{E}_2(t - \Delta t)e^{-i\omega_2(t - \Delta t)}$ where $\boldsymbol{\varepsilon}_{0n}$ corresponds to a time-independent vector, $\mathbf{E}_n(t)$ is the temporal shape of the laser pulse (e.g. Gaussian, sech^2), and Δt is the time delay between the ω_n pulses. We will employ the rotating-wave approximation i.e. we will assume that $\hbar\omega_1$ is resonant with the first transition and $\hbar\omega_2$ is resonant with the second transition. The probability for the two-photon transition is given by:³

$$\begin{aligned}
P_{E_f \leftarrow E_i}(t_f) &\equiv P(E_F, \epsilon) = |\langle \Phi_f | \Psi(t_f) \rangle|^2 \\
P(E_F, \epsilon) &= \left| \left(\frac{-i}{\hbar} \right)^2 \int_{t_0}^{t_f} dt \int_{t_0}^{t_f} dt' (\boldsymbol{\mu}_{F,A} \cdot \boldsymbol{\varepsilon}(t)) (\boldsymbol{\mu}_{A,g} \cdot \boldsymbol{\varepsilon}(t')) \right. \\
&\quad \left. \times e^{i(E_F + \epsilon)t/\hbar} e^{-iE_g t'/\hbar} \langle \chi_{E_F} | e^{-i\hat{H}_A(t-t')/\hbar} | \chi_g \rangle \right|^2 \\
&= \left| \left(\frac{-i}{\hbar} \right)^2 (\boldsymbol{\mu}_{F,A} \cdot \boldsymbol{\varepsilon}_{02}) (\boldsymbol{\mu}_{A,g} \cdot \boldsymbol{\varepsilon}_{01}) \right. \\
&\quad \times \int_{t_0}^{t_f} dt \int_{t_0}^{t_f} dt' e^{i(E_F + \epsilon)t/\hbar} e^{-iE_g t'/\hbar} \mathbf{E}_2(t - \Delta t) e^{-i\omega_2(t - \Delta t)} \mathbf{E}_1(t') e^{-i\omega_1 t'} \\
&\quad \left. \times \langle \chi_{E_F} | e^{-i\hat{H}_A(t-t')/\hbar} | \chi_g \rangle \right|^2 \\
&= \left| \left(\frac{-i}{\hbar} \right)^2 (\boldsymbol{\mu}_{F,A} \cdot \boldsymbol{\varepsilon}_{02}) (\boldsymbol{\mu}_{A,g} \cdot \boldsymbol{\varepsilon}_{01}) \right. \\
&\quad \times \int_{t_0}^{t_f} dt \int_{t_0}^{t_f} dt' e^{i(E_F + \epsilon - \hbar\omega_2)t/\hbar} e^{-i(E_g + \hbar\omega_1)t'/\hbar} e^{-i\omega_2 \Delta t} \\
&\quad \left. \times \mathbf{E}_2(t - \Delta t) \mathbf{E}_1(t') \langle \chi_{E_F} | e^{-i\hat{H}_A(t-t')/\hbar} | \chi_g \rangle \right|^2
\end{aligned} \tag{1.23}$$

where \hat{H}_A is the nuclear Hamiltonian for the intermediate excited state. We can re-express this term:

³ Note that in the one-photon case we used first-order perturbation theory, while here we are using second-order. The first-order term is not included here as we are assuming the ground state and final state are not directly coupled i.e. the first photon (pump) is energetically insufficient to access the final state (photodetach the ground state anion).

$$e^{-i\hat{H}_A(t-t')/\hbar} = \int dE_A |\chi_{E_A}\rangle \langle \chi_{E_A}| e^{-iE_A(t-t')/\hbar} \quad (1.24)$$

and Eq. 1.23 can be further simplified as:

$$P(E_F, \epsilon) \propto \left| \int dE_F \langle \chi_{E_F} | \chi_{E_A} \rangle \langle \chi_{E_A} | \chi_g \rangle \bar{\epsilon}_2(E_F + \epsilon - E_A) \bar{\epsilon}_1(E_A - E_g) \right|^2 \quad (1.25)$$

where

$$\bar{\epsilon}_1(\bar{E}) = \int dt e^{i\bar{E}t/\hbar} e^{-i\omega_1 t} \mathbf{E}_1(t) \quad \bar{\epsilon}_2(\bar{E}) = \int dt e^{i\bar{E}t/\hbar} e^{-i\omega_2(t-\Delta t)} \mathbf{E}_2(t - \Delta t) \quad (1.26)$$

But, again, to explicitly express the two-photon time-dependent photoelectron spectrum $P(\epsilon, \Delta t)$ we must evaluate the integral over dE_F . From Eq. 1.23:

$$\begin{aligned} P(\epsilon, \Delta t) &\propto \int_{t_0}^{t_f} dt \int_{t_0}^t dt' \int_{t_0}^{t_f} dt'' \int_{t_0}^{t''} dt''' e^{-i\omega_2(t-\Delta t)} e^{-i\omega_1(t')} e^{-i\omega_2(t''-\Delta t)} e^{-i\omega_1(t''')} \\ &\quad \times \int dE_F \langle \chi_g | e^{i\hat{H}_A(t''-t''')/\hbar} | \chi_{E_F} \rangle e^{-iE_F(t''-t)/\hbar} \langle \chi_{E_F} | e^{-i\hat{H}_A(t-t')/\hbar} | \chi_g \rangle \\ &\quad \times e^{i\epsilon t/\hbar} e^{-iE_g t'/\hbar} e^{-i\epsilon t''/\hbar} e^{iE_g t'''/\hbar} \mathbf{E}_2(t - \Delta t) \mathbf{E}_1(t') \mathbf{E}_2(t'' - \Delta t) \mathbf{E}_1(t''') \\ P(\epsilon, \Delta t) &\propto \int_{t_0}^{t_f} dt \int_{t_0}^{t_f} dt'' e^{-i\omega_2(t-\Delta t)} e^{-i\omega_2(t''-\Delta t)} \mathbf{E}_2(t - \Delta t) \mathbf{E}_2(t'' - \Delta t) \\ &\quad \times \int_{t_0}^t dt' \int_{t_0}^{t''} dt''' e^{-i\omega_1(t')} e^{-i\omega_1(t''')} e^{i\epsilon(t-t'')/\hbar} e^{iE_g(t'''-t')/\hbar} \mathbf{E}_1(t') \mathbf{E}_1(t''') \quad (1.27) \\ &\quad \times \langle \chi_g | e^{-i\hat{H}_A(t'''-t'')/\hbar} e^{-i\hat{H}_F(t''-t)/\hbar} e^{-i\hat{H}_A(t-t')/\hbar} | \chi_g \rangle \\ P(\epsilon, \Delta t) &\propto \int_{t_0}^{t_f} dt \int_{t_0}^{t_f} dt'' e^{-i\omega_2(t-\Delta t)} e^{-i\omega_2(t''-\Delta t)} \mathbf{E}_2(t - \Delta t) \mathbf{E}_2(t'' - \Delta t) \\ &\quad \times \int_{t_0}^t dt' \int_{t_0}^{t''} dt''' e^{-i\omega_1(t')} e^{-i\omega_1(t''')} e^{i\epsilon(t-t'')/\hbar} e^{iE_g(t'''-t')/\hbar} \mathbf{E}_1(t') \mathbf{E}_1(t''') \\ &\quad \times \langle \chi_g | e^{-i\hat{H}_A(t'''-t'')/\hbar} e^{-i\hat{H}_F(t''-t)/\hbar} e^{-i\hat{H}_A(t-t')/\hbar} | \chi_g \rangle \end{aligned}$$

In the continuum limit ($t_f \rightarrow \infty$), we can succinctly express the total photodetachment spectrum:

$$P(\epsilon, \Delta t) \propto \int_{t_0}^{\infty} dt \int_{t_0}^{\infty} dt'' \epsilon_2(t - \Delta t) \epsilon_2(t'' - \Delta t) \times \langle \tilde{\chi}_g | e^{-i\hat{H}_A(t'')/\hbar} e^{-i(\hat{H}_F + \epsilon)(t-t'')/\hbar} e^{-i\hat{H}_A t/\hbar} | \tilde{\chi}_g \rangle \quad (1.28)$$

where

$$|\tilde{\chi}_g\rangle = \int_{t_0}^t dt' \epsilon_1(t') e^{i(E_g - \hat{H}_A)t'/\hbar} |\chi_g\rangle \quad (1.29)$$

1.6 Dissociation Pathways

The $\Gamma^- \cdot N$ complexes explored here exhibit a number of energetically accessible dissociation pathways, including autodetachment of the nascent TNIs and internal conversion to the anionic ground state followed by dissociation to yield Γ^- or dissociation to other species. We briefly elaborate on these pathways here.

Autodetachment is the spontaneous emission of an electron from a metastable anion [32, 63, 64]. For TNIs with energy levels that lie within a manifold of neutral vibrational states, nonadiabatic coupling between the anion and neutral states can facilitate electron loss. When this process occurs following the statistical randomization of energy, the electron typically carries ~ 0 eV eKE, and the process is known as thermionic emission [65, 66].

Internal conversion refers to the relaxation of a molecule from a higher lying electronic state to a lower electronic state *via* coupling of the electronic and vibrational energy levels. For the range of pump energies employed here, the $\Gamma^- \cdot N$ clusters are excited to low-lying electronic states and internally convert back to the $\Gamma^- \cdot N$ anion ground state. This process produces a vibrationally excited species in the ground electronic state. Once internal conversion to the ground state has occurred, the $\Gamma^- \cdot N$ complex may dissociate to produce Γ^- or a variety of ionic fragments depending on the nature of the “N” species. This unimolecular dissociation of the cluster may proceed by a statistical or non-statistical mechanism, as described in more detail below.

Statistical Dissociation

Statistical unimolecular dissociation can be modelled by Rice-Ramsperger-Kassel-Marcus (RRKM) theory [67–69], as in Chs. 3 and 4. Based on the vibrational frequencies and rota-

tional constant(s) of the reactant and the transition state, the microcanonical rate constant $k_{\text{RRKM}}(E)$ for a statistical unimolecular reaction is given by:

$$k_{\text{RRKM}}(E) = \frac{W(E - E_0)}{h \cdot \rho(E)} \quad (1.30)$$

where E is the energy provided to the system (given by the pump photon), E_0 is the zero point energy, $W(E - E_0)$ is the number of available states at the transition state configuration, and $\rho(E)$ is the density of reactant states. RRKM theory relies on several key assumptions, including: energized molecules pass through the transition state only once, the energy is randomly distributed among each vibrational mode, and intramolecular vibrational energy redistribution (IVR) is rapid and complete on the timescale of the reaction. Measured dissociation lifetimes that are poorly modelled by RRKM calculations may indicate the presence of a dynamical barrier that renders these assumptions inaccurate. If the reaction lacks a distinct transition state along the potential curve (i.e. the potential is barrierless), variational transition state theory may be used to identify the transition state by calculating the rate constant along the potential energy curve; the location that yields the minimum rate constant corresponds to the transition state. For the iodide-associated complexes in Chs. 3 and 4, the $\text{I}^- \cdots \text{N}$ stretch coordinate expected to lead to dissociation is calculated to have a barrierless potential [57, 70].

The Beyer-Swinehart algorithm [71] is commonly used to calculate the sum and density of states based on the harmonic oscillator vibrational frequencies (ω) for the reactant and transition state, which are easily calculated (e.g. in Gaussian [33]). The Beyer-Swinehart algorithm counts the number of states based on the idea that if a state exists at energy E , a state must also exist at energy $E + \omega$ up to the maximum available energy in the system (given by the pump photon energy). The Stein-Rabinovitch modification [72] to the Beyer-Swinehart algorithm allows for the convolution of harmonic frequencies with additional anharmonic frequencies to produce a more accurate density of states, as described below.

Modifications may be made to explicitly treat low-energy modes as free or hindered rotors as appropriate [73, 74]. The microcanonical density of states arises from the canonical partition function Q_{rot} for an N -dimensional system:

$$Q_{\text{rot}}(T) = \frac{1}{\sigma h^N} \int_0^\infty e^{-\hat{H}(p,q)/k_{\text{B}}T} dp^N dq^N \quad (1.31)$$

where σ is the symmetry number, \hat{H} is the Hamiltonian, and $k_{\text{B}}T$ is the product of the Boltzmann constant and the temperature. For a two-dimensional rotor, the classical Hamiltonian

is given by:

$$\hat{H} = \frac{1}{2I} \left(p_\theta^2 + \frac{p_\phi^2}{\sin^2\theta} \right) + V(\theta, \phi) \quad (1.32)$$

for inertia I , momentum p , and an angle-dependent potential V that depends on the nature of the rotor (e.g. free, linearly hindered, harmonically hindered, etc). For a hindered rotor arising from an ion-dipole interaction as in the case of the $\Gamma^- \cdot N$ clusters here, the potential of the rotor is of the form [75]:

$$V(\theta) = \frac{V_0}{2} \cos(1 - \sigma\theta) \quad (1.33)$$

where V_0 is the height of the barrier for the cosine potential and σ refers to the symmetry (the number of wells). The barrier and the symmetry can be calculated (e.g. in Gaussian) by calculating the potential as a function of rotor rotation angle and fitting to this cosine potential. The density of states $N(E)$ is then given by the inverse Laplace transform of $Q_{\text{rot}}(T)$, and the total density of states is then given by the convolution of the harmonic and rotational densities.

1.7 Computational Methods

While considerable computational work has been done to examine the anions of various nucleic acid constituents (see Refs. [21, 76] for reviews) the addition of weakly-bound iodine as well as the interest in photoexcited charge transfer states here poses additional computational challenges and expense. Here, we briefly comment on the success and appropriateness of a variety of computational methods for describing the properties and energetics of the DB and VB anions of iodide-nucleobase clusters.

Either wavefunction methods such as Møller-Plesset perturbation theory (MP2) or coupled cluster singles and doubles (CCSD) or long-range corrected density functional theory (LC-DFT) are needed to properly describe the inherent long-range attractive electrostatic potential present for DB anions [32]. Additionally, post-Hartree-Fock methods such as MP2 or CCSD account for electron correlation effects that contribute significantly to the excess electron binding characteristics of DB anions by way of dispersion-type interactions between the electron and the neutral molecule [30, 77]. The diffuse nature of DB anions also necessitates the use of additional diffuse basis functions [78] such as augmented correlation-consistent Dunning basis sets (aug-cc-pVNZ for N=D (double), T (triple), etc.) [79] or split-valence-type Pople basis sets with additional diffuse functions such as 6-31++G** or

6-311+G**. However, Pople basis sets have been contraindicated in the past by Simons and co-workers for calculating the binding energies of DB anions as these valence-type sets may produce relatively wide variation in calculated results from one set to another [80]. It has been noted for states with negative EAs that diffuse basis functions tend to converge to the DB anion and can produce unreliable results for VB states [81–84].

Takayanagi and co-workers have employed LC-DFT with various DFT functionals and diffuse basis sets to accurately describe both DB and VB anionic states of biomolecules including uracil, uracil-water, thymine, adenine, $I^- \cdot U$, and $I^- \cdot T$ [30, 37, 60, 85, 86]. Their work has found that the BH&HLYP hybrid exchange-correlation functional with a large, diffuse basis set such as 6-311++G(2d,p) with additional diffuse sp functions can successfully describe both the DB and VB states of uracil, while B3LYP cannot describe the uracil DB anion state at all, even with the use of diffuse basis functions, as this functional significantly overestimates the stability of the VB state [30, 37, 85]. This lack of a DB state was also observed in time-dependent DFT (TD-DFT) calculations of iodide-pyrimidine nucleobase complexes by Dessent and co-workers [58]. However, Takayanagi et al have shown that long-range corrected functionals such as CAM-B3LYP and ω B97XD with appropriately large Pople split-valence or Dunning correlation-consistent basis sets were found to successfully describe DB and VB states of uracil, $I^- \cdot U$, $I^- \cdot T$, and adenine. In general, for states with negative EAs (i.e. TNIs), EOM-CC methods are the most appropriate to describe the properties of TNIs and electronic resonances with electron-correlation and appropriate state-to-state couplings [51].

To address the dramatic computational expense introduced by the presence of iodine, an effective core potential or pseudopotential [87, 88] is often used to approximate the core electrons of iodine as “frozen”. Though this approximation may result in some loss of accuracy, the impact is likely relatively minor and the reduction in the number of electrons and in the basis set size is critical for the feasibility of these calculations.

1.8 Summary of Systems Studied

Photodissociation of iodide-nitromethane

Nitromethane possesses a large dipole moment (4.62 D) similar to the uracil and thymine nucleobases of interest here. With its simpler structure, iodide-nitromethane ($I^- \cdot CH_3NO_2$) clusters serve as an excellent, simpler model system for understanding the dynamics in iodide-nucleobase complexes. Previous work in our group has shown that following near-VDE photoexcitation, the DB anion of the complex is formed within the cross-correlation of the pump and probe laser pulses and clear conversion from the DB anion to form a VB anion is observed [89]. The dissociation channels for the bi-exponentially decaying VB anion, however, were not able to be probed in this study, as the IR probe is energetically insufficient to

photodetach the possible photofragments of $\Gamma \cdot \text{CH}_3\text{NO}_2$ including Γ^- , NO_2^- , and CH_2NO_2^- .

With a higher energy UV probe, we measure the formation of Γ^- as the major dissociation pathway with monoexponential formation in 10s of ps. This result indicates that the $\Gamma \cdot \text{CH}_3\text{NO}_2$ VB anion fast decay likely proceeds by internal conversion to the anion ground state followed by evaporation of Γ^- . We apply RRKM theory to examine the statistical nature of this dissociation and find that RRKM underestimates the timescale for Γ^- dissociation by two orders of magnitude. We conclude that IVR in the cluster may act as a dynamical bottleneck in the dissociation process with inefficient IVR from $-\text{NO}_2$ modes excited in the VB anion to the $\Gamma \cdot \cdot \cdot \text{CH}_3\text{NO}_2$ modes active in the dissociation of the complex.

Photodissociation of iodide-uracil

TRPES and excited state electronic structure calculations in collaboration with photofragment action spectroscopy measurements were employed to probe the electron attachment and photodissociation channels of $\Gamma \cdot \text{U}$ binary clusters. Building from earlier TRPES studies of $\Gamma \cdot \text{N}$ binary complexes [59, 60, 86, 90, 91], both near-VDE and $\pi - \pi^*$ photoexcited clusters are probed. Electronic structure calculations reveal that near-VDE photoexcitation is expected to correspond to a direct optical excitation from an I(5p) orbital to create a DB anion, with no direct optical excitation to form the VB anion. Evidence for subsequent partial conversion of the DB anion to form the VB anion in ≤ 200 fs in this pump regime has been previously measured [59]. Near 4.7 eV, the $\pi - \pi^*$ photoexcitation is expected to dominate, with no optical excitation to form either TNI.

Photofragment action spectra show formation of Γ^- and the deprotonated uracil anion $[\text{U-H}]^-$ fragments in both of these photoexcitation regimes with Γ^- as the dominant channel. TRPES with higher energy UV probe pulses measures the formation of Γ^- in both pump energy regimes, with bi-exponential Γ^- formation with near-VDE pump energies and mono-exponential formation following $\pi - \pi^*$ excitation. The 10s to 100s of ps Γ^- formation timescales in both pump energy regimes were found to be orders of magnitude slower than expected for statistical unimolecular dissociation as predicted by RRKM calculations for mono-exponential dissociation. This dynamical bottleneck is expected to be similar to that observed in $\Gamma \cdot \text{CH}_3\text{NO}_2$ clusters, with slow IVR from VB anion ring-puckering modes to the low energy iodide-uracil stretch coordinate acting as a bottleneck to dissociation. Near-VDE bi-exponential Γ^- formation in ~ 20 ps and 150 ps is thus expected to arise from internal conversion and dissociation of the DB and VB anions, respectively. $\pi - \pi^*$ excitation produces only the VB anion, so mono-exponential decay is as expected by this mechanism.

Iodide-uracil-water clusters

To explore the effects of microhydration, $\Gamma \cdot \text{U} \cdot \text{H}_2\text{O}$ clusters were examined with both near-VDE photoexcitation as well as $\pi - \pi^*$ base-centered photoexcitation with both IR and

UV probe photon energies.

Near-VDE photoexcitation

Near-VDE photoexcitation of $\Gamma^- \cdot \text{U} \cdot \text{H}_2\text{O}$ clusters produces cross-correlation limited formation of the DB anion with formation of the VB anion following in 400 fs. This DB to VB anion partial conversion timescale is slightly delayed from that of the $\Gamma^- \cdot \text{U}$ binary complex, and may reflect reorientation of the water molecule to a different binding site around uracil to a conformer with a lower conversion barrier. The VB anion long decay lifetime is considerably longer lived upon the addition of water compared to the DB anion and likely reflects preferential VB anion stabilization due to the increased interaction energy with the higher excess electron density of the VB anion. Γ^- is found to form bi-exponentially as in $\Gamma^- \cdot \text{U}$ clusters, suggesting that a similar decay mechanism is active.

$\pi - \pi^*$ photoexcitation

Following $\pi - \pi^*$ photoexcitation at 260 nm (4.77 eV), TRPES of $\Gamma^- \cdot \text{U} \cdot \text{H}_2\text{O}$ measures the instantaneous formation of the VB state of the complex with bi-exponential decay, expected to be by autodetachment, in ~ 500 fs and ~ 200 ps. The addition of water increases the long-time decay constant by an order of magnitude indicating that the presence of water stabilizes the VB anion relative to autodetachment. The measured autodetachment signal exhibits an intensity “overshoot” at positive time delays that may correspond to absorption of the probe pulse by the VB state to produce an additional source of autodetachment signal. The formation of Γ^- remains the major dissociation channel but with bi-exponential formation of Γ^- in tens and hundreds of ps. We expect that, as in $\pi - \pi^*$ photoexcited $\Gamma^- \cdot \text{U}$ clusters, formation of Γ^- in 10s of ps corresponds to internal conversion of the excited cluster to the ground state, followed by dissociation that may be hindered by a dynamical bottleneck. The long bi-exponential formation of Γ^- unique to $\Gamma^- \cdot \text{U} \cdot \text{H}_2\text{O}$ clusters in this pump energy regime may correspond to decay of the cluster to form a secondary species such as $\Gamma^- \cdot \text{H}_2\text{O}$, which can subsequently decay to produce Γ^- in 100s of ps.

1.9 References

- [1] E. Alizadeh and L. Sanche, “Precursors of solvated electrons in radiobiological physics and chemistry”, *Chem. Rev.* **112**, 5578–5602 (2012).
- [2] B. Boudaïffa, P. Cloutier, D. Hunting, M. A. Huels, and L. Sanche, “Resonant formation of DNA strand breaks by low-energy (3 to 20 eV) electrons”, *Science* **287**, 1658–1660 (2000).

- [3] F. Martin, P. D. Burrow, Z. L. Cai, P. Cloutier, D. Hunting, and L. Sanche, “DNA strand breaks induced by 0-4 eV electrons: The role of shape resonances”, *Phys. Rev. Lett.* **93**, 068101 (2004).
- [4] L. Sanche, “Low energy electron-driven damage in biomolecules”, *Eur. Phys. J. D* **35**, 367–390 (2005).
- [5] R. Barrios, P. Skurski, and J. Simons, “Mechanism for damage to DNA by low-energy electrons”, *J. Phys. Chem. B* **106**, 7991–7994 (2002).
- [6] J. Berdys, I. Anusiewicz, P. Skurski, and J. Simons, “Damage to model DNA fragments from very low-energy (< 1 eV) electrons”, *J. Am. Chem. Soc.* **126**, 6441–6447 (2004).
- [7] S. Ptasińska, S. Denifl, S. Gohlke, P. Scheier, E. Illenberger, and T. D. Märk, “Decomposition of thymidine by low-energy electrons: Implications for the molecular mechanisms of single-strand breaks in DNA”, *Angew. Chem. Int. Ed.* **45**, 1893–1896 (2006).
- [8] J. Simons, “How do low-energy (0.1-2 eV) electrons cause DNA-strand breaks?”, *Acc. Chem. Res.* **39**, 772–779 (2006).
- [9] H.-Y. Chen, P.-Y. Yang, H.-F. Chen, C.-L. Kao, and L.-W. Liao, “DFT reinvestigation of DNA strand breaks induced by electron attachment”, *J. Phys. Chem. B* **118**, 11137–11144 (2014).
- [10] D. Voet, W. B. Gratzer, R. A. Cox, and P. Doty, “Absorption spectra of nucleotides, polynucleotides, and nucleic acids in the far ultraviolet”, *Biopolymers* **1**, 193–208 (1963).
- [11] T. Gustavsson, Á. Bányász, E. Lazzarotto, D. Markovitsi, G. Scalmani, M. J. Frisch, V. Barone, and R. Improta, “Singlet excited-state behavior of uracil and thymine in aqueous solution: a combined experimental and computational study of 11 uracil derivatives”, *J. Am. Chem. Soc.* **128**, 607–619 (2006).
- [12] M. Sapunar, W. Domcke, and N. Došlić, “UV absorption spectra of DNA bases in the 350 - 190 nm range: assignment and state specific analysis of solvation effects”, *Phys. Chem. Chem. Phys.* **21**, 22782–22793 (2019).
- [13] J. H. Hendricks, S. A. Lyapustina, H. L. de Clercq, and K. H. Bowen, “The dipole bound-to-covalent anion transformation in uracil”, *J. Chem. Phys.* **108**, 8–11 (1998).
- [14] J. Schiedt, R. Weinkauff, D. M. Neumark, and E. W. Schlag, “Anion spectroscopy of uracil, thymine and the amino-oxo and amino-hydroxy tautomers of cytosine and their water clusters”, *Chem. Phys.* **239**, 511–524 (1998).
- [15] E. Surdutovich, A. V. Yakubovich, and A. V. Solov’yov, “Biodamage via shock waves initiated by irradiation with ions”, *Sci. Rep.* **3**, 1289 (2013).
- [16] J. Zhao, M. Wang, A. Fu, H. Yang, and Y. Bu, “Hydrated electron transfer to nucleobases in aqueous solutions revealed by ab initio molecular dynamics simulations”, *ChemPhysChem* **16**, 2348–2356 (2015).

- [17] J. Kohanoff, M. McAllister, G. A. Tribello, and B. Gu, “Interactions between low energy electrons and DNA: a perspective from first-principles simulations”, *J. Phys.: Condens. Matter* **29**, 383001 (2017).
- [18] B. H. Yun, Y. A. Lee, S. K. Kim, V. Kuzmin, A. Kolbanovskiy, P. C. Dedon, N. E. Geacintov, and V. Shafirovich, “Photosensitized oxidative DNA damage: from hole injection to chemical product formation and strand cleavage”, *J. Am. Chem. Soc.* **129**, 9321–9332 (2007).
- [19] A. Yokoya and T. Ito, “Photon-induced Auger effect in biological systems: a review”, *Int. J. Radiat. Biol.* **93**, 743–756 (2017).
- [20] C. E. Crespo-Hernández, B. Cohen, P. M. Hare, and B. Kohler, “Ultrafast excited-state dynamics in nucleic acids”, *Chem. Rev.* **104**, 1977–2020 (2004).
- [21] R. Improta, F. Santoro, and L. Blancafort, “Quantum mechanical studies on the photophysics and the photochemistry of nucleic acids and nucleobases”, *Chem. Rev.* **116**, 3540–3593 (2016).
- [22] A. P. Breen and J. A. Murphy, “Reactions of oxyl radicals with DNA”, *Free Radical Biol. Med.* **18**, 1033–1077 (1995).
- [23] M. Mucke, M. Braune, S. Barth, M. Förstel, T. Lischke, V. Ulrich, T. Arion, U. Becker, A. Bradshaw, and U. Hergenhausen, “A hitherto unrecognized source of low-energy electrons in water”, *Nat. Phys.* **6**, 143–146 (2010).
- [24] H. Nikjoo, S. Uehara, D. Emfietzoglou, and A. Brahme, “Heavy charged particles in radiation biology and biophysics”, *New J. Phys.* **10**, 075006 (2008).
- [25] Y. He, C. Wu, and W. Kong, “Photophysics of methyl-substituted uracils and thymines and their water complexes in the gas phase”, *J. Phys. Chem. A* **108**, 943–949 (2004).
- [26] A. Kumar and M. D. Sevilla, “Low-energy electron attachment to 5′-thymidine monophosphate: modeling single strand breaks through dissociative electron attachment”, *J. Phys. Chem. B* **111**, 5464–5474 (2007).
- [27] A. Kumar and M. D. Sevilla, “Role of excited states in low-energy electron (LEE) induced strand breaks in DNA model systems: influence of aqueous environment”, *ChemPhysChem* **10**, 1426–1430 (2009).
- [28] C. A. Morgado, K. Y. Pichugin, and L. Adamowicz, “Stabilization of an excess electron on uracil by water. Ab initio study”, *Phys. Chem. Chem. Phys.* **6**, 2758–2762 (2004).
- [29] T. Frigato, D. Svozil, and P. Jungwirth, “Valence- and dipole-bound anions of the thymine-water complex: ab initio characterization of the potential energy surfaces”, *J. Phys. Chem. A* **110**, 2916–2923 (2006).
- [30] H. Motegi and T. Takayanagi, “Theoretical study on the transformation mechanism between dipole-bound and valence-bound anion states of small uracil-water clusters and their photoelectron spectra”, *J. Mol. Struct.-THEOCHEM* **907**, 85–92 (2009).

- [31] K. D. Jordan and F. Wang, “Theory of dipole-bound anions”, *Annu. Rev. Phys. Chem.* **54**, 367–396 (2003).
- [32] J. Simons, “Molecular anions”, *J. Phys. Chem. A* **112**, 6401–6511 (2008).
- [33] M. J. Frisch, G. W. Trucks, H. B. Schlegel, G. E. Scuseria, M. A. Robb, J. R. Cheeseman, G. Scalmani, V. Barone, B. Mennucci, G. A. Petersson, H. Nakatsuji, M. Caricato, X. Li, H. P. Hratchian, A. F. Izmaylov, J. Bloino, G. Zheng, J. L. Sonnenberg, M. Hada, M. Ehara, K. Toyota, R. Fukuda, J. Hasegawa, M. Ishida, T. Nakajima, Y. Honda, O. Kitao, H. Nakai, T. Vreven, J. A. Montgomery Jr., J. E. Peralta, F. Ogliaro, M. J. Bearpark, J. Heyd, E. N. Brothers, K. N. Kudin, V. N. Staroverov, R. Kobayashi, J. Normand, K. Raghavachari, A. P. Rendell, J. C. Burant, S. S. Iyengar, J. Tomasi, M. Cossi, N. Rega, N. J. Millam, M. Klene, J. E. Knox, J. B. Cross, V. Bakken, C. Adamo, J. Jaramillo, R. Gomperts, R. E. Stratmann, O. Yazyev, A. J. Austin, R. Cammi, C. Pomelli, J. W. Ochterski, R. L. Martin, K. Morokuma, V. G. Zakrzewski, G. A. Voth, P. Salvador, J. J. Dannenberg, S. Dapprich, A. D. Daniels, Ö. Farkas, J. B. Foresman, J. V. Ortiz, J. Cioslowski, and D. J. Fox, *Gaussian 09, Revision C.01*, 2009.
- [34] R. Bachorz, W. Klopper, M. Gutowski, X. Li, and K. H. Bowen, “Photoelectron spectrum of valence anions of uracil and first-principles calculations of excess electron binding energies”, *J. Chem. Phys.* **129**, 054309 (2008).
- [35] T. Sommerfeld, “Intramolecular electron transfer from dipole-bound to valence orbitals: uracil and 5-chlorouracil”, *J. Phys. Chem. A* **108**, 9150–9154 (2004).
- [36] D. Svozil, T. Frigato, Z. Havlas, and P. Jungwirth, “Ab initio electronic structure of thymine anions”, *Phys. Chem. Chem. Phys.* **7**, 840–845 (2005).
- [37] T. Takayanagi, T. Asakura, and H. Motegi, “Theoretical study on the mechanism of low-energy dissociative electron attachment for uracil”, *J. Phys. Chem. A* **113**, 4795–4801 (2009).
- [38] O. Dolgounitcheva, V. G. Zakrzewski, and J. V. Ortiz, “Anionic and neutral complexes of uracil and water”, *J. Phys. Chem. A* **103**, 7912–7917 (1999).
- [39] O. Dolgounitcheva, V. G. Zakrzewski, and J. V. Ortiz, “Diffuse-bound and valence-bound anions of cytosine”, *J. Phys. Chem. A* **105**, 8782–8786 (2001).
- [40] R. Bachorz, W. Klopper, and M. Gutowski, “Coupled-cluster and explicitly correlated perturbation-theory calculations of the uracil anion”, *J. Chem. Phys.* **126**, 085101 (2007).
- [41] O. H. Crawford, “Negative ions of polar molecules”, *Mol. Phys.* **20**, 585–591 (1971).
- [42] S. Carles, F. Lecomte, J. P. Schermann, and C. Desfrancois, “Gas-phase experimental and theoretical studies of adenine, imidazole, pyrrole, and water non-covalent complexes”, *J. Phys. Chem. A* **104**, 10662–10668 (2000).

- [43] M. Hanus, M. Kabelac, J. Rejnek, F. Ryjacek, and P. Hobza, “Correlated ab initio study of nucleic acid bases and their tautomers in the gas phase, in a microhydrated environment, and in aqueous solution. Part 3. Adenine”, *J. Phys. Chem. B* **108**, 2087–2097 (2004).
- [44] I. Kulakowska, M. Geller, B. Lesyng, and K. L. Wierzchowski, “Dipole moments of 2,4-diketopyrimidines: Part II: Uracil, thymine and their derivatives”, *Biochim. Biophys. Acta, Nucleic Acids Protein Synth.* **361**, 119–130 (1974).
- [45] J. Smets, W. J. McCarthy, and L. Adamowicz, “Dipole-bound electron attachment to uracil-water complexes. Theoretical ab initio study”, *J. Phys. Chem.* **100**, 14655–14660 (1996).
- [46] J. Smets, D. M. A. Smith, Y. Elkadi, and L. Adamowicz, “Search for stable anions of uracil-water clusters. Ab initio theoretical studies”, *J. Phys. Chem. A* **101**, 9152–9156 (1997).
- [47] A. F. Jalbout and L. Adamowicz, “Dipole-bound anions of adenine-water clusters. ab initio study”, *J. Phys. Chem. A* **105**, 1033–1038 (2001).
- [48] M. Hanus, F. Ryjáček, M. Kabeláč, T. Kubař, T. V. Bogdan, S. A. Trygubenko, and P. Hobza, “Correlated ab initio study of nucleic acid bases and their tautomers in the gas phase, in a microhydrated environment and in aqueous solution. guanine: surprising stabilization of rare tautomers in aqueous solution”, *J. Am. Chem. Soc.* **125**, 7678–7688 (2003).
- [49] C. Desfrancois, H. Abdoul-Carime, and J.-P. Schermann, “Ground-state dipole-bound anions”, *Int. J. Mod. Phys. B* **10**, 1339–1395 (1996).
- [50] C. E. H. Dessent, J. Kim, and M. A. Johnson, “Spectroscopic observation of vibrational Feshbach resonances in near-threshold photoexcitation of $X^- \cdot \text{CH}_3\text{NO}_2$ ($X^- = \text{I}^-$ and Br^-)”, *Faraday Discuss.* **115**, 395–406 (2000).
- [51] T.-C. Jagau, K. B. Bravaya, and A. I. Krylov, “Extending quantum chemistry of bound states to electronic resonances”, *Annu. Rev. Phys. Chem.* **68**, 525–553 (2017).
- [52] D. M. Cyr, G. A. Bishea, M. G. Scarton, and M. A. Johnson, “Observation of charge-transfer excited states in the $\text{I}^- \cdot \text{CH}_3\text{I}$, $\text{I}^- \cdot \text{CH}_3\text{Br}$, and $\text{I}^- \cdot \text{CH}_2\text{Br}_2$ SN2 reaction intermediates using photofragmentation and photoelectron spectroscopies”, *J. Chem. Phys.* **97**, 5911–5914 (1992).
- [53] W. H. Robertson and M. A. Johnson, “Molecular aspects of halide ion hydration: the cluster approach”, *Annu. Rev. Phys. Chem.* **54**, 173–213 (2003).
- [54] C. E. H. Dessent, C. G. Bailey, and M. A. Johnson, “Dipole-bound excited states of the $\text{I}^- \cdot \text{CH}_3\text{CN}$ and $\text{I}^- \cdot (\text{CH}_3\text{CN})_2$ ion-molecule complexes: evidence for asymmetric solvation”, *J. Chem. Phys.* **103**, 2006–2015 (1995).

- [55] C. E. H. Dessent, C. G. Bailey, and M. A. Johnson, “Observation of the dipole-bound excited state of the Γ^- -acetone ion-molecule complex”, *J. Chem. Phys.* **102**, 6335–6338 (1995).
- [56] C. E. H. Dessent, J. Kim, and M. A. Johnson, “Photochemistry of halide ion-molecule clusters: dipole-bound excited states and the case for asymmetric solvation”, *Acc. Chem. Res.* **31**, 527–534 (1998).
- [57] W.-L. Li, A. Kunin, E. Matthews, N. Yoshikawa, C. E. H. Dessent, and D. M. Neumark, “Photodissociation dynamics of the iodide-uracil (Γ^- U) complex”, *J. Chem. Phys.* **145**, 044319 (2016).
- [58] E. Matthews, R. Cercola, G. Mensa-Bonsu, D. M. Neumark, and C. E. H. Dessent, “Photoexcitation of iodide ion-pyrimidine clusters above the electron detachment threshold: Intracuster electron transfer versus nucleobase-centred excitations”, *J. Chem. Phys.* **148**, 084304 (2018).
- [59] S. B. King, M. A. Yandell, A. B. Stephansen, and D. M. Neumark, “Time-resolved radiation chemistry: Dynamics of electron attachment to uracil following UV excitation of iodide-uracil complexes”, *J. Chem. Phys.* **141**, 224310 (2014).
- [60] S. B. King, A. B. Stephansen, Y. Yokoi, M. A. Yandell, A. Kunin, T. Takayanagi, and D. M. Neumark, “Electron accommodation dynamics in the DNA base thymine”, *J. Chem. Phys.* **143**, 024312 (2015).
- [61] A. Kunin, W.-L. Li, and D. M. Neumark, “Dynamics of electron attachment and photodissociation in iodide-uracil-water clusters via time-resolved photoelectron imaging”, *J. Chem. Phys.* **149**, 084301 (2018).
- [62] V. S. Batista, M. T. Zanni, B. J. Greenblatt, D. M. Neumark, and W. H. Miller, “Femtosecond photoelectron spectroscopy of the I_2^- anion: a semiclassical molecular dynamics simulation method”, *J. Chem. Phys.* **110**, 3736–3747 (1999).
- [63] J. Simons, “Propensity rules for vibration-induced electron detachment of anions”, *J. Am. Chem. Soc.* **103**, 3971–3976 (1981).
- [64] P. K. Acharya, R. A. Kendall, and J. Simons, “Vibration-induced electron detachment in molecular anions”, *J. Am. Chem. Soc.* **106**, 3402–3407 (1984).
- [65] E. E. B. Campbell and R. D. Levine, “Delayed ionization and fragmentation en route to thermionic emission: statistics and dynamics”, *Annu. Rev. Phys. Chem.* **51**, 65–98 (2000).
- [66] J. U. Andersen, E. Bonderup, and K. Hansen, “Thermionic emission from clusters”, *J. Phys. B: At., Mol. Opt. Phys.* **35**, R1 (2002).
- [67] R. Gilbert and S. Smith, *Theory of unimolecular and recombination reactions* (Blackwell Scientific Publications, London, 1990).
- [68] T. Baer and W. L. Hase, *Unimolecular reaction dynamics: theory and dynamics* (Oxford University Press, USA, New York, 1996).

- [69] J. I. Steinfeld, J. S. Francisco, and W. L. Hase, *Chemical kinetics and dynamics* (Prentice-Hall, New Jersey, 1999).
- [70] A. Kunin, W.-L. Li, and D. M. Neumark, “Time-resolved photoelectron imaging of iodide-nitromethane ($\text{I}^- \cdot \text{CH}_3\text{NO}_2$) photodissociation dynamics”, *Phys. Chem. Chem. Phys.* **18**, 33226–33232 (2016).
- [71] T. Beyer and D. F. Swinehart, “Number of multiply-restricted partitions”, *Commun. ACM* **16**, 379–379 (1973).
- [72] S. E. Stein and B. S. Rabinovitch, “Accurate evaluation of internal energy level sums and densities including anharmonic oscillators and hindered rotors”, *J. Chem. Phys.* **58**, 2438–2445 (1973).
- [73] M. J. T. Jordan, S. C. Smith, and R. G. Gilbert, “Variational transition state theory: a simple model for dissociation and recombination reactions of small species”, *J. Phys. Chem.* **95**, 8685–8694 (1991).
- [74] W. L. Hase and L. Zhu, “An analytic hindered rotor model for calculating micro-canonical variational unimolecular rate constants from reaction path properties”, *Int. J. Chem. Kinet.* **26**, 407–419 (1994).
- [75] W. Forst, “Sum and density of states of polyatomic systems with hindered rotors”, *J. Comput. Chem.* **17**, 954–961 (1996).
- [76] J. D. Gu, J. Leszczynski, and H. F. Schaefer, “Interactions of electrons with bare and hydrated biomolecules: from nucleic acid bases to DNA segments”, *Chem. Rev.* **112**, 5603–5640 (2012).
- [77] M. Gutowski, P. Skurski, A. I. Boldyrev, J. Simons, and K. D. Jordan, “Contribution of electron correlation to the stability of dipole-bound anionic states”, *Phys. Rev. A* **54**, 1906–1909 (1996).
- [78] X. Li, Z. Cai, and M. D. Sevilla, “DFT calculations of the electron affinities of nucleic acid bases: dealing with negative electron affinities”, *J. Phys. Chem. A* **106**, 1596–1603 (2002).
- [79] T. H. Dunning, “Gaussian basis sets for use in correlated molecular calculations. I. The atoms boron through neon and hydrogen”, *J. Chem. Phys.* **90**, 1007–1023 (1989).
- [80] P. Skurski, M. Gutowski, and J. Simons, “How to choose a one-electron basis set to reliably describe a dipole-bound anion”, *Int. J. Quantum Chem.* **80**, 1024–1038 (2000).
- [81] K. Jordan, “Comment on ab initio ground state potential energy surfaces for anions of polar molecules”, *Chem. Phys. Lett.* **69**, 611–613 (1980).
- [82] M. Guerra, “On the use of diffuse functions for estimating negative electron affinities with LCAO methods”, *Chem. Phys. Lett.* **167**, 315–319 (1990).
- [83] M. Guerra, “Role of standard diffuse functions for computing hyperfine splitting constants in radical anions”, *J. Phys. Chem. A* **103**, 5983–5988 (1999).

- [84] C. Xia, J. Peon, and B. Kohler, “Femtosecond electron ejection in liquid acetonitrile: evidence for cavity electrons and solvent anions”, *J. Chem. Phys.* **117**, 8855–8866 (2002).
- [85] Y. Yokoi, K. Kano, Y. Minoshima, and T. Takayanagi, “Application of long-range corrected density-functional theory to excess electron attachment to biomolecules”, *Comput. Theor. Chem.* **1046**, 99–106 (2014).
- [86] A. B. Stephansen, S. B. King, Y. Yokoi, Y. Minoshima, W.-L. Li, A. Kunin, T. Takayanagi, and D. M. Neumark, “Dynamics of dipole- and valence bound anions in iodide-adenine binary complexes: A time-resolved photoelectron imaging and quantum mechanical investigation”, *J. Chem. Phys.* **143**, 104308 (2015).
- [87] K. A. Peterson, D. Figgen, E. Goll, H. Stoll, and M. Dolg, “Systematically convergent basis sets with relativistic pseudopotentials. II. Small-core pseudopotentials and correlation consistent basis sets for the post-d group 16-18 elements”, *J. Chem. Phys.* **119**, 11113–11123 (2003).
- [88] K. A. Peterson, B. C. Shepler, D. Figgen, and H. Stoll, “On the spectroscopic and thermochemical properties of ClO, BrO, IO, and their anions”, *J. Phys. Chem. A* **110**, 13887 (2006).
- [89] M. A. Yandell, S. B. King, and D. M. Neumark, “Decay dynamics of nascent acetonitrile and nitromethane dipole-bound anions produced by intracluster charge-transfer”, *J. Chem. Phys.* **140**, 184317 (2014).
- [90] M. A. Yandell, S. B. King, and D. M. Neumark, “Time-resolved radiation chemistry: photoelectron imaging of transient negative ions of nucleobases”, *J. Am. Chem. Soc.* **135**, 2128–2131 (2013).
- [91] S. B. King, M. A. Yandell, and D. M. Neumark, “Time-resolved photoelectron imaging of the iodide-thymine and iodide-uracil binary cluster systems”, *Faraday Discuss.* **163**, 59–72 (2013).

Chapter 2

Experimental Methods

Now, here, you see, it takes all the running you can do, to keep in the same place. If you want to get somewhere else, you must run at least twice as fast as that!

Lewis Carroll

2.1 Overview

The original gas-phase time-resolved photoelectron spectroscopy (TRPES) experimental apparatus employed for the work in this thesis has been described in detail in the theses of Benjamin Jefferys Greenblatt [1] and Martin Zanni [2]. The upgrade to the current velocity map imaging (VMI) detection scheme is described in detail in the theses of Alison Davis [3] and Arthur Bragg [4]. The implementation and some details of the currently employed KMLabs femtosecond laser system are described in the theses of Graham Griffin [5] and Ryan Young [6]. The generation of iodide-nucleobase binary clusters as well as details regarding VMI detection and image reconstruction is also discussed in detail in the theses of Margaret Yandell [7] and Sarah King [8]. Details pertinent to the generation of iodide-nucleobase-water clusters are described here, as well as practical details and recent updates to the operation of the KMLabs laser system. Attempts to upgrade the current thermal desorption cluster source to one based on laser desorption are described in some detail later in Ch. 9.

An overview of the TRPES apparatus is presented in Fig. 2.1. Briefly, the gas phase iodide-associated clusters of interest are generated in a heated, pulsed anion cluster source. The cluster of interest is mass-selected and then intersected by time-delayed ultrafast pump and probe laser pulses. These pulses are generated by a KMLabs Ti:sapphire femtosecond laser system. Photodetached electrons are detected with a velocity map imaging (VMI) detection scheme and the electron binding energy (eBE) distributions are reconstructed for each time delay to produce the photoelectron spectrum. We now consider each of those components in more detail in the following sections.

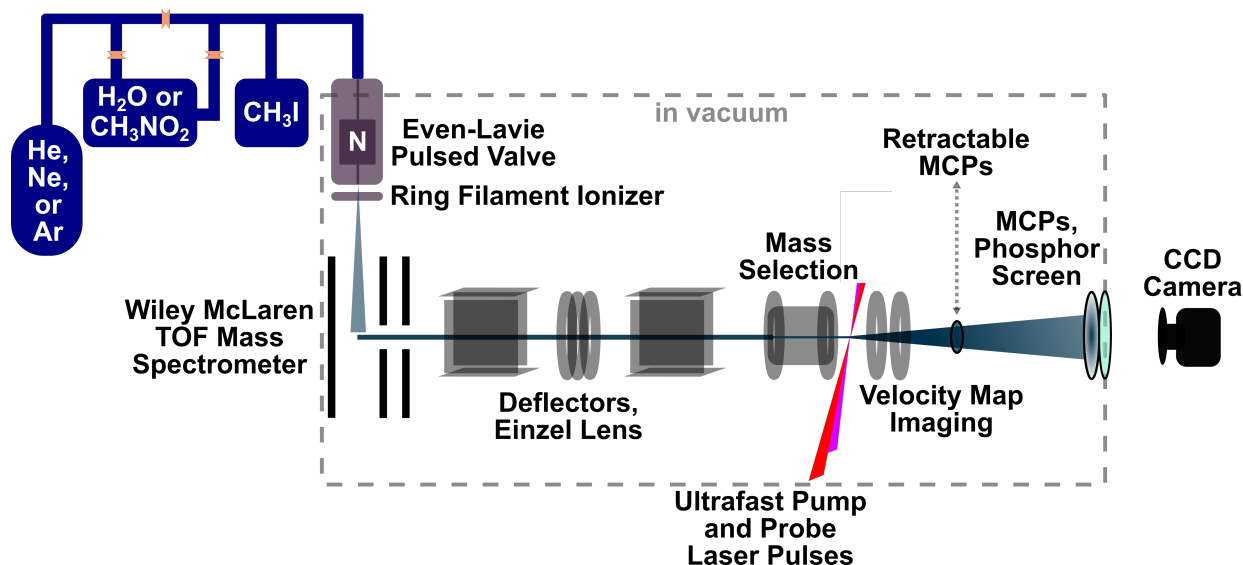


Figure 2.1: Experimental apparatus for TRPES of iodide-associated clusters in the Neumark group.

2.2 Cluster Source

Gas-phase clusters are formed by passing 375 – 550 kPa of helium, neon, or argon buffer gas over a reservoir of liquid methyl iodide (CH_3I , Sigma-Aldrich, $\geq 99.0\%$). For iodide-nitromethane ($\text{I}^- \cdot \text{CH}_3\text{NO}_2$) clusters, a reservoir is filled with liquid nitromethane (CH_3NO_2 , Sigma-Aldrich, $\geq 95\%$) and the reservoir is chilled in a bath of ice water for efficient cluster formation due to the high vapor pressure of CH_3NO_2 . For water-containing clusters, the reservoir is instead filled with deionized water, and helium backing gas should be used. The reservoir has two gas line connections as shown in Fig. 2.1; the water should come up just below the level of the horizontal arm connection. The water reservoir, CH_3I reservoir, and the rest of the gas line to the chamber is wrapped in heating tape and heated to 20 – 40 °C. The gas line towards the chamber should be heated to a somewhat higher temperature than the water reservoir. The upper gas line connecting the backing gas to the chamber should be closed to force the helium to pass over the water.

The gas mixture is flowed into an Even-Lavie pulsed solenoid valve (HT HP HRR E.L.-7-3-2004 #160) operating at 500 Hz [9]. Although the valve is capable of running at 1 kHz, the produced molecular beam is not stable when the valve is run higher than 550 Hz. The gas is flowed to a filter-capped solid sample holder (350 mm³) where solid samples of nucleobases of interest may be loaded. The sample holder sits inside the valve body which is enclosed by a resistive heating unit. Without heating, normal valve operation will heat the valve body to ~ 70 °C, so a water cooling jacket should be used for samples for which heating is undesirable (e.g. CH_3NO_2). Although the valve temperature controller can heat the valve up to 300 °C, heating above 240 °C has been found to compromise the sealing of the polyimide gaskets (Potomac Photonics, Inc.). The valve is sealed by a stainless steel high pressure assembly consisting of an outer tube, plunger, spring, and two ruby guides for the plunger. Over time, the ends of the plunger wear down and the plunger becomes slightly shortened; when this happens, sealing the valve may become difficult or impossible and the plunger must be replaced. The plunger rests against a trumpet shape, 150 μm (42° cone) supersonic expansion nozzle. The spring forces the plunger to the “closed” position, and when a current is applied a strong magnetic field forces the valve open for $\sim 10 - 15$ μs (set by the user) to allow the gas to supersonically expand into vacuum.

Supersonic expansion allows for the formation of clusters. Briefly, the adiabatic expansion through a small nozzle from a high pressure region (backed valve) to a low pressure region (vacuum chamber) collisionally cools the gas molecules. The internal energy of the molecules is thus converted to translational kinetic energy, producing a high speed beam of internally cold molecules or clusters. For a nozzle size larger than the mean free path of the gas molecules, i.e. the average distance a molecule can travel before meeting a collision partner, collisions will be frequent and result in effective cooling and clustering. The mean free path (λ) for a particle described by the ideal gas law is given by Eq. 2.1:

$$\lambda = \frac{k_{\text{B}}T}{\sqrt{2}\pi d^2 p} \quad (2.1)$$

where k_{B} is the Boltzmann constant, T is the temperature, d is the molecular or atomic diameter, and p is the gas pressure. For example, the mean free path for 400 kPa of room temperature helium gas is ~ 30 nm, significantly smaller than the 150 μm valve nozzle.

The center of a thoriated tungsten ring filament ionizer sits 7 mm below the valve expansion nozzle to produce anions and anionic clusters. High energy electron impact ionization of the backing gas produces lower energy secondary electrons, and attachment of a secondary electron to the cluster creates the anions of interest. The filament carries 4 – 7 A and is biased by a 285 – 400 V pulsed voltage. Depending on the backing gas and cluster of interest, the ionizer is typically pulsed ~ 70 – 115 μs after the valve fires. The final anionic clusters produced in our cluster source have an internal energy spread of up to ~ 300 meV above the ground state. A skimmer collimates the molecular beam as it passes from the “source” vacuum region with the valve to the “0D” differentially pumped region that encloses a Wiley-McLaren time-of-flight (TOF) mass spectrometer. Note that for clusters containing water, the use of liquid nitrogen foreline traps for both the source and 0D regions is highly recommended to prolong pump oil longevity.

2.3 Cluster Selection and Optimization

The collimated molecular beam of clusters passes into a Wiley-McLaren TOF mass spectrometer [10] in which the clusters are orthogonally extracted and separated in time based on their mass. The repeller plate is held at -2 kV and the extractor plate is typically most effective in the range of ~ -1.4 kV – -1.7 kV. The CH_3I in the system may be used to calibrate the Wiley-McLaren for any cluster of interest based on the masses and known typical TOFs in our apparatus for I^- (126.9 amu, ~ 33 μs), $\text{I}^- \cdot \text{CH}_3\text{I}$ (268.8 amu, ~ 47 – 48 μs), and $\text{I}^- \cdot (\text{CH}_3\text{I})_2$ (410.8 amu, ~ 58 μs). From these, the TOF for a given mass cluster can be interpolated or extrapolated within the mass range of ~ 50 – 450 amu. An example mass spectrum for typical source conditions to produce iodide-uracil-water ($\text{I}^- \cdot \text{U} \cdot \text{H}_2\text{O}$) is shown in Fig 2.2.

Two sets of deflectors are used to steer the clusters downstream in the “1D” and “2D” differentially pumped regions ($\sim \pm 20$ V) and an einzel lens radially focuses the beam (0.65 – 0.8 kV). Finally, a rereferencing tube serves two functions: first, it acts as a mass gate to isolate the species of interest based on its time-of-flight; second, it acts as a potential switch to rereference the high voltage of the experiment to ground [11]. The second plate of the rereferencing tube serves as the repeller plate for the velocity map imaging (VMI) detection scheme, described in more detail in the following subsection.

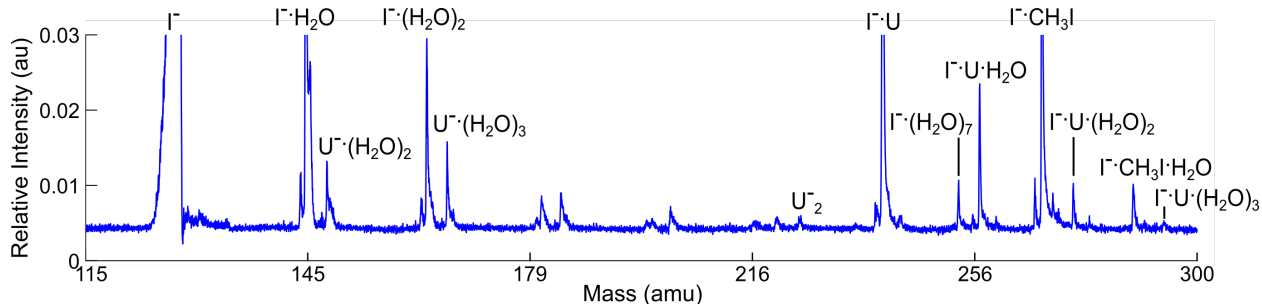


Figure 2.2: Example mass spectrum for the production of $\text{I}^- \cdot \text{U} \cdot (\text{H}_2\text{O})_n$ clusters. The y-axis provides the cluster intensity relative to I^- , which is the most intense feature in the spectrum.

2.4 Detection

A retractable ion detector close to the region of laser interaction allows one to optimize the ion signal and ensure proper mass selection. 25 mm microchannel plates (MCPs) are mounted on a push-pull vacuum sealed linear motion feedthrough and are retracted to the edge of the chamber once the ion signal is ideal for the experiment to allow photodetached electrons to reach a second set of MCPs further downstream.

A velocity map imaging detection scheme [12, 13] is used to measure the photoelectron kinetic energy (eKE) and photoelectron angular distributions (PAD) of the ejected electrons. The repeller plate, which is part of the rereferencing tube as described above, is held at -4 kV and the extraction plate at -2.811 kV. With the current Wiley-McLaren voltage settings of -2 kV for the repeller plate, the rereferencing tube/VMI repeller can be reduced as low as -1.5 kV before the mass-gating properties are compromised. This is also the voltage limit before the VMI image becomes too large to visualize photodetachment of both spin orbit peaks of I^- on the detector for calibration (see below). The photodetached electrons are detected with a pair of chevron-stacked 70 mm MCPs ($\sim 1.5 - 1.6$ kV), a phosphor screen (5.25 kV), and a charge-coupled device (CCD) camera. The camera images are read by a LabView data acquisition program [6] on the data collection computer. Basis Set EXpansion (BASEX) reconstruction methods [14] are used to reconstruct the photoelectron kinetic energy distributions, and Polar Onion Peeling (POP) [15, 16] is used for the PADs. The details of our VMI and reconstruction methods have been described in considerable detail recently in Margaret Yandell's [7] and Sarah King's [8] theses.

The VMI is calibrated by photodetaching I^- to the $\text{I}(^2\text{P}_{3/2})$ and $\text{I}(^2\text{P}_{1/2})$ lower and upper spin-orbit states of iodine and scaling the eKE axis to bring the spin-orbit splitting of the two peaks to match the known literature value of 0.9427 eV [17]. These peaks are 3.0589 eV for detachment to $\text{I}(^2\text{P}_{3/2})$ [18] and 4.0016 eV for detachment to $\text{I}(^2\text{P}_{1/2})$. For the typical mass gate voltage of -4 kV and extraction plate voltage of -2.811 kV, the VMI eKE

calibration factor is usually ~ 1.06 . Photodetachment of iodide is also used to calibrate the exact laser wavelengths generated on the table. For typical 800 nm probe pulses of 80 – 100 $\mu\text{J}/\text{pulse}$, there is enough intensity to generate a small amount of 2-photon detachment to the lower spin orbit state of iodine; all other pulses employed have enough energy to detach Γ^- directly. The resolution of our experiment is approximately 0.05 eV, and is limited by the femtosecond laser pulses rather than the VMI design.

2.5 Triggering

Although the triggering scheme for the apparatus is subject to change as equipment upgrades are made, it is valuable to consider the general triggering scheme since much of the apparatus is pulsed. The KMLabs femtosecond laser system provides the reference trigger for the machine. As the laser operates at 1 kHz repetition rate but the Even-Lavie pulsed valve is only stable at 500 Hz, the KMLabs trigger is first cut in half (DEI PDG-2510) before triggering the cluster source. Note that the reference trigger from the laser is a 3 V signal and is insufficient to trigger this DEI box which requires a trigger of 4 V. Therefore, the reference trigger is first taken to a Stanford DG535 digital delay generator (DDG) box to produce a high impedance output of 4 V before it can be reduced to 500 Hz to trigger the rest of the experiment.

The triggering timescales and pulsewidths for the experiment are controlled by multiple Stanford DG535 DDG boxes. A general scheme is provided in Fig. 2.3. It is important that the cluster source components and mass gate all be triggered relative to one another so that the experimental timing can be delayed to appropriately line up the ions, laser, and detector. The time of arrival for the laser at the chamber is fixed by the KMLabs laser output and the path length for the beam on the table; the triggering for the clusters is therefore delayed so that the pulsed packet of ions will arrive to meet the laser correctly. This “offset” time for the experiment must be optimized daily and is referred to in our lab as the “A-timing”.

The approximate relative firing times between the Even-Lavie valve, ionizer, and Wiley-McLaren plates are shown in Fig. 2.3. The time of the Wiley-McLaren firing is used as the trigger for the oscilloscope used to monitor the ion signal. Thus, the cluster TOFs referenced in Sec. 2.3 above are relative to the onset of the Wiley-McLaren firing. The optimal time delay between the pulses for the repeller and extractor plates for generation of clusters of ~ 250 amu was found to be -440 ns (i.e. extractor plate fires slightly prior to repeller); this timing is highly sensitive to the cabling length used and may be optimized for focusing different cluster masses as needed. Note that a number of previously used homebuilt pulse boxes [2] including those used for the ionizer and Wiley-McLaren have been replaced with DEI PVX-4140 boxes after problems arose with the stability of the produced TTL pulses with age. Note that the $\pm\text{AB}$ gating for triggering DEI boxes is typically the opposite of the gate required to trigger the homebuilt boxes, as reflected in Fig. 2.3.

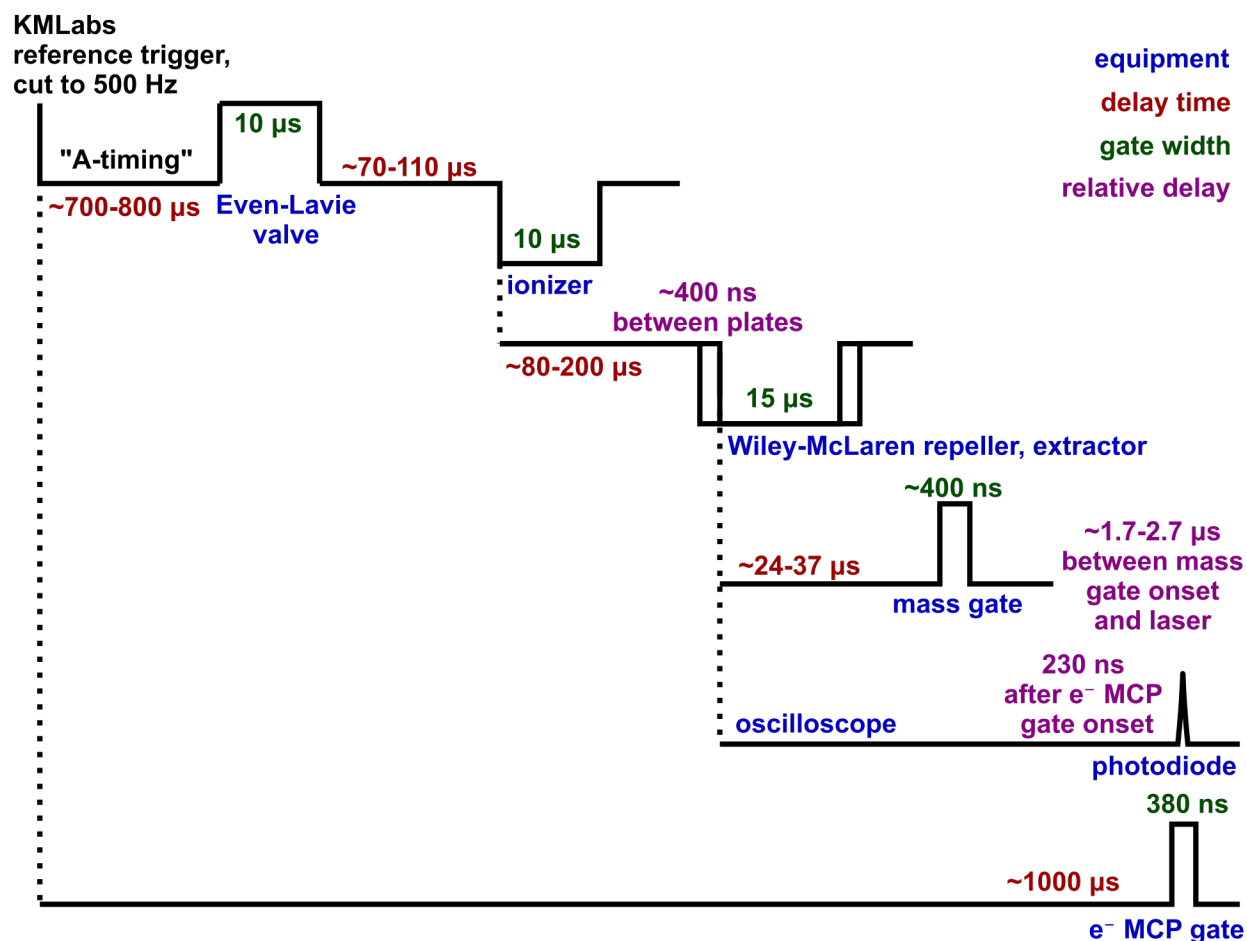


Figure 2.3: Triggering scheme for the experiment. Each row corresponds to a separate DDG box (or the oscilloscope). Vertical dashed lines indicate the trigger for each item on separate boxes. Not to scale.

The Wiley-McLaren firing onset also provides the trigger for the rereferencing tube/mass gate. The mass gate is held at -4 kV and pulsed to ground briefly ($\sim 400 \text{ ns}$) at the arrival time of the mass of interest to allow the desired species to enter and reject the others. The duration of the mass gate can be decreased as necessary for better isolation if other species exhibit similar TOFs as the desired cluster (e.g. in $\text{I}^- \cdot \text{U} \cdot \text{H}_2\text{O}$ clusters). The electron detector MCPs are gated to maintain the front plate voltage at 700 V and pulse to ground for the arrival of the ejected electrons. Maintaining the front plate of the pair at a higher voltage reduces the gain for the impinging residual ions ($\sim 6 - 8 \mu\text{s}$ later) to protect the MCPs from damage. The gate is 380 ns wide and must pulse to ground 230 ns prior to the signal of the laser arrival as read by a photodiode immediately in front of the chamber entrance window.

2.6 Femtosecond Laser System

We first provide an overview of the general laser system, followed by detailed subsections dedicated to the various stages of the ultrafast system and the triggering and software that controls the laser. The principles of ultrafast laser design and operation have been reviewed in considerable detail [19–23], so the focus here is on only the elements specific to our system. In brief, we use a 2008 KMLabs Ti:sapphire Griffin oscillator and multi-pass Dragon amplifier system that outputs 1 kHz, 40 fs pulses centered at 790 nm with approximately 2 mJ/pulse. The oscillator is pumped by a Coherent Verdi Nd:YVO₄ laser, while the amplifier is pumped by a Lee Laser Nd:YAG laser. The laser hardware, power supplies, and triggering are interfaced by a computer with KMCtrl 5.1 software to operate the oscillator, and DragonMaster V1 software to control the amplifier and to interface the entire system together. A number of original, proprietary optical components and other hardware in the system have been replaced since 2015; the manufacturer and item are parenthetically indicated here wherever possible.

Oscillator

The KMLabs Griffin Oscillator produces near transform-limited (≤ 20 fs) pulses of approximately 3.5 – 4.5 nJ at a repetition rate of 83 MHz centered near 785 nm with ~ 45 – 65 nm of bandwidth. The oscillator [24] relies on Kerr lens modelocking [25] enabled by the Kerr nonlinearity of the Ti:sapphire gain medium [26] to produce a pulsetrain of ultrashort pulses.

The oscillator is pumped by a Coherent Verdi V-5 Nd:YVO₄ which outputs 4.2 W continuous wave (CW) light at 532 nm. The Verdi rests on a cooling block that is cooled by an 18.7 °C water chiller. The output beam is periscoped up (Lambda Research Optics VEAL-PM-1906B-VIS) and steered in (Thorlabs BB1-E02) at 16° into the cavity of the Griffin oscillator. The oscillator cavity consists of a focusing lens for the pump and two curved mirrors, each on individual translation stages, with a Ti:sapphire crystal on a rotation stage and translation rail. Two irises in the cavity provide the alignment for the green pump beam to the output coupler (CVI Laser Optics UVFS 30 arcmin wedge, custom coated for 10% transmission). In CW lasing mode, the oscillator typically produces ~ 800 mW of power, although this can be as high as 1 W. Shortening the cavity by ~ 0.65 – 0.7 mm [27] allows sufficiently strong Kerr lens self-focusing to suppress CW operation and enable passive modelocking when a prism is jogged.

The cavity contains a fused silica prism pair for compensation of group velocity dispersion (GVD) introduced by the Ti:sapphire crystal [28, 29]. Note that overinsertion of the prisms can create problems with achieving stable modelocking. The correct prism position is determined by pulling out each prism one at a time until lasing is lost, and then reinserting the prism ~ 100 stepper motor steps to stabilize the power. In May 2019, P2, the prism

closest to the output coupler, was unbolted and physically translated to allow for better range of movement fully across the beam.

It is helpful to note that the range of prism movement allowed by the stepper motors extends beyond the translation range provided in the KMCtrl 5.1 program. The KMCtrl program loads default settings from a preferences.txt file, which dictates the initial prism position on a scale from 0 – 700. The value of this number in the preferences file does not move the position of the motors/prisms in the cavity, only the initial reading in the program. Therefore, if the prisms are at the translation limit in the program and a wider range of translation is needed, the .txt file can be edited to set the starting position in the program to a lower or higher value as needed, and then upon loading the program the prism positions can be toggled up to new program or stepper motor limit.

Stretcher and Pulse Picking

The ultrashort pulse from the oscillator must be temporally stretched before it can be efficiently amplified to avoid losses from self-focusing and self-phase modulation in the Ti:sapphire crystal [30, 31]. Stretching also prevents damage in the amplifier by high peak power.

The beam from the oscillator is periscoped up (Lambda Research Optics Inc. PAG-PM-1906B-NIR) into the stretcher and collimated. Note that our stretcher input here does not contain a Faraday rotator to prevent beam propagation back to the oscillator, but this has generally not been found to be an issue in our system. However, the stretcher design could be simplified considerably by employing a Faraday rotator and removing several meters of path length of silver mirrors steering the beam into and out from the stretcher. Reducing the number of silver steering mirrors in this manner would also provide more seed power to the amplifier. Our stretcher is a single-grating stretcher with a parabolic mirror and two flat mirrors [32]. The final, temporally stretched pulse can be as long as 200 – 300 ps. When properly aligned, the stretcher has >40% efficiency and should yield a stretched beam power >100 mW.

A Pockels cell and two polarizers are used to reduce the seed repetition rate to 1 kHz for the amplifier by rotating the polarization of select pulses [21]. The Pockels cell and driver are housed in a proprietary KMLabs housing. The housing uses the same 18.7 °C chilled water supply as the Coherent Verdi. The Pockels cell high voltage is 5.3 kV and the current is <-1.0 mA. Bergmann Messgeräte Entwicklung (BME) KG Pockels cell driver heads are recommended if replacement is eventually needed. Back-propagating amplified spontaneous emission (ASE) from a slightly misaligned amplifier ring will degrade the polarizers and require eventual replacement as well. With the Pockels cell defeated by a waveplate in the beam, the seed power entering the amplifier ring should be approximately 100 mW.

Amplifier

The Dragon amplifier is a 13-pass multipass [33] Ti:sapphire amplifier that produces a 1 kHz amplified, uncompressed beam of 3.0 – 3.5 mJ/pulse. The amplifier is pumped by a Lee Laser Nd:YAG. The multipass mirrors form an amplifier ring where the 13 passes are overlapped only at the crystal. Two 500 mm focal length curved mirrors focus the 785 nm seed at the crystal, while the rest of the amplifier mirrors (Alpine Research Optics) serve to steer the recollimated beam. A camera views the crystal to verify the overlap of the seed passes as well as the pump beam overlap with the seed.

The KMLabs amplifier employs helium gas cryocooling [34] for the Ti:sapphire crystal to help prevent problems that arise from thermal lensing due to the high energy load on the pumped amplifier crystal [35]. For cryocooling, the crystal is mounted in a small vacuum chamber (cryocell) and held under vacuum by a 2 L/s ion pump (Duniway VA2-MINI-VAC-B). Windows mounted at Brewster’s angle are Torr-Sealed to tubes mounted to the cryocell (Duniway G-045X conflat) for the input and output beams. The cryocell typically achieves a final temperature of -225 °C with no pump load or -223 °C at full pump power. The pressure indicated by the ion pump at this lowest temperature is typically 1×10^{-9} and reads “0.0” μA of current. At room temperature, the pressure is $\leq 10^{-6}$ Torr with a current reading of $< 10 \mu\text{A}$. If the ion pump current exceeds 220 μA while the laser is amplified, the pump laser will be tripped off for safety. With these operating pressures, the ion pump has a typical lifetime of approximately 3 – 6 years, although building power failure has been found to shorten this lifespan.

The Ti:sapphire crystal is Brewster cut, 10 mm thick and mounted in a copper mount. A 0.01” thickness 3” x 3” sheet of indium foil (ESPI Metals, 5025-002) is cut to match the size of the crystal mount. The indium sheet acts as a gasket and a thermal interface between the crystal mount and the cryohead. Images of both of these are provided in Fig. 2.4. Note that cryocooled Ti:sapphire has maximum gain efficiency centered closer to 785 nm, so it is advantageous when aligning the oscillator to have more intensity towards somewhat bluer wavelengths [20]. The original optics in the amplifier ring are coated closer to 800 nm; gradual replacement of these mirrors as they age with new mirrors coated slightly bluer will ultimately improve the amplifier efficiency.

The amplifier crystal was replaced with a refurbished crystal in April 2017 after no clean spots remained on the crystal for amplification. The exact seating of the foil, crystal housing, and thermocouple contacts when assembled at room temperature following crystal replacement can affect the exact temperature reading in the system upon cryocooling. It was also found that, following the crystal replacement, the seed beam in the ring is imperfectly collimated. The two 500 mm focal length mirrors that focus the beam are mounted to account for the difference in index of refraction in the Ti:sapphire crystal compared to air. In May 2019, these curved mirrors were unmounted and moved slightly in an attempt to fix



Figure 2.4: Left: Mounted amplifier crystal. A small burn can be seen on the bottom right corner of the crystal. Center: Indium foil cut to fit the amplifier crystal mount. Right: Aperture mask with fully amplified beam. Increasing beam divergence can be seen with successive passes (right to left).

the collimation in the ring, but perfect collimation was not achieved. As a result, it is not possible to perfectly overlap the last few passes in the crystal.

An aperture mask is used in the amplifier to aid alignment, help suppress ASE, and control beam divergence that can arise from thermal lensing [36]. The mask currently in use has 12 apertures (the 13th pass through the amplifier is picked off before the mask), with a 2 mm diameter aperture for the first pass and 1.75 mm diameter apertures for the subsequent passes. The spacing between the center of adjacent holes is 3 mm. The mask should be level and placed roughly orthogonal to the seed beams, although it is not critical that the placement be perfectly perpendicular. A gain flattening filter could be implemented in front of the mask to slice off the spectral center for the middle $\sim 4 - 8$ passes. This combats gain narrowing in the Ti:sapphire crystal that occurs as a result of the amplification process [20], and it could ultimately produce pulse durations of sub-20 fs from the system at the cost of relatively minor power loss.

Amplifier Pump

The amplifier is pumped by a 2011 Lee Laser (now defunct, acquired by Coherent) LDP-200MQG Nd:YAG laser operating at 1 kHz and frequency-doubled to 532 nm. The pump temperature for the lasing cooling water should be set to 20.0 °C, while the LBO crystal temperature for second harmonic generation (SHG) should be 32.6 °C. These settings yield the maximum power output at the laser head of approximately 20.3 W (20.8 A) at the typical operating setting of 69% current on the power supply. These temperatures should be occasionally tuned to optimize power output as the laser ages. The Lee laser is externally

triggered by a DDG card that is triggered by the modelocked pulse train in the oscillator (see Triggering section below). The Lee laser power supply default error is “Laserbox Open” and may result from a multitude of situations other than the lids of the laser box actually being open. These include: oscillator is not modelocked, Lee laser is set to externally triggered but not receiving a stable trigger, and other internal errors with the Lee laser.

The Lee laser output is periscoped up (CVI Y2-0725-45P) and then telescoped up by a Galilean telescope (CVI PLCC-25.4-38.6-C-532, PLCX-25.4-103.0-C-532 nm) before being focused down (CVI PLCX-25.4-206.0-UV-532 nm) slightly in front of the Ti:sapphire amplifier crystal. The lens that focuses into the crystal is on a translation stage so that the focusing may be fine-tuned. The focus may be selected to be somewhat in front of the crystal or somewhat behind, but should not be directly at the crystal as this will produce too much gain, as evidenced by the power differential between the pump-only power and the amplified power. It was found in May 2019 that the telescope design may yield a pump beam that is overly large on many of the optics causing unnecessary power loss on the edges of the beam. Re-design of the telescope will improve the attainable pump power at the entrance to the cryocell which is currently 15.8 W. Ideally, there should be $\leq 10\%$ power loss from the laser head to the cryocell. Note that fused silica is necessarily a better choice than BK7 as the substrate for these telescope lenses as fused silica has higher resistance to color-center (f-center) formation. These material defect sites of uneven absorption are likely to degrade the pump beam quality.

Compressor

The compressor is composed of two compressor gratings (Newport Corporation Richardson Gratings, 53114ZD02-340R, 2" x 4", 1200 grooves/mm) and a silver-coated roof mirror. The gratings are mounted individually in rotatable, translatable tip-tilt mounts to control the leveling, grating parallelism, and grating separation. The first compressor grating has been translated on the breadboard from its initial position to strike a cleaner portion of the grating to extend its lifetime. The angle of incidence for the first compressor grating should be similar to but not exactly match the angle of incidence in the stretcher to account for dispersion introduced by the materials in the amplifier and Pockels cell [20]. Misalignment of the grating parallelism or incident angle can manifest as problems with second (group delay, GDD) or third-order (GVD) dispersion, respectively, detectable when characterizing the pulse as described in more detail in the following subsection. Grating parallelism can be ensured by picking off a very small portion of the beam with window wedges and neutral density (ND) filters and focusing the beam with a 50 cm focal lens onto a camera. The focal spot should be round; if the gratings are not parallel, the beam will focus to a horizontal line. Note that the mount for the second compressor grating has a considerable amount of slip in the rotation micrometer so extreme care must be taken to ensure control of the direction of the high power beam.

The current compressor efficiency is $\sim 60\%$ yielding a final power output of approximately $1.7 - 2.1$ mJ/pulse. Note that while ruled diffraction gratings generally have a high damage threshold, they unfortunately also have significant power loss. In the future, highly efficient holographic gratings could be employed along with a dielectric-coated roof mirror instead of silver.

Pulse characterization- GRENOUILLE

A Swamp Optics Near-IR 8-20-USB GRENOUILLE (GRating-Eliminated No-nonsense Observation of Ultrafast Incident Laser Light E-fields) is used to characterize the laser pulse. GRENOUILLE is a robust, simplified variant of Frequency-Resolved Optical Gating (FROG) and provides many advantages over autocorrelation measurements that have been used in the past [37, 38]. QuickFrog software (Femtosoftware Technologies) is used to retrieve the pulse.

The GRENOUILLE has two read-out modes: spatial mode and temporal mode. Spatial mode is used to correctly align the beam inside the GRENOUILLE, and then temporal mode may be used to read out the FROG measurement and the temporal and spectral phase and full width at half maximum (FWHM). The internal cameras in the GRENOUILLE are extremely sensitive and are limited to ~ 100 nJ of power from the KMLabs system before they may become permanently burned. To attenuate the beam, it is necessarily better to use at least one window wedge to sample the beam rather than multiple ND filters if the most accurate measurement is desired. It is also important that the input alignment iris not be overly closed so as to avoid introducing a diffraction pattern to the beam. However, the intensity bars in the program (Fig. 2.5, upper right) must remain at 3 green bars to ensure enough intensity for an accurate measurement; too little intensity will yield an artificially short or clean pulse.

Issues with third-order dispersion are observed in a GRENOUILLE trace as a smaller peak on one side of the pulse that may increase or decrease in intensity as the inter-grating distance is tuned but not disappear fully. It is corrected by adjusting the angle of incidence on the first compressor grating while maintaining grating parallelism and then re-optimizing the inter-grating distance.

Note that the QuickFrog program has trouble correctly reading in both the spatial and temporal cameras of the GRENOUILLE at the same time due to a very small damaged electrical connection. If the spatial camera is incorrectly read in as the temporal camera, the pulse duration will read $\geq 60 - 100$ fs and cannot be made shorter. If the temporal camera is read in as the spatial camera, the observed beam profile will be overly small in diameter and will saturate in intensity very easily.

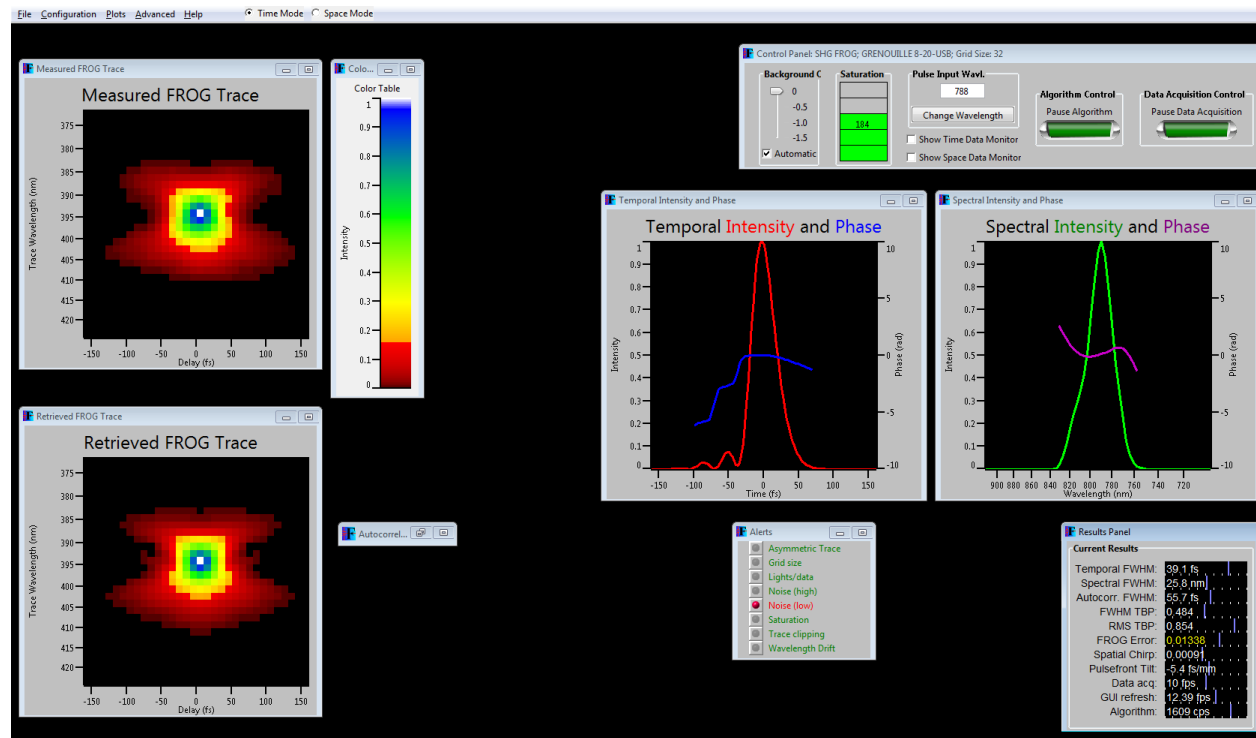


Figure 2.5: Example image from the QuickFrog pulse retrieval software of the temporal read-out for a typical 39 fs FWHM pulse.

Software, Triggering, and Interlocks

In July 2015, the original motherboard and hard drive for the KM computer controlling the software and the interface of the software with the laser hardware failed. The software was sourced and reinstalled on separate computers on two occasions following additional computer failure but unfortunately full, failure-free communication between the KM software and hardware could not be recovered. In April 2019, a gently used KM computer that previously operated a KMLabs Griffin Oscillator and Dragon Amplifier of the same age was acquired from Prof. Stephen Leone’s group at UC Berkeley, and correctly connecting our existing KM hardware into this recovered KM computer successfully restored functionality and full hardware-to-software communication.

The triggering and interlocks for the laser system are derived from the modelocking of the oscillator as major damage can occur in the system if, for example, CW light is amplified. A schematic of the triggering system is shown in Fig. 2.6. A photodiode in the oscillator cavity views the rear face of the Ti:sapphire crystal and the pulsetrain registered by the photodiode provides the trigger for the rest of the laser system. The intensity and stability of the light on the photodiode is thus critical to the operation of the laser. The “Oscillator Monitor” BNC

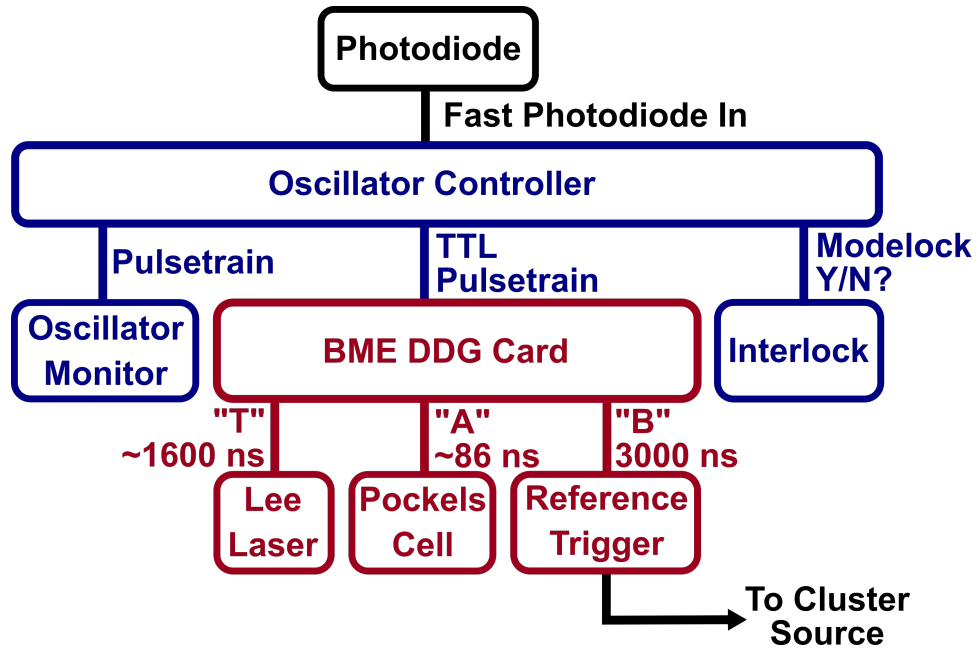


Figure 2.6: KMLabs laser triggering system. The photodiode in the oscillator cavity (black) views the modelocked pulsetrain to trigger the oscillator controller unit (blue). The pulsetrain can be observed (oscillator monitor), interlocked, or converted to TTL to trigger the amplifier box components (red).

read-out from the KM computer provides a view of this photodiode signal. When viewed on a self-triggered oscilloscope at $50\ \Omega$ termination, the amplitude of the pulsetrain should be approximately $60 - 80\ \text{mV}$ to ensure stable triggering. Even if the “Modelock Yes/No” interlock is not tripped, lower intensity on the photodiode ($\leq 35 - 40\ \text{mV}$) provides unstable triggering for the rest of the system. Typically if this occurs, the DragonMaster program reads out an “Actual PRF” (pulse repetition frequency) of $0.7 - 0.9\ \text{kHz}$ instead of $1\ \text{kHz}$. As the KM laser provides the reference trigger for the cluster source of the experiment, unstable triggering can also create problems with pressure stability in the chamber, for example.

The $83\ \text{MHz}$ oscillator pulsetrain is converted to TTL and read by a DDG PCI card (Bergmann Messgeräte Entwicklung KG BME-SG02p5) that sets the repetition rate as $1\ \text{kHz}$ and then provides this $1\ \text{kHz}$ trigger for the Pockels cell and amplifier pump laser. The DDG card produces 3 TTL outputs; the channels for the Pockels cell and Lee laser are $2\ \text{V}$ signals and the final channel produces a reference trigger output of $3\ \text{V}$. When operating correctly, the channels have $<250\ \text{ps}$ jitter. In June 2017, the DDG card failed and was found to produce TTL outputs with several hundred ns up to tens of μs of jitter on the rising edge for each channel. This produced an unstable reference trigger for the experiment and unstable timing for the pump laser, and the card was replaced. Note that similar

problems with jitter in this DDG card can manifest if the oscillator photodiode intensity is too weak, as described above.

In October 2016 the “Modelock Yes/No” sensor that provides an interlock fault for amplifier failed. The output is high/low 3 V/0 V for modelocked/not modelocked. Failure of the chip caused a constant voltage of 0.7 V, enough to trigger the system to always view “Modelock Yes” even with the oscillator completely off. The main controller board in the oscillator controller was replaced with a new board to remedy this problem, but the new motor control board for the prism stepper motors was determined to be incompatible with the older prism pair in our oscillator. As a result, the motor board from the old oscillator controller was substituted into the new oscillator controller. Following this change, the prism operation in the KMCtrl software was found to be swapped from the original settings, i.e. “P1” in the software now adjusts the prism closest to the output coupler (P2 in the manual), and “P2” adjusts the prism closest to the crystal subassembly (P1). Note that the FTDI stepperboard chip on the motor controller board frequently fails to initiate when power to the oscillator controller is toggled on/off. This is a known hardware issue that can be remedied by soldering together pins 25 (AGND) and 26 (TEST) directly on the chip.

2.7 Generation of Pump and Probe Laser Pulses

Typically, a 50:50 beamsplitter is used to separate the KMLabs laser power for the pump and probe lines. For the experiments herein, the pump pulse is generated by either a Light Conversion TOPAS optical parametric amplifier or by a frequency-tripling set-up. The KMLabs fundamental may be used as the probe or the light may be frequency-doubled or frequency-tripled. A number of other schemes have also been employed and are described in the following subsections. We first consider the TOPAS operation, and then explore various nonlinear optical details and the experimental time-resolution that results from these pump-probe schemes.

TOPAS

The Light Conversion TOPAS-C (Traveling-Wave Optical Parametric Amplifier of White-Light Continuum) generates tunable visible wavelengths from the KMLabs fundamental by optical parametric amplification [39, 40]. This tunable visible light can then be frequency-doubled in a nonlinear crystal to produce tunable UV pump pulses for the experiment.

Briefly, the input to the TOPAS is split by 2.5% transmittance beamsplitter to create a low power seed arm and a high power pump arm. The seed beam is telescoped down by a lens pair, passed through two motorized Brewster plates to create an adjustable time delay to match the two arms, and focused by a third lens before being split by a second beamsplitter. 20% of the seed beam is transmitted to a variable filter, a second motorized delay stage, a half

waveplate, and finally to a sapphire plate to generate a white-light continuum. The variable filter allows adjustment of the input intensity to ensure stable white light generation. The white light passes through a dispersive plate and is focused into a β -barium borate (BBO) nonlinear crystal (2 mm, 28°). The other 80% of the seed beam is noncollinearly recombined with the white light in the BBO for parametric pre-amplification of the white light continuum to produce the desired infrared (IR) signal. The diverging signal beam is isolated and then recollimated in a Galilean telescope before recombining with the initially split-off high power pump arm.

The 97.5% pump beam arm is first reflected by a series of mirrors to add length to better match the pump and seed arm lengths. The pump beam is then telescoped down (to approximately 0.6 cm) for more efficient final amplification. The pump and signal beams are then recombined in a second BBO crystal (2 mm, 28° , “NC-2”) for parametric amplification. Both BBO crystals are on rotatable stages to optimize the phase matching angles for the desired wavelengths. Some nonlinear processes in the TOPAS require the use of a final dichroic mirror (“DM-3”) to dump residual pump light before the beam exits the TOPAS. Externally, a third BBO crystal (300 μm , 23° or 30° depending on nonlinear process) in a “mixer” unit then produces the desired visible light, and a detachable filter unit contains two dichroic beamsplitting optics to dump the idler, residual pump beam, and undoubled signal pulses depending on the wavelengths of interest. If more power is desired or the mixer crystal or filter are burned over time, the mixer and filter may both be detached and substituted with our own thicker crystal and dichroic beamsplitters. The crystal angles and delays are controlled by the Light Conversion WinTOPAS computer software.

The TOPAS is pumped by approximately 0.9 – 1.0 mJ/pulse from the KMLabs system. Even relatively minor changes to the TOPAS input power from changes to the KMLabs system can require realignment of the internal telescopes to ensure appropriate beam collimation. If the pump beam inside the TOPAS is not correctly collimated but rather comes to a focus in the TOPAS, the beam can destroy expensive optics. In the past, this undesired focus typically occurs near NC-2, DM-3, the external mixing BBO, or inside the detachable IR filter. In NC-2 or the mixing BBO, overpumping or focusing will generate white light in a rainbow pattern similar to that generated in the sapphire plate and will eventually burn the crystal. Near the DM-3 or in the filter, the coating of these optics will burn. The pump collimation is best checked by blocking the seed, placing an iris for the pump beam after the mixer unit, and examining the beam diameter as far away as possible. The seed collimation is best checked in a similar fashion after first setting the TOPAS to produce 650 nm for easiest visualization. The mounts for the lenses inside the TOPAS have a considerable amount of horizontal freedom and care should be taken to maintain the correct horizontal pointing when translating and remounting the lenses to fix the collimation.

Other Nonlinear Optical Schemes

Some studies, e.g. those of Chs. 4 and 6, employ 260 nm (4.77 eV) as the pump pulse, which is more efficiently generated by frequency-tripling the fundamental of the KM laser rather than *via* the TOPAS. With $\sim 50\%$ of the KMLabs output, a tripler with thin (90 μm) BBOs can easily generate the ~ 10 $\mu\text{J}/\text{pulse}$ needed as a pump for the iodide-nucleobase cluster experiments. With more power and thicker crystals, up to 250 $\mu\text{J}/\text{pulse}$ of 260 nm light can be generated for 260 nm pump, 260 nm probe experiments. A CaF_2 window can be used to reflect a very small amount of light for the pump pulse.

A relatively high energy probe pulse can also be generated by recombining 800 nm light with the residual, undoubled visible TOPAS output to create a probe pulse near 3.6 eV, as in Ch. 4. 800 nm light can also be recovered from the TOPAS when the SHS (second harmonic of signal) TOPAS scheme is employed, with the benefit that this probe pulse has a similar table path length as the pump pulse from the TOPAS. However, the recovered 800 nm probe pulses are expected to be considerably temporally stretched compared to pre-TOPAS 800 nm pulses.

As VMI requires vertical polarization [12], the periscopes that raise the height of the pump and probe beams from the table to the chamber must appropriately preserve or flip the laser polarization to maintain the cylindrical symmetry requirements. On the chamber level, the pump and probe pulses can be recombined in a dichroic beamsplitter, annular mirror, or with two vertically offset square mirrors. A 1 m uncoated UVFS focal length lens (Eksma Optics, 110-1245ET) is placed 1 m from the chamber center to focus the beams at the region of ion-laser interaction.

The pump and probe pulses must be spatially and temporally overlapped at the chamber. The spatial overlap is fine-adjusted by using a mirror to pick-off the focused beams in front of the chamber to a 100 μm pinhole at a 1 m distance from the focusing lens to optimize the pump-probe beam overlap. Temporal overlap is found by optimizing sum frequency generation (SFG) of the pump and probe pulses in a BBO on the chamber level. A UVFS Pellin-Broca prism is used to spatially separate the pump, probe, and SFG light and an old chamber window is inserted in the beams after the lens to appropriately offset the time-zero (t_0) or optimum temporal overlap for inside the chamber. For 400 nm probe schemes, for which SFG with the UV pump pulse is not feasible due to the non-physical phase matching angle, the UV pump pulse is first temporally overlapped with an 800 nm pulse, and then the 400 nm probe pulse is brought to temporally match the 800 nm pulse. The inlet chamber window is 3 mm uncoated UVFS.

Cross-Correlation

To determine the instrumental response function for a given pump-probe laser scheme, the cross-correlation of the two laser pulses is measured. To do this, t_0 is found by SFG in the thinnest possible BBO as described above, and the SFG signal is sent to a photodiode and read by an oscilloscope. The stage is scanned to follow the range of stage positions or time delays for which the SFG signal has intensity. This intensity is fit to a Gaussian fitting function from which the Gaussian σ or the FWHM of the laser overlap is extracted. An example cross-correlation and fit for 260 nm/800 nm is shown in Fig. 2.7.

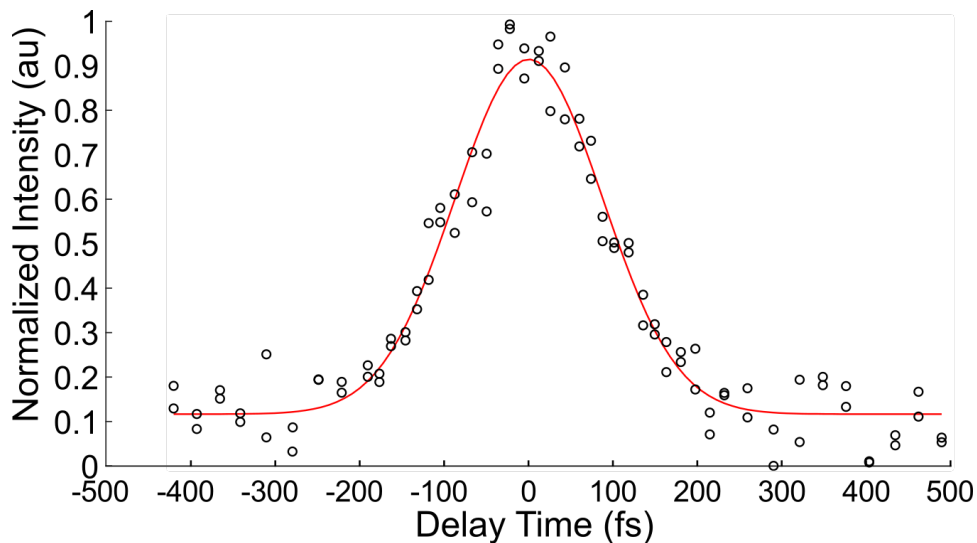


Figure 2.7: Example cross-correlation and Gaussian fit for 260 nm/800 nm. The σ for this cross-correlation fit is 85 fs, so the FWHM measured outside the vacuum chamber is 200 fs.

For UV/UV-type pump/probe schemes where SFG of the two wavelengths is not possible or differential frequency generation (DFG) is too weak, the cross-correlation of each individual UV pulse should be measured with 800 nm, and then the σ for each pulse and the UV/UV cross-correlation σ (σ_{cc}) can be calculated:

$$\sigma_{cc}^2 = \sigma_{\text{pump}}^2 + \sigma_{\text{probe}}^2 \quad (2.2)$$

2.8 Experimental Considerations

Finally, we close this chapter with some practical considerations that are important for experimental success.

Choosing the Pump and Probe Characteristics

Wavelength

While the 3.15 eV probe pulse is sufficiently energetic to photodetach both the TNIs as well as photofragments such as Γ^- [18], there is an advantage to first employing an IR probe to photodetach the TNIs and then repeating the experiment with higher probe photon energy to detect the photofragments. The photodetachment cross section of the DB anion has been found to fall off quickly with increasing photon energy. The Wigner threshold law has been used to describe the near threshold atomic anionic photodetachment cross section as follows:

$$\sigma \propto (h\nu_{\text{probe}} - eBE)^{(\ell+1/2)} \quad (2.3)$$

where σ is the photodetachment cross section, $h\nu_{\text{probe}}$ is the probe laser photon energy, and ℓ is the angular momentum of the outgoing photodetached electron [41]. Since the Wigner threshold law, Brauman and co-workers have developed generalized expressions for photodetachment cross sections for polyatomic molecular anions in the low energy region from 0.1 eV to 3.0 eV above threshold [42]. For DB anions in particular, both theoretical [43] and experimental [44] work have found the photodetachment cross sections to instead vary as

$$\sigma \propto (h\nu_{\text{probe}})^{-2} \quad (2.4)$$

as a result of the very diffuse nature of the DB orbital. Thus, it is advisable to use the lowest energy probe available to photodetach the $\Gamma^- \cdot \text{N}$ DB anion, and then use a higher energy UV probe to examine the cluster photofragments for the best results.

Focal length

Naturally, the 1 m focal lens does not focus the UV and IR wavelengths to the same spot size, and a smaller spot size will lead to higher laser intensity and therefore stronger photoabsorption/photodetachment. As in Eq. 2.5, the focused beam waist (w_F) of a Gaussian beam is given by:

$$w_F = \frac{\lambda f}{\pi w_0} \quad (2.5)$$

where λ is the wavelength, f is the focal length of the lens, and w_0 is the initial beam waist at the lens. For a 1 m focus, the focused beam waist of the KMLabs fundamental is ~ 75

μm , while that of the UV pulses generated either by frequency-tripling or the TOPAS is, in practice, typically $\sim 120 \mu\text{m}$ due to divergence that can arise in the TOPAS and a decrease in the beam diameter from the apertures of the nonlinear crystals. To achieve higher intensity for a low power pulse, a shorter focal length lens can be placed closer to the chamber (e.g. 50 cm). The beam diameter propagating through the chamber is ultimately limited by 6 mm laser baffles inside the chamber. While a shorter focal length provides increased laser intensity, the stronger divergence of the beam after focusing also produces more laser noise in the chamber. Note that the pump beam should overfill the probe beam to ensure that only molecules that have been photoexcited are probed; this is especially important as studies on this project move increasingly towards probe energies $\geq 4 \text{ eV}$.

Power

While higher laser power or higher focused intensity will produce better TRPES signal, it is important to avoid artifacts arising from multiphoton absorption of the pump pulse (and possibly the probe pulse, as discussed further in Ch. 6). The percentage of molecules pumped should generally be $\leq 1 - 2\%$. The ratio of the number of molecules absorbing one photon (N_{OP}) to the number of molecules originally in the ground state (N_{GS}) is:

$$\frac{N_{\text{OP}}}{N_{\text{GS}}} = \frac{\sigma N_{\text{h}\nu}}{\pi w_{\text{F}}^2} \quad (2.6)$$

where σ is the cross section, $N_{\text{h}\nu}$ is the number of photons in the laser pulse, and w_{F} is the focused beam waist.

Let us briefly consider some experimental values. A typical supersonic expansion produces approximately 10^{13} molecules/ cm^3 . The ring filament ionizer produces negative ions of a fraction of this number density (estimated to be $\sim 10^{-4}$), and our cluster source produces a wide variety of molecular and ionic species beyond the cluster of interest for the experiment (as in Fig. 2.2). Based on the typical intensity of the ions on the MCPs and the known MCP gain, we can estimate that the number density of the mass-selected final clusters of interest is approximately $10^4 - 10^5$ molecules/ cm^3 depending on the cluster. Intensities for binary clusters are typically an order of magnitude higher than those of the $\Gamma \cdot \text{U} \cdot \text{H}_2\text{O}$ clusters in Chs. 5 and 6. The typical photoabsorption or photodetachment cross section for molecular anions at the UV pump photon energies employed here is $\sim 1 \text{ Mb}$ or 10^{-18} cm^2 (e.g. [45]) while cross sections for atomic anions are approximately one order of magnitude larger (e.g. [46]). For our cluster number density and the beam waist and focusing conditions described above, a pump pulse of $7 - 10 \mu\text{J}/\text{pulse}$ (i.e. $\sim 10^{13}$ photons) is sufficient to pump the clusters of interest without inducing multiphoton effects.

Fitting TRPES Data

Typically, the time-dynamics of the measured features are well-described by the convolution of a Gaussian instrumental response with i exponential functions, as in Eq. 2.7:

$$I(t) = \frac{1}{\sigma_{cc}\sqrt{2\pi}} \exp\left(\frac{-t^2}{2\sigma_{cc}^2}\right) \cdot \begin{cases} I_0, t < 0 \\ I_0 + \sum A_i \exp\left(\frac{-t}{\tau_i}\right), t \geq 0 \end{cases} \quad (2.7)$$

Here, σ_{cc} is the Gaussian full width at the half-maximum (FWHM) given by the cross-correlation of the pump and probe laser pulses, I_0 is the signal background, A_i are the coefficients of the exponential functions, and τ_i are the corresponding rise or decay lifetimes for each exponential. When fitting data, it is important to use physically reasonable fitting parameters, particularly for σ_{cc} . If t_0 was incorrectly determined when setting the stage positions for data collection, it may be necessary to offset the delays for a given data set. Occasionally, it has been necessary to revise the fits of our data from mono-exponential to bi-exponential fits [47] or vice-versa [48]. In general, this fitting decision can be assisted by examining the residuals of the fit for both mono-exponential and bi-exponential fitting. When a sufficient number of exponential functions is employed, the residuals should be randomly distributed, not systematically high or low in one particular region.

2.9 References

- [1] B. J. Greenblatt, “Femtosecond photoelectron spectroscopy: a new tool for the study of anion dynamics”, PhD thesis (University of California, Berkeley, 1999).
- [2] M. T. Zanni, “Photodissociation and charge transfer dynamics of negative ions studied with femtosecond photoelectron spectroscopy”, PhD thesis (University of California, Berkeley, 1999).
- [3] A. V. Davis, “Time-resolved photoelectron spectroscopy and imaging studies of anion dynamics”, PhD thesis (University of California, Berkeley, 2002).
- [4] A. E. Bragg, “Excited-state dynamics of molecular and cluster anions studied with time -resolved photoelectron spectroscopy and imaging”, PhD thesis (University of California, Berkeley, 2004).
- [5] G. B. Griffin, “Time resolved photoelectron imaging of electronic relaxation dynamics in anionic clusters”, PhD thesis (University of California, Berkeley, 2009).
- [6] R. M. Young, “Dynamics of excess electrons in atomic and molecular clusters”, PhD thesis (University of California, Berkeley, 2011).

- [7] M. A. Yandell, “Charge accommodation dynamics of cluster and molecular anions produced by photo-initiated intracluster charge transfer”, PhD thesis (University of California, Berkeley, 2014).
- [8] S. B. King, “Time-resolved radiation chemistry: dynamics of electron attachment to nucleobases and small molecules”, PhD thesis (University of California, Berkeley, 2015).
- [9] U. Even, “The Even-Lavie valve as a source for high intensity supersonic beam”, *EPJ Techn. Instrum.* **2**, 17 (2015).
- [10] W. C. Wiley and I. H. McLaren, “Time-of-flight mass spectrometer with improved resolution”, *Rev. Sci. Instrum.* **26**, 1150–1157 (1955).
- [11] L. A. Posey, M. J. Deluca, and M. A. Johnson, “Demonstration of a pulsed photoelectron spectrometer on mass-selected negative ions: O^- , O_2^- , and O_4^- ”, *Chem. Phys. Lett.* **131**, 170–174 (1986).
- [12] A. Eppink and D. H. Parker, “Velocity map imaging of ions and electrons using electrostatic lenses: application in photoelectron and photofragment ion imaging of molecular oxygen”, *Rev. Sci. Instrum.* **68**, 3477–3484 (1997).
- [13] B. Whitaker, *Imaging in molecular dynamics* (Cambridge University Press, Apr. 28, 2007), 268 pp.
- [14] V. Dribinski, A. Ossadtchi, V. Mandelshtam, and H. Reisler, “Reconstruction of Abel-transformable images: the Gaussian basis-set expansion Abel transform method”, *Rev. Sci. Instrum.* **73**, 2634–2642 (2002).
- [15] C. Bordas, F. Paulig, H. Helm, and D. L. Huestis, “Photoelectron imaging spectrometry: principle and inversion method”, *Rev. Sci. Instrum.* **67**, 2257–2268 (1996).
- [16] G. M. Roberts, J. L. Nixon, J. Lecointre, E. Wrede, and J. R. R. Verlet, “Toward real-time charged-particle image reconstruction using polar onion-peeling”, *Rev. Sci. Instrum.* **80**, 053104 (2009).
- [17] C. E. Moore, *Atomic energy levels, vol. 35 of national standards reference data series, 2nd ed.* (National Bureau of Standards, Washington, DC, 1971).
- [18] R. J. Peláez, C. Blondel, C. Delsart, and C. Drag, “Pulsed photodetachment microscopy and the electron affinity of iodine”, *J. Phys. B- At. Mol. Opt.* **42**, 125001 (2009).
- [19] P. M. W. French, “The generation of ultrashort laser pulses”, *Rep. Prog. Phys.* **58**, 169–262 (1995).
- [20] S. Backus, C. G. Durfee, M. M. Murnane, and H. C. Kapteyn, “High power ultrafast lasers”, *Rev. Sci. Instrum.* **69**, 1207–1223 (1998).
- [21] C. Rullière, *Femtosecond laser pulses* (Springer-Verlag GmbH, 2004).

- [22] J.-C. Diels and W. Rudolph, *Ultrashort laser pulse phenomena (optics & photonics series)* (Academic Press, 2006).
- [23] A. Weiner, *Ultrafast optics* (Wiley-Blackwell, July 3, 2009), 598 pp.
- [24] M. T. Asaki, C.-P. Huang, D. Garvey, J. Zhou, H. C. Kapteyn, and M. M. Murnane, “Generation of 11-fs pulses from a self-mode-locked Ti:sapphire laser”, *Opt. Lett.* **18**, 977 (1993).
- [25] D. E. Spence, P. N. Kean, and W. Sibbett, “60-fsec pulse generation from a self-mode-locked Ti:sapphire laser”, *Opt. Lett.* **16**, 42 (1991).
- [26] G. Cerullo, S. D. Silvestri, V. Magni, and L. Pallaro, “Resonators for Kerr-lens mode-locked femtosecond Ti:sapphire lasers”, *Opt. Lett.* **19**, 807 (1994).
- [27] I. P. Christov, H. C. Kapteyn, M. M. Murnane, C.-P. Huang, and J. Zhou, “Space–time focusing of femtosecond pulses in a Ti:sapphire laser”, *Opt. Lett.* **20**, 309 (1995).
- [28] R. L. Fork, O. E. Martinez, and J. P. Gordon, “Negative dispersion using pairs of prisms”, *Opt. Lett.* **9**, 150 (1984).
- [29] O. E. Martinez, J. P. Gordon, and R. L. Fork, “Negative group-velocity dispersion using refraction”, *J. Opt. Soc. Am. A* **1**, 1003 (1984).
- [30] D. Strickland and G. Mourou, “Compression of amplified chirped optical pulses”, *Opt. Commun.* **56**, 219–221 (1985).
- [31] M. D. Perry, T. Ditmire, and B. C. Stuart, “Self-phase modulation in chirped-pulse amplification”, *Opt. Lett.* **19**, 2149 (1994).
- [32] J. Zhou, C.-P. Huang, C. Shi, M. M. Murnane, and H. C. Kapteyn, “Generation of 21-fs millijoule-energy pulses by use of Ti:sapphire”, *Opt. Lett.* **19**, 126 (1994).
- [33] S. Backus, J. Peatross, C. P. Huang, M. M. Murnane, and H. C. Kapteyn, “Ti:sapphire amplifier producing millijoule-level, 21-fs pulses at 1 kHz”, *Opt. Lett.* **20**, 2000 (1995).
- [34] S. J. Backus, H. C. Kapteyn, and M. M. Murnane, “Ultrashort pulse amplification in cryogenically cooled amplifiers”, United States Patent US 6,804,287 (2002).
- [35] S. Backus, R. Bartels, S. Thompson, R. Dollinger, H. C. Kapteyn, and M. M. Murnane, “High-efficiency, single-stage 7-kHz high-average-power ultrafast laser system”, *Opt. Lett.* **26**, 465 (2001).
- [36] S. Yang, R. Hua, C. Milne, B. Bruner, and R. D. Miller, “Multipass Ti:sapphire amplifier based on a parabolic mirror”, *Opt. Commun.* **234**, 385–390 (2004).
- [37] R. Trebino, K. W. DeLong, D. N. Fittinghoff, J. N. Sweetser, M. A. Krumbügel, B. A. Richman, and D. J. Kane, “Measuring ultrashort laser pulses in the time-frequency domain using frequency-resolved optical gating”, *Rev. Sci. Instrum.* **68**, 3277–3295 (1997).
- [38] R. Trebino, *Frequency-resolved optical gating: the measurement of ultrashort laser pulses* (Springer US, Oct. 30, 2012), 448 pp.

- [39] G. Cerullo and S. D. Silvestri, “Ultrafast optical parametric amplifiers”, *Rev. Sci. Instrum.* **74**, 1–18 (2003).
- [40] C. Manzoni and G. Cerullo, “Design criteria for ultrafast optical parametric amplifiers”, *J. Opt.* **18**, 103501 (2016).
- [41] E. P. Wigner, “On the behavior of cross sections near thresholds”, *Phys. Rev.* **73**, 1002–1009 (1948).
- [42] K. J. Reed, A. H. Zimmerman, H. C. Andersen, and J. I. Brauman, “Cross sections for photodetachment of electrons from negative ions near threshold”, *J. Chem. Phys.* **64**, 1368–1375 (1976).
- [43] V. E. Chernov, A. V. Dolgikh, and B. A. Zon, “Analytic description of dipole-bound anion photodetachment”, *Phys. Rev. A* **72**, 052701 (2005).
- [44] C. G. Bailey, C. E. H. Dessent, M. A. Johnson, and K. H. Bowen, “Vibronic effects in the photon energy-dependent photoelectron spectra of the CH_3CN^- dipole-bound anion”, *J. Chem. Phys.* **104**, 6976–6983 (1996).
- [45] P. Warneck, “Photodetachment of NO_2^- ”, *Chem. Phys. Lett.* **3**, 532–533 (1969).
- [46] R. S. Berry, “Small free negative ions”, *Chem. Rev.* **69**, 533–542 (1969).
- [47] A. Kunin, W.-L. Li, and D. M. Neumark, “Dynamics of electron attachment and photodissociation in iodide-uracil-water clusters via time-resolved photoelectron imaging”, *J. Chem. Phys.* **149**, 084301 (2018).
- [48] S. B. King, A. B. Stephansen, Y. Yokoi, M. A. Yandell, A. Kunin, T. Takayanagi, and D. M. Neumark, “Electron accommodation dynamics in the DNA base thymine”, *J. Chem. Phys.* **143**, 024312 (2015).

Chapter 3

Photodissociation Dynamics of Iodide-Nitromethane Complexes

She generally gave herself very good advice (though she very seldom followed it).

Lewis Carroll

The content and figures of this chapter are adapted from:

A. Kunin, W.-L. Li, and D. M. Neumark, “Time-resolved photoelectron imaging of iodide-nitromethane ($\text{I}^- \cdot \text{CH}_3\text{NO}_2$) photodissociation dynamics” *Phys. Chem. Chem. Phys.* **18**, 33226 (2016)

with permission from the PCCP Owner Societies.

3.1 Abstract

Femtosecond time-resolved photoelectron spectroscopy is used to probe the decay channels of iodide-nitromethane ($\text{I}^- \cdot \text{CH}_3\text{NO}_2$) binary clusters photoexcited at 3.56 eV, near the vertical detachment energy (VDE) of the cluster. The production of I^- is observed, and its photoelectron signal exhibits a mono-exponential rise time of 21 ± 1 ps. Previous work has shown that excitation near the VDE of the $\text{I}^- \cdot \text{CH}_3\text{NO}_2$ complex transfers an electron from iodide to form a dipole-bound state of CH_3NO_2^- that rapidly converts to a valence bound (VB) anion. The long appearance time for the I^- fragment suggests that the VB anion decays by back transfer of the excess electron to iodide, reforming the $\text{I}^- \cdot \text{CH}_3\text{NO}_2$ anion and resulting in evaporation of iodide. Comparison of the measured lifetime to that predicted by RRKM theory suggests that the dissociation rate is limited by intramolecular vibrational energy redistribution in the re-formed anion between the high frequency CH_3NO_2 vibrational modes and the much lower frequency intermolecular $\text{I}^- \cdot \text{CH}_3\text{NO}_2$ stretch and bends, the predominant modes involved in cluster dissociation to form I^- . Evidence for a weak channel identified as $\text{HI} + \text{CH}_2\text{NO}_2^-$ is also observed.

3.2 Introduction

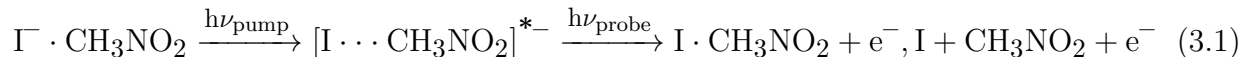
Anions with close-lying dipole bound (DB) and valence bound (VB) states are of considerable interest in understanding how closely spaced states with very different electronic properties are coupled to one another [1–3]. This problem underlies the complex dynamics of low-energy electron attachment to nucleobases [4–7] and, more generally, reductive damage to DNA [8–10]. DB and VB transient anions formed by the capture of low energy electrons have been implicated in the cleavage of covalent bonds in DNA bases [6, 11], but the roles of the two types of states are not yet fully understood. The coupling between DB and VB states and the apparent conversion of the DB anion to the VB anion of nucleobases has been observed experimentally [1, 12–14] and studied theoretically [15, 16]. Nitromethane, CH_3NO_2 , is also capable of forming both DB and VB negative ions [2, 17], and as such it can serve as a model system to better understand the formation of and transition between DB and VB states in more complex molecules such as nucleobases. Negative ion photoelectron spectroscopy experiments on nitromethane are able to distinguish between the two anionic forms [17], and in our group, time-resolved photoelectron imaging (TRPEI) experiments on binary clusters of iodide-nitromethane ($\text{I}^- \cdot \text{CH}_3\text{NO}_2$) have demonstrated complete and rapid conversion of the DB anion to the VB anion [18]. In this work, we employ TRPEI with a higher energy probe pulse to investigate more closely the decay dynamics of $\text{I}^- \cdot \text{CH}_3\text{NO}_2$ clusters and examine the dissociation channels that lead to formation of I^- and other anion fragment products.

Nitromethane can capture low energy electrons to form DB anions through vibrational Feshbach resonances [19, 20], and the VB anion is readily seen in the pulsed anion sources

often used in photoelectron spectroscopy instruments [17, 21]. The C–NO₂ moiety is nearly planar in the DB anion, just as in neutral CH₃NO₂ [22], but this group is pyramidal in the VB anion. The dissociative pathways of these anions have been investigated in dissociative electron attachment studies that have detected CH₂NO₂[−], NO₂[−], CH₃[−], and O[−] fragments, among others [23, 24]. The nitromethane anion has also been shown to undergo rapid vibrational autodetachment following excitation of one quantum into any of the C–H stretching modes [25]. Weber and co-workers found that in clusters of nitromethane anions with methyl iodide, excitation of a C–H stretching mode in either constituent was able to induce dissociative electron transfer to form I[−] fragments [26].

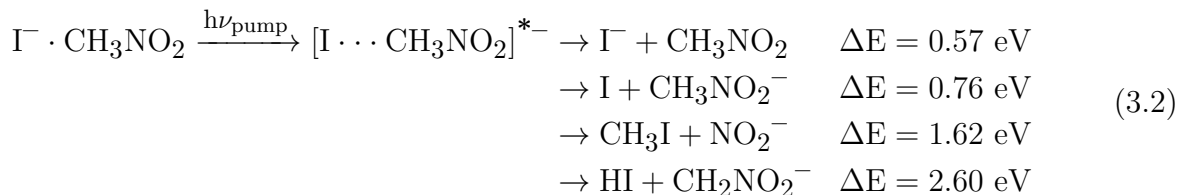
Binary clusters of iodide-nitromethane (I[−]·CH₃NO₂) have also been studied as a model system to examine the dynamics of electron capture and attachment to nitromethane and other species which are also capable of forming both DB and VB anions. Dessent and Johnson [19] found that photoexcitation of I[−]·CH₃NO₂ near its vertical detachment energy (VDE) of 3.60 eV yielded I[−] and NO₂[−] ion photofragments in a branching ratio of 25:1, a result that appeared to be approximately statistical when the clusters were analyzed in frequency groups using Rice-Ramsperger-Kassel-Marcus (RRKM) theory. In addition, a photofragment species that was suggested to be the CH₃NO₂[−] DB anion was also observed, according to the results of field detachment studies [19, 27]. Our research group has carried out time-resolved experiments on I[−]·CH₃NO₂ clusters [18] to gain insight into analogous experiments on iodide-nucleobase clusters, including iodide-uracil (I[−]·U) [7, 12, 28], iodide-thymine [13, 28], and iodide-adenine [14].

In our previous TRPEI work on I[−]·CH₃NO₂ clusters, these species were excited with a femtosecond pump photon near the VDE of the cluster to initiate charge transfer from iodide to the nitromethane moiety and probed with a 1.56 eV near-infrared femtosecond probe pulse in the following scheme:



Formation of the cluster DB anion was observed within the cross-correlation of the pump and probe laser pulses [18]. This DB feature was found to decay mono-exponentially on the order of 500 fs while the VB anion feature rise time was approximately 400 fs, providing experimental evidence that the DB anion acts as a “doorway” and decays to form the VB anion. The VB anion was found to decay bi-exponentially on the order of 2 ps and 1200 ps. This bi-exponential decay was attributed in part to autodetachment, which produces electrons with nearly zero kinetic energy. However, several other decay channels are also

possible [18, 19, 27], including:¹



In the present TRPEI study, a 3.14 eV probe pulse was used to interrogate $\text{I}^- \cdot \text{CH}_3\text{NO}_2$ clusters following photoexcitation near the cluster VDE. This higher probe photon energy makes it possible to observe the formation of dissociation products with larger electron binding energies (eBEs), including iodide (eBE = 3.059 eV) and NO_2^- (VDE = 2.273 ± 0.005 eV) [29]. Photodetachment from I^- was observed with a rise time of 21 ± 1 ps. There is also evidence observed for weak production of the nitromethide anion, CH_2NO_2^- (VDE = 2.635 ± 0.010 eV) [30].² The DB and VB states of $\text{I}^- \cdot \text{CH}_3\text{NO}_2$ were also observed and measured to rise and decay with time constants similar to those of our previous work [18]. The long iodide rise time was modeled using RRKM theory to calculate the statistical unimolecular decay lifetime of $\text{I}^- \cdot \text{CH}_3\text{NO}_2$ clusters, which were calculated to form I^- in 294 fs following a pump excitation energy of 3.56 eV. The discrepancy between the experimental rise and the statistical result here may reflect weak coupling between intramolecular and intermolecular modes, leading to slowed intramolecular vibrational energy redistribution (IVR) in the cluster [31–34]. The results here suggest that the VB anion decays not only via autodetachment, but also by electron back-transfer to I to eventually evaporate I^- after slow IVR, and possibly via a minor alternative pathway to form HI and the nitromethide anion.

3.3 Experimental Methods

The TRPEI apparatus has been described in detail previously [35, 36], but is briefly summarized here. $\text{I}^- \cdot \text{CH}_3\text{NO}_2$ clusters were formed by passing 400 kPa of argon gas over a reservoir of iodomethane vapor and an ice-chilled reservoir of liquid nitromethane through a 500 Hz pulsed Even-Lavie valve equipped with a water-cooled jacket. The gas was supersonically expanded into vacuum through a ring electrode ionizer. The resulting anionic clusters

¹ The ΔE values provided refer to the asymptotic energy difference between the indicated reactants and products, and were calculated in this work at the MP2/aug-cc-pVDZ level of theory using the Gaussian 09 computing package, as described in the Methods section and detailed in the supplementary material.

² The VDE is calculated from Metz et al. by $\text{VDE} = h\nu - e\text{KE}_{\text{max}}$ where $h\nu$ is the photon energy and $e\text{KE}_{\text{max}}$ is the measured eKE of the maximum intensity peak of the photoelectron spectrum.

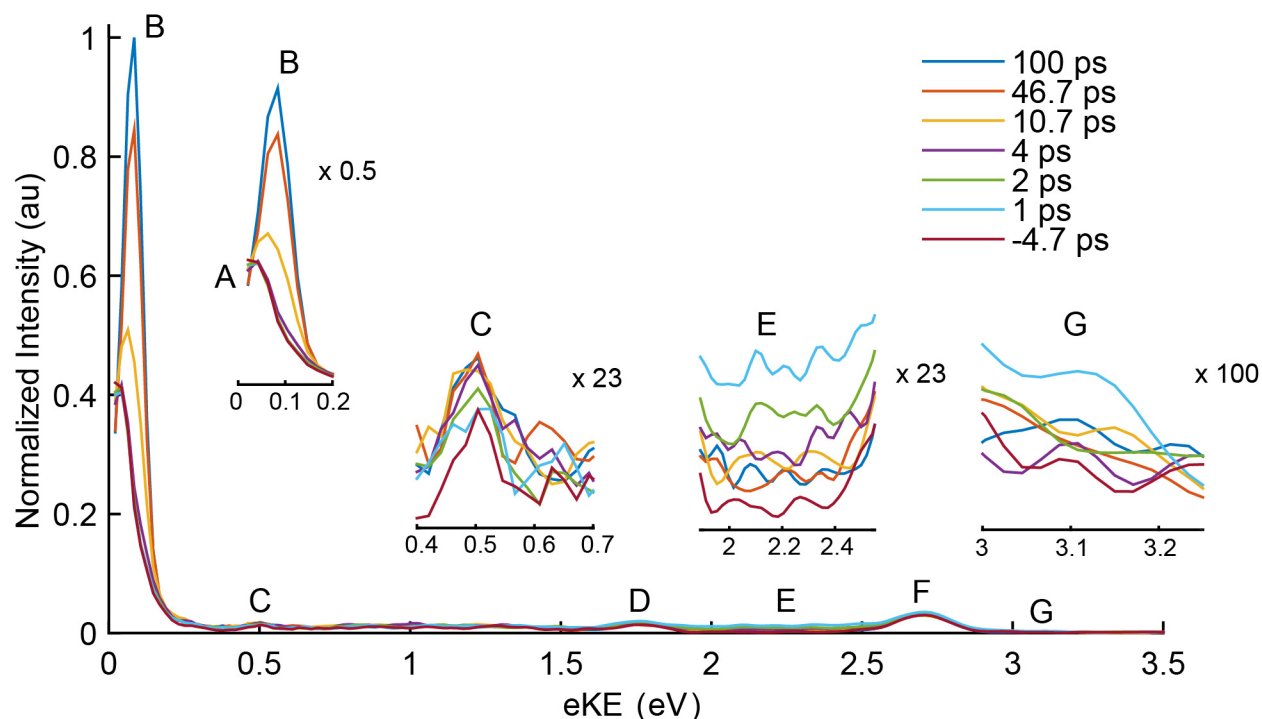


Figure 3.1: Photoelectron spectrum of $\text{I}^- \cdot \text{CH}_3\text{NO}_2$ at 3.56 eV pump and 3.14 eV probe at selected delay times.

were perpendicularly extracted using a Wiley-McLaren time-of-flight mass spectrometer [37] and mass-selected to isolate the desired $\text{I}^- \cdot \text{CH}_3\text{NO}_2$ binary clusters.

The mass-selected clusters were excited and photodetached by femtosecond ultraviolet pump and probe laser pulses whose delay was controlled by a delay stage. A KM Labs Griffin Oscillator and Dragon Amplifier generated 1 kHz, 40 fs pulses centered at 790 nm with 1.9 mJ/pulse. These were split between a Light Conversion TOPAS-C optical parametric amplifier to generate 11 μJ pump pulses at 3.56 eV (348 nm), and a frequency-doubling set-up to generate 30 μJ probe pulses at 3.14 eV (395 nm). The cross-correlation of the pump and probe laser pulses measured outside the chamber was approximately 185 fs.

Photoelectrons were analyzed using a velocity map imaging apparatus [38]; photoelectrons were detected using position-sensitive chevron-stacked microchannel plates coupled to a phosphor screen and imaged by a charge-coupled device camera. The photoelectron kinetic energy (eKE) distributions were reconstructed using the basis-set expansion (BASEX) method [39].

3.4 Results

Photoelectron spectra of $\Gamma \cdot \text{CH}_3\text{NO}_2$ at 3.56 eV pump excitation energy and 3.14 eV probe energy are shown at selected delay times in Fig. 3.1. The spectra are dominated by two partially overlapped features, A and B, at eKE values below 0.2 eV, but there are several additional weak time-dependent features that are magnified in the various insets. Feature A, near zero eKE, is apparent at negative time delays when the probe precedes the pump pulse and also at zero delay, while feature B, at a slightly higher eKE of 0.08 ± 0.05 eV, grows in over tens of picoseconds and is very intense. The time-resolved photoelectron spectrum for the overlapped features A and B at 3.56 eV pump excitation energy and 3.14 eV probe energy is shown in Fig. 3.2; the y-axis is electron binding energy (eBE), where $\text{eBE} = h\nu_{\text{probe}} - \text{eKE}$. This plot shows feature B growing in at an eBE of 3.06 eV. Fig. 3.3 shows the time-dependent normalized integrated intensity of feature B from the photoelectron spectrum in Fig. 3.2. Feature A is located near zero eKE and is present even in the absence of the probe pulse. Based on these attributes and our previous results, feature A is assigned to autodetachment from pump-excited $\Gamma \cdot \text{CH}_3\text{NO}_2$. From the binding energy of feature B, its narrow width, and its integrated time-dependence, we assign feature B to photodetachment of atomic iodide produced by the dissociation of photoexcited $\Gamma \cdot \text{CH}_3\text{NO}_2$.

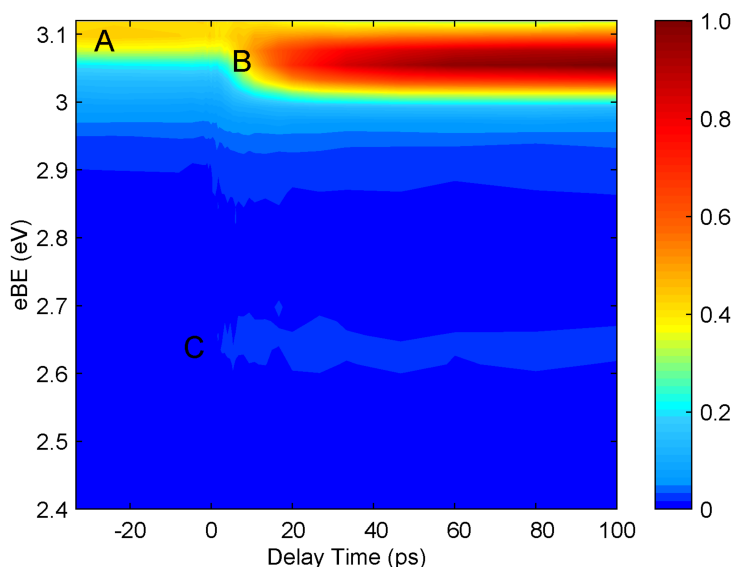


Figure 3.2: Time-resolved photoelectron spectrum for features B (eBE = 3.06 eV) and C (eBE = 2.64 eV) at pump-probe delays for $\Gamma \cdot \text{CH}_3\text{NO}_2$ at 3.56 eV pump excitation energy and 3.14 eV probe energy.

Feature C is a weaker time-dependent feature near 0.5 ± 0.05 eV eKE and appears to be relatively narrow as seen in the inset. Feature C is also apparent in Fig. 3.2 as a

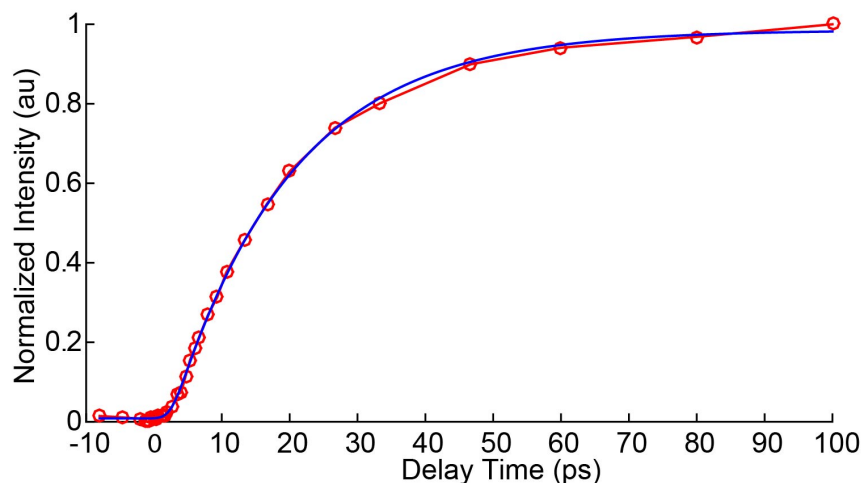


Figure 3.3: Normalized integrated intensity of feature B from excitation at 3.56 eV vs. delay time. The rise time for feature B is 21 ± 1 ps.

low intensity feature appearing at positive time delays with an eBE of 2.64 eV. The time-dependent normalized integrated intensity for the rise of feature C is shown in Figure 3.4, and the long-time decay dynamics are shown in Fig. 3.S1. Two of the larger remaining peaks in the spectrum, feature D near 1.75 eV and feature F near 2.7 eV, do not exhibit any time-dependence, so no inset is provided. The time-dependent and broad feature E, between 1.8 eV eKE and 2.6 eV eKE, has some contributions to its intensity on either side of this range from features D and F. Feature G, near 3.1 ± 0.1 eV eKE, is also time-dependent but very weak and narrow. The normalized integrated intensities showing the rise and decay dynamics for features E and G are shown in Figs. 3.S2 and 3.S3, respectively.

Feature C corresponds in eBE and in spectral shape relatively well to photodetachment from the bare nitromethide anion, CH_2NO_2^- [30], which is an energetically accessible channel according to Eq. 3.2. Features D and F correspond to direct detachment from $\text{I}^- \cdot \text{CH}_3\text{NO}_2$ by two probe photons to form $\text{I}(^2\text{P}_{1/2}) \cdot \text{CH}_3\text{NO}_2$ and $\text{I}(^2\text{P}_{3/2}) \cdot \text{CH}_3\text{NO}_2$, respectively. The eKEs of features E and G indicate that they are from probe-induced detachment from the VB and DB anions generated by the pump pulse, as discussed in our previously published results [18].

3.5 Analysis

To capture the rise and decay of features B, C, E, and G, the time-resolved signals are fit to the convolution of a Gaussian experimental response and multiple exponential functions using Eq. 3.3.

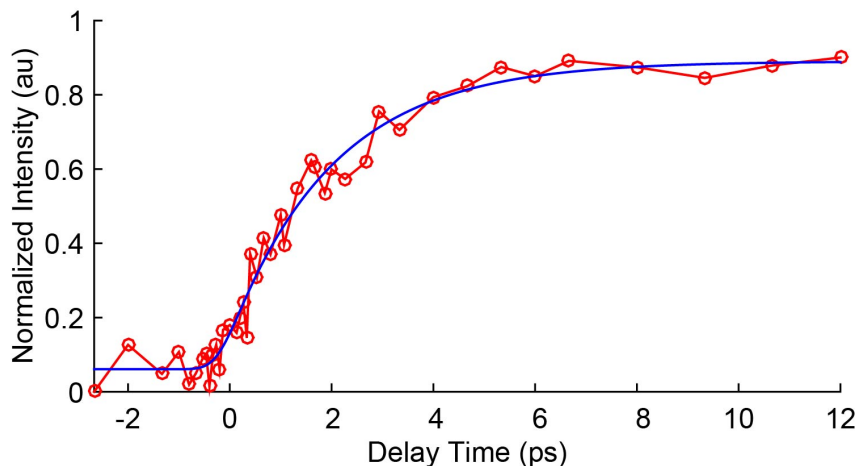


Figure 3.4: Normalized integrated intensity of feature C at short time delays from excitation of 3.56 eV vs. delay time. The rise time for feature C is 2.1 ± 0.2 ps.

$$I(t) = \frac{1}{\sigma_{cc}\sqrt{2\pi}} \exp\left(\frac{-t^2}{2\sigma_{cc}^2}\right) \cdot \begin{cases} I_0, t < 0 \\ I_0 + \Sigma A_i \exp\left(\frac{-t}{\tau_i}\right), t \geq 0 \end{cases} \quad (3.3)$$

I_0 is the signal background, σ_{cc} is the Gaussian full width at the half-maximum given by the cross-correlation of the pump and probe laser pulses, A_i is the coefficient for each exponential term, and τ_i is the lifetime for each rise or decay exponential. Fig. 3.3 shows the fit of Eq. 3.3 to the integrated intensity of Γ^- . The Γ^- feature has a mono-exponential rise time of 21 ± 1 ps and does not exhibit any decay. The fit to feature C, tentatively assigned to CH_2NO_2^- , is shown in Fig. 3.4 at delay times out to 12 ps, and longer time results are shown in Fig. 3.S1. Feature C exhibits a rise time of 2.1 ± 0.2 ps, and fits to a mono-exponential decay which is longer than the timescale of this experiment (1000+ ps). Feature E, the VB anion, exhibits a rise time of 0.33 ± 0.15 ps and a bi-exponential decay of 2.2 ± 0.3 ps and 1100 ± 700 ps. Feature G, the DB anion, rises very quickly, within the cross-correlation of our pump and probe laser pulses, and decays mono-exponentially in 0.88 ± 0.22 ps. These rise and decay times for the DB and VB anions are within the error bars of our previously reported values, a cross-correlation limited DB rise and 0.63 ± 0.11 ps decay, and a VB rise of 0.37 ± 0.04 ps and bi-exponential decay of 2.3 ± 0.2 ps and 1100 ± 200 ps following photoexcitation at 3.55 eV [18]. The results match relatively well despite the lower signal intensity for the DB and VB features in the present study.

The long lifetime of the Γ^- feature suggests a statistical mechanism may be relevant here, in which, for example, the iodide is ejected from highly vibrationally excited $\Gamma^- \cdot \text{CH}_3\text{NO}_2$ formed subsequent to UV excitation. To test this, we have employed Rice-Ramsperger-

Kassel-Marcus (RRKM) calculations [40, 41] to model the lifetime for statistical unimolecular decay of $\text{I}^- \cdot \text{CH}_3\text{NO}_2$ to $\text{I}^- + \text{CH}_3\text{NO}_2$. RRKM theory calculates the microcanonical rate constant, $k(E)$, for statistical unimolecular dissociation for a species at a given energy E via Eq. 3.4.

$$k(E) = \frac{G(E - E_0)}{h \cdot N(E)} \quad (3.4)$$

Here $N(E)$ is the density of states of the reactant, $G(E - E_0)$ is the sum of states of the transition state, where E_0 is the zero point energy (ZPE) corrected energy difference between the reactant and transition state, and h is Planck's constant. E is the maximum energy provided to the system, taken to be the pump pulse energy.

The details of the calculations performed in this work using the Gaussian 09 computing package [42] may found in the supplementary material. The calculated potential energy surface at the MP2/aug-cc-pVDZ level for dissociation of $\text{I}^- \cdot \text{CH}_3\text{NO}_2$ to form I^- and CH_3NO_2 is shown in Fig. 3.S4. The calculated sum and density of states from the Beyer-Swinehart algorithm [43] and rate constant $k(E)$ for pump excitation at 3.56 eV are given in Table 3.S1. The loose transition state expected for this reaction is located variationally, in order to yield the lowest calculated $k(E)$ [44]. With corrections made to appropriately treat low-energy hindered internal rotor modes, RRKM theory calculates statistical unimolecular decay for $\text{I}^- \cdot \text{CH}_3\text{NO}_2$ to occur in approximately 294 fs following pump excitation at 3.56 eV, and with all modes simply treated harmonically this lifetime is 414 fs. This result is considerably faster than the experimental result of iodide rise time of 21 ± 1 ps following pump excitation at 3.56 eV; this discrepancy is explored in more detail in the following section.

3.6 Discussion

The work presented here provides new insights into the dynamics of photoexcited $\text{I}^- \cdot \text{CH}_3\text{NO}_2$ complexes. Using a higher probe photon energy, 3.14 eV, than in our previous TRPEI experiment, we are able to observe very prominent, time-dependent I^- production with a rise time of 21 ± 1 ps, as well as a much weaker feature that appears to correspond to CH_2NO_2^- production with a rise time of 2.1 ± 0.2 ps; neither of these species could be photodetached in our previous study at 1.56 eV probe energy. The cluster DB and VB anions are also observed, with similar time-dependence as reported previously [18].

The intensity of the iodide signal in Fig. 3.1 is significantly greater than that of any other feature in the spectrum, even with the intensity of the autodetachment feature A removed. The iodide feature is approximately 30 times more intense than either the nitromethide anion or the VB anion, and 130 times more intense than the DB anion. The photodetachment

cross section of iodide at 314 nm is approximately $3 \times 10^{-17} \text{ cm}^2$ [45], compared to a typical molecular cross section of approximately $0.7 \times 10^{-18} \text{ cm}^2$ for NO_2^- at 314 nm [46]. If the photodetachment cross section for the VB anion is similarly on the order of 10^{-18} cm^2 , this would indicate that despite its high photoelectron signal intensity, I^- is present in an approximately 1:1 ratio with the VB anion. Note that the VB CH_3NO_2^- anion may or may not be complexed with the neutral I atom; the two cannot be readily distinguished in our TRPE spectra [18]. In any case, dissociation to $\text{I}^- + \text{CH}_3\text{NO}_2$ is a major channel whose dynamics are now accessible to our experiment.

We next examine possible mechanisms for I^- formation. Previous work applying TRPEI to iodide-uracil ($\text{I}^- \cdot \text{U}$) clusters showed that photoexcitation near the VDE transfers the excess electron to the uracil, forming a temporary negative ion that decays by autodetachment [12] and by back-electron transfer to the I^- [47]; the latter process results in vibrationally excited $\text{I}^- \cdot \text{U}$ from which the I^- is ejected. A similar mechanism is likely for $\text{I}^- \cdot \text{CH}_3\text{NO}_2$, since photoexcitation is known to initiate electron transfer to the CH_3NO_2 , leading to a DB state that converts within approximately 500 fs to a VB state. The VB signal (also seen here as Feature E) decays bi-exponentially with time constants of 2 ps and > 1 ns. The amplitude of the VB signal drops by about 80% within 2 ps. Given the large I^- signal seen here, it seems reasonable to attribute most or all of this drop to back-electron transfer, re-forming $\text{I}^- \cdot \text{CH}_3\text{NO}_2$ which subsequently fragments.

The dissociation rate of $\text{I}^- \cdot \text{CH}_3\text{NO}_2$ to form I^- was found not to match the predictions of RRKM statistical unimolecular decay; the calculated and experimental lifetimes are 294 fs and 21 ps, respectively. In the case of $\text{I}^- \cdot \text{U}$, the RRKM lifetime of 8.6 ps was also less than the experimental lifetime of 86 ± 7 ps [47], but the discrepancy here is about a factor of 7 larger. A key tenet of RRKM theory is that vibrational energy is randomly distributed and that this IVR is fast and complete on the timescale of the unimolecular reaction. This condition is unlikely to be satisfied given the sub-ps RRKM lifetime, suggesting that dissociation is not the rate-limiting step in I^- production even without considering the discrepancy with experiment. Given the large disparity between the I^- experimental rise time and the RRKM statistical decay calculations presented here, either back-electron transfer or IVR must be the rate-limiting step to dissociation.

If back-electron transfer from the VB anion to reform $\text{I}^- \cdot \text{CH}_3\text{NO}_2$ is the rate-limiting step, there would need to be some charged, intermediate state corresponding to the precursor of $\text{I}^- \cdot \text{CH}_3\text{NO}_2$. While the dynamics of the $\text{I}^- \cdot \text{CH}_3\text{NO}_2$ electronic ground state species are challenging to observe uniquely from the direct detachment signal and the bare CH_3NO_2^- anion, there does not appear to be any signal in the TRPEI spectrum corresponding to a charged species from a delayed charge-transfer intermediate. Thus, we turn our attention to the process of IVR in the $\text{I}^- \cdot \text{CH}_3\text{NO}_2$ cluster.

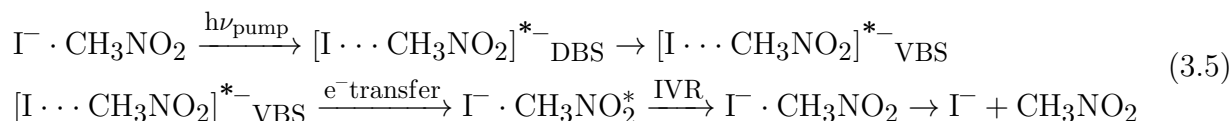
It is likely that back-electron transfer from the VB state of CH_3NO_2^- leads to con-

siderable vibrational excitation of $-\text{NO}_2$ wagging and stretching modes in the re-formed $\text{I}^- \cdot \text{CH}_3\text{NO}_2$, since the $\text{C}-\text{NO}_2$ moiety is pyramidal in the VB anion and planar in the neutral. As determined by the calculations here and presented in Table 3.S2, $\text{I}^- \cdot \text{CH}_3\text{NO}_2$ clusters have three low frequency ($<100 \text{ cm}^{-1}$) modes corresponding to an iodide-nitromethane stretch and two approximately symmetric iodide-nitromethane bends. All other modes in the system are nitromethane internal vibrational modes with considerably higher frequencies, with the exception of the 27.4 cm^{-1} frequency associated with the internal methyl rotor. The question then is whether vibrational energy flow from the high frequency intramolecular modes excited by back-electron transfer into the low-frequency modes needed for dissociation will be the rate-limiting step for fragmentation to $\text{I}^- + \text{CH}_3\text{NO}_2$.

One can gain insight into this issue from the extensive experimental and theoretical studies of gas phase $\text{S}_{\text{N}}2$ reactions $\text{X}^- + \text{CH}_3\text{Y} \rightarrow \text{CH}_3\text{X} + \text{Y}^-$, where X and Y are typically halogen atoms but can also be molecular species [32, 33, 48]. These reactions proceed via $\text{X}^- \cdot \text{CH}_3\text{Y}$ and $\text{Y}^- \cdot \text{CH}_3\text{X}$ ion-dipole complexes separated by a barrier. Classical trajectory calculations by Hase [34, 49] have shown that vibrational energy flow between the low-frequency intermolecular modes and high-frequency intramolecular modes of these complexes can be very inefficient and acts as a “dynamical bottleneck.” As a result, randomization of vibrational energy therefore often does not occur during the course of a reactive (or non-reactive) collision. This leads to non-statistical dynamics that are experimentally observable, such as deviations in the measured product angular and energy distributions from statistical models [50, 51], or a non-statistical dependence of the rate constant on the internal energy of the reactants [52].

In the $\text{S}_{\text{N}}2$ studies, a bimolecular collision $\text{X}^- + \text{CH}_3\text{Y}$ collision is likely to lead to excitation of the low frequency intermolecular modes of the $\text{X}^- \cdot \text{CH}_3\text{Y}$ complex, with vibrational energy flow into the higher frequency intramolecular modes acting as a dynamical bottleneck. We propose that our experiment presents the opposite scenario, with the bottleneck between the initially excited CH_3NO_2 modes and the low-frequency $\text{I}^- \cdot \text{CH}_3\text{NO}_2$ intermolecular modes limiting the dissociation rate. This scenario has indeed been described in trajectory studies on the unimolecular dynamics of the $\text{Cl}^- \cdot \text{CH}_3\text{Br}$ and $\text{Br}^- \cdot \text{CH}_3\text{Cl}$ complexes [34], where, for example, the dissociation lifetime of the latter complex when there is significant intramolecular excitation was found to exceed 25 ps, considerably exceeding the calculated RRKM lifetime of 0.5 ps.

The following scheme describes the overall proposed mechanism:



Hase and co-workers are currently carrying out trajectory calculations on $\text{I}^- \cdot \text{CH}_3\text{NO}_2$ to test the proposed mechanism. We note that if the argument about the dynamical bottleneck limiting the dissociation of $\text{I}^- \cdot \text{CH}_3\text{NO}_2$ is confirmed, it is also likely to apply to the discrepancy between the experimental and RRKM dissociation lifetimes in $\text{I}^- \cdot \text{U}$ [47].

In their investigation of the photoexcitation of $\text{I}^- \cdot \text{CH}_3\text{NO}_2$, Johnson and co-workers [19, 27] also observed formation of NO_2^- and CH_3NO_2^- anion photofragments. NO_2^- photofragments were reported to be observed in an approximately statistical 1:25 ratio with I^- photofragments. NO_2^- was not observed in the present TRPEI study, and given this branching ratio in addition to the cross sections cited above, photodetachment signal corresponding to NO_2^- is expected to be more than 1000 times weaker than the iodide signal observed here, essentially undetectable. The CH_3NO_2^- anion, if formed here, may not be distinguishable from the $\text{I} \cdot \text{CH}_3\text{NO}_2^-$ complex as the nitromethane VB anion and iodine-associated VB anion are similarly bound (eBE = 0.9 eV for CH_3NO_2^- VB anion) [17], making it challenging to observe when photoelectron spectroscopy is the primary product characterization method.

A weak signal that appears to correspond to the nitromethide anion was also observed in the current experiment, indicating that a $\text{CH}_2\text{NO}_2^- + \text{HI}$ decay channel may also exist. In the $\text{I}^- \cdot \text{U}$ study, photofragment action spectra collected for $\text{I}^- \cdot \text{U}$ showed the formation of $[\text{U}-\text{H}]^-$ photofragments following photoexcitation near the VDE of the cluster, with I^- as the primary photofragment and $[\text{U}-\text{H}]^-$ as a minor product. $[\text{U}-\text{H}]^-$ was not observed in the time-resolved studies likely as a result of low production efficiency and a small photodetachment cross section for the species. In the present study, the possible formation of nitromethide anion in 2.1 ± 0.2 ps suggests that CH_2NO_2^- may form as part of the VB anion decay due to the close match-up of lifetimes. Note that the production of CH_2NO_2^- is only energetically accessible when the HI fragment is also formed; the C-H bond is too high in energy for CH_2NO_2^- to be a feasible product otherwise.

3.7 Conclusions

TRPEI has been used to probe the decay dynamics of $\text{I}^- \cdot \text{CH}_3\text{NO}_2$ binary clusters excited at 3.56 eV, near the cluster VDE of 3.60 eV. The formation of I^- was observed with a rise time of 21 ± 1 ps. This channel is attributed to photoexcitation in which the excess electron is transferred from the I atom to form $\text{I} \cdot \text{CH}_3\text{NO}_2^-$, followed by back-electron transfer to re-form vibrationally excited $\text{I}^- \cdot \text{CH}_3\text{NO}_2$ that then dissociates to $\text{I}^- + \text{CH}_3\text{NO}_2$. Statistical calculations employing RRKM theory yield a substantially shorter lifetime of ~ 300 fs as compared to the experimental value, suggesting the presence of a dynamical bottleneck to unimolecular dissociation. This bottleneck is most likely from inefficient vibrational energy transfer from the intramolecular CH_3NO_2 vibrations excited by the back-electron transfer to the low-frequency intermolecular modes that must be energized for dissociation to occur.

This result is commensurate with previous theoretical work on gas phase $X^- \cdot CH_3Y$ complexes for halogens. In addition, a weak signal associated with $CH_2NO_2^- + HI$ production was observed with a rise time of 2.1 ps.

3.8 Supplementary Material

Theoretical Methods

The potential energy surface for the unimolecular decomposition of electronic ground state $I^- \cdot CH_3NO_2$ to form I^- was calculated at the MP2 level with an augmented Dunning basis set aug-cc-pVDZ for C, H, O, and N, with an expanded basis set with an increased set of diffuse functions for iodide, MP2/aug-cc-pVDZ(-pp) [53] using the Gaussian 09 computing package [42]. By scanning along the iodide-nitromethane stretching coordinate and optimizing the structure geometry and frequencies in 0.1 Å intervals from 2.5 Å to 15 Å, the potential energy surface was found to be barrierless.

As the potential is barrierless, variational transition state theory was used to calculate the transition state by calculating the rate constant $k(E)$ using Eq. 3.4 for each optimized distance to determine the minimum rate constant. The reactant species and transition state structures, frequencies, and energies were optimized at the MP2/aug-cc-pVDZ(-pp) level of theory. The calculated vibrational frequencies were scaled using a scaling factor of 0.9615 for MP2 calculations to account for anharmonicities [54]. The Beyer-Swinehart direct count algorithm [43] with the Stein-Rabinovitch modification [55] was employed to calculate the density of states for the reactant and sum of states for the transition state to determine the RRKM rate constant for unimolecular dissociation from the calculated frequencies and energy. The iodide-nitromethane low energy interaction modes involving rotation of iodide relative to the C–N nitromethane bond in-plane and out-of-plane were best treated as hindered rotational motions, as well as the methyl rotor mode in nitromethane, which is a free rotor in the neutral species but a hindered rotor in the anion due to the interaction between the methyl group and pyramidalized nitro group. The barrier height and symmetry for hindered rotors was calculated by performing relaxed potential energy scans at the MP2/aug-cc-pVDZ(-pp) level in 10° increments along the rotational motion. Using this variational approach, the transition state was calculated to be when the iodide-nitromethane I–C distance is 9.0 Å. The energy barrier E_0 between the reactant and the transition state was calculated to be 0.467 eV, and 0.466 eV when corrected for ZPEs. Additionally, the $I^- \cdot CH_3NO_2 \rightarrow HI + CH_2NO_2^-$ decay channel was calculated to have a reaction energy of 2.6 eV at the MP2/aug-cc-pVDZ(-pp) level.

Table 3.S1: Beyer-Swinehart calculated densities and sums of states for the $\Gamma^- \cdot \text{CH}_3\text{NO}_2$ ground state and transition state including treatment of low-frequency hindered internal rotational modes.

Ground state density ($/\text{cm}^{-1}$)	Transition state sum	$k_{\text{RRKM}}(E)$ (1/s)	Lifetime (fs)
5.97326×10^5	6.78309×10^7	3.40441×10^{12}	294

Table 3.S2: $\Gamma^- \cdot \text{CH}_3\text{NO}_2$ calculated vibrational frequencies (cm^{-1}) at the optimized, ground state geometry. Calculation performed at the MP2/aug-cc-pVDZ(-pp) level of theory. The modes in boldface type correspond to the $\Gamma^- \cdots \text{CH}_3\text{NO}_2$ intermolecular stretch and bends.

27.4	55.4	59.2
75.2	479.5	593.9
658.2	925.2	1092.6
1107.5	1358.4	1430.0
1443.0	1454.6	1725.1
3131.2	3242.2	3281.0

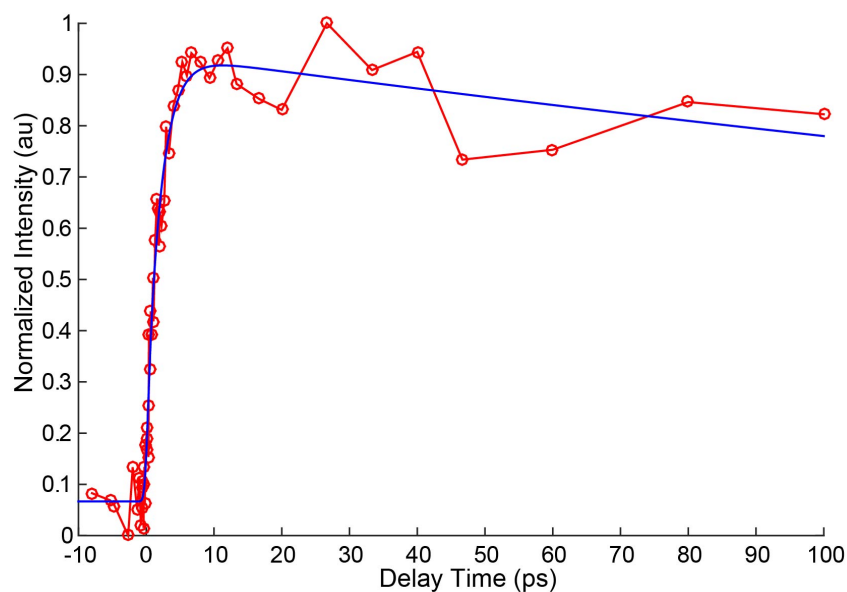


Figure 3.S1: Normalized integrated intensity of feature C for long time delays from excitation at 3.56 eV vs. delay time. The rise time for feature C is 2.1 ± 0.2 ps and the decay time is on the order of ns.

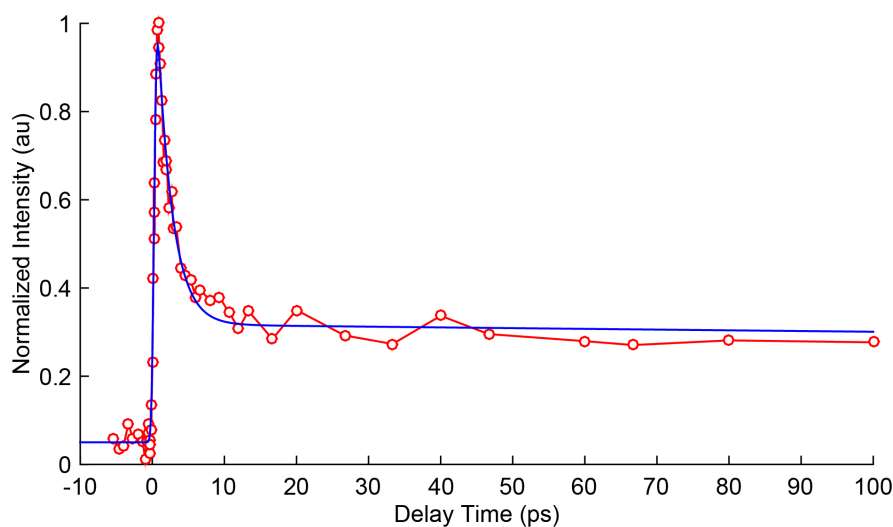


Figure 3.S2: Normalized integrated intensity of feature E from excitation at 3.56 eV vs. delay time. The rise time for feature E is 0.33 ± 0.15 ps and the bi-exponential decay times are 2.2 ± 0.3 ps and 1100 ± 700 ps.

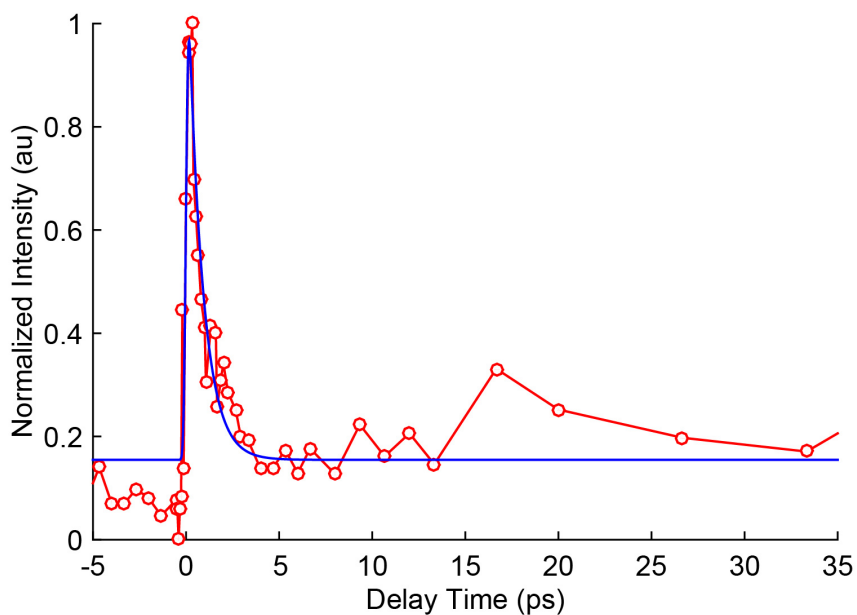


Figure 3.S3: Normalized integrated intensity of feature G from excitation at 3.56 eV vs. delay time. The rise time for feature G is cross-correlation limited, and the decay time is 0.88 ± 0.22 ps.

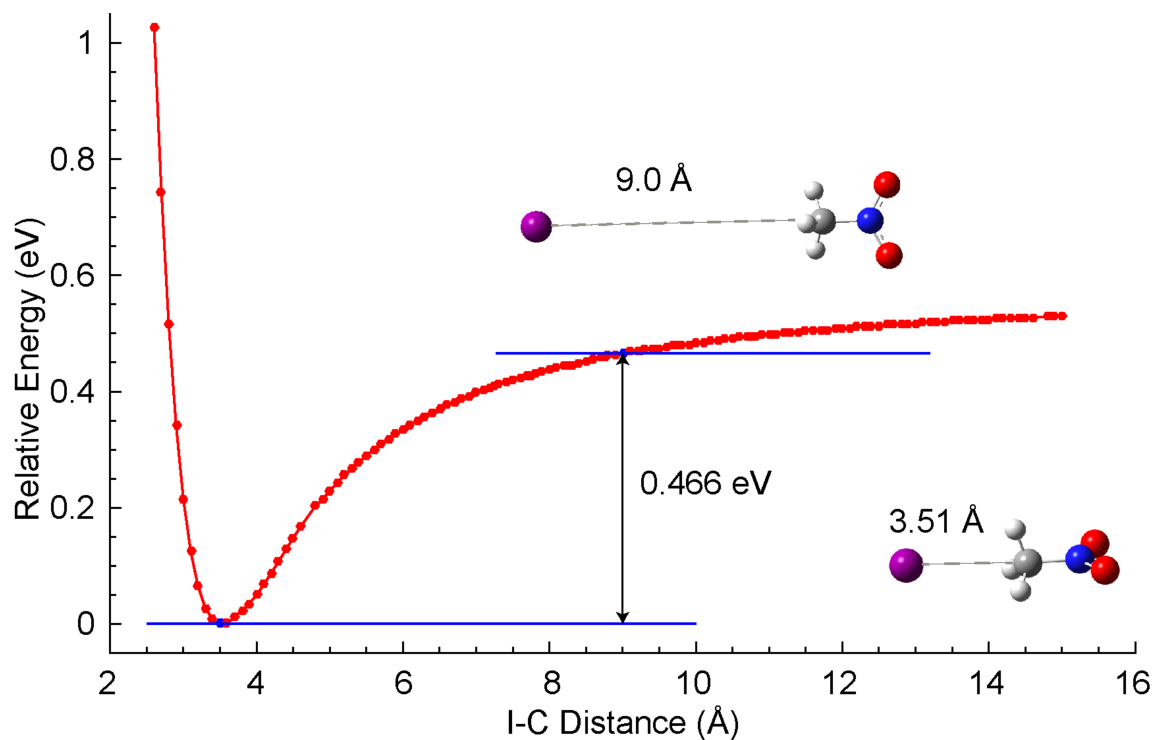


Figure 3.S4: Potential energy curve calculated by geometry optimization at frozen I-C distances. The calculations were performed at the MP2/aug-cc-pVDZ(-pp) level of theory. All energies are ZPE corrected.

3.9 References

- [1] J. H. Hendricks, S. A. Lyapustina, H. L. de Clercq, and K. H. Bowen, “The dipole bound-to-covalent anion transformation in uracil”, *J. Chem. Phys.* **108**, 8–11 (1998).
- [2] R. N. Compton, H. S. Carman, C. Desfrancois, H. Abdoul-Carime, J. P. Schermann, J. H. Hendricks, S. A. Lyapustina, and K. H. Bowen, “On the binding of electrons to nitromethane - dipole and valence bound anions”, *J. Chem. Phys.* **105**, 3472–3478 (1996).
- [3] T. Sommerfeld, “Coupling between dipole-bound and valence states: the nitromethane anion”, *Phys. Chem. Chem. Phys.* **4**, 2511–2516 (2002).
- [4] S. Denifl, S. Ptasińska, G. Hanel, B. Gstir, M. Probst, P. Scheier, and T. D. Märk, “Electron attachment to gas-phase uracil”, *J. Chem. Phys.* **120**, 6557–6565 (2004).
- [5] S. Denifl, S. Ptasińska, M. Probst, J. Hrušák, P. Scheier, and T. D. Märk, “Electron attachment to the gas-phase DNA bases cytosine and thymine”, *J. Phys. Chem. A* **108**, 6562–6569 (2004).
- [6] P. D. Burrow, G. A. Gallup, A. M. Scheer, S. Denifl, S. Ptasińska, T. D. Märk, and P. Scheier, “Vibrational Feshbach resonances in uracil and thymine”, *J. Chem. Phys.* **124**, 124310 (2006).
- [7] M. A. Yandell, S. B. King, and D. M. Neumark, “Time-resolved radiation chemistry: photoelectron imaging of transient negative ions of nucleobases”, *J. Am. Chem. Soc.* **135**, 2128–2131 (2013).
- [8] B. Boudaïffa, P. Cloutier, D. Hunting, M. A. Huels, and L. Sanche, “Resonant formation of DNA strand breaks by low-energy (3 to 20 eV) electrons”, *Science* **287**, 1658–1660 (2000).
- [9] J. Simons, “How do low-energy (0.1-2 eV) electrons cause DNA-strand breaks?”, *Acc. Chem. Res.* **39**, 772–779 (2006).
- [10] J. D. Gu, J. Leszczynski, and H. F. Schaefer, “Interactions of electrons with bare and hydrated biomolecules: from nucleic acid bases to DNA segments”, *Chem. Rev.* **112**, 5603–5640 (2012).
- [11] A. M. Scheer, C. Silvernail, J. A. Belot, K. Aflatooni, G. A. Gallup, and P. D. Burrow, “Dissociative electron attachment to uracil deuterated at the N₁ and N₃ positions”, *Chem. Phys. Lett.* **411**, 46–50 (2005).
- [12] S. B. King, M. A. Yandell, A. B. Stephansen, and D. M. Neumark, “Time-resolved radiation chemistry: Dynamics of electron attachment to uracil following UV excitation of iodide-uracil complexes”, *J. Chem. Phys.* **141**, 224310 (2014).
- [13] S. B. King, A. B. Stephansen, Y. Yokoi, M. A. Yandell, A. Kunin, T. Takayanagi, and D. M. Neumark, “Electron accommodation dynamics in the DNA base thymine”, *J. Chem. Phys.* **143**, 024312 (2015).

- [14] A. B. Stephansen, S. B. King, Y. Yokoi, Y. Minoshima, W.-L. Li, A. Kunin, T. Takayanagi, and D. M. Neumark, “Dynamics of dipole- and valence bound anions in iodide-adenine binary complexes: A time-resolved photoelectron imaging and quantum mechanical investigation”, *J. Chem. Phys.* **143**, 104308 (2015).
- [15] T. Sommerfeld, “Intramolecular electron transfer from dipole-bound to valence orbitals: uracil and 5-chlorouracil”, *J. Phys. Chem. A* **108**, 9150–9154 (2004).
- [16] H. Motegi and T. Takayanagi, “Theoretical study on the transformation mechanism between dipole-bound and valence-bound anion states of small uracil-water clusters and their photoelectron spectra”, *J. Mol. Struct.-THEOCHEM* **907**, 85–92 (2009).
- [17] C. L. Adams, H. Schneider, K. M. Ervin, and J. M. Weber, “Low-energy photoelectron imaging spectroscopy of nitromethane anions: electron affinity, vibrational features, anisotropies, and the dipole-bound state”, *J. Chem. Phys.* **130**, 074307 (2009).
- [18] M. A. Yandell, S. B. King, and D. M. Neumark, “Decay dynamics of nascent acetonitrile and nitromethane dipole-bound anions produced by intracuster charge-transfer”, *J. Chem. Phys.* **140**, 184317 (2014).
- [19] C. E. H. Dessent, J. Kim, and M. A. Johnson, “Spectroscopic observation of vibrational Feshbach resonances in near-threshold photoexcitation of $X^- \cdot CH_3NO_2$ ($X^- = I^-$ and Br^-)”, *Faraday Discuss.* **115**, 395–406 (2000).
- [20] F. Lecomte, S. Carles, C. Desfrancois, and M. A. Johnson, “Dipole bound and valence state coupling in argon-solvated nitromethane anions”, *J. Chem. Phys.* **113**, 10973–10977 (2000).
- [21] D. J. Goebbert, K. Pichugin, and A. Sanov, “Low-lying electronic states of CH_3NO_2 via photoelectron imaging of the nitromethane anion”, *J. Chem. Phys.* **131**, 164308 (2009).
- [22] A. P. Cox and S. Waring, “Microwave spectrum and structure of nitromethane”, *J. Chem. Soc., Faraday Trans. 2* **68**, 1060–1071 (1972).
- [23] W. Sailer, A. Pelc, S. Matejcik, E. Illenberger, P. Scheier, and T. D. Märk, “Dissociative electron attachment study to nitromethane”, *J. Chem. Phys.* **117**, 7989–7994 (2002).
- [24] E. Alizadeh, F. Ferreira da Silva, F. Zappa, A. Mauracher, M. Probst, S. Denifl, A. Bacher, T. D. Märk, P. Limão-Vieira, and P. Scheier, “Dissociative electron attachment to nitromethane”, *Int. J. Mass Spectrom.* **271**, 15–21 (2008).
- [25] C. L. Adams, H. Schneider, and J. M. Weber, “Vibrational autodetachment-intramolecular vibrational relaxation translated into electronic motion”, *J. Phys. Chem. A* **114**, 4017–4030 (2010).
- [26] B. J. Knurr, A. B. McCoy, and J. M. Weber, “Vibrationally induced charge transfer in a bimolecular model complex in vacuo”, *J. Chem. Phys.* **138**, 224301 (2013).

- [27] C. E. H. Dessent and M. A. Johnson, "Photoinitiation of gas-phase SN2 reactions through the Evans-Polanyi excited state surface", *J. Am. Chem. Soc.* **119**, 5067–5068 (1997).
- [28] S. B. King, M. A. Yandell, and D. M. Neumark, "Time-resolved photoelectron imaging of the iodide-thymine and iodide-uracil binary cluster systems", *Faraday Discuss.* **163**, 59–72 (2013).
- [29] K. M. Ervin, J. Ho, and W. C. Lineberger, "Ultraviolet photoelectron spectrum of nitrite anion", *J. Phys. Chem.* **92**, 5405–5412 (1988).
- [30] R. B. Metz, D. R. Cyr, and D. M. Neumark, "Study of the 2B_1 and 2A_2 states of CH_2NO_2 via ultraviolet photoelectron spectroscopy of the $CH_2NO_2^-$ anion", *J. Phys. Chem.* **95**, 2900–2907 (1991).
- [31] P. Manikandan, J. Zhang, and W. L. Hase, "Chemical dynamics simulations of $X^- + CH_3Y \rightarrow XCH_3 + Y^-$ gas-phase SN2 nucleophilic substitution reactions. Nonstatistical dynamics and nontraditional reaction mechanisms", *J. Phys. Chem. A* **116**, 3061–3080 (2012).
- [32] W. L. Hase, "Simulations of gas-phase chemical reactions: applications to SN2 nucleophilic substitution", *Science* **266**, 998–1002 (1994).
- [33] M. L. Chabinye, S. L. Craig, C. K. Regan, and J. I. Brauman, "Gas-phase ionic reactions: dynamics and mechanism of nucleophilic displacements", *Science* **279**, 1882 (1998).
- [34] H. Wang, G. H. Peslherbe, and W. L. Hase, "Trajectory studies of SN2 nucleophilic substitution. 4. Intramolecular and unimolecular dynamics of the $I^- \cdots CH_3Br$ and $ClCH_3 \cdots Br^-$ complexes", *J. Am. Chem. Soc.* **116**, 9644–9651 (1994).
- [35] A. Davis, R. Wester, A. E. Bragg, and D. M. Neumark, "Time-resolved photoelectron imaging of the photodissociation of I_2^- ", *J. Chem. Phys.* **118**, 999–1002 (2003).
- [36] A. E. Bragg, J. R. R. Verlet, A. Kammrath, O. Cheshnovsky, and D. M. Neumark, "Electronic relaxation dynamics of water cluster anions", *J. Am. Chem. Soc.* **127**, 15283–15295 (2005).
- [37] W. C. Wiley and I. H. McLaren, "Time-of-flight mass spectrometer with improved resolution", *Rev. Sci. Instrum.* **26**, 1150–1157 (1955).
- [38] A. Eppink and D. H. Parker, "Velocity map imaging of ions and electrons using electrostatic lenses: application in photoelectron and photofragment ion imaging of molecular oxygen", *Rev. Sci. Instrum.* **68**, 3477–3484 (1997).
- [39] V. Dribinski, A. Ossadtchi, V. Mandelshtam, and H. Reisler, "Reconstruction of Abel-transformable images: the Gaussian basis-set expansion Abel transform method", *Rev. Sci. Instrum.* **73**, 2634–2642 (2002).
- [40] T. Baer and W. L. Hase, *Unimolecular reaction dynamics: theory and dynamics* (Oxford University Press, USA, New York, 1996).

- [41] R. Gilbert and S. Smith, *Theory of unimolecular and recombination reactions* (Blackwell Scientific Publications, London, 1990).
- [42] M. J. Frisch, G. W. Trucks, H. B. Schlegel, G. E. Scuseria, M. A. Robb, J. R. Cheeseman, G. Scalmani, V. Barone, B. Mennucci, G. A. Petersson, H. Nakatsuji, M. Caricato, X. Li, H. P. Hratchian, A. F. Izmaylov, J. Bloino, G. Zheng, J. L. Sonnenberg, M. Hada, M. Ehara, K. Toyota, R. Fukuda, J. Hasegawa, M. Ishida, T. Nakajima, Y. Honda, O. Kitao, H. Nakai, T. Vreven, J. A. Montgomery Jr., J. E. Peralta, F. Ogliaro, M. J. Bearpark, J. Heyd, E. N. Brothers, K. N. Kudin, V. N. Staroverov, R. Kobayashi, J. Normand, K. Raghavachari, A. P. Rendell, J. C. Burant, S. S. Iyengar, J. Tomasi, M. Cossi, N. Rega, N. J. Millam, M. Klene, J. E. Knox, J. B. Cross, V. Bakken, C. Adamo, J. Jaramillo, R. Gomperts, R. E. Stratmann, O. Yazyev, A. J. Austin, R. Cammi, C. Pomelli, J. W. Ochterski, R. L. Martin, K. Morokuma, V. G. Zakrzewski, G. A. Voth, P. Salvador, J. J. Dannenberg, S. Dapprich, A. D. Daniels, Ö. Farkas, J. B. Foresman, J. V. Ortiz, J. Cioslowski, and D. J. Fox, *Gaussian 09, Revision C.01*, 2009.
- [43] T. Beyer and D. F. Swinehart, “Number of multiply-restricted partitions”, *Commun. ACM* **16**, 379–379 (1973).
- [44] J. I. Steinfeld, J. S. Francisco, and W. L. Hase, *Chemical kinetics and dynamics* (Prentice-Hall, New Jersey, 1999).
- [45] R. S. Berry, “Small free negative ions”, *Chem. Rev.* **69**, 533–542 (1969).
- [46] P. Warneck, “Photodetachment of NO_2^- ”, *Chem. Phys. Lett.* **3**, 532–533 (1969).
- [47] W.-L. Li, A. Kunin, E. Matthews, N. Yoshikawa, C. E. H. Dessent, and D. M. Neumark, “Photodissociation dynamics of the iodide-uracil (I⁻U) complex”, *J. Chem. Phys.* **145**, 044319 (2016).
- [48] J. Xie, R. Otto, J. Mikosch, J. Zhang, R. Wester, and W. L. Hase, “Identification of atomic-level mechanisms for gas-phase $\text{X}^- + \text{CH}_3\text{Y}$ SN2 reactions by combined experiments and simulations”, *Acc. Chem. Res.* **47**, 2960–2969 (2014).
- [49] G. H. Peslherbe, H. Wang, and W. L. Hase, “Unimolecular dynamics of $\text{Cl}^- \cdots \text{CH}_3\text{Cl}$ intermolecular complexes formed by $\text{Cl}^- + \text{CH}_3\text{Cl}$ association”, *J. Chem. Phys.* **102**, 5626–5635 (1995).
- [50] S. T. Graul and M. T. Bowers, “The nonstatistical dissociation dynamics of chloride(bromomethane) $\text{Cl}^-(\text{CH}_3\text{Br})$: evidence for vibrational excitation in the products of gas-phase SN2 reactions”, *J. Am. Chem. Soc.* **113**, 9696–9697 (1991).
- [51] J. Mikosch, S. Trippel, C. Eichhorn, R. Otto, U. Lourderaj, J. X. Zhang, W. L. Hase, M. Weidemüller, and R. Wester, “Imaging nucleophilic substitution dynamics”, *Science* **319**, 183–186 (2008).
- [52] A. A. Viggiano, R. A. Morris, J. S. Paschkewitz, and J. F. Paulson, “Kinetics of the gas-phase reactions of chloride anion, Cl^- with CH_3Br and CD_3Br : experimental evidence for nonstatistical behavior?”, *J. Am. Chem. Soc.* **114**, 10477–10482 (1992).

- [53] K. A. Peterson, B. C. Shepler, D. Figgen, and H. Stoll, “On the spectroscopic and thermochemical properties of ClO, BrO, IO, and their anions”, *J. Phys. Chem. A* **110**, 13887 (2006).
- [54] J. P. Merrick, D. Moran, and L. Radom, “An evaluation of harmonic vibrational frequency scale factors”, *J. Phys. Chem. A* **111**, 11683–11700 (2007).
- [55] S. E. Stein and B. S. Rabinovitch, “Accurate evaluation of internal energy level sums and densities including anharmonic oscillators and hindered rotors”, *J. Chem. Phys.* **58**, 2438–2445 (1973).

Chapter 4

Photodissociation Dynamics of Iodide-Uracil Complexes

Finding meaning, like losing
meaning, involves pleasure as
well as pain.

Lewis Carroll

The content and figures of this chapter are adapted from:

W.-L. Li, A. Kunin, E. Matthews, N. Yoshikawa, C. E. H. Dessent, and D. M. Neumark, “Photodissociation dynamics of the iodide-uracil ($I^- \cdot U$) complex” *J. Chem. Phys.* **145**, 044319 (2016)

with the permission of AIP Publishing.

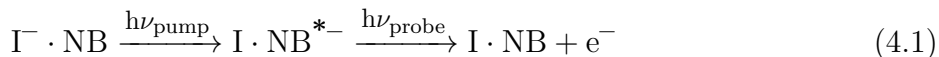
4.1 Abstract

Photofragment action spectroscopy and femtosecond time-resolved photoelectron imaging are utilized to probe the dissociation channels in iodide-uracil ($\text{I}^- \cdot \text{U}$) binary clusters upon photoexcitation. The photofragment action spectra show strong I^- and weak $[\text{U}-\text{H}]^-$ ion signal upon photoexcitation. The action spectra show two bands for I^- and $[\text{U}-\text{H}]^-$ production peaking around 4.0 and 4.8 eV. Time-resolved experiments measured the rate of I^- production resulting from excitation of the two bands. At 4.03 eV and 4.72 eV, the photoelectron signal from I^- exhibits rise times of 86 ± 7 ps and 36 ± 3 ps, respectively. Electronic structure calculations indicate that the lower energy band, which encompasses the vertical detachment energy (4.11 eV) of $\text{I}^- \cdot \text{U}$, corresponds to excitation of a dipole-bound state of the complex, while the higher energy band is primarily a $\pi - \pi^*$ excitation on the uracil moiety. Although the nature of the two excited states is very different, the long lifetimes for I^- production suggest that this channel results from internal conversion to the $\text{I}^- \cdot \text{U}$ ground state followed by evaporation of I^- . Rice-Ramsperger-Kassel-Marcus (RRKM) calculations suggest, as in Ch. 3, that the dissociation rate may be limited by intramolecular vibrational energy redistribution in the internally converted, ground state anion.

4.2 Introduction

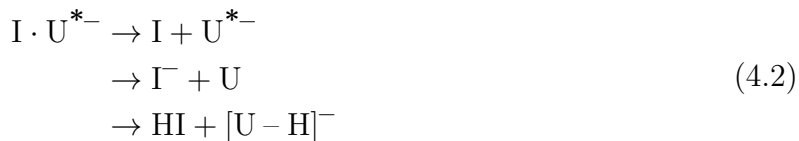
High energy radiation is capable of producing free electrons as it passes through matter, and these free electrons can generate large quantities of lower energy secondary electrons [1]. Both primary and secondary electrons can cause damage to DNA in living cells [1]. Extensive studies have shown that free electrons with energy well below the ionization potential of DNA constituents can cause both single- and double-strand breaks in DNA [2–12]. Experimental and theoretical investigations have been performed to understand the underlying DNA damage mechanism at the molecular level. Theoretical studies suggest that cleavage is initiated by electron attachment to one component of the DNA strand to form a transient negative ion, followed by subsequent fragmentation [13–17]. The unoccupied low-lying π^* anti-bonding orbitals of nucleobases and dissociative σ^* orbital of phosphate groups are possible sites of electron capture [13–15, 17]. Experimentally, dissociative electron attachment studies of uracil find that the dominant channel at low collision energy is the production of the deprotonated nucleobase, where the H loss occurs at the nitrogen positions [18]. O–H and P=O/P–O bond breaks are also observed as a result of electron attachment to the phosphate group [15]. We have previously studied electron-nucleobase interactions by photoexcitation of gas phase iodide nucleobase (NB) anions, in which low energy electrons that are photodetached from the iodide are captured by the nucleobase, forming a temporary negative ion whose subsequent dynamics are followed by time-resolved photoelectron spectroscopy [19–23]. In this paper, we characterize the products of this photoexcitation in more detail, focusing primarily on the mechanism by which I^- is formed by ultraviolet excitation of iodide-uracil anions.

In previous work, femtosecond pump-probe experiments based on the following excitation and detection scheme were carried out on $\text{I}^- \cdot \text{uracil}$ ($\text{I}^- \cdot \text{U}$) [19, 21], $\text{I}^- \cdot \text{thymine}$ ($\text{I}^- \cdot \text{T}$) [20, 22], and $\text{I}^- \cdot \text{adenine}$ ($\text{I}^- \cdot \text{A}$) complexes [23].



An ultraviolet pump pulse photexcites the complex, forming a transient $\text{I} \cdot \text{NB}^{*-}$ species in which neutral iodine is bound to a dipole-bound (DB) or valence-bound (VB) nucleobase anion. This temporary negative anion is photodetached by a near-infrared probe pulse and the resulting photoelectron (PE) spectrum is measured. The PE spectrum enables one to determine if a DB and/or VB nucleobase anion is formed [24–26], to follow the conversion of a DB anion to a VB anion [27], and to measure the lifetime of either species with respect to electron loss and other possible decay channels. Experiments on $\text{I}^- \cdot \text{U}$ and $\text{I}^- \cdot \text{T}$ were performed at pump photon energies in two energy ranges: near 4.0 eV, which is very close to the vertical detachment energy (VDE) of the complexes, and around 4.7 eV, well above the VDE. Excitation at the lower energy range yields both DB and VB anions. The time-evolving spectra suggest that some of the DB states convert to VB states on a timescale of several hundred femtoseconds. At the higher energies, the VB state is formed instantaneously within the time resolution of our experiment (<150 fs), and there is no evidence for a DB state. These short-time electron attachment dynamics have been interpreted with the aid of electronic structure calculations that have considered the energetics and structure of the DB and VB anions [26, 28–31].

At longer times, the DB and VB features in $\text{I}^- \cdot \text{U}$ and $\text{I}^- \cdot \text{T}$ exhibit either mono-exponential or bi-exponential decay. One of these decay channels was established to be autodetachment [19, 20], in which a very low energy electron is emitted from the temporary negative ion created by the pump pulse. However, other channels are energetically accessible:



The time-resolved PE imaging (TRPEI) experiments carried out thus far on these complexes used a probe wavelength of 790 nm (1.57 eV), which was sufficiently energetic to photodetach $\text{I} \cdot \text{U}^{*-}$ and U^{*-} , but not I^- or the deprotonated $[\text{U} - \text{H}]^-$ anion, for which the corresponding neutral electron affinities are 3.059 eV [32] and 3.481 eV [33], respectively. In the current study, we carry out photofragment action spectroscopy on $\text{I}^- \cdot \text{U}$ from 3.6 – 5.2 eV to determine the yields of I^- and $[\text{U} - \text{H}]^{*-}$ as a function of UV excitation energy,

and thus gaining insight into which of the energetically accessible decay channels are active. We find that the action spectra for both fragments comprise two broad bands with maxima at approximately 4.0 eV and 4.8 eV. Complementary TRPEI experiments at higher probe photon energies have also been carried out at 4.03 and 4.72 eV with the specific goal of time-resolving the appearance of the I^- channel. These long lifetimes suggest that I^- is produced by internal conversion from the excited state $I \cdot U^{*-}$ created by the pump pulse to the ground $I^- \cdot U$, followed by statistical decay to $I^- + U$.

4.3 Experimental Methods

Photodepletion (absorption) and photofragment action spectra were conducted in a custom-modified Bruker AmaZon Ion Trap mass spectrometer in the Dessent group at the University of York [34, 35]. The $I^- \cdot U$ clusters were generated by electrospraying solutions of uracil and iodide in deionized water (nucleobase solutions were 1×10^{-4} mol/dm³, mixed with droplets of the t-butyl ammonium iodide (TBAI) at 1×10^{-2} mol/dm³). All chemicals were purchased from Sigma-Aldrich and used without further purification. The $I^- \cdot U$ clusters were mass-selected and isolated in the instrumental ion-trap prior to laser irradiation. The photofragment ion intensity was then recorded using the normal functions of the mass spectrometer. UV light for the photofragmentation experiment was produced by a Nd:YAG (Continuum Surelite) pumped optical parametric oscillator (Continuum Horizon), producing ~ 2 mJ across 225 – 310 nm. The spectral resolution is determined by the laser step size (1 nm or ~ 0.018 eV in the mid-spectral region) for the action spectra presented here. All spectra are corrected for laser power.

The femtosecond time-resolved photoelectron imaging apparatus at Berkeley has been described in detail previously [36, 37]. $I^- \cdot U$ clusters were produced by thermal desorption of solid uracil (Sigma-Aldrich, $\geq 99.0\%$) loaded in an Even-Lavie pulsed valve and then entrained by 40 psig argon carrier gas mixed with iodomethane vapor. The gas mixture was supersonically expanded into vacuum and passed through a ring electrode ionizer for secondary electron attachment to form the binary cluster anions. The anionic clusters were then perpendicularly extracted and analyzed using a Wiley-McLaren time-of-flight mass spectrometer. Clusters of interest were isolated by a mass gate before interacting with the pump and probe laser beams. Two pump-probe schemes were used in these experiments. Near the VDE, the pump pulse (308 nm, 4.03 eV, 5 μ J/pulse) was generated from a 1 kHz, 2.0 mJ 790 nm pulse (KM Labs Griffin Oscillator and Dragon Amplifier) by frequency doubling the second harmonic signal of an optical parametric amplifier (OPA) (Light Conversion TOPAS-C). The probe pulse (344 nm, 3.61 eV, 8 μ J/pulse) was formed by combining the residual TOPAS-C signal and the fundamental 790 nm pulse. For excitation well above the VDE, the pump pulse (263 nm, 4.72 eV, 5 μ J/pulse) was produced by frequency tripling the fundamental pulse and the probe (395 nm, 3.15 eV, 80 μ J/pulse) was generated by doubling the fundamental pulse. The cross-correlation of the pump and probe pulses was less than 150

fs for 308 nm/344 nm and 200 fs for 263 nm/395 nm. After laser interaction, the resulting photoelectrons were extracted and analyzed by velocity map imaging (VMI) onto a position-sensitive microchannel plate detector. The photoelectron kinetic energy (eKE) distributions and photoelectron angular distributions (PADs) were reconstructed from the images using basis-set expansion (BASEX) [38] reconstruction methods.

4.4 Results

The negative ion electrospray mass spectrum of the mixed $\text{I}^- + \text{U}$ solution is displayed in Fig. 4.S1. The spectrum is dominated by the I^- ion and the $\text{I}^- \cdot \text{TBAI}$ salt cluster; the $\text{I}^- \cdot \text{U}$ cluster signal is weaker but clearly visible. The photodepletion (absorption) spectrum for the $\text{I}^- \cdot \text{U}$ cluster was obtained across the region from approximately 3.6 eV to 5.2 eV and is shown in Fig. 4.1a. The spectrum has an onset at approximately 3.75 eV and the first strong absorption band is observed near 4.0 eV, indicating that an excited state of the cluster exists in the region below the VDE of $\text{I}^- \cdot \text{U}$ of 4.11 eV [19–21], as would be expected for the DBS observed previously [21]. Continuously strong absorption is observed up to approximately 5.2 eV, consistent with significant direct electron detachment from the cluster.

Fig. 4.1b shows the photofragmentation action spectrum of I^- . Similar to the absorption spectrum, the I^- signal has an onset at approximately 3.75 eV. The first strong I^- ion production band is observed with a band maximum at 4.0 eV. Another strong I^- production region lies between 4.2 eV to 5.3 eV, peaking at 4.8 eV. The intensity ratio for 4.0 eV/4.8 eV for I^- is approximately 3:2. The action spectrum of $[\text{U}-\text{H}]^-$ is shown in Fig. 4.1c; the most intense $[\text{U}-\text{H}]^-$ photofragment bands occur around 4.0 eV and 4.8 eV, similar to the I^- signal. The intensity ratio at 4.0 eV/4.8 eV for $[\text{U}-\text{H}]^-$ is 4:1. The photofragmentation mass spectrum of $\text{I}^- \cdot \text{U}$ obtained at 4.78 eV (Fig. 4.S2) shows I^- as the dominant photofragment and $[\text{U}-\text{H}]^-$ as a minor photofragment. Thus, the dominant cluster photofragmentation process (i.e. excluding electron detachment) is cluster fission: $\text{I}^- \cdot \text{U} \rightarrow \text{I}^- + \text{U}$.

To investigate the time-resolved dissociation dynamics, TRPEI spectra were recorded at excitation energies of 4.03 eV and 4.72 eV, near the two band maxima in the photofragment action spectra. Fig. 4.2 shows representative time-resolved spectra at pump and probe energies of 4.03 eV and 3.61 eV (343 nm), respectively. Three major features are observed in the spectra. The most intense feature A occurs near eKE = 0. Its intensity does not obviously change with varying pump-probe delays, and it is attributed to autodetachment resulting from excitation at the pump energy [19–21].

A sharp feature B is observed at eKE = 0.55 ± 0.06 eV. Its intensity at negative delay time, in which the probe pulse arrives before the pump pulse, is zero and increases for positive delays until it reaches a plateau. Based on its kinetic energy and narrow peak width, we can readily assign feature B to photodetachment of I^- by the probe pulse. The contour plot of

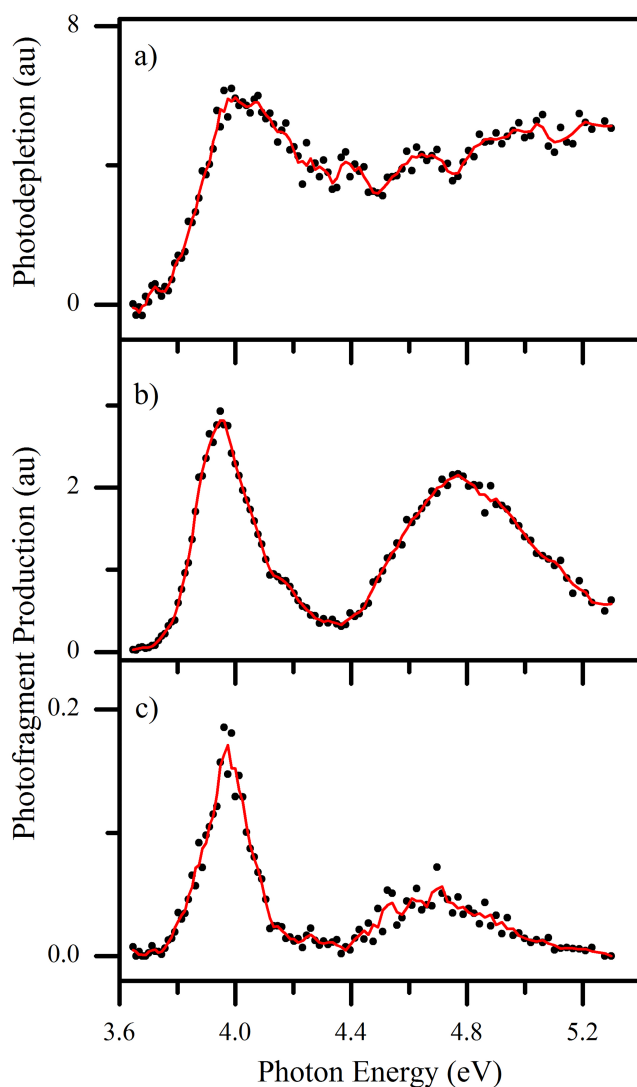


Figure 4.1: a) Photodepletion (absorption) spectrum of $\text{I}^- \cdot \text{U}$ displayed with the corresponding photofragment action spectra of the (b) I^- and (c) $[\text{U-H}]^-$ photofragments. The solid lines represent 3 point smooths through the data points.

background-subtracted signal for feature B is shown in Fig. 4.3. A very weak feature C is observed near 3.5 ± 0.1 eV eKE, and its intensity is also time-dependent. This feature is assigned as photodetachment from the DBS by the probe pulse, which has been examined in detail previously [21]. Although the probe pulse is sufficiently energetic to photodetach the $[\text{U-H}]^-$ anion, no evidence for this species is seen in either Fig. 4.2 or 4.3.

Fig. 4.4 shows representative TRPEI spectra at an excitation energy of 4.72 eV and a

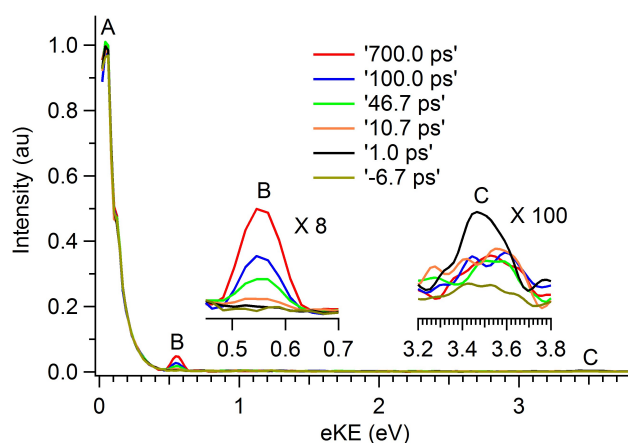


Figure 4.2: Photoelectron spectrum of $I^- \cdot U$ species at 4.03 eV pump and 3.61 eV probe at selected delay times.

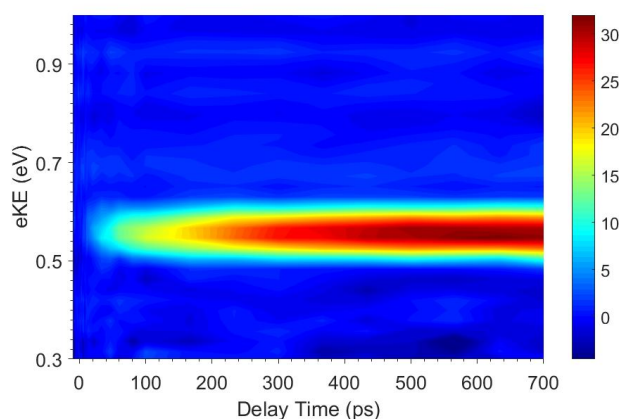


Figure 4.3: Time-resolved photoelectron spectra for feature B for $I^- \cdot U$ at an excitation energy of 4.03 eV (near the VDE) and probe energy of 3.61 eV.

probe energy of 3.15 eV (395 nm). The pump-only spectrum at -100 ps shows a strong autodetachment peak A near zero-eV eKE (see inset) as well as a peak C around 0.6 eV. Feature C is attributed to the direct detachment of $I^- \cdot U$ by the pump pulse. The time-dependent feature B occurs at slightly higher kinetic energy than feature A, 0.09 ± 0.02 eV at large positive delay times, and, as in Fig. 4.2, is readily assigned to detachment of I^- by the probe pulse. Note that the probe energy used in Fig. 4.2 would have placed feature B directly on top of feature C, where it would be even more difficult to discern since the probe pulse at 343 nm is considerably weaker than that at 395 nm (see Section 4.2). The contour plot of background-subtracted signal for feature B with respect to the most negative delay time is shown in Fig. 4.5.

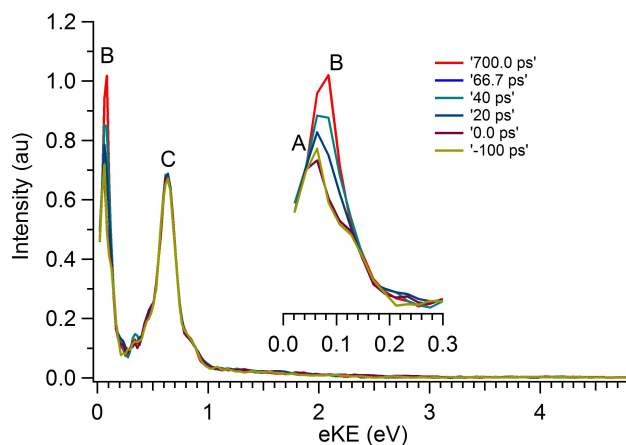


Figure 4.4: Photoelectron spectrum of $\text{I}^- \cdot \text{U}$ with 4.72 eV pump (significantly above the VDE) and 3.15 eV probe at selected delay times.

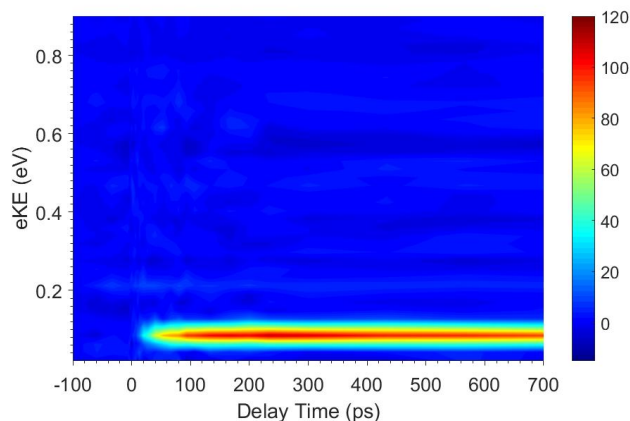


Figure 4.5: Time-resolved photoelectron spectrum for feature B for $\text{I}^- \cdot \text{U}$ with an excitation energy of 4.72 eV and probe energy of 3.15 eV.

4.5 Analysis

The photofragment action spectrum for I^- in Fig. 4.1 shows evidence for two dissociative electronic states of $\text{I}^- \cdot \text{U}$ at 4.0 eV and 4.8 eV. These transitions can be assigned with the aid of equation of motion coupled cluster singles and doubles (EOM-CCSD) excited states calculations. The anion ground state geometry optimization was first performed at MP2 level with an augmented Dunning basis set aug-cc-pVDZ for C, H, O, N [39] and aug-cc-pVDZ-pp with an expanded basis set with an increased set of diffuse functions for iodide [39–41] (MP2/aug-cc-pVDZ-(pp)). The optimized structure was used in the EOM-CCSD calculation. All calculations were performed using the Gaussian 09 program [42]. Table

Table 4.1: EOM-CCSD calculated transition channels, excitation energies, oscillator strength, and final state configurations. Calculated at the EOM-CCSD/aug-cc-pVZ-(pp) level of theory. The tabulated excitation energies are offset by -0.52 eV from the calculated values to facilitate comparison with the experimental data.

Excitation Energy (eV)	Oscillator Strength	Transition Channel	Final State Configuration
4.04	0.0879	I(5p)–DB	I(5p⁵)U⁻(DB¹)
4.06	0.0956	I(5p)–DB	I(5p⁵)U⁻(DB¹)
4.23	0.1176	I(5p)–DB	I(5p⁵)U⁻(DB¹)
4.49	0.0011	I(5p) – π^*	I(5p ⁵)U ⁻ ($\pi^4\pi^{*1}$)
4.56	0.0016	I(5p) – π^*	I(5p ⁵)U ⁻ ($\pi^4\pi^{*1}$)
4.61	0.0000	I(5p) – π^*	I(5p ⁵)U ⁻ ($\pi^4\pi^{*1}$)
4.66	0.0400	I(5p) – σ^*	I(5p⁵)U⁻(σ^{*1})
4.68	0.0274	I(5p) – σ^*	I(5p⁵)U⁻(σ^{*1})
4.77	0.3100	$\pi - \pi^*$	I⁻(5p⁶)U($\pi^3\pi^{*1}$)

4.1 presents the transition channels, excitation energies, corresponding oscillator strength, and final state configurations. The six electronic transitions with largest oscillator strength are marked bold in Table 4.1. All the excitation energies are offset by -0.52 eV for comparison with experiment. Three electronic transitions from 4.04 to 4.24 eV correspond to transitions from a 5p orbital on the iodide anion to form a DBS of the complex. These three channels contribute to the strong absorption band around 4.0 eV. The most intense transition, calculated at 4.77 eV, is the $\pi - \pi^*$ transition on the nucleobase. This and two weaker transitions contribute to the strong absorption band around 4.8 eV. Therefore the lower and higher bands in the I⁻ action spectrum are primarily from I(5p)–DB and $\pi - \pi^*$ transitions, respectively. The calculation also shows three very weak transitions between 4.5 eV to 4.6 eV corresponding to electron transfer from the I(5p) orbital to the π^* anti-bonding orbital, i.e. direct formation of the anion VB state by optical excitation.

We next consider the time-dependent photoelectron signals in Figs. 4.2 – 4.5. The integrated intensity change of feature B at 4.03 eV is fit using Eq. 4.3. The fitting for feature B yields a mono-exponential rise time of 86 ± 7 ps, as shown in Fig. 4.6. The DBS decays bi-exponentially with time constants of 6 ps and 2800 ps (Fig. 4.S3), which lies within error bars of the previously reported values, 8.5 ps and 2000 ps, from earlier experiments at an excitation energy of 4.00 eV [21].

$$I(t) = I_0 - \Sigma A_i \exp(-t/\tau_i) \tag{4.3}$$

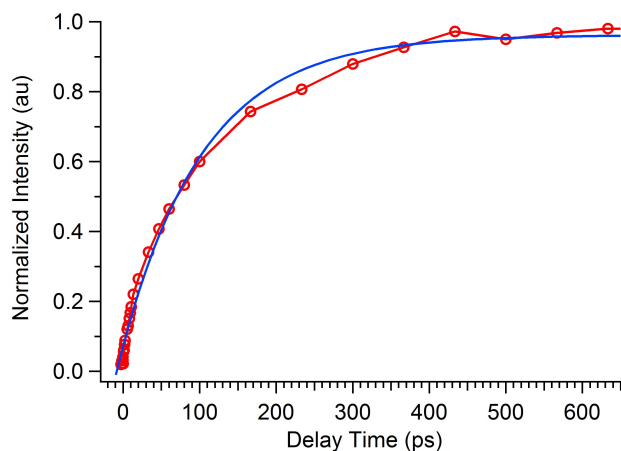


Figure 4.6: Integrated intensity of feature B from excitation at 4.03 eV vs. delay time. The rise time for feature B is 86 ± 7 ps.

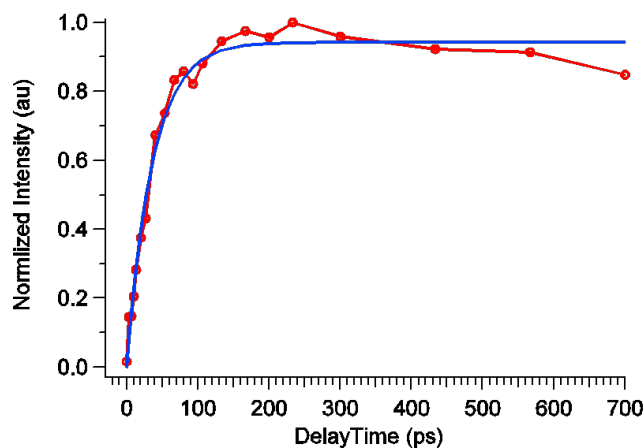


Figure 4.7: Integrated intensity of feature B from excitation at 4.72 eV vs. delay time. The rise time for feature B is 36 ± 3 ps.

At 4.72 eV, the intensity integration was performed over the range from 0.02 eV to 0.2 eV, which includes both features A and B since they are partially overlapped. In previous work, the autodetachment feature A exhibited some time-resolved dynamics [19–21]. However, its intrinsic intensity change as a function of time was very minor compared to the total intensity change of features A and B observed in the current experiment. Thus, the major intensity change between 0.02 eV to 0.2 eV is caused by feature B and therefore can be used to represent the dynamics of feature B. The integrated intensity of feature B from 0.02 to 0.2 eV is shown in Fig. 4.7. This feature also fits well to a mono-exponential rise, but has a faster rise time of 36 ± 3 ps compared to excitation at 4.03 eV.

The long time constants for I^- formation and their drop with increasing pump energy suggest a statistical decay channel; a possible overall mechanism is internal conversion from the excited $\text{I}\cdot\text{U}^{*-}$ state to a highly vibrationally excited $\text{I}^- \cdot \text{U}$ ground state that decays to $\text{I}^- + \text{U}$. This process should be amenable to a statistical treatment such as RRKM theory [43, 44]. It is thus useful to carry out RRKM calculations of the dissociation rate at the two excitation energies and compare these results with our experimental values.

According to RRKM theory, the microcanonical reaction rate constant $k(\text{E})$ for a given energy depends on the sum of states of the transition state, $G(\text{E} - \text{E}_0)$, and the density of states of the reactant, $N(\text{E})$, as expressed in Eq. 4.4. Here, E is the total maximum energy provided to the system (pump pulse), and E_0 is the difference in energy between the zero-point energy (ZPE) of the reactant and transition state.

$$k(\text{E}) = \frac{G(\text{E} - \text{E}_0)}{h \cdot N(\text{E})} \quad (4.4)$$

The reactant species was taken to be the electronic ground state $\text{I}^- \cdot \text{U}$ configuration. Calculations by Takayanagi and co-workers [31] find that dissociation of $\text{I}^- \cdot \text{U}$ clusters to $\text{I}^- + \text{U}$ proceeds without an exit barrier with a reaction endothermicity of 0.97 eV, calculated at the CAM-B3LYP/aug-cc-pVDZ+ α (H:2s2p) level of theory. Since this barrierless potential does not have a distinct transition state on the potential energy curve (Fig. 4.S4), we employed a variational transition state theory approach [45] by calculating the rate constants along the reaction path to locate the transition state that gave the minimum rate constant. The dissociation potential energy curve was calculated by selecting the I–N1 distance as the reaction coordinate (Fig. 4.S4). Geometry optimizations and vibrational frequency calculations were performed at each I–N1 distance from 2 Å to 20 Å at increments of 0.25 Å and at increments of 0.05 – 0.1 Å near the transition state. All geometry optimizations and frequency calculations were performed at the MP2/aug-cc-pVDZ(-pp) level of theory. The energy barrier E_0 was calculated as the ZPE-corrected energy difference between the reactant $\text{I}^- \cdot \text{U}$ and the transition state $[\text{I}^- \cdot \text{U}]^\ddagger$. A scaling factor of 0.9615 [46] corresponding to the MP2/aug-cc-pVDZ level of theory was used to scale the Gaussian-produced vibrational frequencies to account for anharmonicities. To capture the transition state variationally, the rate coefficient for each reactant $\text{I}^- \cdot \text{U}$ and transition state $[\text{I}^- \cdot \text{U}]^\ddagger$ pair was calculated using Eq. 4.4 to determine the transition state that yielded a minimum value for the rate constant. The sum and density of states were calculated by implementing the Beyer-Swinehart direct count algorithm with the Stein-Rabinovitch modification [47] for the sum and density of states from the vibrational and rotational frequencies of each species, including explicit treatment for hindered internal rotors [48]. The barrier height and symmetry for hindered internal rotors were calculated by performing relaxed potential energy scans in Gaussian 09 at the MP2/aug-cc-pVDZ level across the rotational movement in increments of 10°.

As shown in Fig. 4.S4, the dissociation rate constant declines when the I–N1 distance is smaller than 9 Å and increases when the I–N1 distance is greater than 9 Å, so the transition state structure used was the optimized geometry for when I–N1 is 9 Å (Fig. 4.S4). At an I–N1 distance of 9 Å, the calculated barrier height from $\text{I}^- \cdot \text{U}$ to $[\text{I}^- \cdot \text{U}]^\ddagger$ was found to be 0.943 eV, and the ZPE-corrected barrier height, or reaction energy was calculated to be 0.947 eV. The total reaction endothermicity was calculated to be 1.10 eV (CCSD). Treating all frequencies harmonically produces an RRKM calculated time constant of 5.3 ps and 2.8 ps for the two excitation energy regions, smaller than the experimental values of 86 ps and 36 ps, respectively. The frequencies of the $\text{I}^- \cdot \cdot \text{U}$ (Table 4.S1) in-plane rocking mode and out-of-plane twisting mode drop dramatically with increasing $\text{I}^- \cdot \cdot \text{U}$ distance and are better treated as hindered rotors in the RRKM analysis. Calculated sums and densities of states for the reactant and transition state species are listed in Table 4.S2. When the $\text{I}^- \cdot \text{U}$ binary cluster is excited at a photon energy 4.03 eV, i.e. 3.08 eV above the ZPE-corrected reaction energy of 0.947 eV, the RRKM calculated life time is 8.6 ps. At 4.72 eV, i.e. an excess energy of 3.77 eV, the RRKM calculated life time is 4.4 ps. The calculated lifetimes are about a factor of ten shorter than the experimental results of 86 ± 7 ps and 36 ± 3 ps. However, this result approximately reproduces the ratio of the experimental lifetimes at the two pump energies.

4.6 Discussion

According to the photofragment action spectra (Fig. 4.1), I^- and $[\text{U-H}]^-$ production exhibits maxima around 4.0 eV and 4.8 eV. EOM-CCSD calculations (Table 4.1) show that $\text{I}^- \cdot \text{U}$ has two intense resonant excitation regimes which, when shifted by -0.52 eV, line up reasonably well with the experimental maxima. The transitions near 4.0 eV correspond to excitation from the anion ground state to the DBS by promotion of an electron from the $\text{I}(5\text{p})$ orbital to the DB orbital (DBO). Near 4.8 eV, the $\pi - \pi^*$ transition, localized on the uracil moiety, is dominant and there are considerably weaker transitions representing excitations from $\text{I}(5\text{p})$ orbitals to a σ^* orbital on the nucleobase. Excitation from $\text{I}(5\text{p})$ orbitals to the π^* orbital on the uracil yields excitation energies around 4.5 eV, and the oscillator strengths for these $\text{I}(5\text{p})-\pi^*$ excitation channels are near zero so the minimum resonant excitation is expected around 4.5 eV. It thus appears that the two maxima in the photofragment action spectra correspond to two very different electronic excitations, one of which leaves neutral iodine complexed to a DB state of U^- , while the other produces I^- complexed to electronically excited uracil. Nonetheless, both final states fragment primarily to I^- with $[\text{U-H}]^-$ as a minor channel.

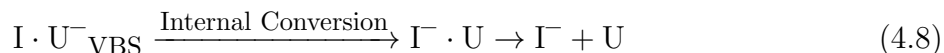
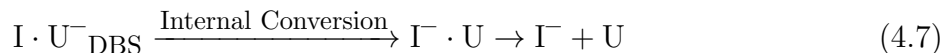
The time-resolved experiment shows the production of I^- at both 4.03 eV and 4.72 eV excitation energies, exhibiting a slow mono-exponential rise in both cases. The fitted rise time constants are fairly long (86 ps and 36 ps, respectively), indicating that statistical decay is likely occurring in both energy regimes. Although the statistical RRKM simulated rise

times of 8.6 ps and 4.4 ps underestimate the experimental time constants by an order of magnitude, it roughly reproduces the ratio of the experimental lifetimes at the two pump energies. As suggested in Ch. 3, it is possible that the discrepancy between the experimental and RRKM results arises due to a dynamical bottleneck for dissociation due to inefficient intramolecular vibrational energy redistribution in the ground state anion. We now consider the mechanisms by which the two very different nascent excited states can relax to form vibrationally excited $\Gamma \cdot \text{U}$ in its ground electronic state.

At 4.72 eV, it is quite straightforward to put forth such a mechanism. Our calculations indicate that when the $\Gamma \cdot \text{U}$ binary cluster is excited at 4.72 eV, the $\pi - \pi^*$ transition of uracil dominates. This $\pi - \pi^*$ transition produces an excited state with an electronic configuration of $\Gamma(5p^6)\text{U}(\pi^3\pi^{*1})$. Internal conversion could occur from this $\pi - \pi^*$ excited state to the ground state configuration $\Gamma(5p^6)\text{U}(\pi^4\pi^{*0})$, i.e. the electron in the π^* anti-bonding orbital falls back to the π orbital in the electronic ground state. Experiments on gas phase uracil have shown the internal conversion following $\pi - \pi^*$ excitation could occur within ~ 1 ps [49–52], leaving uracil in a vibrationally excited electronic ground state, and one expects a similar time constant in $\Gamma \cdot \text{U}$. Upon internal conversion, the highly vibrationally excited cluster can evaporate iodide, whose presence is readily seen in our TRPEI experiment. While it would be desirable to detect decay of the hot $\Gamma \cdot \text{U}$ as it dissociates to $\Gamma + \text{U}$, the VDE of this complex is likely to be similar to that of the cold complex (4.11 eV), which is considerably higher than the probe photon energy. The overall proposed mechanism is given by Equation 4.5.



The assignment of the band at 4.03 eV as photoexcitation to a complex with an electronic configuration of $\text{I}(5p^5)\text{U}^-(\text{DB}^1)$ is consistent with our earlier time-resolved experiments [21] that showed formation of a complexed DB state ($\text{I} \cdot \text{U}^-_{\text{DBS}}$) of the uracil anion in this energy range. These experiments also revealed that a complexed VB state ($\text{I} \cdot \text{U}^-_{\text{VBS}}$) was formed with a slight delay relative to the DB state; this observation was tentatively attributed to partial conversion of the DB state to the VB state. Regardless, in order for Γ^- to be a decay product, there needs to be back-transfer of the excess electron from the nucleobase to the iodine, forming hot $\Gamma \cdot \text{U}$ that can then dissociate. The overall mechanisms are then represented by Eqs. 4.6 – 4.8:



Intuitively, this process might seem more facile from the VB state, given the considerable size mismatch between the DB and I(5p) orbitals. Experimentally, there is evidence for back-transfer (i.e. fragmentation to Γ^-) in photoexcited $\Gamma^- \cdot \text{CH}_3\text{NO}_2$ complexes [53], in which the initially formed $\text{I} \cdot \text{CH}_3\text{NO}_2^-$ DB state converts within 250 fs to a $\text{I} \cdot \text{CH}_3\text{NO}_2^-$ VB state [27], but not in photoexcited $\Gamma^- \cdot \text{CH}_3\text{CN}$ where no such conversion to a VB state occurs [54]. Based on these considerations, Eq. 4.8 is likelier route to Γ^- production than Eq. 4.7.

Our previous time-resolved experiments [21] showed that at a pump energy of 4.00 eV, signals associated with $\text{I} \cdot \text{U}^-_{\text{DBS}}$ and $\text{I} \cdot \text{U}^-_{\text{VBS}}$ exhibited biexponential decay with time constants of 8.5 and 200 ps for the DB complex and 16 and 460 ps for the VB complex. The fast decays in both cases were attributed to autodetachment from the complex, but since both fast time constants are considerably shorter than the Γ^- appearance time of 86 ps, it is possible that they represent back-transfer to form vibrationally hot $\Gamma^- \cdot \text{U}$, which then dissociates, particularly in the case of the VB complex.

In comparing the results obtained here around 4.7 eV to our earlier time-resolved experiments in this energy range, it is important to understand whether one or two photoexcitation channels are operative. The results here clearly show that $\pi - \pi^*$ excitation leads to fragmentation to Γ^- . Our previous results using pump energies from 4.6 – 4.9 eV and a 790 nm probe pulse indicated prompt formation of an $\text{I} \cdot \text{U}^-_{\text{VBS}}$ complex whose lifetime with respect to autodetachment is 410 fs [19, 20]. We attributed formation of this complex to capture of the electron photodetached from the Γ^- into the empty π^* orbital on the uracil, essentially a two-step process as opposed to direct optical excitation into the π^* ; the latter is indeed shown to be very weak in the EOM-CCSD results in Table 4.1. Nonetheless, as pointed out in our first paper in this series [19], it is possible to form the $\text{I} \cdot \text{U}^-_{\text{VBS}}$ complex via Eq. 4.9 :



Here, $\pi - \pi^*$ excitation on the uracil is followed by electron transfer from the iodide into the empty π orbital. This mechanism is appealing because it implies that only a single photoexcitation process occurs around 4.7 eV. However, the instantaneous appearance of the $\text{I} \cdot \text{U}^-_{\text{VBS}}$ complex means that the electron transfer step would have to be exceedingly fast, i.e. less than 50 fs. While this cannot be ruled out, it seems unlikely given the negligible spatial overlap between the HOMO on the Γ^- and the π MO on the uracil. Moreover, autodetachment signal characteristic of the $\text{I} \cdot \text{U}^-_{\text{VBS}}$ complex remains strong out to 5.3 eV, well beyond the $\pi - \pi^*$ band in Fig. 4.1b. It would thus appear that two photoexcitation pathways are operative around 4.7 eV, but a more quantitative theoretical treatment is needed to sort out this issue.

4.7 Conclusions

Photofragment action spectroscopy and femtosecond time-resolved photoelectron imaging are utilized to probe the dissociation channels in the $\Gamma^- \cdot \text{U}$ binary complex upon photoexcitation. The photofragment action spectra show both I^- and $[\text{U-H}]^-$ ion signal upon photoexcitation, with $\Gamma^- \cdot \text{U} \rightarrow \text{I}^- + \text{U}$ as the dominant dissociation channel. The action spectra show two bands for I^- and $[\text{U-H}]^-$ production, with band maxima located at 4.0 eV and 4.8 eV. With the aid of electronic structure calculations, these bands are assigned, respectively, to excitation of a dipole-bound state of the complex and $\pi - \pi^*$ excitation of the uracil moiety.

The $\Gamma^- \cdot \text{U} \rightarrow \text{I}^- + \text{U}$ channel is observed in TRPES via photodetachment of the I^- product. Time-resolved experiments are reported at excitation energies of at 4.03 eV and 4.72 eV, where the I^- signal exhibits rise times of 86 ± 7 ps and 36 ± 3 ps, respectively. These long lifetimes are suggestive of internal conversion to the $\Gamma^- \cdot \text{U}$ ground state followed by statistical dissociation, a hypothesis tested by carrying out RRKM calculations of the dissociation rate. At 4.72 eV, internal conversion is likely associated with rapid electronic relaxation of the uracil following $\pi - \pi^*$ excitation. At 4.03 eV, there must be back-transfer of a dipole- or valence-bound electron back to the iodine atom, with the latter being more likely. The $\Gamma^- \cdot \text{U} \rightarrow \text{HI} + [\text{U-H}]^-$ channel is not observed in the time-resolved experiments, most likely as a result of low $[\text{U-H}]^-$ production efficiency and a low photodetachment cross section.

4.8 Supplementary Material

Table 4.S1: Vibrational frequencies (cm^{-1}) of the $\Gamma^- \cdot \text{U}$ ground state, transition state, and bare neutral uracil at the MP2/aug-cc-pVDZ(-pp) level of theory.

$\Gamma^- \cdot \text{U}$ Ground State			$\Gamma^- \cdot \text{U}$ Transition State			Uracil Neutral		
54.9	57.8	97.0	-8.9	11.8	23.0			
154.1	183.3	380.1	144.4	165.5	380.5	142.3	160.9	381.0
425.1	515.3	537.8	397.2	512.3	533.2	389.0	510.9	532.3
561.0	677.4	724.4	552.8	579.6	685.4	551.9	561.9	689.3
751.5	778.3	799.7	724.5	743.6	770.7	720.7	742.0	769.3
840.5	973.8	984.8	810.1	954.0	973.7	805.1	941.0	970.8
998.2	1090.6	1213.8	985.0	1085.9	1206.6	983.8	1085.5	1202.6
1232.2	1369.9	1386.9	1241.1	1381.4	1401.3	1241.7	1383.5	1398.7
1414.9	1518.0	1658.8	1418.9	1501.6	1667.6	1415.8	1503.1	1669.2
1730.4	1763.4	3218.3	1750.9	1782.4	3246.9	1754.0	1788.0	3247.7
3222.7	3276.8	3607.8	3284.8	3599.8	3640.7	3284.5	3592.7	3644.7

Table 4.S2: Beyer-Swinehart calculated densities and sums of states for the $\text{I}^- \cdot \text{U}$ ground state and transition state including treatment of low-frequency hindered internal rotational modes.

Excitation Energy (eV)	$\text{I}^- \cdot \text{U}$ ground state density ($/\text{cm}^{-1}$)	$\text{I}^- \cdot \text{U}$ transition state sum	$k_{\text{RRKM}}(\text{E})$ (1/s)	Lifetime (ps)
4.03	3.75466×10^{15}	1.45548×10^{16}	1.16213×10^{11}	8.6
4.72	1.00448×10^{17}	7.61756×10^{17}	2.27349×10^{11}	4.4

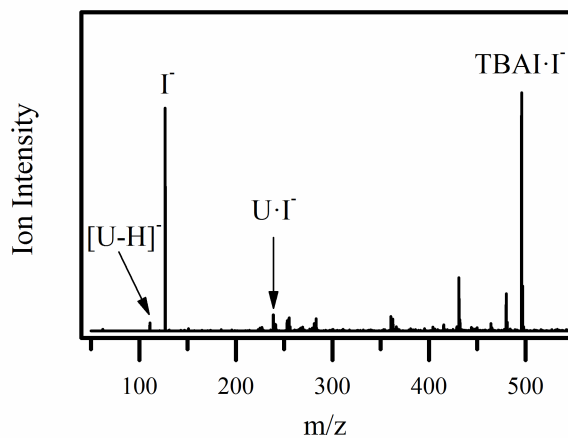


Figure 4.S1: Negative ion ESI-MS of an iodide/uracil solution.

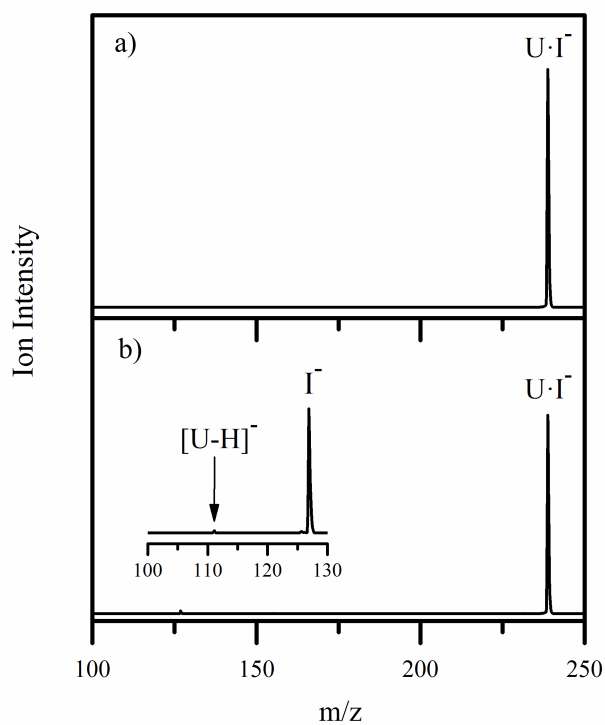


Figure 4.S2: a) Isolation of the $\text{I}^- \cdot \text{U}$ cluster prior to laser irradiation, and b) photofragmentation mass spectrum of $\text{I}^- \cdot \text{U}$ obtained at 260 nm (4.78 eV) showing production of I^- as the dominant photofragment and $[\text{U-H}]^-$ as a minor photofragment.

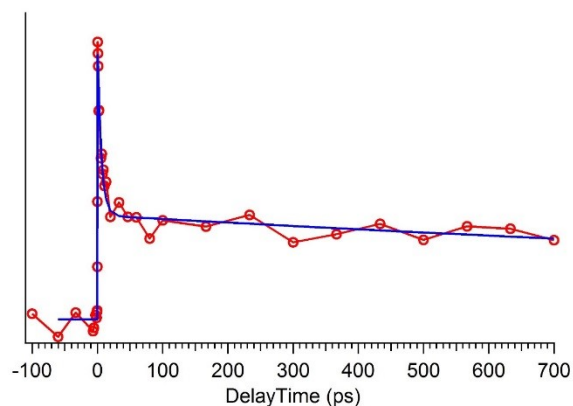


Figure 4.S3: Time-resolved photoelectron spectrum for feature C at pump-probe delays for $\text{I}^- \cdot \text{U}$ with an excitation energy of 4.03 eV and probe energy of 3.61 eV. The rise time constant is 0.3 ps, the decay time constant are 6 ps and 2800 ps.

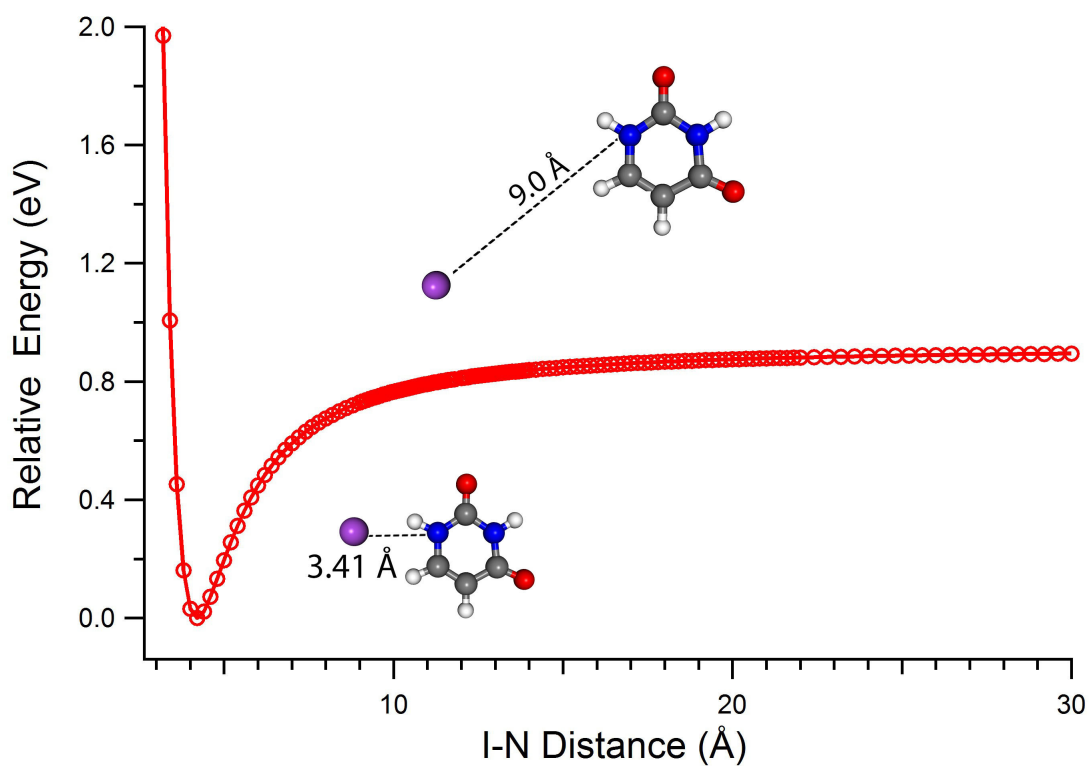


Figure 4.S4: Potential energy curve calculated by geometry optimization at frozen I–N1 distances. The calculations are performed at MP2/aug-cc-pvDZ-(pp) level of theory. All energies are ZPE corrected.

4.9 References

- [1] C. von Sonntag, *The chemical basis of radiation biology* (Taylor and Francis, London, 1987).
- [2] K. Aflatooni, G. A. Gallup, and P. D. Burrow, “Electron attachment energies of the DNA bases”, *J. Phys. Chem. A* **102**, 6205–6207 (1998).
- [3] M. A. Huels, I. Hahndorf, E. Illenberger, and L. Sanche, “Resonant dissociation of DNA bases by subionization electrons”, *J. Chem. Phys.* **108**, 1309–1312 (1998).
- [4] B. Boudaïffa, P. Cloutier, D. Hunting, M. A. Huels, and L. Sanche, “Resonant formation of DNA strand breaks by low-energy (3 to 20 eV) electrons”, *Science* **287**, 1658–1660 (2000).
- [5] M. A. Huels, B. Boudaïffa, P. Cloutier, D. Hunting, and L. Sanche, “Single, double, and multiple double strand breaks induced in DNA by 3-100 eV electrons”, *J. Am. Chem. Soc.* **125**, 4467–4477 (2003).
- [6] G. Hanel, B. Gstir, S. Denifl, P. Scheier, M. Probst, B. Farizon, M. Farizon, E. Illenberger, and T. D. Märk, “Electron attachment to uracil: effective destruction at subexcitation energies”, *Phys. Rev. Lett.* **90**, 188104 (2003).
- [7] S. Denifl, S. Ptasińska, M. Probst, J. Hrušák, P. Scheier, and T. D. Märk, “Electron attachment to the gas-phase DNA bases cytosine and thymine”, *J. Phys. Chem. A* **108**, 6562–6569 (2004).
- [8] F. Martin, P. D. Burrow, Z. L. Cai, P. Cloutier, D. Hunting, and L. Sanche, “DNA strand breaks induced by 0-4 eV electrons: The role of shape resonances”, *Phys. Rev. Lett.* **93**, 068101 (2004).
- [9] L. Sanche, “Low energy electron-driven damage in biomolecules”, *Eur. Phys. J. D* **35**, 367–390 (2005).
- [10] D. Huber, M. Beikircher, S. Denifl, F. Zappa, S. Matejcik, A. Bacher, V. Grill, T. D. Märk, and P. Scheier, “High resolution dissociative electron attachment to gas phase adenine”, *J. Chem. Phys.* **125**, 084304 (2006).
- [11] L. Sanche, “Biological chemistry: beyond radical thinking”, *Nature* **461**, 358–359 (2009).
- [12] C.-R. Wang, J. Nguyen, and Q.-B. Lu, “Bond breaks of nucleotides by dissociative electron transfer of nonequilibrium prehydrated electrons: a new molecular mechanism for reductive DNA damage”, *J. Am. Chem. Soc.* **131**, 11320–11322 (2009).
- [13] J. Simons, “How do low-energy (0.1-2 eV) electrons cause DNA-strand breaks?”, *Acc. Chem. Res.* **39**, 772–779 (2006).
- [14] J. D. Gu, Y. M. Xie, and H. F. Schaefer, “Near 0 eV electrons attach to nucleotides”, *J. Am. Chem. Soc.* **128**, 1250–1252 (2006).

- [15] X. Pan and L. Sanche, “Dissociative electron attachment to DNA basic constituents: The phosphate group”, *Chem. Phys. Lett.* **421**, 404–408 (2006).
- [16] J. D. Gu, J. Leszczynski, and H. F. Schaefer, “Interactions of electrons with bare and hydrated biomolecules: from nucleic acid bases to DNA segments”, *Chem. Rev.* **112**, 5603–5640 (2012).
- [17] H.-Y. Chen, P.-Y. Yang, H.-F. Chen, C.-L. Kao, and L.-W. Liao, “DFT reinvestigation of DNA strand breaks induced by electron attachment”, *J. Phys. Chem. B* **118**, 11137–11144 (2014).
- [18] A. M. Scheer, C. Silvernail, J. A. Belot, K. Aflatooni, G. A. Gallup, and P. D. Burrow, “Dissociative electron attachment to uracil deuterated at the N₁ and N₃ positions”, *Chem. Phys. Lett.* **411**, 46–50 (2005).
- [19] M. A. Yandell, S. B. King, and D. M. Neumark, “Time-resolved radiation chemistry: photoelectron imaging of transient negative ions of nucleobases”, *J. Am. Chem. Soc.* **135**, 2128–2131 (2013).
- [20] S. B. King, M. A. Yandell, and D. M. Neumark, “Time-resolved photoelectron imaging of the iodide-thymine and iodide-uracil binary cluster systems”, *Faraday Discuss.* **163**, 59–72 (2013).
- [21] S. B. King, M. A. Yandell, A. B. Stephansen, and D. M. Neumark, “Time-resolved radiation chemistry: Dynamics of electron attachment to uracil following UV excitation of iodide-uracil complexes”, *J. Chem. Phys.* **141**, 224310 (2014).
- [22] S. B. King, A. B. Stephansen, Y. Yokoi, M. A. Yandell, A. Kunin, T. Takayanagi, and D. M. Neumark, “Electron accommodation dynamics in the DNA base thymine”, *J. Chem. Phys.* **143**, 024312 (2015).
- [23] A. B. Stephansen, S. B. King, Y. Yokoi, Y. Minoshima, W.-L. Li, A. Kunin, T. Takayanagi, and D. M. Neumark, “Dynamics of dipole- and valence bound anions in iodide-adenine binary complexes: A time-resolved photoelectron imaging and quantum mechanical investigation”, *J. Chem. Phys.* **143**, 104308 (2015).
- [24] J. H. Hendricks, S. A. Lyapustina, H. L. de Clercq, J. T. Snodgrass, and K. H. Bowen, “Dipole bound, nucleic acid base anions studied via negative ion photoelectron spectroscopy”, *J. Chem. Phys.* **104**, 7788–7791 (1996).
- [25] J. Schiedt, R. Weinkauff, D. M. Neumark, and E. W. Schlag, “Anion spectroscopy of uracil, thymine and the amino-oxo and amino-hydroxy tautomers of cytosine and their water clusters”, *Chem. Phys.* **239**, 511–524 (1998).
- [26] R. Bachorz, W. Klopper, M. Gutowski, X. Li, and K. H. Bowen, “Photoelectron spectrum of valence anions of uracil and first-principles calculations of excess electron binding energies”, *J. Chem. Phys.* **129**, 054309 (2008).

- [27] M. A. Yandell, S. B. King, and D. M. Neumark, “Decay dynamics of nascent acetonitrile and nitromethane dipole-bound anions produced by intracuster charge-transfer”, *J. Chem. Phys.* **140**, 184317 (2014).
- [28] T. Sommerfeld, “Intramolecular electron transfer from dipole-bound to valence orbitals: uracil and 5-chlorouracil”, *J. Phys. Chem. A* **108**, 9150–9154 (2004).
- [29] T. Takayanagi, T. Asakura, and H. Motegi, “Theoretical study on the mechanism of low-energy dissociative electron attachment for uracil”, *J. Phys. Chem. A* **113**, 4795–4801 (2009).
- [30] H. Motegi and T. Takayanagi, “Theoretical study on the transformation mechanism between dipole-bound and valence-bound anion states of small uracil-water clusters and their photoelectron spectra”, *J. Mol. Struct.-THEOCHEM* **907**, 85–92 (2009).
- [31] Y. Yokoi, K. Kano, Y. Minoshima, and T. Takayanagi, “Application of long-range corrected density-functional theory to excess electron attachment to biomolecules”, *Comput. Theor. Chem.* **1046**, 99–106 (2014).
- [32] R. J. Peláez, C. Blondel, C. Delsart, and C. Drag, “Pulsed photodetachment microscopy and the electron affinity of iodine”, *J. Phys. B- At. Mol. Opt.* **42**, 125001 (2009).
- [33] H.-T. Liu, C.-G. Ning, D.-L. Huang, and L.-S. Wang, “Vibrational spectroscopy of the dehydrogenated uracil radical by autodetachment of dipole-bound excited states of cold anions”, *Angew. Chem. Int. Ed.* **53**, 2464–2468 (2014).
- [34] A. Sen and C. E. H. Dessent, “Communication: Photoactivation of nucleobase bound platinum II metal complexes: Probing the influence of the nucleobase”, *J. Chem. Phys.* **141**, 241101 (2014).
- [35] A. Sen, T. F. M. Luxford, N. Yoshikawa, and C. E. H. Dessent, “Solvent evaporation versus proton transfer in nucleobase-Pt(CN)_{4,6}²⁻ dianion clusters: a collisional excitation and electronic laser photodissociation spectroscopy study”, *Phys. Chem. Chem. Phys.* **16**, 15490–15500 (2014).
- [36] A. Davis, R. Wester, A. E. Bragg, and D. M. Neumark, “Time-resolved photoelectron imaging of the photodissociation of I₂⁻”, *J. Chem. Phys.* **118**, 999–1002 (2003).
- [37] A. E. Bragg, J. R. R. Verlet, A. Kammrath, O. Cheshnovsky, and D. M. Neumark, “Electronic relaxation dynamics of water cluster anions”, *J. Am. Chem. Soc.* **127**, 15283–15295 (2005).
- [38] V. Dribinski, A. Ossadtchi, V. Mandelshtam, and H. Reisler, “Reconstruction of Abel-transformable images: the Gaussian basis-set expansion Abel transform method”, *Rev. Sci. Instrum.* **73**, 2634–2642 (2002).
- [39] R. A. Kendall, T. H. Dunning, and R. J. Harrison, “Electron-affinities of the 1st-row atoms revisited - systematic basis-sets and wave-functions”, *J. Chem. Phys.* **96**, 6796–6806 (1992).

- [40] K. A. Peterson, D. Figgen, E. Goll, H. Stoll, and M. Dolg, “Systematically convergent basis sets with relativistic pseudopotentials. II. Small-core pseudopotentials and correlation consistent basis sets for the post-d group 16-18 elements”, *J. Chem. Phys.* **119**, 11113–11123 (2003).
- [41] K. A. Peterson, B. C. Shepler, D. Figgen, and H. Stoll, “On the spectroscopic and thermochemical properties of ClO, BrO, IO, and their anions”, *J. Phys. Chem. A* **110**, 13887 (2006).
- [42] M. J. Frisch, G. W. Trucks, H. B. Schlegel, G. E. Scuseria, M. A. Robb, J. R. Cheeseman, G. Scalmani, V. Barone, B. Mennucci, G. A. Petersson, H. Nakatsuji, M. Caricato, X. Li, H. P. Hratchian, A. F. Izmaylov, J. Bloino, G. Zheng, J. L. Sonnenberg, M. Hada, M. Ehara, K. Toyota, R. Fukuda, J. Hasegawa, M. Ishida, T. Nakajima, Y. Honda, O. Kitao, H. Nakai, T. Vreven, J. A. Montgomery Jr., J. E. Peralta, F. Ogliaro, M. J. Bearpark, J. Heyd, E. N. Brothers, K. N. Kudin, V. N. Staroverov, R. Kobayashi, J. Normand, K. Raghavachari, A. P. Rendell, J. C. Burant, S. S. Iyengar, J. Tomasi, M. Cossi, N. Rega, N. J. Millam, M. Klene, J. E. Knox, J. B. Cross, V. Bakken, C. Adamo, J. Jaramillo, R. Gomperts, R. E. Stratmann, O. Yazyev, A. J. Austin, R. Cammi, C. Pomelli, J. W. Ochterski, R. L. Martin, K. Morokuma, V. G. Zakrzewski, G. A. Voth, P. Salvador, J. J. Dannenberg, S. Dapprich, A. D. Daniels, Ö. Farkas, J. B. Foresman, J. V. Ortiz, J. Cioslowski, and D. J. Fox, *Gaussian 09, Revision C.01*, 2009.
- [43] R. Gilbert and S. Smith, *Theory of unimolecular and recombination reactions* (Blackwell Scientific Publications, London, 1990).
- [44] T. Baer and W. L. Hase, *Unimolecular reaction dynamics: theory and dynamics* (Oxford University Press, USA, New York, 1996).
- [45] J. I. Steinfeld, J. S. Francisco, and W. L. Hase, *Chemical kinetics and dynamics* (Prentice-Hall, New Jersey, 1999).
- [46] J. P. Merrick, D. Moran, and L. Radom, “An evaluation of harmonic vibrational frequency scale factors”, *J. Phys. Chem. A* **111**, 11683–11700 (2007).
- [47] S. E. Stein and B. S. Rabinovitch, “Accurate evaluation of internal energy level sums and densities including anharmonic oscillators and hindered rotors”, *J. Chem. Phys.* **58**, 2438–2445 (1973).
- [48] T. Beyer and D. F. Swinehart, “Number of multiply-restricted partitions”, *Commun. ACM* **16**, 379–379 (1973).
- [49] H. Kang, K. T. Lee, B. Jung, Y. J. Ko, and S. K. Kim, “Intrinsic lifetimes of the excited state of DNA and RNA bases”, *J. Am. Chem. Soc.* **124**, 12958–12959 (2002).
- [50] S. Ullrich, T. Schultz, M. Z. Zgierski, and A. Stolow, “Electronic relaxation dynamics in DNA and RNA bases studied by time-resolved photoelectron spectroscopy”, *Phys. Chem. Chem. Phys.* **6**, 2796–2801 (2004).

- [51] S. Matsika, “Radiationless decay of excited states of uracil through conical intersections”, *J. Phys. Chem. A* **108**, 7584–7590 (2004).
- [52] C. Canuel, M. Mons, F. Piuzzi, B. Tardivel, I. Dimicoli, and M. Elhanine, “Excited states dynamics of DNA and RNA bases: characterization of a stepwise deactivation pathway in the gas phase”, *J. Chem. Phys.* **122**, 074316 (2005).
- [53] C. E. H. Dessent, J. Kim, and M. A. Johnson, “Spectroscopic observation of vibrational Feshbach resonances in near-threshold photoexcitation of $X^- \cdot \text{CH}_3\text{NO}_2$ ($X^- = \text{I}^-$ and Br^-)”, *Faraday Discuss.* **115**, 395–406 (2000).
- [54] C. E. H. Dessent, C. G. Bailey, and M. A. Johnson, “Dipole-bound excited states of the $\text{I}^- \cdot \text{CH}_3\text{CN}$ and $\text{I}^- \cdot (\text{CH}_3\text{CN})_2$ ion-molecule complexes: evidence for asymmetric solvation”, *J. Chem. Phys.* **103**, 2006–2015 (1995).

Chapter 5

Dynamics of Electron Attachment and Photodissociation in Iodide-Uracil-Water Clusters

“Would you tell me, please,
which way I ought to go from
here?”

“That depends a good deal on
where you want to get to,” said
the Cat.

Lewis Carroll

The content and figures of this chapter are adapted from:

A. Kunin, W.-L. Li, and D. M. Neumark, “Dynamics of electron attachment and photodissociation in iodide-uracil-water clusters via time-resolved photoelectron imaging” *J. Chem. Phys.* **149**, 084301 (2018)

with the permission of AIP Publishing.

5.1 Abstract

The dynamics of low energy electron attachment to monohydrated uracil are investigated using time-resolved photoelectron imaging to excite and probe iodide-uracil-water ($\text{I}^- \cdot \text{U} \cdot \text{H}_2\text{O}$) clusters. Upon photoexcitation of $\text{I}^- \cdot \text{U} \cdot \text{H}_2\text{O}$ at 4.38 eV, near the measured cluster vertical detachment energy of $4.40 \text{ eV} \pm 0.05 \text{ eV}$, formation of both the dipole bound (DB) anion and valence bound (VB) anion of $\text{I}^- \cdot \text{U} \cdot \text{H}_2\text{O}$ is observed and characterized using a probe photon energy of 1.58 eV. The measured binding energies for both anions are larger than those of the non-hydrated iodide-uracil ($\text{I}^- \cdot \text{U}$) counterparts, indicating that the presence of water stabilizes the transient negative ions. The VB anion exhibits a somewhat delayed 400 fs rise when compared to $\text{I}^- \cdot \text{U}$, suggesting that partial conversion of the DB anion to form the VB anion at early times is promoted by geometric rearrangement of the water molecule. We propose that the water-binding-site around uracil may shift at early times to an isomer with a lower energetic barrier for DB to VB anion conversion. At a higher probe photon energy, 3.14 eV, I^- re-formation is measured to be the major photodissociation channel. This product exhibits a bi-exponential rise; the fast component likely arises from DB anion decay by internal conversion to the anion ground state followed by dissociation to I^- , and the slow component from internal conversion of the VB anion.

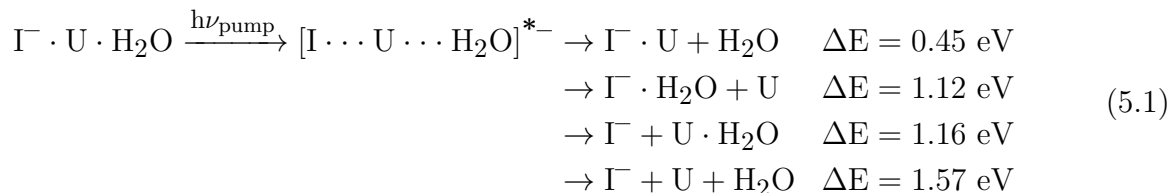
5.2 Introduction

Low energy electrons have been shown to induce single and double strand breaks in DNA and can ultimately contribute to mutations, genetic damage, and cancer [1]. Electronic structure calculations indicate that the nucleobase may be the site of initial electron attachment for DNA [2–4], and that electron attachment can form either a conventional valence bound (VB) anion by attachment to the π^* orbital of the base [3, 5] or a dipole bound (DB) anion due to the large molecular dipole moments of nucleobases [6]. Dissociative electron attachment experiments suggest that an initially formed DB state acts as a gateway to formation of a VB anion [7]. Formation of these transient negative ions (TNIs) then leads to the fragmentation of gas phase nucleobases, nucleosides and nucleotides [8, 9]. Our group has previously examined the dynamics of low energy electron attachment to the nucleobases uracil, thymine, and adenine via time-resolved photoelectron imaging (TRPEI) of iodide-nucleobase clusters [10–12]. We observed the formation and decay of DB and VB TNIs along with photofragmentation to form I^- [13]. The addition of water has been shown to increase the electron affinity of nucleobases [14], mediate nucleobase proton transfer [15], and affect the excited state lifetimes and ultimately the photostability of pyrimidine nucleobases, specifically thymine [16, 17]. In this study, we examine the dynamics of electron attachment to and subsequent dissociation of monohydrated uracil using TRPEI of iodide-uracil-water ($\text{I}^- \cdot \text{U} \cdot \text{H}_2\text{O}$) clusters, and compare these results to non-hydrated iodide-uracil ($\text{I}^- \cdot \text{U}$) in order to assess the role of microhydration in these dynamics.

Photoelectron spectroscopy is a powerful tool to detect and identify the presence of both DB and VB anions as they are readily distinguished by differing electron binding energies as well as photodetachment spectral profiles [18, 19]. The excess electron of the DB anion is bound by the molecular dipole moment. Hence, the electron binding energy is very low, often less than 100 meV, and the photoelectron spectrum comprises a narrow peak since the geometry of the weakly bound, diffuse anion does not differ significantly from that of the neutral. In VB anions, on the other hand, the excess electron occupies a valence orbital. Even when the neutral species on which the VB anion is based has a closed shell, these anions exhibit higher binding energies of hundreds of meV and more significant geometric distortion from the structure of the corresponding neutral, yielding broad photoelectron spectral profiles. In the case of both uracil and uracil-water, the VB anion geometric distortion is largely in the ring puckering coordinate [10, 20].

Uracil-water anion clusters have been previously studied with photoelectron spectroscopy by Bowen, Weinkauff, and co-workers [14, 21]. Although the ground state of the gas phase uracil anion is a DB state [18, 22], only a VB state is evidenced in the photoelectron spectrum of $U^- \cdot H_2O$. The $U^- \cdot H_2O$ VB anion was measured to have a vertical detachment energy (VDE), the energy difference between the anion and the neutral species at the equilibrium geometry of the anion, of approximately 850 meV. Theory has suggested for both uracil-water [23, 24] and thymine-water anion clusters [25] that the VB anion is preferentially stabilized over the DB anion as a result of the interaction energy of the solvating species being greater for the higher density excess electron distribution in the VB anion than in the DB anion.

In the present study, we examine the dynamics of TNI formation and decay for $I^- \cdot U \cdot H_2O$ clusters photoexcited near the cluster VDE using TRPEI. Photoexcitation with an ultraviolet photon initiates electron transfer from the iodide to the nucleobase moiety. Photoexcitation in this energy regime is expected to form either or both the DB and the VB anions, and these nascent TNIs may energetically access several possible decay channels, calculated in this work,¹ including:



The TNIs can also undergo autodetachment to one or more neutral species plus an electron.

¹ Calculated in the present study using the Gaussian 09 computing package at the MP2/aug-cc-pVDZ-pp level of theory; see Methods section for computational details.

We employ two different probe photon energies to photodetach the TNIs and ionic photodissociation products to examine the dynamics for formation and decay of each species. A probe pulse of 1.58 eV is able to photodetach the relatively weakly bound DB and VB anions, as both TNIs generally have electron binding energies below 1 eV. A higher energy probe pulse of 3.14 eV is also used here to detach ionic photofragments, all of which have significantly higher binding energies; the electron affinity of atomic iodine is 3.059 eV, for example [26].

Here, we observe the formation of both DB and VB anions from photoexcited $\text{I}^- \cdot \text{U} \cdot \text{H}_2\text{O}$. Both TNIs exhibit a larger binding energy than the DB and VB anions from the analogous process in $\text{I}^- \cdot \text{U}$, indicating stabilization of the anions by the interaction of water. Following photoexcitation, the $\text{I}^- \cdot \text{U} \cdot \text{H}_2\text{O}$ DB anion is observed instantaneously while the VB anion signal exhibits a rise time of ~ 400 fs suggesting that the DB anion undergoes a partial conversion to form the VB anion. A similar delay was seen for $\text{I}^- \cdot \text{U}$ complexes excited near their VDE, but the distinction between DB and VB formation dynamics is more pronounced here. The I^- photofragment signal exhibits a bi-exponential rise of ~ 7 ps and ~ 320 ps, likely arising from TNI decay at early times by internal conversion to the anion ground state by back-electron transfer to the I atom, followed by loss of I^- . It is possible that the faster I^- rise originates from the DB anion and the slower rise from the VB anion.

5.3 Experimental and Theoretical Methods

The TRPEI apparatus has been described in detail previously [27, 28] and is briefly summarized here. $\text{I}^- \cdot \text{U} \cdot \text{H}_2\text{O}$ clusters were formed by passing approximately 550 kPa helium carrier gas over a reservoir of iodomethane and a second reservoir of deionized liquid water. Both reservoirs and the connecting gas line were heated to approximately 40 °C with heating tape. The gas was passed through a pulsed Even-Lavie valve operating at 500 Hz that contained a cartridge of solid uracil (Sigma-Aldrich, $\geq 99.0\%$) heated to 220 °C. The gas mixture was supersonically expanded into vacuum through a ring electrode ionizer. The resultant anionic clusters were perpendicularly extracted using a Wiley McLaren time-of-flight mass spectrometer [29] and mass-selected to isolate the $\text{I}^- \cdot \text{U} \cdot \text{H}_2\text{O}$ species.

The $\text{I}^- \cdot \text{U} \cdot \text{H}_2\text{O}$ clusters were excited and photodetached by femtosecond pump and probe laser pulses delayed by a delay stage. Two pump-probe schemes were used in this study: the pump pulse of 283 nm (4.38 eV) was used with either an infrared probe pulse of 785 nm (1.58 eV) or an ultraviolet probe pulse of 395 nm (3.14 eV). A KMLabs Griffin Oscillator and Dragon Amplifier were used to generate 40 fs laser pulses centered at 785 nm with 1.85 mJ/pulse at a repetition rate of 1 kHz. These pulses were split to an optical parametric amplifier (LightCon TOPAS-C) to generate the pump pulses and to a frequency-doubling setup using a β -barium borate (BBO) crystal to generate the probe pulses. The pump and frequency-doubled probe pulse energies were 12 μJ /pulse at 283 nm and 65 μJ /pulse at 395

nm, respectively. Alternatively, the residual fundamental was recovered from the doubling process and used as a probe with energies of 80 $\mu\text{J}/\text{pulse}$ at 785 nm. The cross-correlation of the pump and probe laser pulses was approximately 185 fs for 283 nm/785 nm, and 220 fs for 283 nm/395 nm.

The resultant photoelectrons were analyzed by velocity map imaging [30] on a position-sensitive chevron-stacked microchannel plate detector coupled to a phosphor screen and imaged by a charge-coupled device camera. Basis-set expansion (BASEX) methods [31] were used to reconstruct the photoelectron kinetic energy (eKE) distributions.

Several of the lowest-lying possible conformations of the $\text{I}^- \cdot \text{U} \cdot \text{H}_2\text{O}$ cluster were calculated here to better understand the geometry and energetics of the experimentally observed $\text{I}^- \cdot \text{U} \cdot \text{H}_2\text{O}$ clusters. The Gaussian 09 computing package [32] was used to calculate the optimized geometries and energies of the $\text{I}^- \cdot \text{U} \cdot \text{H}_2\text{O}$ cluster at the MP2 level with an augmented Dunning basis set aug-cc-pVDZ for C, H, O, and N atoms and an expanded basis set with an increased set of diffuse functions aug-cc-pVDZ(-pp) for iodide [33]. Following geometry optimization, the vibrational frequencies for each of the cluster structures were calculated to confirm that each structure is a true minimum on the potential energy surface. For each of these anionic conformers, the corresponding structures and dipole moments for neutral iodine-uracil-water were also calculated both in the anion ground state geometry (single point calculation) and in the optimized neutral geometry, as well as the optimized geometry for neutral uracil-water, without iodine. This was done to estimate structural changes and binding properties of the $\text{I}^- \cdot \text{U} \cdot \text{H}_2\text{O}$ DB anion, as described in more detail in Section 5.6.1. For the lowest-lying anion conformer of $\text{I}^- \cdot \text{U} \cdot \text{H}_2\text{O}$ calculated here, we performed equation of motion coupled cluster singles and doubles (EOM-CCSD) excited state calculations (EOM-CCSD/aug-cc-pVDZ(-pp)) to examine the nature of the possible electronic transitions resulting from photoexcitation.

5.4 Results

Fig. 5.1 shows a single-photon photoelectron spectrum of $\text{I}^- \cdot \text{U} \cdot \text{H}_2\text{O}$ collected at $h\nu_{\text{photon}} = 4.74$ eV, plotted as a function of electron binding energy (eBE) where $\text{eBE} = h\nu_{\text{photon}} - \text{eKE}$. The peak of this spectrum arises from direct photodetachment of $\text{I}^- \cdot \text{U} \cdot \text{H}_2\text{O}$ and yields a cluster VDE of 4.40 ± 0.05 eV. This VDE corresponds to photodetachment to the lower iodine spin-orbit state ($^2\text{P}_{3/2}$) from the $\text{I}^- \cdot \text{U} \cdot \text{H}_2\text{O}$ anion. The upper $^2\text{P}_{1/2}$ spin-orbit state is expected to lie approximately 0.94 eV higher in energy [12, 34–36] and is thus energetically inaccessible in this work. The smaller peak near the maximum eBE of 4.74 eV (i.e. the photon energy) is from electrons with $\text{eKE} \approx 0$ eV resulting from autodetachment from photoexcited $\text{I}^- \cdot \text{U} \cdot \text{H}_2\text{O}$; these autodetachment signals have been measured in our previous work on $\text{I}^- \cdot \text{U}$ clusters [35, 36], among others.

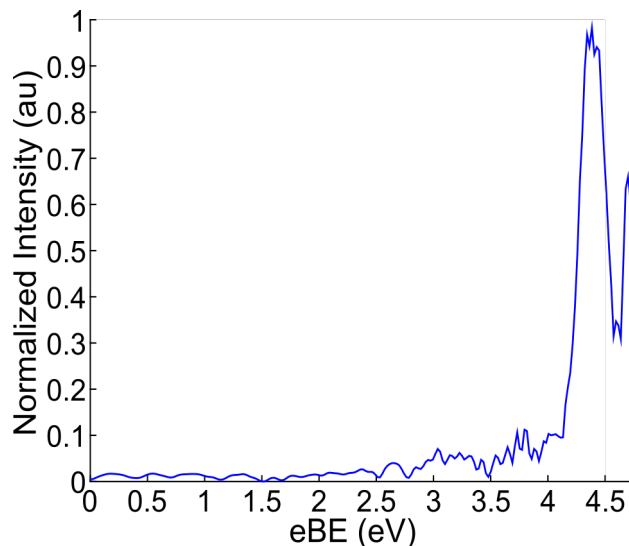


Figure 5.1: Single photon, laser noise subtracted, photoelectron spectrum for $\text{I}^- \cdot \text{U} \cdot \text{H}_2\text{O}$ clusters taken at 4.74 eV. The VDE for $\text{I}^- \cdot \text{U} \cdot \text{H}_2\text{O}$ was determined to be 4.40 ± 0.05 eV.

Time-resolved photoelectron spectra of $\text{I}^- \cdot \text{U} \cdot \text{H}_2\text{O}$ at 4.38 eV pump excitation energy and 1.58 eV probe energy are shown as a function of eBE ($= h\nu_{\text{probe}} - e\text{KE}$) up to 1 eV eBE and for early times up to 7 ps in Fig. 5.2. These spectra exhibit two features below 1 eV eBE, both of which are prominent at time delays below 5 ps: feature A, a relatively intense and spectrally narrow feature below 0.38 eV eBE, and feature B which is less intense and

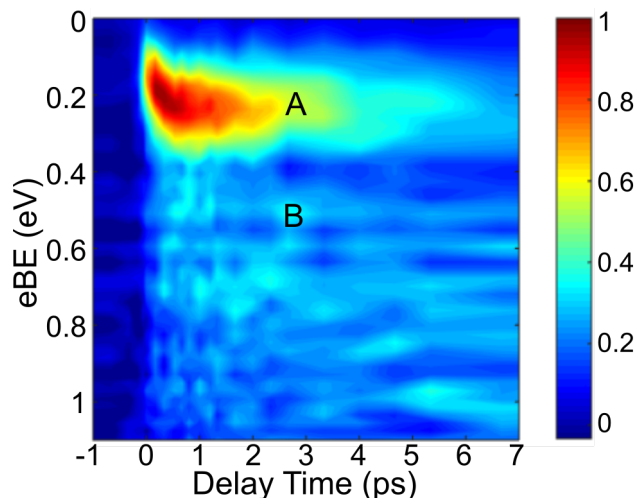


Figure 5.2: Representative background-subtracted time-resolved photoelectron spectra for features A (eBE = 0.02 – 0.38 eV) and B (eBE = 0.40 – 1.00 eV) at short pump-probe delays for $\text{I}^- \cdot \text{U} \cdot \text{H}_2\text{O}$ at 4.38 eV pump excitation energy and 1.58 eV probe energy.

broader, covering 0.4 eV eBE – 1 eV eBE. Based on our previously published results on $\Gamma^- \cdot \text{U}$ clusters at excitation energies near their VDE of 4.11 eV [10], we can confidently assign feature A as the DB anion of the $\Gamma^- \cdot \text{U} \cdot \text{H}_2\text{O}$ complex and feature B as the VB anion of the $\Gamma^- \cdot \text{U} \cdot \text{H}_2\text{O}$ complex based on the eBE range and the spectral shape of each feature. As seen prominently in Fig. 5.2, the eBE of the DB anion shifts to higher binding energy at longer time delays until the feature decays. Fig. 5.S1 presents the data of Fig. 5.2 as a waterfall plot. While feature B may appear to have some structure or progression in the time-resolved photoelectron spectra, the ± 0.05 eV resolution of this experiment precludes the possibility of analyzing these relatively smaller intensity changes.

The time-resolved photoelectron spectra for $\Gamma^- \cdot \text{U} \cdot \text{H}_2\text{O}$ at 4.38 eV pump excitation energy and 3.14 eV probe energy are shown in Fig. 5.3, plotted from 1.2 to 3.14 eV eBE. The most prominent feature, feature D, is located at 3.06 ± 0.05 eV eBE and is spectrally narrow but very intense, growing in strongly over 10s of ps. Based on its binding energy, spectral shape, and time-dependent monotonic rise, feature D is assigned to photodetachment of atomic iodide produced following pump photoexcitation of $\Gamma^- \cdot \text{U} \cdot \text{H}_2\text{O}$ clusters. Feature C, located at the maximum eBE edge of the spectrum or approximately 0 eV eKE, is very spectrally narrow and exhibits an initial depletion at early times with intensity recovery at longer times. An analogous feature is also observed at the maximum eBE edge of the TRPEI data at 1.58 eV probe energy but is omitted here from Fig. 5.2 for clarity as it overlaps with another feature, as described below in more detail. The characteristics of feature C are very similar in nature to those previously observed for autodetachment from $\Gamma^- \cdot \text{U}$ clusters [36], so it can

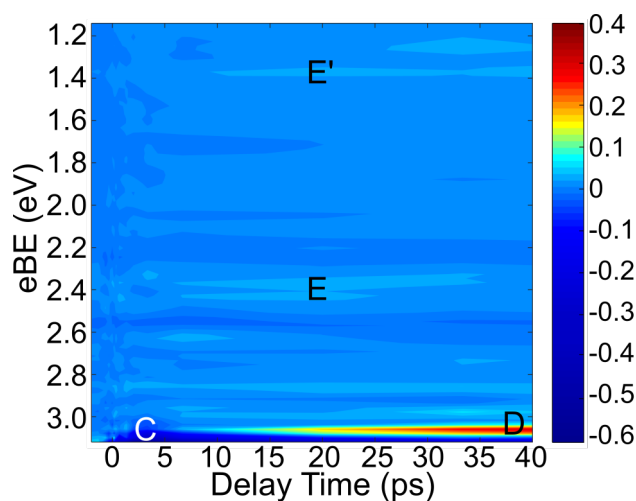


Figure 5.3: Representative background-subtracted time-resolved photoelectron spectra for features C (maximum eBE, eKE ~ 0 eV), D (eBE = 3.06 eV), E (eBE = 2.29 – 2.99 eV), and E' (eBE = 1.14 – 1.64 eV) for $\Gamma^- \cdot \text{U} \cdot \text{H}_2\text{O}$ at 4.38 eV pump excitation energy and 3.14 eV probe energy.

be assigned as autodetachment from photoexcited $\text{I}^- \cdot \text{U} \cdot \text{H}_2\text{O}$ clusters. Fig. 5.S2 presents a magnified view of the data in Fig. 5.3 for the energy region from 3.00 to 3.12 eV to better show the distinction between features C and D.

At lower eBEs there is a weak intensity, broad region exhibiting time dependence from approximately 2.3 eV to 3.0 eV eBE, denoted feature E, and also from approximately 1.14 – 1.64 eV eBE, feature E'. Feature E' is also weakly observed in the 1.58 eV probe TRPEI data but overlaps spectrally with the autodetachment feature and the full feature is not captured by the 1.58 eV probe limit, so it is omitted from Fig. 5.2 for clarity. Fig. 5.S3 presents the data of Fig. 5.3 as a waterfall plot with feature C omitted to allow a clearer view of features E and E'. Though noisy, these features appear to have somewhat different rise and decay dynamics from one another. We explore possible assignments for these weak features in the supplementary material.

Multiple low-lying isomers have been calculated for uracil-water [37–39] and several have been calculated here for $\text{I}^- \cdot \text{U} \cdot \text{H}_2\text{O}$; the resulting structures, relative energies, and VDEs of the lowest lying six isomers of $\text{I}^- \cdot \text{U} \cdot \text{H}_2\text{O}$ are presented in Table 5.1. Six energetically low-lying unique isomers of $\text{I}^- \cdot \text{U} \cdot \text{H}_2\text{O}$ were found within 2 kcal/mol of one another. It is unsurprising that structures such as those of Table 5.1 a), b), and c) are the lowest lying isomers given that the iodide-water ion-dipole interaction is expected to be stronger than the uracil-water dipole-dipole interaction, but within our heated cluster source all of these isomers and many more are possible. The calculated VDEs of these clusters are all close to the experimentally measured VDE of 4.40 ± 0.05 eV. The experimental results seen here likely represent an ensemble average of the dynamics of several low-lying isomers.

Table 5.S1 presents calculated structures and dipole moments for the neutral iodine-uracil-water in the geometry of both the anion ground state and the optimized neutral, as well as the neutral uracil-water geometry. The anion ground state geometry can be approximated to be the Franck-Condon geometry for the DB anion as it is initially formed, and the optimized neutral iodine-uracil-water structures serve as an approximation for the equilibrium geometry of the $\text{I}^- \cdot \text{U} \cdot \text{H}_2\text{O}$ DB anion since the diffuse, excess electron is expected to minimally perturb the neutral geometry. These structures can be used to estimate the possible evolution of the geometry of the DB anion as well as the magnitude of the dipole moment binding the excess electron, and are discussed in more detail in Section 5.6.1.

Table 5.2 presents the results of the EOM-CCSD excited state calculation for the lowest-lying calculated $\text{I}^- \cdot \text{U} \cdot \text{H}_2\text{O}$ anion conformer, corresponding to the structure in Table 5.1(a). Seven excited state transition channels were calculated to exist below 5.3 eV; the three lowest in energy are within 0.25 eV of one another and correspond to transitions from an iodide 5p orbital to the DB orbital with considerable oscillator strength. The calculated DB orbital as well as the calculated π^* orbital accessed in the higher energy transitions are shown in Fig. 5.S4. In similar calculations performed by our group for $\text{I}^- \cdot \text{U}$ [13], the calculated energy

values were compared to an experimental photodepletion (absorption) spectrum of $\Gamma^- \cdot \text{U}$ and found to exceed the experimental energies by 0.52 eV. No experimental photodepletion spectrum has been measured for $\Gamma^- \cdot \text{U} \cdot \text{H}_2\text{O}$ but this approximate 0.5 eV energy overestimate is expected to be similar for the $\Gamma^- \cdot \text{U} \cdot \text{H}_2\text{O}$ results here, which would place these three lowest transition channels in the range of approximately 4.28 eV – 4.51 eV, close to the pump excitation energy of 4.38 eV used here. Hence, at this pump energy, one expects excitation to a DB state of the complex. Based on these results for the $\Gamma^- \cdot \text{U} \cdot \text{H}_2\text{O}$ conformer in Table 5.1(a), we can conclude that the effect of the hydrogen bonding of the water molecule to iodide is to increase both the VDE of the cluster as well as the excitation energy for the formation of the DB state. Thus, for the conformers of Table 5.1(b), (c), and (e), the results for these calculated transition channels will likely be similar. For Table 5.1(d) and (f), the VDE is calculated to be somewhat lower, and likely the excitation energy for the formation of the DB state will be proportionately somewhat lower as well.

5.5 Analysis

Feature A in Fig. 5.2, corresponding to a DB state, shows a pronounced time-dependent shift in its VDE. To better quantify this effect, the spectral shape of feature A can be fit to a Gaussian function at all time delays for which the intensity of the feature is non-zero. The binding energy corresponding to the peak of this Gaussian is plotted as a function of pump-probe time delay in Fig. 5.4. The DB anion VDE shifts from approximately 140 meV to 230 meV in 1 ps and increases to approximately 275 meV in 15 ps. Beyond 15 ps, the intensity of feature A is too small to accurately fit to a Gaussian function.

The normalized, integrated intensities for both the $\Gamma^- \cdot \text{U} \cdot \text{H}_2\text{O}$ DB anion and VB anion (Feature B) up to 7 ps time delay are shown together for comparison in Fig. 5.5. The corresponding intensities out to 300 ps are presented in Fig. 5.6. To capture the time-dependent dynamics of these features, the integrated signals are fit to the convolutions of a Gaussian instrumental response and multiple exponential functions according to Eq. 5.2:

$$I(t) = \frac{1}{\sigma_{cc}\sqrt{2\pi}} \exp\left(\frac{-t^2}{2\sigma_{cc}^2}\right) \cdot \begin{cases} I_0, t < 0 \\ I_0 + \sum A_i \exp\left(\frac{-t}{\tau_i}\right), t \geq 0 \end{cases} \quad (5.2)$$

σ_{cc} is the Gaussian full width at the half-maximum given by the cross-correlation of the pump and probe laser pulses, I_0 is the signal background, A_i are the coefficients of the i exponential functions, and τ_i are the corresponding rise or decay lifetimes for each exponential.

Table 5.3 summarizes the fit rise and decay time constants for the $\Gamma^- \cdot \text{U} \cdot \text{H}_2\text{O}$ DB and VB anions and for Γ^- , the exponential fitting function amplitudes A_i , and the intensity ratio

Table 5.1: The six energetically lowest-lying calculated structures for $\text{I}^- \cdot \text{U} \cdot \text{H}_2\text{O}$ anion complexes. Relative energies supplied are relative to the ground state structure, 0.00 kcal/mol by definition, and corrected for zero point energies. The (a) and (e) structures are the only ones which have both O-H bonds of water outside of the uracil plane, so the side views for (a) and (e) are provided under their respective structures. The VDEs presented here correspond to the difference in energy between the $\text{I}^- \cdot \text{U} \cdot \text{H}_2\text{O}$ anion and the lower iodine spin orbit state ($^2\text{P}_{3/2}$) of $\text{I} \cdot \text{U} \cdot \text{H}_2\text{O}$ at the equilibrium geometry of the anion. Within the heated cluster source, all of these isomers and more energetically higher-lying ones are likely to form.

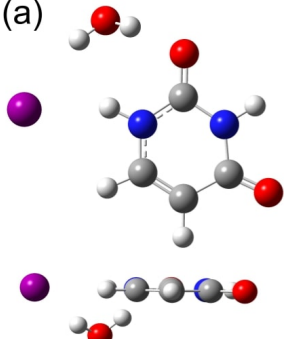
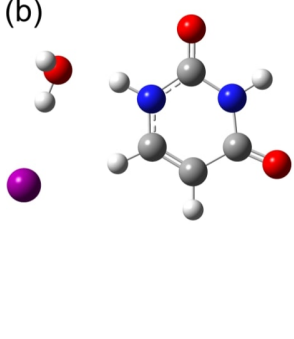
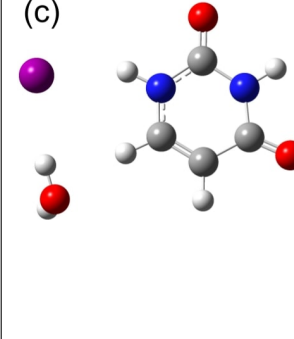
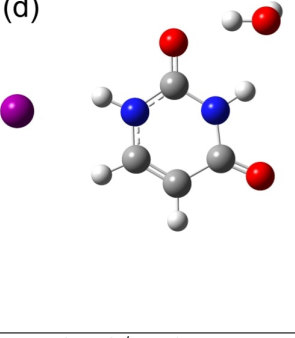
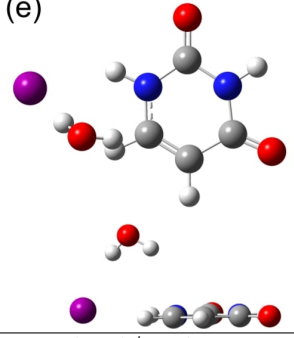
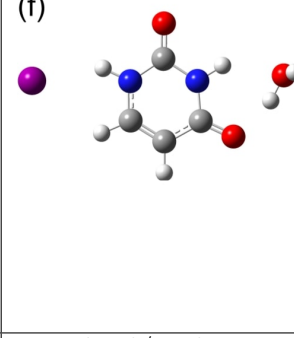
	(a) 	(b) 	(c) 
Relative Energy	0.00 kcal/mol	0.59 kcal/mol	0.92 kcal/mol
VDE	4.57 eV	4.50 eV	4.62 eV
	(d) 	(e) 	(f) 
Relative Energy	1.65 kcal/mol	1.79 kcal/mol	1.87 kcal/mol
VDE	4.33 eV	4.62 eV	4.31 eV

Table 5.2: EOM-CCSD/aug-cc-pVDZ(-pp) calculated electronic transition channels, energies, and corresponding oscillator strengths for the lowest-lying calculated anion conformer of $\Gamma^- \cdot \text{U} \cdot \text{H}_2\text{O}$, corresponding to structure in Table 5.1 a). The excitation energies here have not been offset and are the calculated values. See Analysis section for more details.

Excitation Energy (eV)	Oscillator Strength	Transition Channel	Final State Configuration
4.7964	0.0809	I(5p)–DB	I(5p ⁵)[U·H ₂ O]-(DB ¹)
4.8823	0.1003	I(5p)–DB	I(5p ⁵)[U·H ₂ O]-(DB ¹)
5.0283	0.1624	I(5p)–DB	I(5p ⁵)[U·H ₂ O]-(DB ¹)
5.0774	0.0104	I(5p) – π^*	I(5p ⁵)U ⁻ ($\pi^4\pi^{*1}$)H ₂ O
5.0966	0.0282	I(5p) – π^*	I(5p ⁵)U ⁻ ($\pi^4\pi^{*1}$)H ₂ O
5.2240	0.0652	I(5p) – π^*	I(5p ⁵)U ⁻ ($\pi^4\pi^{*1}$)H ₂ O
5.2695	0.1368	$\pi - \pi^*$	$\Gamma^-(5p^6)U(\pi^3\pi^{*1})H_2O$

of the DB anion to the VB anion. This intensity ratio is measured, as in $\Gamma^- \cdot \text{U}$, for a set time near the intensity maxima of both features, ~ 400 fs, from the un-normalized integrated intensities. Fits to the data in Figs. 5.5 and 5.6 based on Eq. 5.2 are shown as solid blue and red lines for the DB and VB anions, respectively. These fits yield a DB anion cross-correlation limited rise time and a bi-exponential decay of 4.1 ± 0.2 ps and 410 ± 140 ps and formation of the VB anion in 400 ± 140 fs with bi-exponential decay in 6.1 ± 2.4 ps and 650 ± 100 ps. The large error bars for the long-time decays are in part due to the values being longer than the maximum pump-probe delay used in the 1.58 eV probe experiment, 300 ps. For ease of comparison to our previous work on $\Gamma^- \cdot \text{U}$ clusters photoexcited at 40 meV below and 30 meV above the cluster VDE [10], the fit rise and decay time constants as well as the amplitudes from the exponential fitting functions for $\Gamma^- \cdot \text{U}$ DB and VB anions are also presented in Table 5.3. Additionally, Fig. 5.7 compares the normalized integrated intensity and exponential fits out to 35 ps for the $\Gamma^- \cdot \text{U} \cdot \text{H}_2\text{O}$ DB anion (blue) to the intensities and fits for the $\Gamma^- \cdot \text{U}$ DB anion photoexcited at VDE -40 meV (purple) and VDE $+30$ meV (green).

Fig. 5.8 presents the normalized integrated intensity and fitted bi-exponential rise for the iodide signal produced from the photoexcited $\Gamma^- \cdot \text{U} \cdot \text{H}_2\text{O}$. Photodetachment from Γ^- appears in 6.7 ± 3.8 ps and 320 ± 30 ps. The result for formation of iodide from $\Gamma^- \cdot \text{U}$ clusters photoexcited 80 meV below the VDE fit with a bi-exponential rise is also presented in Table 5.3 for comparison. This data was originally fit in Li et al. by a mono-exponential rise function but has been revised here to fit the data more accurately with a bi-exponential fit. These fits are shown for comparison in Fig. 5.S5, and are discussed in more detail in Section 5.6.

The normalized integrated intensities for the weak features E and E', which may corre-

spond to two metastable TNI decay products, are shown in Fig. 5.S6. These features are quite noisy but can be fit to a mono-exponential rise and mono-exponential decay. Feature E has a rise time of 3.5 ± 1.4 ps and a decay time of 500 ± 80 ps and feature E' has a rise time of 8.7 ± 3.7 ps and a decay time of 675 ± 120 ps. Further discussion of these two features is restricted to the Supplementary Material.

5.6 Discussion

The work presented here examines the ultrafast dynamics of the DB and VB TNIs for $\text{I}^- \cdot \text{U} \cdot \text{H}_2\text{O}$. The DB anion formed by photoexcitation of $\text{I}^- \cdot \text{U} \cdot \text{H}_2\text{O}$ near the VDE appears within the cross-correlation of the pump and probe laser pulses, followed by the rise of the VB anion in 400 fs. Here, we examine the dynamics of the prompt formation of $\text{I}^- \cdot \text{U} \cdot \text{H}_2\text{O}$ TNIs and the subsequent decay channels, along with possible pathways for the observed re-formation of iodide as a photofragment. We also provide a comparison to previously observed dynamics for $\text{I}^- \cdot \text{U}$ clusters photoexcited near the VDE to better understand the role of water in the electron attachment and decay processes.

In our past work on $\text{I}^- \cdot \text{U}$ clusters photoexcited near the VDE, the TNI lifetimes and exponential fit coefficients were found to exhibit considerable excitation energy dependence [10]. It is thus central in this discussion for the comparison of $\text{I}^- \cdot \text{U} \cdot \text{H}_2\text{O}$ clusters to $\text{I}^- \cdot \text{U}$

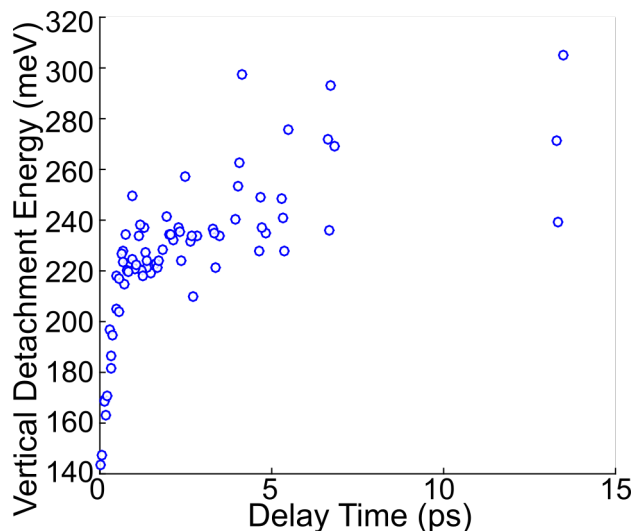


Figure 5.4: Concatenated VDEs for feature A for each delay time up to 15 ps. Feature A exhibits a fast increase in VDE from approximately 140 meV to 230 meV within 1 ps, followed by a gradual increase in the VDE thereafter until the intensity of the feature decays to a point where it can no longer be fit with an analytical function. After 15 ps, feature A decays to only $\sim 20\%$ of its maximum intensity.

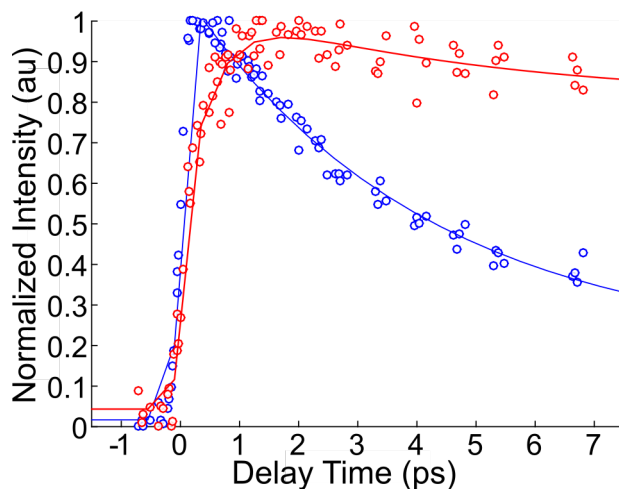


Figure 5.5: Concatenated normalized integrated intensities for features A (blue, DB anion) and B (red, VB anion) at short time delays.

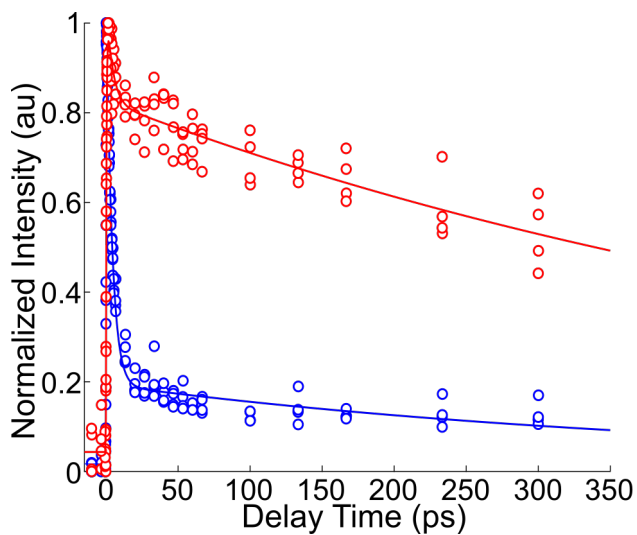


Figure 5.6: Concatenated normalized integrated intensities for feature A (blue, DB anion) and feature B (red, VB anion) from excitation at 4.38 eV and probed with 1.58 eV. The rise time for feature A is cross-correlation limited and the decay is 4.1 ± 0.2 ps and 410 ± 140 ps. The rise time for feature B is 400 ± 140 fs and decays bi-exponentially in 6.1 ± 2.4 ps and 650 ± 100 ps.

Table 5.3: Lifetimes and exponential fit coefficients A_i for the DB and VB anions of $\Gamma^- \cdot U \cdot H_2O$ and comparison to $\Gamma^- \cdot U$. A_1 refers to the coefficient for τ_{rise} , A_2 for $\tau_{\text{decay},1}$, and A_3 for $\tau_{\text{decay},2}$. The $\Gamma^- \cdot U$ data for the DB and VB anions are reprinted with permission from Ref. [10]. The $\Gamma^- \cdot U$ data for the Γ^- feature are from Ch. 4.

DB Anion								
Cluster	$h\nu_{\text{pump}} - \text{VDE}$	τ_{rise} (fs)	$\tau_{\text{decay},1}$ (ps)	$\tau_{\text{decay},2}$ (ps)	A_1	A_2	A_3	DB/VB Ratio
$\Gamma^- \cdot U \cdot H_2O$	-20 meV	< 185	4.1 ± 0.2	410 ± 140	...	0.88	0.17	1.12
$\Gamma^- \cdot U$	-40 meV	260 ± 50	7.1 ± 0.7	1200 ± 100	-0.47	0.51	0.50	1.41
$\Gamma^- \cdot U$	+30 meV	120 ± 90	5.0 ± 0.6	500 ± 130	-0.26	0.66	0.26	1.04
VB Anion								
Cluster	$h\nu_{\text{pump}} - \text{VDE}$	τ_{rise} (fs)	$\tau_{\text{decay},1}$ (ps)	$\tau_{\text{decay},2}$ (ps)	A_1	A_2	A_3	
$\Gamma^- \cdot U \cdot H_2O$	-20 meV	400 ± 140	6.1 ± 2.4	650 ± 100	-0.60	0.27	0.73	
$\Gamma^- \cdot U$	-40 meV	200 ± 20	13.9 ± 1.4	450 ± 40	-0.75	0.56	0.44	
$\Gamma^- \cdot U$	+30 meV	220 ± 40	5.6 ± 1.5	80 ± 30	-0.65	0.54	0.35	
Γ^-								
Cluster	$h\nu_{\text{pump}} - \text{VDE}$	$\tau_{\text{rise},1}$ (ps)	$\tau_{\text{rise},2}$ (ps)	A_1	A_2			
$\Gamma^- \cdot U \cdot H_2O$	-20 meV	6.7 ± 3.8	320 ± 30	-0.15	-0.86			
$\Gamma^- \cdot U$	-80 meV	17.5 ± 1.6	150 ± 10	-0.16	-0.79			

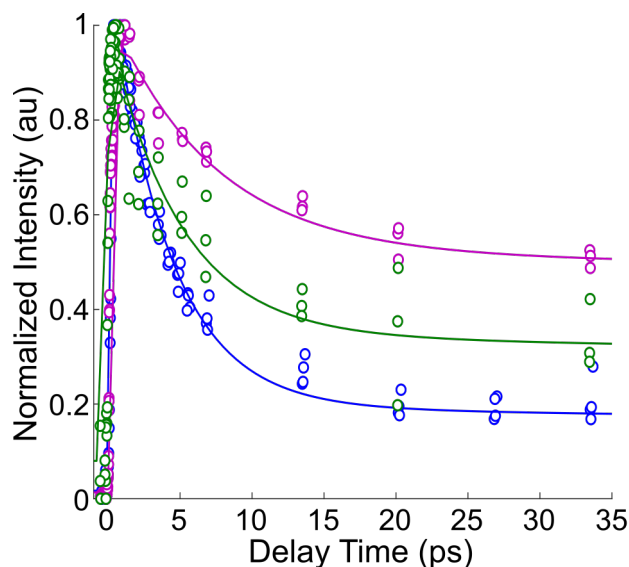


Figure 5.7: Comparison of the normalized integrated intensities for the $\Gamma^- \cdot U \cdot H_2O$ DB anion (blue, 20 meV below $\Gamma^- \cdot U \cdot H_2O$ VDE) and the $\Gamma^- \cdot U$ DB anion (purple, 40 meV below $\Gamma^- \cdot U$ VDE; green, 30 meV above VDE). The $\Gamma^- \cdot U$ data is adapted with permission from Ref. [10].

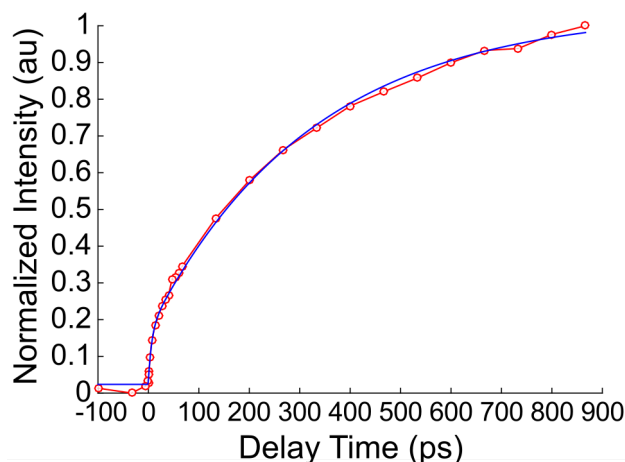


Figure 5.8: Normalized integrated intensity for feature D at 4.38 eV pump excitation energy and 3.14 eV probe energy. Feature D rises bi-exponentially with time constants of 6.7 ± 3.8 ps and 320 ± 30 ps.

clusters to distinguish between dynamical effects that are due to the addition of water versus those effects that likely stem from differences in pump excitation energy or internal energy. To aid in this comparison, the previous $\Gamma \cdot U$ DB and VB anion results for pump excitation energies both 40 meV below the VDE (-40 meV) and 30 meV above the VDE ($+30$ meV) are compared here to $\Gamma \cdot U \cdot H_2O$ clusters photoexcited 20 meV below the VDE (-20 meV). A higher probe energy of 3.61 eV capable of photodetaching Γ^- was applied only to $\Gamma \cdot U \cdot H_2O$ clusters photoexcited 80 meV below the VDE [13]. The iodide re-formation dynamics observed in that work are reconsidered here in light of the present $\Gamma \cdot U \cdot H_2O$ results.

We begin by briefly considering the nature of the excited states of the photoexcited $\Gamma \cdot U \cdot H_2O$ complex. The EOM-CCSD calculations performed here (Table 5.2), although energetically offset from our experimental results, suggest that the lowest energy transitions activated near the VDE correspond to an electronic transition from the I(5p) orbital to the DB state of $\Gamma \cdot U \cdot H_2O$. These calculated results are similar to the calculations performed previously by our group for the excited state transition channels of $\Gamma \cdot U$ [13], which also found that the only electronic transitions energetically near the VDE of the complex were transitions from I(5p) to the DB orbital, with comparable oscillator strengths to those given in Table 5.2. Thus, photoexcitation of $\Gamma \cdot U \cdot H_2O$ near its VDE is expected to directly access the DB orbital.

Before examining the TNIs separately, it is useful to note first the observed binding energy ranges for each feature. In previous work on $\Gamma \cdot U$ clusters, the DB anion was observed between 0 and 0.2 eV eBE, and the VB anion was observed in the range from 0.3 to 0.7 – 0.8 eV eBE [10]. Both of these energy ranges are slightly narrower and approximately 0.2

eV lower in maximum eBE than for the corresponding features in $\Gamma^- \cdot \text{U} \cdot \text{H}_2\text{O}$. The increase in eBE for the $\Gamma^- \cdot \text{U} \cdot \text{H}_2\text{O}$ DB and VB anions relative to that seen in TRPEI of $\Gamma^- \cdot \text{U}$ confirms that the water molecule is associated in both TNIs over the course of our measurements, and that it stabilizes both the DB and VB anions.

5.6.1 Formation and VDE shifting of the DB anion

The formation of the DB state of $\Gamma^- \cdot \text{U} \cdot \text{H}_2\text{O}$ was found to be instantaneous in this work (< 185 fs), while for $\Gamma^- \cdot \text{U}$ at -40 meV the DB anion rise was 260 ± 50 fs, and at $+30$ meV was 120 ± 90 fs [10]. The $\Gamma^- \cdot \text{U} \cdot \text{H}_2\text{O}$ DB anion rise thus more closely resembles the dynamics of $+30$ meV photoexcited $\Gamma^- \cdot \text{U}$ rather than -40 meV. This result is perhaps unsurprising considering that an analogous VDE-relative pump excitation energy between $\Gamma^- \cdot \text{U} \cdot \text{H}_2\text{O}$ and $\Gamma^- \cdot \text{U}$ may result in differing amounts of internal energy between the two clusters, given that the addition of water, depending on its geometric positioning, will add several vibrational modes to the cluster. Thus, considering this excitation energy dependence, we expect that the fast rise dynamics here for the $\Gamma^- \cdot \text{U} \cdot \text{H}_2\text{O}$ DB anion are similar to the $\Gamma^- \cdot \text{U}$ DB anion.

As shown in Fig. 5.4, the $\Gamma^- \cdot \text{U} \cdot \text{H}_2\text{O}$ DB anion exhibits an increase in the VDE at early times from 140 meV to approximately 230 meV within 1 ps, followed by a less steep, continued increase thereafter until the anion decays to $< 20\%$ of its maximum intensity, which occurs in approximately 15 ps. This is in contrast to the previously observed VDE shifting of iodine-associated nucleobase cluster DB anions in TRPEI studies [10, 11], where, in the case of $\Gamma^- \cdot \text{U}$, the VDE of the DB anion increased from 75 meV to 115 meV in approximately 700 fs. It then declined to a long-time value of 95 meV by 20 ps, the VDE of bare U^- , indicating that the I atom had departed. These $\Gamma^- \cdot \text{U}$ VDE shifting dynamics were found not to exhibit any excitation energy dependence for pump energies within ± 100 meV of the VDE in the previous work on $\Gamma^- \cdot \text{U}$ clusters. Due to this lack of excitation energy dependence in the VDE shifting, it is apparent that the differences in DB anion VDE shifting between $\Gamma^- \cdot \text{U} \cdot \text{H}_2\text{O}$ and $\Gamma^- \cdot \text{U}$ are effects induced by the presence of the water molecule. We now examine the early time and long-time VDE shifting dynamics separately.

In iodine-associated DB anions formed in the Franck-Condon region, the exchange repulsion between the electrons of iodine and the DB electron is expected to destabilize the species due to excluded volume effects [40–43]. This repulsive interaction drives the DB anion to a lower energy geometry from the vertical excitation region to the DB equilibrium geometry; as this interaction is absent in the neutral, the result is an increase in the VDE at early times. Within 1 ps of the DB state formation, the $\Gamma^- \cdot \text{U} \cdot \text{H}_2\text{O}$ DB anion VDE is measured to increase approximately 164% from the initial value. In $\Gamma^- \cdot \text{U}$, the DB anion of $\Gamma^- \cdot \text{U}$ exhibited a VDE increase from 75 meV to 115 meV in approximately 700 fs, or a 153% increase [10]. From this, it appears that the initial rise of the VDE for the $\Gamma^- \cdot \text{U} \cdot \text{H}_2\text{O}$ DB anion follows a similar iodine excluded volume perturbation mechanism [40–43] as $\Gamma^- \cdot \text{U}$ at early times, and thus that the initial VDE increase in $\Gamma^- \cdot \text{U} \cdot \text{H}_2\text{O}$ is likely governed by the

motion of iodine relative to the uracil-water moiety.

For $\Gamma^- \cdot \text{U} \cdot \text{H}_2\text{O}$, after the initial sharp VDE increase, the DB anion VDE is found to increase by ~ 50 meV until approximately 15 ps when the decay of the DB anion is too substantial to analytically fit the VDE. This increase is opposite to the drop in VDE for the DB state of $\Gamma^- \cdot \text{U}$, although it occurs on a similar time scale. It is possible the longer-time VDE shifts in the two systems have a similar origin, namely the loss of an I atom. For all $\Gamma^- \cdot \text{U} \cdot \text{H}_2\text{O}$ isomers presented in Table 5.S1, the calculated dipole moment of the neutral $\text{U} \cdot \text{H}_2\text{O}$ species is significantly larger than that of the iodine-associated $\text{U} \cdot \text{H}_2\text{O}$ species, leading to an increase in the binding energy if neutral iodine shifts away. In contrast, I atom loss from the DB state of $\Gamma^- \cdot \text{U}$ results in a decreased dipole moment and a decrease in the binding energy [10]. Thus, the loss of neutral iodine from the cluster in ~ 15 ps can account for the observed VDE shifting at intermediate times in both $\Gamma^- \cdot \text{U} \cdot \text{H}_2\text{O}$ and $\Gamma^- \cdot \text{U}$.

5.6.2 Formation and energetics of the VB anion

In $\Gamma^- \cdot \text{U}$, the rise of the VB anion subsequent to photoexcitation near the VDE was found to be ~ 200 fs and was largely independent of photon energy. Therefore, the somewhat longer ~ 400 fs VB anion rise seen for $\Gamma^- \cdot \text{U} \cdot \text{H}_2\text{O}$ is attributed to the addition of the water molecule. Given that the initial electronic excitation is to the DB state of $\Gamma^- \cdot \text{U} \cdot \text{H}_2\text{O}$, the 400 fs rise time may reflect partial conversion of the DB anion to form the VB anion. This mechanism has been suggested previously from our work on $\Gamma^- \cdot \text{U}$ clusters photoexcited near the VDE [10], but the more obvious distinction between the DB and VB rise times in the presence of water argues more strongly in its favor. Moreover, it is now well-established from experiment and theory that the VB state of $\text{U}^- \cdot \text{H}_2\text{O}$ is lower in energy than the DB state [14, 21, 23, 24]. Here, as in our previous work on $\Gamma^- \cdot \text{U}$, however, there is unfortunately no direct match of VB anion rise and DB anion decay timescales as has been observed for $\Gamma^- \cdot \text{Adenine}$ and $\Gamma^- \cdot \text{CH}_3\text{NO}_2$ [12, 44].

Calculations by Takayanagi et al. for the DB and VB anions of $\text{U}^- \cdot \text{H}_2\text{O}$ indicate that for various $\text{U}^- \cdot \text{H}_2\text{O}$ DB anion isomers, the barrier height for a DB to VB anion conversion can vary from 0.43 – 3.00 kcal/mol [24]. The authors expect the barrier to isomerization of water to a different binding site around uracil is approximately 1 – 5 kcal/mol as well, and thus predict water-binding-site-change isomerization pathways to be active among the various conformers of the DB anion to form a DB anion with a lower VB anion conversion barrier [24]. Therefore, in $\Gamma^- \cdot \text{U} \cdot \text{H}_2\text{O}$, it is possible that a small structural change in the water binding site in the DB anion to lower the energetic conversion barrier will delay the VB anion formation relative to that in $\Gamma^- \cdot \text{U}$ by on the order of ~ 100 fs.

5.6.3 Decay channels of the DB and VB anion and the re-formation of iodide

The $\Gamma^- \cdot \text{U} \cdot \text{H}_2\text{O}$ DB and VB anion exhibit bi-exponential decay dynamics with fast decay lifetimes of 4 ps and 6 ps, respectively, and longer decay lifetimes of 410 ps and 650 ps, respectively, while the iodide photofragment signal undergoes bi-exponential rise with time constants of approximately 7 ps and 320 ps. We have previously suggested that for $\Gamma^- \cdot \text{U}$ DB and VB anion bi-exponential decay, the fast decay may be internal conversion to the anion ground state by back-electron transfer to the I atom which then dissociates after some delay to yield $\text{U} + \Gamma^-$ [13]. For $\Gamma^- \cdot \text{U} \cdot \text{H}_2\text{O}$, the observation that the two fast TNI decays are each slightly faster than the fast Γ^- rise time lends support to this attribution, but here we also consider our past measurements of Γ^- signal from iodide-associated clusters to explain the bi-exponential Γ^- rise dynamics.

Previously, the Γ^- signal from $\Gamma^- \cdot \text{U}$ was fit to a mono-exponential function with a rise time of 86 ps. However, as discussed in Section 5.5, an improved fit results from assuming a bi-exponential rise with time constants of 17.5 ± 1.6 ps and 150 ± 10 ps (Table 5.3). A comparison of the mono-exponential and bi-exponential fits for the rise of Γ^- from $\Gamma^- \cdot \text{U}$ is presented here in Fig. 5.S5. The fast rise time from the revised fit is up to a few ps longer than the fast DB and VB anion decays at comparable excitation energies. Hence, the revised fitting of our previous data yields a more consistent set of time constants across the two systems and further supports the association of the fast decay constants for the TNIs with internal conversion (IC) to the ground state, followed by fragmentation to Γ^- .

In $\Gamma^- \cdot \text{CH}_3\text{NO}_2$ clusters photoexcited near their VDE, the DB to VB anion transition is complete and occurs within 500 fs. In those species, a long, clearly mono-exponential Γ^- re-formation rise time was observed to be an order of magnitude slower than the fast component of the VB anion bi-exponential decay (21 ps vs 2 ps, respectively) [45]. This delay was attributed to a dynamical bottleneck between IC and photofragmentation to Γ^- . For both $\Gamma^- \cdot \text{U}$ and $\Gamma^- \cdot \text{U} \cdot \text{H}_2\text{O}$, in which the DB anion does not undergo a complete VB conversion, it is possible that IC of the DB anion leads to the fast Γ^- rise component observed here for both systems, while the slow Γ^- rise is from internal conversion of the VB anion and significantly delayed iodide ejection, as in $\Gamma^- \cdot \text{CH}_3\text{NO}_2$.

For $\Gamma^- \cdot \text{U} \cdot \text{H}_2\text{O}$, we must also consider that production of $\Gamma^- \cdot \text{H}_2\text{O}$ may also be an active decay channel here following internal conversion, as the asymptotic barrier to dissociation of water from uracil was calculated here to be less than 0.5 eV (Eq. 5.1); however, the binding energy of this species (VDE = 3.51 ± 0.02 eV) [46, 47] is too high to photodetach in the present experiment. Once formed, $\Gamma^- \cdot \text{H}_2\text{O}$ could then dissociate on a longer timescale to yield Γ^- . Further experiments with a probe energy greater than 3.51 eV are planned to determine if $\Gamma^- \cdot \text{H}_2\text{O}$ formation is also a dissociation channel and measure the relevant timescales as compared to the TNIs and iodide re-formation. It is also worth noting that Γ^- re-formation

from $\Gamma \cdot \text{U}$ was measured with only one pump excitation energy at -80 meV, so the role of excitation energy dependence in directly comparing the $\Gamma \cdot \text{U}$ results with $\Gamma \cdot \text{U} \cdot \text{H}_2\text{O}$ is unclear.

The long-time decay of both the $\Gamma \cdot \text{U} \cdot \text{H}_2\text{O}$ DB anion and VB anion is likely to be autodetachment. Though difficult to record temporally, photoelectron signal is measured here for 0 eV eKE electrons arising from autodetachment and has been measured previously for $\Gamma \cdot \text{U}$, among other systems [10, 35, 36]. Here, the long-time decay of the $\Gamma \cdot \text{U} \cdot \text{H}_2\text{O}$ DB anion is quite similar to that of the $+30$ meV photoexcited $\Gamma \cdot \text{U}$ DB anion, consistent with the other lifetimes as described above. The long decay time constant of the $\Gamma \cdot \text{U} \cdot \text{H}_2\text{O}$ VB anion, however, is quite a bit longer than that of the $+30$ meV photoexcited $\Gamma \cdot \text{U}$ VB anion, which could arise from the presence of water stabilizing the VB anion relative to autodetachment. Theoretical work by Takayanagi et al. and Adamowicz et al. on $\text{U}^- \cdot \text{H}_2\text{O}$ clusters predicts the VB anion to be stabilized more than the DB anion due to the increased excess electron density on the uracil ring for the VB anion compared to the diffuse DB anion [21, 23, 24]. Although here the DB anion to VB anion conversion is not found to be faster or have a smaller population intensity ratio of DB anion to VB anion (Table 5.3), this very long VB anion lifetime may indicate that the VB anion is preferentially stabilized to autodetachment.

As indicated earlier, the water molecule is known to be associated with both of the TNIs due to the increased eBEs of the features, but neutral iodine may leave the $\Gamma \cdot \text{U} \cdot \text{H}_2\text{O}$ DB anion in approximately 15 ps as evidenced in the VDE shifting dynamics (Fig. 5.4). It is possible that neutral iodine loss similarly occurs for the VB anion, which for both species would leave behind a $\text{U}^- \cdot \text{H}_2\text{O}$ anion capable of decay only by autodetachment rather than internal conversion. Interestingly, a recent study of photofragment action spectroscopy of photoexcited $\Gamma \cdot \text{U}$ clusters found that electron detachment dissociation channels, rather than ionic photofragment formation channels, were the dominant decay pathways for the non-hydrated clusters, and these electron detachment pathways are expected to be important here as well, as exemplified by the relatively large A3 exponential amplitude for the $\Gamma \cdot \text{U} \cdot \text{H}_2\text{O}$ VB anion long decay (Table 5.3) [48].

5.7 Conclusions

$\Gamma \cdot \text{U} \cdot \text{H}_2\text{O}$ clusters have been investigated using TRPEI to examine the dynamics of low energy electron attachment to uracil-water following photoexcitation of the clusters near the cluster VDE of 4.40 eV, where a DB state of the overall complex is accessed. We observe the formation of the DB and VB TNIs of $\Gamma \cdot \text{U} \cdot \text{H}_2\text{O}$ and the relative stabilization of these anions in the presence of water as indicated by an increase in the binding energy of both TNIs. The DB anion for $\Gamma \cdot \text{U} \cdot \text{H}_2\text{O}$ appears promptly, whereas there is a ~ 400 fs delay in the appearance of the VB anion. This delay, which is more pronounced than in $\Gamma \cdot \text{U}$ [10], is attributed to a partial conversion of the DB to VB anion, which may be slowed by water-

binding-site rearrangement to lower the energetic barrier to conversion. The DB anion also exhibits a monotonically increasing VDE shift over 15 ps, reflecting stabilization of the DB state followed by loss of a neutral I atom.

The TNIs exhibit bi-exponential decay, and the I^- photofragment signals exhibit a bi-exponential rise with time constants of 6.7 ps and 320 ps. Comparison of these time constants, along with those seen previously for $I^- \cdot U$ and $I^- \cdot CH_3NO_2$ [10, 13, 44, 45], suggests that fast decay of the TNIs reflects internal conversion to the anion ground state in which the electron has back-transferred to the I atom, followed by fragmentation to I^- . We speculate that the fast and slow components of the I^- rise reflect IC from the DB and VB anions, respectively. At longer times the TNIs likely decay by autodetachment, with the VB anion exhibiting a long decay time that suggests it is stabilized relative to autodetachment by the presence of water.

5.8 Supplementary Material

Assignment of Features E and E'

Features E and E' appear a few ps after the appearance of the DB and VB anions and exhibit mono-exponential decay with long lifetimes similar to the long decay lifetimes of the TNIs. Interestingly, the VDEs of features E and E' ($\sim 2.6 \pm 0.1$ eV and $\sim 1.4 \pm 0.1$ eV, respectively) correspond to the calculated VDEs of the uracil anionic tautomers aU_{N3C5} (VDE = 2.58 eV) and aU_{N1C5} (VDE = 1.38 eV) [5] arising from proton transfer from either of the uracil NH groups to the alkene carbon closest to the imide portion of the uracil ring, and thus could correspond to bare or iodine-associated uracil tautomer anions in the present study. The longer rise time of these features suggests that if these tautomers are formed, they arise from the decay of the TNIs of $I^- \cdot U \cdot H_2O$. We have calculated [32] these tautomers to both lie approximately 22 kcal/mol above the canonical uracil, well beyond what can be formed in our cluster source, and we have calculated the VDEs of the ground state $I^- \cdot U \cdot H_2O$ with these uracil tautomers to both be approximately 4.35 eV, close to the VDE of the ground state tautomer, so the single photon photoelectron spectrum here is not expected to show any evidence for or against the presence of tautomers. No such tautomers were observed in previous TRPEI studies of $I^- \cdot U$ with fairly similar source conditions to those used here [10, 13, 35, 36], suggesting that if these features are uracil tautomers, the presence of water may lower the barrier for tautomerization.

Table 5.S1: Structures and dipole moments (μ) for neutral iodine-uracil-water in the ground state anion geometry and in the neutral equilibrium geometry, and for neutral uracil-water optimized without iodine. The blue arrows indicate the direction and relative magnitude of μ . Shading is used to guide the eye for each isomer column. See Methods for computational details.

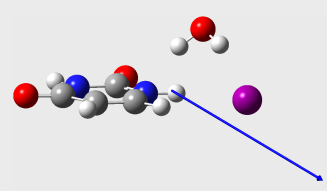
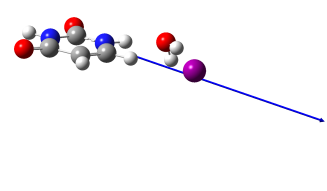
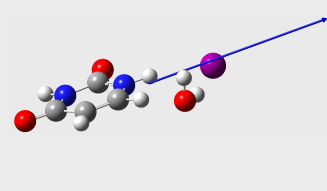
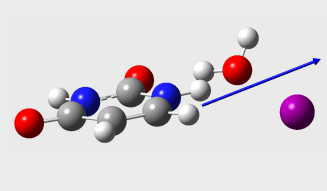
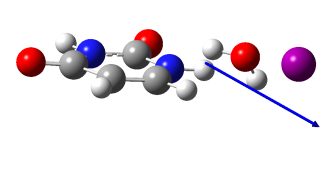
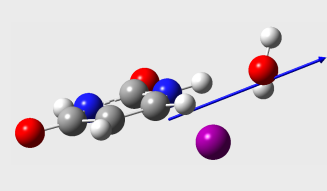
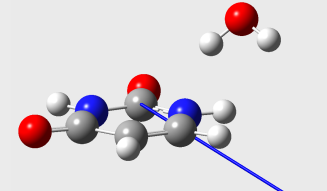
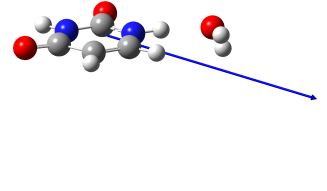
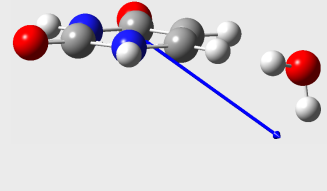
Isomer	a)	b)	c)
Structure, anion geometry			
μ , anion geometry	6.93 D	8.72 D	7.37 D
Structure, neutral geometry			
μ , neutral geometry	3.72 D	3.71 D	4.90 D
Structure, optimized U·H ₂ O			
μ , optimized U·H ₂ O	5.90 D	7.84 D	6.53 D

Table 5.S1, continued.

Isomer	d)	e)	f)
Structure, anion geometry			
μ , anion geometry	8.02 D	6.15 D	7.70 D
Structure, neutral geometry			
μ , neutral geometry	6.40 D	3.01 D	5.65 D
Structure, optimized U·H ₂ O			
μ , optimized U·H ₂ O	7.02 D	5.08 D	6.80 D

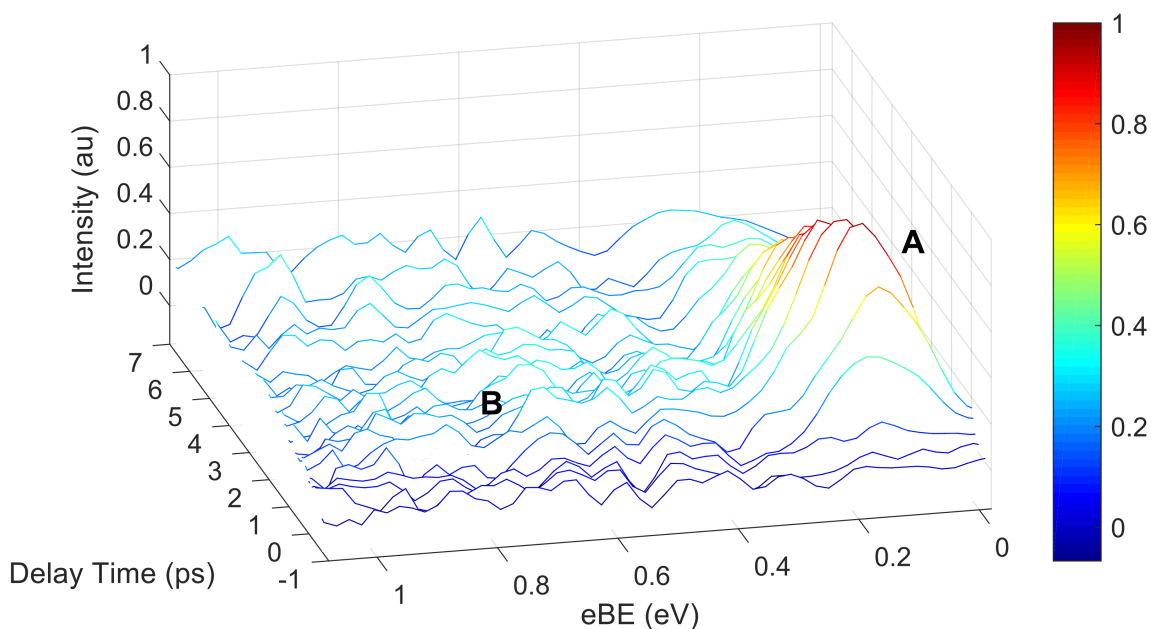


Figure 5.S1: Time-resolved photoelectron spectra corresponding to Fig. 5.2 presented as a waterfall plot.

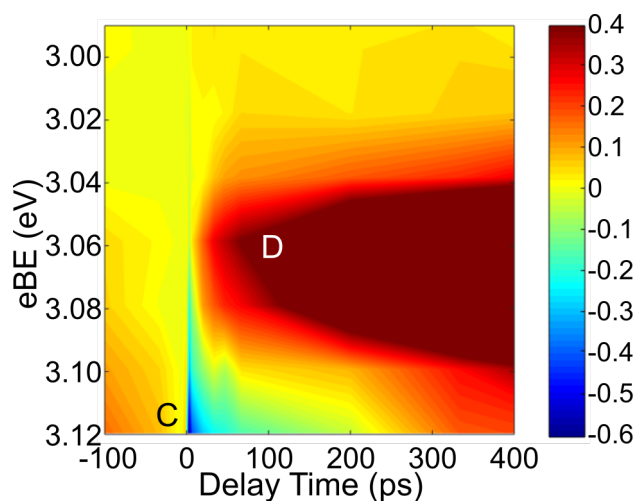


Figure 5.S2: Representative background-subtracted time-resolved photoelectron spectra for features C (maximum eBE, $eKE \sim 0$ eV) and D ($eBE = 3.06$ eV), for $\text{I}^- \cdot \text{U} \cdot \text{H}_2\text{O}$ at 4.38 eV pump excitation energy and 3.14 eV probe energy. It can be seen clearly that the two features each occupy distinct energy space and exhibit different dynamics. Feature D is found to grow monotonically in intensity as a function of time, while feature C exhibits an initial depletion in intensity with an intensity recovery at longer times.

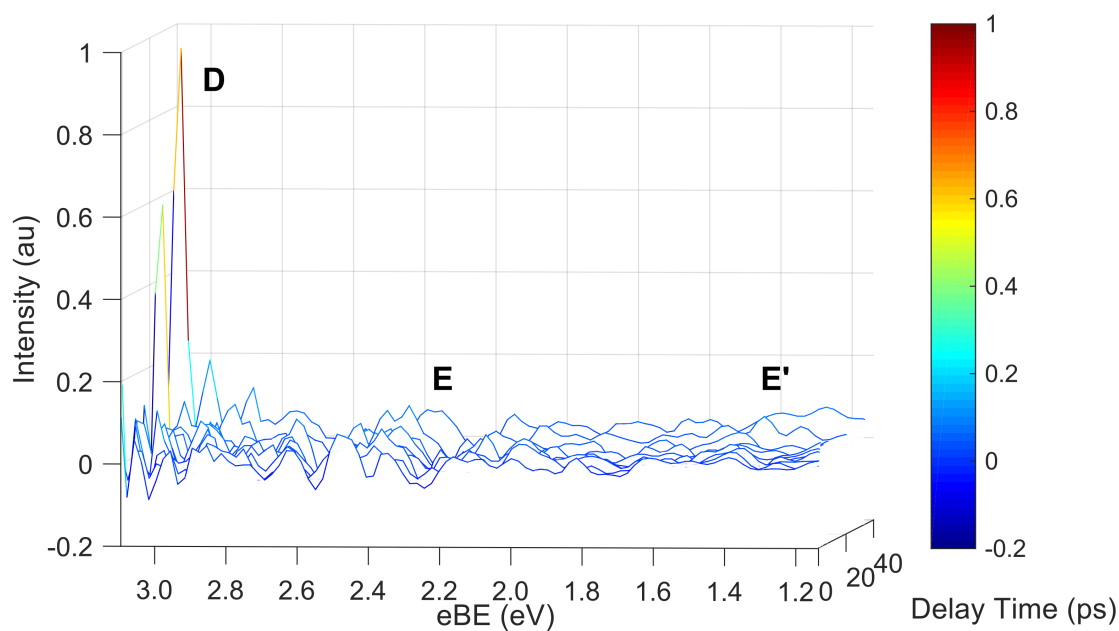


Figure 5.S3: Time-resolved photoelectron spectra corresponding to Fig. 5.3 presented as a waterfall plot. Feature C, the strongly negative autodetachment feature, has been omitted for clarity to allow perspective of the features E and E'.

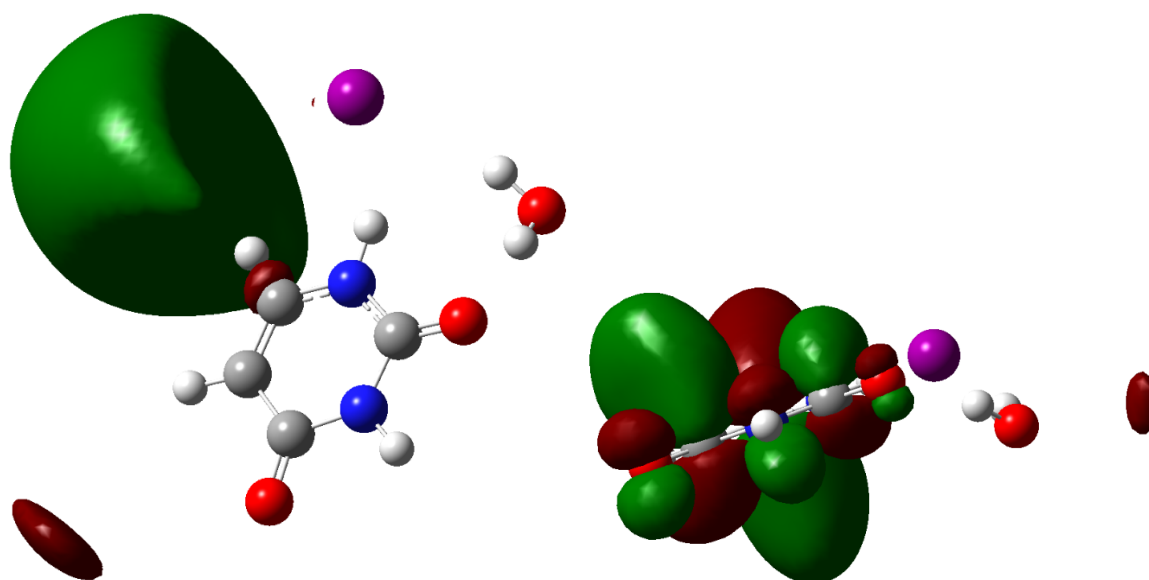


Figure 5.S4: EOM-CCSD/aug-cc-pVDZ(-pp) calculated molecular orbital images for the DB excited state (left) and VB excited state (right) for the lowest-lying calculated anion conformer of $I^- \cdot U \cdot H_2O$.

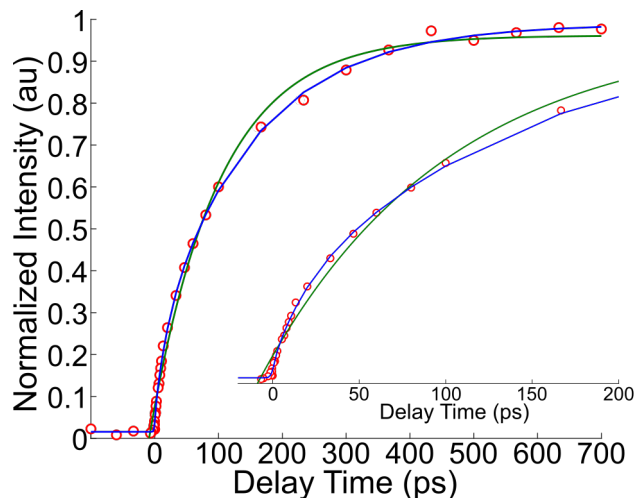


Figure 5.S5: Comparison of fits for the I^- feature from our past work: mono-exponential fit (green) from Ch. 4 and bi-exponential fit (blue) using Eq. 5.2. The $I^- \cdot U$ data for the I^- feature are reproduced from Ch. 4.

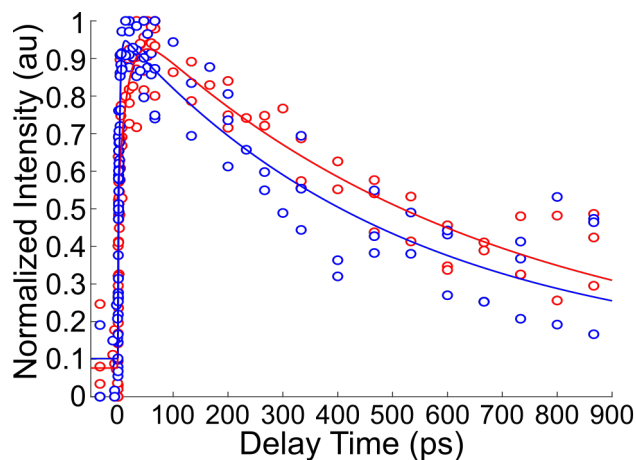


Figure 5.S6: Concatenated normalized integrated intensities for features E (blue) and E' (red) from excitation at 4.38 eV and probed at 3.14 eV. Feature E has a fit rise time of 3.5 ± 1.4 ps and a decay time of 500 ± 80 ps. Feature E' has a fit rise time of 8.7 ± 3.7 ps and a decay time of 675 ± 120 ps.

5.9 References

- [1] B. Boudaïffa, P. Cloutier, D. Hunting, M. A. Huels, and L. Sanche, “Resonant formation of DNA strand breaks by low-energy (3 to 20 eV) electrons”, *Science* **287**, 1658–1660 (2000).
- [2] R. Barrios, P. Skurski, and J. Simons, “Mechanism for damage to DNA by low-energy electrons”, *J. Phys. Chem. B* **106**, 7991–7994 (2002).
- [3] J. Simons, “How do low-energy (0.1-2 eV) electrons cause DNA-strand breaks?”, *Acc. Chem. Res.* **39**, 772–779 (2006).
- [4] H.-Y. Chen, P.-Y. Yang, H.-F. Chen, C.-L. Kao, and L.-W. Liao, “DFT reinvestigation of DNA strand breaks induced by electron attachment”, *J. Phys. Chem. B* **118**, 11137–11144 (2014).
- [5] R. Bachorz, W. Klopper, M. Gutowski, X. Li, and K. H. Bowen, “Photoelectron spectrum of valence anions of uracil and first-principles calculations of excess electron binding energies”, *J. Chem. Phys.* **129**, 054309 (2008).
- [6] C. Desfrancois, H. Abdoul-Carime, and J.-P. Schermann, “Ground-state dipole-bound anions”, *Int. J. Mod. Phys. B* **10**, 1339–1395 (1996).
- [7] P. D. Burrow, G. A. Gallup, A. M. Scheer, S. Denifl, S. Ptasińska, T. D. Märk, and P. Scheier, “Vibrational Feshbach resonances in uracil and thymine”, *J. Chem. Phys.* **124**, 124310 (2006).
- [8] G. Hanel, B. Gstir, S. Denifl, P. Scheier, M. Probst, B. Farizon, M. Farizon, E. Illenberger, and T. D. Märk, “Electron attachment to uracil: effective destruction at subexcitation energies”, *Phys. Rev. Lett.* **90**, 188104 (2003).
- [9] S. Ptasińska, S. Denifl, S. Gohlke, P. Scheier, E. Illenberger, and T. D. Märk, “Decomposition of thymidine by low-energy electrons: Implications for the molecular mechanisms of single-strand breaks in DNA”, *Angew. Chem. Int. Ed.* **45**, 1893–1896 (2006).
- [10] S. B. King, M. A. Yandell, A. B. Stephansen, and D. M. Neumark, “Time-resolved radiation chemistry: Dynamics of electron attachment to uracil following UV excitation of iodide-uracil complexes”, *J. Chem. Phys.* **141**, 224310 (2014).
- [11] S. B. King, A. B. Stephansen, Y. Yokoi, M. A. Yandell, A. Kunin, T. Takayanagi, and D. M. Neumark, “Electron accommodation dynamics in the DNA base thymine”, *J. Chem. Phys.* **143**, 024312 (2015).
- [12] A. B. Stephansen, S. B. King, Y. Yokoi, Y. Minoshima, W.-L. Li, A. Kunin, T. Takayanagi, and D. M. Neumark, “Dynamics of dipole- and valence bound anions in iodide-adenine binary complexes: A time-resolved photoelectron imaging and quantum mechanical investigation”, *J. Chem. Phys.* **143**, 104308 (2015).

- [13] W.-L. Li, A. Kunin, E. Matthews, N. Yoshikawa, C. E. H. Dessent, and D. M. Neumark, “Photodissociation dynamics of the iodide-uracil (I^-U) complex”, *J. Chem. Phys.* **145**, 044319 (2016).
- [14] J. Schiedt, R. Weinkauff, D. M. Neumark, and E. W. Schlag, “Anion spectroscopy of uracil, thymine and the amino-oxo and amino-hydroxy tautomers of cytosine and their water clusters”, *Chem. Phys.* **239**, 511–524 (1998).
- [15] K. Khistyayev, A. Golan, K. B. Bravaya, N. Orms, A. I. Krylov, and M. Ahmed, “Proton transfer in nucleobases is mediated by water”, *J. Phys. Chem. A* **117**, 6789–6797 (2013).
- [16] Y. He, C. Wu, and W. Kong, “Decay pathways of thymine and methyl-substituted uracil and thymine in the gas phase”, *J. Phys. Chem. A* **107**, 5145–5148 (2003).
- [17] Y. He, C. Wu, and W. Kong, “Photophysics of methyl-substituted uracils and thymines and their water complexes in the gas phase”, *J. Phys. Chem. A* **108**, 943–949 (2004).
- [18] J. H. Hendricks, S. A. Lyapustina, H. L. de Clercq, J. T. Snodgrass, and K. H. Bowen, “Dipole bound, nucleic acid base anions studied via negative ion photoelectron spectroscopy”, *J. Chem. Phys.* **104**, 7788–7791 (1996).
- [19] R. N. Compton, H. S. Carman, C. Desfrancois, H. Abdoul-Carime, J. P. Schermann, J. H. Hendricks, S. A. Lyapustina, and K. H. Bowen, “On the binding of electrons to nitromethane - dipole and valence bound anions”, *J. Chem. Phys.* **105**, 3472–3478 (1996).
- [20] O. Dolgounitcheva, V. G. Zakrzewski, and J. V. Ortiz, “Anionic and neutral complexes of uracil and water”, *J. Phys. Chem. A* **103**, 7912–7917 (1999).
- [21] J. H. Hendricks, S. A. Lyapustina, H. L. de Clercq, and K. H. Bowen, “The dipole bound-to-covalent anion transformation in uracil”, *J. Chem. Phys.* **108**, 8–11 (1998).
- [22] N. A. Oyler and L. Adamowicz, “Electron attachment to uracil: theoretical ab initio study”, *J. Phys. Chem.* **97**, 11122–11123 (1993).
- [23] C. A. Morgado, K. Y. Pichugin, and L. Adamowicz, “Stabilization of an excess electron on uracil by water. Ab initio study”, *Phys. Chem. Chem. Phys.* **6**, 2758–2762 (2004).
- [24] H. Motegi and T. Takayanagi, “Theoretical study on the transformation mechanism between dipole-bound and valence-bound anion states of small uracil-water clusters and their photoelectron spectra”, *J. Mol. Struct.-THEOCHEM* **907**, 85–92 (2009).
- [25] T. Frigato, D. Svozil, and P. Jungwirth, “Valence- and dipole-bound anions of the thymine-water complex: ab initio characterization of the potential energy surfaces”, *J. Phys. Chem. A* **110**, 2916–2923 (2006).
- [26] R. J. Peláez, C. Blondel, C. Delsart, and C. Drag, “Pulsed photodetachment microscopy and the electron affinity of iodine”, *J. Phys. B- At. Mol. Opt.* **42**, 125001 (2009).

- [27] A. Davis, R. Wester, A. E. Bragg, and D. M. Neumark, “Time-resolved photoelectron imaging of the photodissociation of I_2^- ”, *J. Chem. Phys.* **118**, 999–1002 (2003).
- [28] A. E. Bragg, J. R. R. Verlet, A. Kammrath, O. Cheshnovsky, and D. M. Neumark, “Electronic relaxation dynamics of water cluster anions”, *J. Am. Chem. Soc.* **127**, 15283–15295 (2005).
- [29] W. C. Wiley and I. H. McLaren, “Time-of-flight mass spectrometer with improved resolution”, *Rev. Sci. Instrum.* **26**, 1150–1157 (1955).
- [30] A. Eppink and D. H. Parker, “Velocity map imaging of ions and electrons using electrostatic lenses: application in photoelectron and photofragment ion imaging of molecular oxygen”, *Rev. Sci. Instrum.* **68**, 3477–3484 (1997).
- [31] V. Dribinski, A. Ossadtchi, V. Mandelshtam, and H. Reisler, “Reconstruction of Abel-transformable images: the Gaussian basis-set expansion Abel transform method”, *Rev. Sci. Instrum.* **73**, 2634–2642 (2002).
- [32] M. J. Frisch, G. W. Trucks, H. B. Schlegel, G. E. Scuseria, M. A. Robb, J. R. Cheeseman, G. Scalmani, V. Barone, B. Mennucci, G. A. Petersson, H. Nakatsuji, M. Caricato, X. Li, H. P. Hratchian, A. F. Izmaylov, J. Bloino, G. Zheng, J. L. Sonnenberg, M. Hada, M. Ehara, K. Toyota, R. Fukuda, J. Hasegawa, M. Ishida, T. Nakajima, Y. Honda, O. Kitao, H. Nakai, T. Vreven, J. A. Montgomery Jr., J. E. Peralta, F. Ogliaro, M. J. Bearpark, J. Heyd, E. N. Brothers, K. N. Kudin, V. N. Staroverov, R. Kobayashi, J. Normand, K. Raghavachari, A. P. Rendell, J. C. Burant, S. S. Iyengar, J. Tomasi, M. Cossi, N. Rega, N. J. Millam, M. Klene, J. E. Knox, J. B. Cross, V. Bakken, C. Adamo, J. Jaramillo, R. Gomperts, R. E. Stratmann, O. Yazyev, A. J. Austin, R. Cammi, C. Pomelli, J. W. Ochterski, R. L. Martin, K. Morokuma, V. G. Zakrzewski, G. A. Voth, P. Salvador, J. J. Dannenberg, S. Dapprich, A. D. Daniels, Ö. Farkas, J. B. Foresman, J. V. Ortiz, J. Cioslowski, and D. J. Fox, *Gaussian 09, Revision C.01*, 2009.
- [33] K. A. Peterson, B. C. Shepler, D. Figgen, and H. Stoll, “On the spectroscopic and thermochemical properties of ClO, BrO, IO, and their anions”, *J. Phys. Chem. A* **110**, 13887 (2006).
- [34] J. E. Sansonetti and W. C. Martin, “Handbook of basic atomic spectroscopic data”, *J. Phys. Chem. Ref. Data* **34**, 1559–2259 (2005).
- [35] M. A. Yandell, S. B. King, and D. M. Neumark, “Time-resolved radiation chemistry: photoelectron imaging of transient negative ions of nucleobases”, *J. Am. Chem. Soc.* **135**, 2128–2131 (2013).
- [36] S. B. King, M. A. Yandell, and D. M. Neumark, “Time-resolved photoelectron imaging of the iodide-thymine and iodide-uracil binary cluster systems”, *Faraday Discuss.* **163**, 59–72 (2013).

- [37] J. Smets, W. J. McCarthy, and L. Adamowicz, “Dipole-bound electron attachment to uracil-water complexes. Theoretical ab initio study”, *J. Phys. Chem.* **100**, 14655–14660 (1996).
- [38] J. Smets, D. M. A. Smith, Y. Elkadi, and L. Adamowicz, “Search for stable anions of uracil-water clusters. Ab initio theoretical studies”, *J. Phys. Chem. A* **101**, 9152–9156 (1997).
- [39] T. van Mourik, S. L. Price, and D. C. Clary, “Ab initio calculations on uracil-water”, *J. Phys. Chem. A* **103**, 1611–1618 (1999).
- [40] H.-Y. Chen and W.-S. Sheu, “Precursors of the charge-transfer-to-solvent states in $\Gamma(\text{H}_2\text{O})_n$ clusters”, *J. Am. Chem. Soc.* **122**, 7534–7542 (2000).
- [41] H.-Y. Chen and W.-S. Sheu, “Iodine effect on the relaxation pathway of photoexcited $\Gamma(\text{H}_2\text{O})_n$ clusters”, *Chem. Phys. Lett.* **335**, 475–480 (2001).
- [42] Q. K. Timerghazin and G. H. Peslherbe, “Further insight into the relaxation dynamics of photoexcited $\Gamma(\text{H}_2\text{O})_n$ clusters”, *J. Am. Chem. Soc.* **125**, 9904–9905 (2003).
- [43] F. D. Vila and K. D. Jordan, “Theoretical study of the dipole-bound excited states of $\Gamma(\text{H}_2\text{O})_4$ ”, *J. Phys. Chem. A* **106**, 1391–1397 (2002).
- [44] M. A. Yandell, S. B. King, and D. M. Neumark, “Decay dynamics of nascent acetonitrile and nitromethane dipole-bound anions produced by intracuster charge-transfer”, *J. Chem. Phys.* **140**, 184317 (2014).
- [45] A. Kunin, W.-L. Li, and D. M. Neumark, “Time-resolved photoelectron imaging of iodide-nitromethane ($\Gamma \cdot \text{CH}_3\text{NO}_2$) photodissociation dynamics”, *Phys. Chem. Chem. Phys.* **18**, 33226–33232 (2016).
- [46] G. Markovich, R. Giniger, M. Levin, and O. Cheshnovsky, “Photoelectron spectroscopy of iodine anion solvated in water clusters”, *J. Chem. Phys.* **95**, 9416–9419 (1991).
- [47] G. Markovich, S. Pollack, R. Giniger, and O. Cheshnovsky, “Photoelectron spectroscopy of Cl^- , Br^- , and Γ^- solvated in water clusters”, *J. Chem. Phys.* **101**, 9344–9353 (1994).
- [48] E. Matthews, R. Cercola, G. Mensa-Bonsu, D. M. Neumark, and C. E. H. Dessent, “Photoexcitation of iodide ion-pyrimidine clusters above the electron detachment threshold: Intracuster electron transfer versus nucleobase-centred excitations”, *J. Chem. Phys.* **148**, 084304 (2018).

Chapter 6

Time-resolved Dynamics in Iodide-Uracil-Water Clusters Upon Excitation of the Nucleobase

“How do you know I’m mad?”
said Alice. “You must be,” said
the Cat, “or you wouldn’t have
come here.”

Lewis Carroll

The content and figures of this chapter are adapted from:

A. Kunin, V. S. McGraw, K. G. Lunny, and D. M. Neumark, “Time-resolved dynamics in iodide-uracil-water clusters upon excitation of the nucleobase” *J. Chem. Phys.* **151**, 154304 (2019)

with the permission of AIP Publishing.

6.1 Abstract

The dynamics of iodide-uracil-water ($\text{I}^- \cdot \text{U} \cdot \text{H}_2\text{O}$) clusters following $\pi - \pi^*$ excitation of the nucleobase are probed using time-resolved photoelectron spectroscopy (TRPES). Photoexcitation of this cluster at 4.77 eV results in electron transfer from the iodide moiety to the uracil, creating a valence-bound (VB) anion within the cross-correlation of the pump and probe laser pulses. This species can decay by a number of channels, including autodeachment and dissociation to I^- or larger anion fragments. Comparison of the energetics of the photoexcited cluster and its decay dynamics with those of the bare iodide-uracil ($\text{I}^- \cdot \text{U}$) complex provide a sensitive probe of the effects of microhydration on these species.

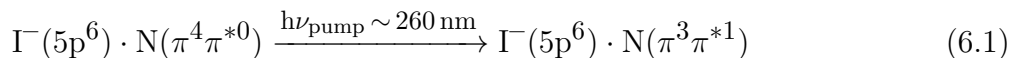
6.2 Introduction

DNA damage has been shown to proceed directly from UV photoexcitation, as well as indirectly from the attachment of low-energy electrons to its constituent nucleobases [1–4]. DNA bases exhibit strong absorption cross-sections for UV radiation, particularly near 260 nm (4.77 eV) [5, 6], and the interaction of nucleobases with surrounding solvent water molecules plays a key role in the relaxation and photostability of nucleobases in this excitation energy regime [7, 8]. The attachment of low-energy electrons induces strand breaks in DNA [2–4], and it has been proposed that the initial site of electron attachment is the nucleobase followed by electronic coupling that facilitates fragmentation at the backbone [9–16]. Photoelectron spectroscopy has shown that the addition of water increases the electron affinity of nucleobases [17, 18], while molecular dynamics simulations find that solution-structure fluctuation likely promotes attachment of bulk hydrated electrons to nucleobases [19]. Our group has previously examined the ultrafast dynamics of electron attachment to nucleobases using time-resolved photoelectron spectroscopy [20] (TRPES) of various iodide-nucleobase ($\text{I}^- \cdot \text{N}$) complexes [21–27] and related model systems [28, 29]. The present study uses TRPES to examine iodide-uracil-water ($\text{I}^- \cdot \text{U} \cdot \text{H}_2\text{O}$) clusters photoexcited at 260 nm and compares these results to those of iodide-uracil ($\text{I}^- \cdot \text{U}$) to understand the role of water in the mechanisms of excitation and charge transfer in these anionic clusters in this UV excitation regime.

$\text{I}^- \cdot \text{N}$ complexes have been previously studied by photofragment action spectroscopy [26, 30, 31] and electronic structure calculations [26, 30, 32] in addition to TRPES. Two regimes of UV photoabsorption have been measured for these complexes [26, 30, 31]. The first is centered near the vertical detachment energy (VDE), the difference in energy between the anion and the neutral clusters at the equilibrium geometry of the anion, which is approximately 4 eV for most $\text{I}^- \cdot \text{N}$ clusters [21, 22, 25]. The second region of UV photoabsorption is a broad band spanning $\sim 4.6 - 5.0$ eV. Excited state calculations for $\text{I}^- \cdot \text{U}$ [26], iodide-thymine ($\text{I}^- \cdot \text{T}$) [30], and $\text{I}^- \cdot \text{U} \cdot \text{H}_2\text{O}$ [32] show that photoexcitation near the VDE corresponds to optical excitation from the iodide (5p) orbital to a dipole-bound (DB) state of the nucleobase.

The nucleobase DB state arises from capture of the excess electron by the relatively large dipole moment of the base [33–37]. In contrast, these same calculations indicate that photoexcitation near 4.7 – 4.8 eV primarily corresponds to base-centered $\pi - \pi^*$ excitation. The dynamics resulting from near-VDE photoexcitation of $\text{I}^- \cdot \text{U} \cdot \text{H}_2\text{O}$ and the effects therein of the water molecule have already been considered in detail [32], so we focus here only on the effect of the addition of water on the dynamics ensuing $\pi - \pi^*$ photoexcitation.

TRPES of $\text{I}^- \cdot \text{N}$ clusters probes the dynamics of photoinduced electron attachment and electronic excitation in nucleobases and traces the time evolution of nascent transient negative ions (TNIs) and anionic decay photofragments. Our TRPES studies with pump excitation energies from 4.60 – 4.90 eV are expected to create a $\pi - \pi^*$ excited state of the nucleobase, as in Eq. 6.1:



Time-resolved studies in this pump excitation regime have found instantaneous formation of the cluster valence-bound (VB) anion with no evidence for the presence of DB states [21, 22]. The VB state corresponds to electron attachment to a valence orbital, the π^* orbital of the base [14, 17, 38]. We have previously proposed [21, 27] for $\text{I}^- \cdot \text{U}$ and $\text{I}^- \cdot \text{T}$ complexes that, subsequent to $\pi - \pi^*$ excitation of the nucleobase, one possible pathway for the photoexcited state is charge transfer from iodide to the empty π orbital to create the VB anion. While this overall mechanism is consistent with experimental results and electronic structure calculations [27], it still awaits theoretical confirmation.

Photofragment action spectroscopy in conjunction with TRPES has identified autodetachment as well as formation of I^- as the major cluster decay pathways in both photoexcitation regimes for $\text{I}^- \cdot \text{U}$ binary clusters [26], although the nature of the time-resolved dynamics of these channels has been found to be clearly different for each set of pump energies [27]. Autodetachment refers to the spontaneous emission of an electron from photoexcitation of an anion resonance embedded within the neutral plus free electron continuum [39–41]; these electrons can be very slow if randomization of vibrational energy occurs prior to electron emission (the thermionic emission limit) [42].

In the present study, we employ TRPES to excite $\text{I}^- \cdot \text{U} \cdot \text{H}_2\text{O}$ complexes near the peak of the base-centered $\pi - \pi^*$ excitation [32] at 260 nm (4.77 eV), and track the resulting dynamics with 1.58 eV or 3.18 eV probe pulses. These experiments, which complement previous work [32] on near-VDE excitation of $\text{I}^- \cdot \text{U} \cdot \text{H}_2\text{O}$ complexes, probe the dynamics of both electronically excited uracil as well as the interaction of low-energy electrons with the nucleobase. TRPES can identify and trace the dynamics of nascent TNIs (eBE ~ 0 eV – 1 eV) [18, 34, 38, 43–46] with 1.58 eV probe pulses, while the higher energy probe is capable of

detecting anionic photofragments such as Γ^- (neutral electron affinity = 3.059 eV) [47]. Here, we observe prompt formation of the VB anion, with autodetachment and the formation of Γ^- as the major decay channels for the photoexcited clusters. The lifetimes of the VB anion and autodetachment features reflect the stabilizing effect of the presence of water, while the Γ^- rise dynamics suggest that additional water-associated fragmentation channels may be active here.

6.3 Experimental Methods

The experimental apparatus employed in this study has been described in detail previously [48, 49] and is briefly summarized here. $\Gamma^- \cdot \text{U} \cdot \text{H}_2\text{O}$ clusters were generated by passing 515 kPa helium buffer gas over a reservoir of distilled water and a reservoir of methyl iodide (CH_3I). The reservoirs and the connecting gas line were wrapped in heating tape; the water reservoir was heated to approximately 30 °C, while the CH_3I reservoir and gas line were heated to approximately 40 °C. The gas mixture was then passed through an Even-Lavie pulsed valve operating at 500 Hz, which contained a sample cartridge of uracil (Sigma-Aldrich, $\geq 99\%$) heated to 240 °C. The gas mixture was expanded into vacuum through a ring-filament ionizer to create anionic clusters, which were then extracted orthogonally into a Wiley-McLaren time-of-flight mass spectrometer [50]. The $\Gamma^- \cdot \text{U} \cdot \text{H}_2\text{O}$ clusters were mass-selected and then intersected by the pump and probe laser pulses.

To generate the pump and probe laser pulses, a KMLabs Griffin Oscillator and Dragon Amplifier were used to produce 45 fs pulses centered at approximately 785 nm (1.58 eV) with 1.8 mJ/pulse. The fundamental was frequency tripled with two β -barium borate (BBO) crystals to produce ~ 10 μJ /pulse of 260 nm (4.77 eV) pump pulses. The residual 785 nm pulses were recovered from the frequency-tripler set-up, and were sent to a delay stage to serve as probe pulses of ~ 80 μJ /pulse. Alternatively, this recovered 785 nm light was frequency-doubled in a BBO to produce ~ 60 μJ /pulse of 390 nm (3.18 eV) probe pulses. In either case, the pump and probe pulses were combined at the chamber in a dichroic beamsplitter. The cross-correlation of 260 nm/785 nm was ≤ 180 fs and that of 260 nm/390 nm was < 300 fs; the latter cross-correlation, measured outside the chamber, is obscured by residual 390 nm light, and the actual cross-correlation is expected to be as much as 50-100 fs shorter than this measured value [26].

The resultant photoelectrons were analyzed by a velocity-map imaging assembly [51] comprising three electron optical elements and a chevron-stacked microchannel plate detector coupled to a phosphor screen imaged by a charge-coupled device camera. Basis-set expansion (BASEX) reconstruction methods were used to reconstruct the 3D photoelectron kinetic energy (eKE) distributions [52].

6.4 Results

Fig. 6.1 presents a laser noise-subtracted, single-photon photoelectron spectrum of $\Gamma^- \cdot \text{U} \cdot \text{H}_2\text{O}$ clusters photodetached at 4.74 eV, as well as an image of the calculated ground state structure of the cluster [32]. The photoelectron spectrum is provided as a function of eKE as well as electron binding energy (eBE) ($\text{eBE} = h\nu_{\text{photon}} - \text{eKE}$). Two features appear in this spectrum: feature A, peaked at approximately 4.69 ± 0.05 eV eBE (0.05 ± 0.05 eV eKE), and feature B, peaked at 4.40 ± 0.05 eV eBE (0.37 ± 0.05 eV eKE). As has been previously determined [32], feature A corresponds to autodetachment of ~ 0 eV eKE electrons from the photoexcited $\Gamma^- \cdot \text{U} \cdot \text{H}_2\text{O}$ clusters, and feature B corresponds to direct detachment to the lower iodine spin-orbit state ($^2\text{P}_{3/2}$) from the $\Gamma^- \cdot \text{U} \cdot \text{H}_2\text{O}$ anion, yielding a VDE of 4.40 eV for $\Gamma^- \cdot \text{U} \cdot \text{H}_2\text{O}$. As both of these features arise from single-photon (pump-only) processes at the pump energy employed in our TRPES experiments, they are also present in all of the TRPE spectra here at these same eKEs.

Fig. 6.2 presents photoelectron spectra at select time delays for $\Gamma^- \cdot \text{U} \cdot \text{H}_2\text{O}$ at 4.77 eV pump excitation energy and 1.58 eV probe energy; here and in other TRPE spectra, $\text{eBE} = h\nu_{\text{probe}} - \text{eKE}$. Feature A exhibits non-zero intensity at negative times and increases in intensity over approximately 10 ps before decreasing back to its initial intensity. Feature B exhibits noisy but similar time dynamics as feature A, likely due to spectral overlap between the two features in this region. Feature C, covering the region from approximately 0.1 eV

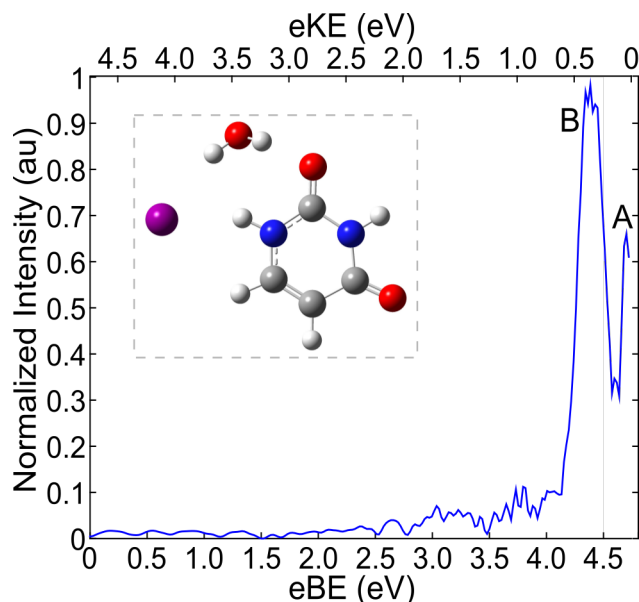


Figure 6.1: Single-photon photoelectron spectrum of $\Gamma^- \cdot \text{U} \cdot \text{H}_2\text{O}$ at 4.74 eV and calculated ground state $\Gamma^- \cdot \text{U} \cdot \text{H}_2\text{O}$ structure (inset).

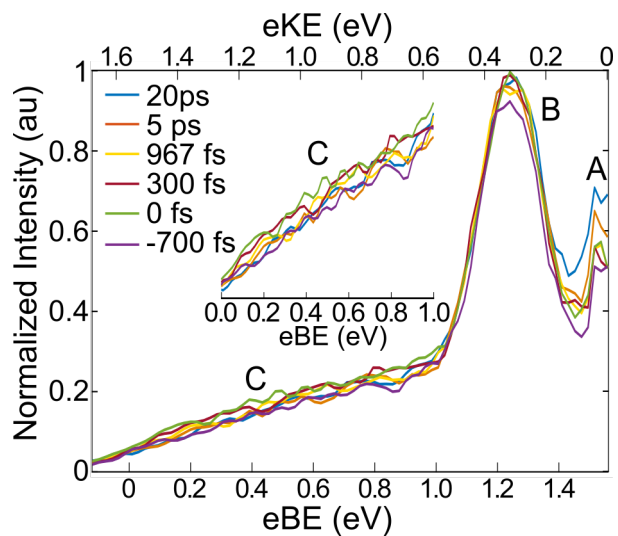


Figure 6.2: Photoelectron spectra of $\text{I}^- \cdot \text{U} \cdot \text{H}_2\text{O}$ at 4.77 eV pump excitation energy and 1.58 eV probe energy at selected delay times.

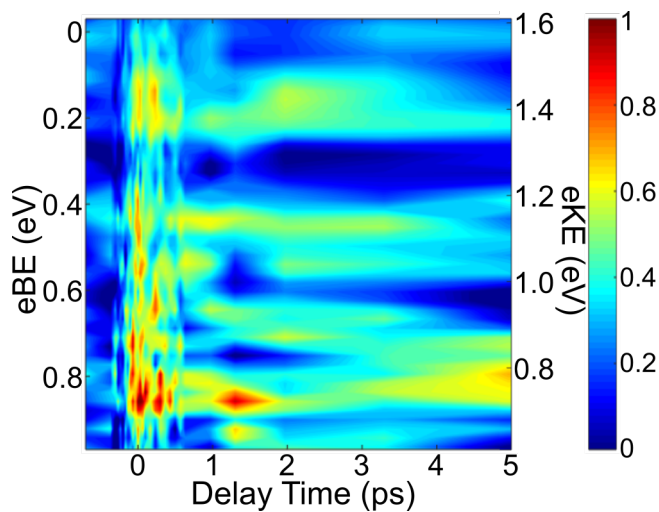


Figure 6.3: Representative background-subtracted time-resolved photoelectron spectra for feature C at short pump-probe delays for $\text{I}^- \cdot \text{U} \cdot \text{H}_2\text{O}$ at 4.77 eV pump excitation energy and 1.58 eV probe energy.

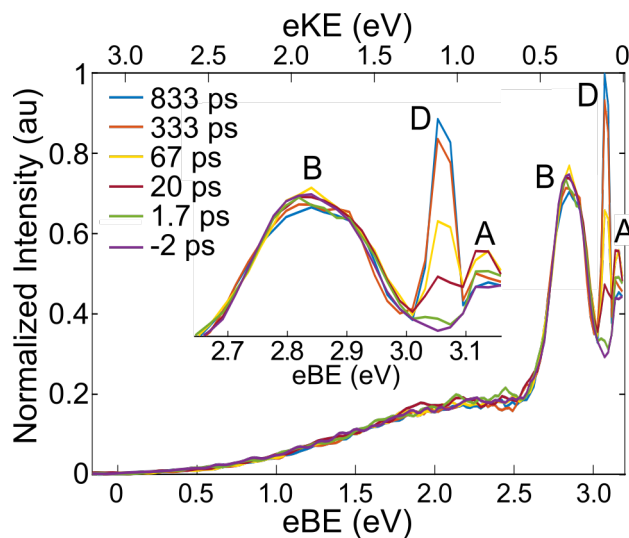


Figure 6.4: Photoelectron spectra of $\text{I}^- \cdot \text{U} \cdot \text{H}_2\text{O}$ at 4.77 eV pump excitation energy and 3.18 eV probe energy at selected delay times.

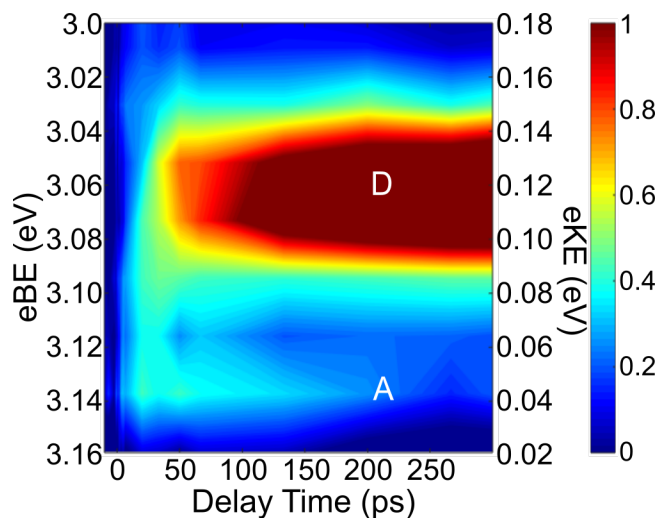


Figure 6.5: Representative background-subtracted time-resolved photoelectron spectra for features A (near maximum eBE, $e\text{KE} \sim 0 - 0.07$ eV), and D ($e\text{BE} = 3.06$ eV) for $\text{I}^- \cdot \text{U} \cdot \text{H}_2\text{O}$ at 4.77 eV pump excitation energy and 3.18 eV probe energy.

– 0.9 eV eBE, is enlarged in the inset. Based on our previous results on $\Gamma^- \cdot \text{U}$ clusters photoexcited at excitation energies in the range of 4.69 – 4.90 eV [21, 22], we can assign feature C as the VB anion of photoexcited $\Gamma^- \cdot \text{U} \cdot \text{H}_2\text{O}$. Time-resolved photoelectron spectra for feature C, background-subtracted with respect to the most negative delay time, are shown in Fig. 6.3 for time delays up to 5 ps.

Fig. 6.4 presents photoelectron spectra at select time delays for $\Gamma^- \cdot \text{U} \cdot \text{H}_2\text{O}$ at 4.77 eV pump excitation energy and 3.18 eV probe energy. Features A and B are the same features seen in Fig. 6.2. The prominent new feature in these spectra, feature D, is located at 3.06 ± 0.05 eV eBE, and this narrow feature grows monotonically in intensity over the course of experiment. Based on the binding energy, spectral shape, and time-dynamics of feature D, we assign feature D to photodetachment of atomic iodide to the $^2\text{P}_{3/2}$ iodine spin-orbit state. Background-subtracted time-resolved photoelectron spectra for features A and D are presented in Fig. 6.5.

6.5 Analysis

The normalized, integrated intensities for the VB anion (red, feature C) and the autodetachment feature (black, feature A) are shown at early, intermediate, and long time delays in Fig. 6.6. The integrated signals are fit to the convolution of a Gaussian instrumental response function with i exponential functions as in Eq. 6.2:

$$I(t) = \frac{1}{\sigma_{cc}\sqrt{2\pi}} \exp\left(\frac{-t^2}{2\sigma_{cc}^2}\right) \cdot \begin{cases} I_0, t < 0 \\ I_0 + \Sigma A_i \exp\left(\frac{-t}{\tau_i}\right), t \geq 0 \end{cases} \quad (6.2)$$

In this equation, σ_{cc} is the Gaussian full width at the half-maximum given by the cross-correlation of the pump and probe laser pulses, I_0 is the signal background, A_i are the coefficients for each exponential function, and τ_i are the corresponding rise or decay lifetimes for each exponential. These fits are shown in Fig. 6.6 as solid red and black lines for the VB anion and autodetachment features, respectively. The VB anion is found to appear within the cross-correlation of the pump and probe laser pulses and decay bi-exponentially. The fits for the $\Gamma^- \cdot \text{U} \cdot \text{H}_2\text{O}$ VB anion decay are 540 ± 240 fs and 220 ± 70 ps. The autodetachment feature was found to remain relatively constant in intensity at negative times. At positive delay times this feature rises to a maximum in 11.3 ± 2.2 ps followed by decay to the negative-time intensity in approximately 285 ± 70 ps.

For ease of comparison to our previous work on $\Gamma^- \cdot \text{U}$ clusters, the normalized, integrated intensities for the VB anion and autodetachment produced from $\Gamma^- \cdot \text{U}$ photoexcited at 4.79 eV are presented in Fig. 6.7 in purple, overlaid with the corresponding $\Gamma^- \cdot \text{U} \cdot \text{H}_2\text{O}$ features

(green) from Fig. 6.5. Fig. 6.8 presents the normalized integrated intensity and fitted rise for the Γ^- signal observed here. The Γ^- formation was found to be bi-exponential, with rise time constants of 32.5 ± 2.6 ps and 230 ± 20 ps. Table 6.1 summarizes the fit rise and decay lifetimes for the VB anion, autodetachment, and Γ^- feature for $\Gamma^- \cdot \text{U} \cdot \text{H}_2\text{O}$ in the present study and for $\Gamma^- \cdot \text{U}$ photoexcited at 4.79 eV from our past work [21, 26].

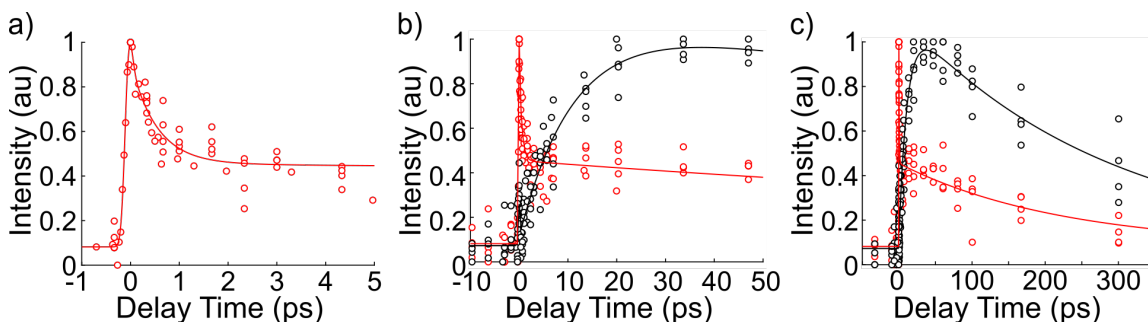


Figure 6.6: Concatenated normalized integrated intensities for features A (black, autodetachment) and C (red, VB anion) at a) early time delays, b) 10s of ps, and c) long time delays from excitation at 4.77 eV and probed with 1.58 eV. Feature A rises in 11.3 ± 2.2 ps and decays in 285 ± 70 ps. The rise time for feature C is cross-correlation limited and the decay is 540 ± 240 fs and 220 ± 70 ps.

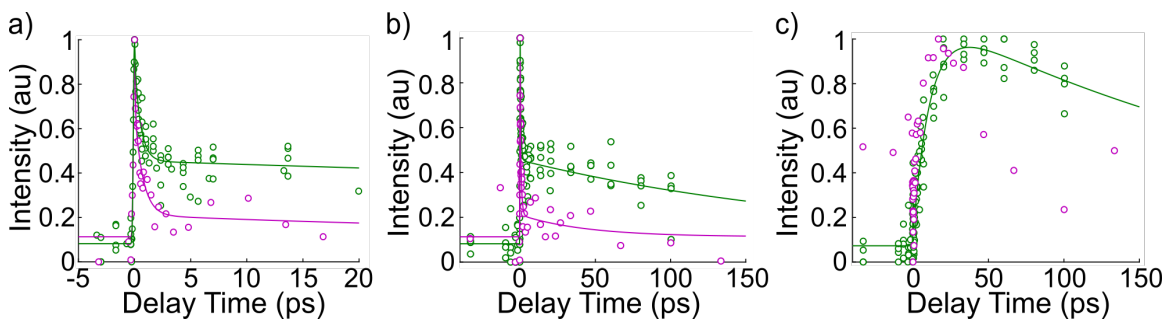


Figure 6.7: Comparison of concatenated normalized integrated intensities for a) the VB anion at early times and b) long times and c) autodetachment dynamics for $\Gamma^- \cdot \text{U} \cdot \text{H}_2\text{O}$ (green) at 4.77 eV pump excitation energy and 1.58 eV probe energy and $\Gamma^- \cdot \text{U}$ (purple) at 4.79 eV pump excitation energy and 1.57 eV probe energy.

6.6 Discussion

This work explores the dynamics of $\Gamma^- \cdot \text{U} \cdot \text{H}_2\text{O}$ clusters photoexcited at 4.77 eV, resonant with the base-centered $\pi - \pi^*$ transition for uracil. We observe instantaneous formation of the VB anion of the cluster following photoexcitation, and bi-exponential decay of this species with time constants of 540 fs and 220 ps. Autodetachment and Γ^- re-formation are

Table 6.1: Lifetimes for the VB anion, autodetachment feature, and Γ^- feature for 4.77 eV pump $\Gamma^- \cdot \text{U} \cdot \text{H}_2\text{O}$ and comparison to previous $\Gamma^- \cdot \text{U}$ studies. The $\Gamma^- \cdot \text{U}$ data for the VB anion and autodetachment dynamics are from Ref. [21], and for the Γ^- feature the data is from Ch. 4.

VB Anion			
Cluster	$h\nu_{\text{pump}}$ (eV)	$\tau_{\text{decay},1}$ (fs)	$\tau_{\text{decay},2}$ (ps)
$\Gamma^- \cdot \text{U} \cdot \text{H}_2\text{O}$	4.77	540 ± 240	220 ± 70
$\Gamma^- \cdot \text{U}$	4.79	390 ± 80	37 ± 20
Autodetachment			
Cluster	$h\nu_{\text{pump}}$ (eV)	τ_{rise} (ps)	τ_{decay} (ps)
$\Gamma^- \cdot \text{U} \cdot \text{H}_2\text{O}$	4.77	11.3 ± 2.2	285 ± 70
$\Gamma^- \cdot \text{U}$	4.79	~ 5	~ 50
Γ^-			
Cluster	$h\nu_{\text{pump}}$ (eV)	$\tau_{\text{rise},1}$ (ps)	$\tau_{\text{rise},2}$ (ps)
$\Gamma^- \cdot \text{U} \cdot \text{H}_2\text{O}$	4.77	32.5 ± 2.6	230 ± 20
$\Gamma^- \cdot \text{U}$	4.72	36 ± 3	

observed as decay channels in this photoexcitation regime. These experiments show that to first order, the dynamics of photoexcited $\Gamma^- \cdot \text{U} \cdot \text{H}_2\text{O}$ are similar to those of $\Gamma^- \cdot \text{U}$ following $\pi - \pi^*$ photoexcitation. However, the addition of a water molecule noticeably affects the rise time of the Γ^- signal as well as the decay dynamics of the VB state, as can be seen from Fig. 6.6 and Table 6.1. As summarized in Eq. 6.3 below, we have previously proposed that

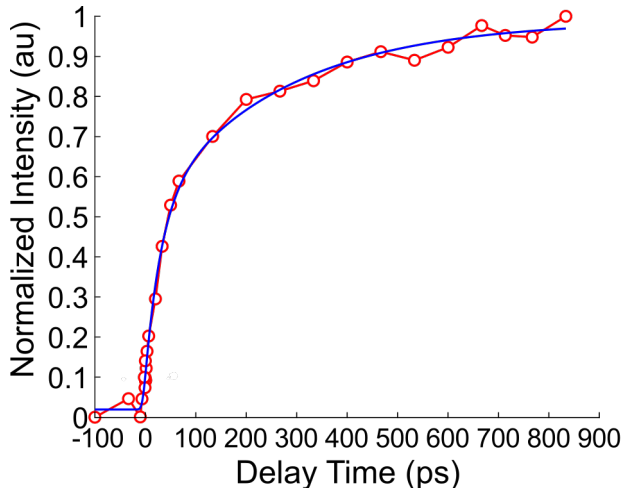
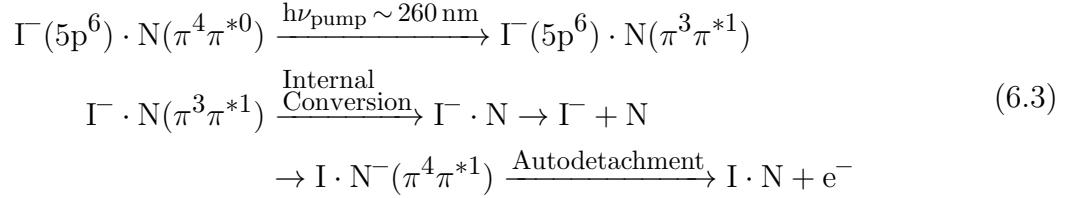


Figure 6.8: Normalized integrated intensity for feature D at 4.77 eV pump excitation energy and 3.18 eV probe energy. Feature D rises bi-exponentially with time constants of 32.5 ± 2.6 ps and 226 ± 20 ps.

the initial $\pi - \pi^*$ iodide-associated photoexcited state decays by two distinct pathways: the $\pi - \pi^*$ excited nucleobase state internally converts to the ground state of the cluster and subsequently evaporates iodide, or iodide transfers a valence electron to fill the hole in the nucleobase π orbital, creating the iodine-associated nucleobase VB anion that then decays by autodetachment [27].

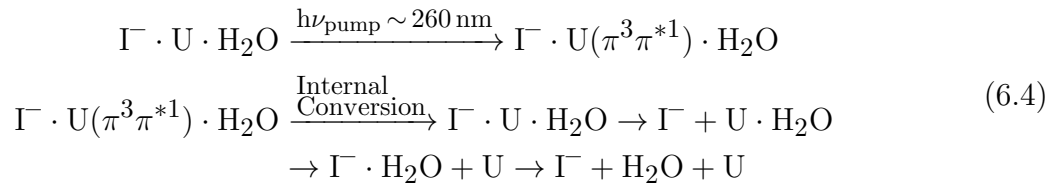


TRPES on $\Gamma^- \cdot U \cdot H_2O$ at this pump energy is sensitive to each of these decay channels. In the subsections that follow, we consider the iodide formation, VB anion, and autodetachment dynamics and the effect of the added water to expand on the basic framework previously set forward.

A. Iodide formation dynamics

TRPES of $\pi - \pi^*$ photoexcited $\Gamma^- \cdot U \cdot H_2O$ clusters finds bi-exponential Γ^- formation in 32.5 ps and 230 ps, in contrast to $\Gamma^- \cdot U$ clusters for which Γ^- was found to appear mono-exponentially in 36 ps [26]. As in Eq. 6.3, we have suggested that due to the previously observed strong connection between the VB anion and the autodetachment dynamics in this pump energy regime, the base-centered $\pi - \pi^*$ excitation is followed by internal conversion to the ground state and subsequent dissociation to produce iodide mono-exponentially [27]. While this mechanism is likely the source of the fast Γ^- rise signal, it alone cannot fully explain the origin of the bi-exponential Γ^- appearance observed here for $\Gamma^- \cdot U \cdot H_2O$ clusters.

Several energetically accessible dissociation channels have been previously calculated for $\Gamma^- \cdot U \cdot H_2O$ clusters, including dissociation to yield $\Gamma^- \cdot H_2O$ clusters [32]. $\Gamma^- \cdot H_2O$ produced as a dissociation product upon photoexcitation could also then further dissociate to yield a second source of Γ^- signal with a delayed rise time, contributing to the bi-exponential rise dynamics observed here, as depicted in Eq. 6.4:



TRPES experiments of $\Gamma^- \cdot \text{H}_2\text{O}$ clusters photoexcited at 4.77 eV pump energy and probed by 4.0 eV and by 4.77 eV probe energies were unable to conclusively identify the formation of $\Gamma^- \cdot \text{H}_2\text{O}$ (VDE = 3.51 ± 0.02 eV) [53, 54] due to poor overall signal levels at these probe energies. However, the existence of this dissociation channel could be verified in future experiments by photofragment action spectroscopy, for example.

B. VB anion formation and decay dynamics

As seen in Fig. 6.3, the VB anion of $\Gamma^- \cdot \text{H}_2\text{O}$ exhibits the strongest intensity near eBE = 0.8 – 0.9 eV, which is approximately 0.2 – 0.3 eV higher than the strongest intensity for the $\Gamma^- \cdot \text{U}$ VB anion from our past work in this $\pi - \pi^*$ pump excitation energy regime [21, 22]. This finding indicates that the presence of water stabilizes the VB anion. In our past work on near-VDE photoexcited $\Gamma^- \cdot \text{U}$ and $\Gamma^- \cdot \text{U} \cdot \text{H}_2\text{O}$ clusters, we previously observed that the addition of water also caused an increase of approximately 0.2 – 0.3 eV eBE in the TNI binding energies [32]. The width of the VB anion photoelectron spectrum is commensurate with the VB anion measured in our past work in this photoexcitation regime as well as our near-VDE photoexcitation studies [21–23, 32]. This breadth arises due to the geometric distortion of the VB anion in the ring puckering coordinate relative to the neutral [55, 56]; thus, the presence of water does not significantly affect the uracil ring puckering as reflected by the VB anion spectral width.

In the present study, the VB anion is found to appear within the cross-correlation of the pump and probe laser pulses and decay bi-exponentially, as is the case for $\Gamma^- \cdot \text{U}$ photoexcited in this excitation energy regime. The fast decay of the $\Gamma^- \cdot \text{U} \cdot \text{H}_2\text{O}$ VB anion is similar to that of the $\text{I} \cdot \text{U}^-$ VB anion formed at 4.79 eV pump energy (Table 6.1), while the long decay is an order of magnitude longer in the water-associated complex. This long-lived VB anion stabilization induced by the addition of water is commensurate with the dynamics that were previously observed in near-VDE photoexcited $\Gamma^- \cdot \text{U} \cdot \text{H}_2\text{O}$ clusters, in which the VB anion long-time decay was found to be significantly longer than in $\Gamma^- \cdot \text{U}$ [32].

In our previous results for $\pi - \pi^*$ photoexcited $\Gamma^- \cdot \text{U}$ and $\Gamma^- \cdot \text{T}$ clusters, we proposed that the VB anion decays by autodetachment because the measured autodetachment signals for both clusters were found to exhibit prompt depletion and recovery near t_0 that mirrored the appearance and fast decay of the VB anion at early times, although the $\Gamma^- \cdot \text{U}$ VB anion exhibited a somewhat longer-lived bi-exponential decay [22, 27]. Given the similarities between the $\Gamma^- \cdot \text{U}$ and $\Gamma^- \cdot \text{U} \cdot \text{H}_2\text{O}$ complexes observed here, it is likely that the bi-exponential decay mechanism for the $\Gamma^- \cdot \text{U} \cdot \text{H}_2\text{O}$ VB anion in the present study is by autodetachment as well. Previously, we have attributed the bi-exponential nature of the VB anion decay to the loss of neutral iodine from the cluster, causing a reduction in the internal energy and resulting in two autodetachment decay components [24]. Neutral iodine loss was implicated our past studies of near-VDE photoexcited $\Gamma^- \cdot \text{U}$, $\Gamma^- \cdot \text{T}$, and $\Gamma^- \cdot \text{U} \cdot \text{H}_2\text{O}$ complexes and is therefore expected to be a reasonable decay pathway [23, 24, 32]. In the $\pi - \pi^*$ photoexcitation regime,

the $I\cdot T^-$ VB anion exhibits mono-exponential decay dynamics, and it has been suggested that the initial autodetachment may be faster compared to iodine loss than in $I\cdot U$ [24]. The bi-exponential $I\cdot U\cdot H_2O$ VB anion decay here further indicates that the bi-exponential or mono-exponential nature of the VB anion decay is sensitive to the electronic structure of the specific nucleobase species.

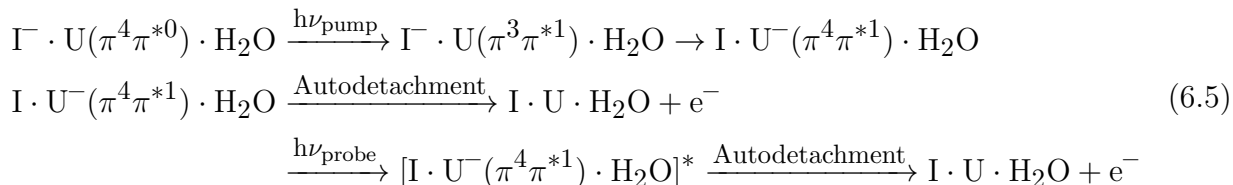
C. Autodetachment dynamics

This section considers the nature of the time-resolved autodetachment signals observed in our TRPES studies. Fig. 6.1 shows that autodetachment signal occurs in the 4.74 eV single-photon PES of $I\cdot U\cdot H_2O$ [32], and therefore clearly arises from a one-photon (pump-only) process. As seen in Figs. 6.2 and 6.4, the autodetachment signal exhibits considerable intensity at all times, including negative times where the probe pulse precedes the pump pulse. Therefore, the normalized, time-resolved signals in Fig. 6.6 show that the autodetachment intensity exhibits little to no decrease below its intensity level at negative times. At positive probe pulse arrival times, the autodetachment signal is found to rise in intensity within 11.3 ps and then decay in approximately 285 ps. Note that our experiment does not directly measure time-resolved autodetachment dynamics since the autodetachment electron signal is generated spontaneously and not by the probe pulse. Instead, the observed time-dependent integrated intensities associated with autodetachment signal arise from probe-based interactions that affect the amount of autodetachment signal that is detected for a given probe arrival time.

Let us compare our past measurements of autodetachment signal arising from $I\cdot N$ complexes to the results here for $\pi-\pi^*$ photoexcited $I\cdot U\cdot H_2O$. Our work on both $I\cdot U\cdot H_2O$ and $I\cdot U$ clusters has measured autodetachment arising from near-VDE photoexcitation [23, 32], as well as from photoexcitation in the region of the base-centered $\pi-\pi^*$ transition (shown for both $I\cdot U\cdot H_2O$ and $I\cdot U$ in Fig. 6.7c) [21, 22, 26]. Each of these past studies, regardless of photoexcitation energy, has shown autodetachment that exhibits depletion at t_0 followed by recovery to or beyond its initial intensity. Near-VDE photoexcitation in both clusters yields autodetachment signal that appears to at least qualitatively mirror the respective TNI dynamics; an example for $I\cdot U\cdot H_2O$ near-VDE pump autodetachment signal is shown in Fig. 6.S1. Concomitant autodetachment signal depletion and recovery at t_0 with time constants that mirror the TNI appearance and fast decay indicates that the probe pulse at early times photodetaches the nascent TNI population that would otherwise decay to produce autodetachment signal in the absence of the probe. At later times, the probe laser interacts with a decreased population of anions that have not already undergone autodetachment, so one expects less depletion of the autodetachment signal and eventually no depletion at all. Under these circumstances, the recovery of the autodetachment signal yields the lifetime of the autodetaching state [57].

This overshoot may arise if the probe pulse is absorbed by the VB anion and excites the

TNI to a higher-lying excited state that subsequently decays by autodetachment, as in Eq. 6.5:



The autodetachment intensity overshoot is only observed in $\Gamma \cdot U$ and $\Gamma \cdot U \cdot H_2O$ clusters, which both exhibit longer-lived, bi-exponentially decaying VB anions. $\Gamma \cdot T$ clusters in this pump energy region, in contrast, do not exhibit autodetachment intensity overshoot, and the VB anion decays mono-exponentially in only ~ 500 fs [24]. As seen in Table 6.1, the long decay lifetimes for the VB anions of $\Gamma \cdot U$ and $\Gamma \cdot U \cdot H_2O$ clusters are in agreement with the decay lifetimes of the excess autodetachment signal. Thus, we believe a mechanism as in Eq. 6.5 is operative here for both $\Gamma \cdot U$ and $\Gamma \cdot U \cdot H_2O$ photoexcited in this pump energy regime.

The presence of water appears to somewhat slow the rise of the autodetachment feature (Table 6.1), and, notably, the autodetachment signal decay lifetime is an order of magnitude longer for $\Gamma \cdot U \cdot H_2O$ than $\Gamma \cdot U$. As has been observed for the $\Gamma \cdot U \cdot H_2O$ VB anion both in the $\pi - \pi^*$ pump energy regime as well as the near-VDE excitation regime, the interaction of water may stabilize the excited cluster to decay by autodetachment, increasing the observed lifetime. The autodetachment signal resulting from $\Gamma \cdot U \cdot H_2O$ also does not appear to have depletion near t_0 as was observed in both $\Gamma \cdot U$ and $\Gamma \cdot T$ clusters [21, 22]. As noted earlier, the autodetachment depletion at early probe arrival times arises due to photodetachment of the VB excited state, which would otherwise be the spontaneous source of autodetached electrons. Lack of notable depletion in the early-time autodetachment signal of $\Gamma \cdot U \cdot H_2O$ as compared to $\Gamma \cdot U$ may therefore indicate that the $\Gamma \cdot U \cdot H_2O$ VB anion is more strongly stabilized relative to autodetachment than $\Gamma \cdot U$ clusters in this photoexcitation regime. Finally, it is interesting to note that the observed autodetachment dynamics in $\pi - \pi^*$ photoexcited $\Gamma \cdot U \cdot H_2O$ clusters are approximately the same in both the 1.58 eV and 3.18 eV probe energy studies (Fig. 6.S2). It is possible, given the relatively high power of the 1.58 eV probe pulses employed in the present study, that the 1.58 eV autodetachment dynamics arise from the absorption of two probe photons by the VB anion, particularly if absorption of the first photon is resonant. This would yield similar autodetachment overshoot dynamics for each probe energy. We consider this possibility in more detail in the Supplementary Material (Fig. 6.S3).

6.7 Conclusions

TRPES has been used to examine TNI formation and photodissociation in $\pi - \pi^*$ photoexcited $\Gamma^- \cdot \text{U} \cdot \text{H}_2\text{O}$ clusters. Production of Γ^- is measured as a major dissociation channel of the photoexcited clusters with bi-exponential formation in 32.5 ps and 230 ps. We suggest that the unique bi-exponential rise dynamics measured in $\Gamma^- \cdot \text{U} \cdot \text{H}_2\text{O}$ clusters in this photoexcitation regime are the result of additional dissociation channels arising from the presence of water. For example, internal conversion of the $\pi - \pi^*$ excited state and subsequent cluster dissociation is expected to yield Γ^- , with long-time rising signal that may be produced by dissociation of $\pi - \pi^*$ photoexcited $\Gamma^- \cdot \text{U} \cdot \text{H}_2\text{O}$ to yield $\Gamma^- \cdot \text{H}_2\text{O}$ that can subsequently decay to yield iodide. We observe instantaneous formation of the VB anion of the complex, and propose that this state arises from charge transfer from iodide to fill the empty π orbital that remains on uracil after the nucleobase is photoexcited, consistent with the proposed mechanism for $\Gamma^- \cdot \text{U}$ binary clusters. The VB anion of $\Gamma^- \cdot \text{U} \cdot \text{H}_2\text{O}$ exhibits increased binding energy compared to the VB anion of $\Gamma^- \cdot \text{U}$ clusters in this photoexcitation regime. The VB anion is found to decay bi-exponentially, as in $\Gamma^- \cdot \text{U}$, but the long decay lifetime is an order of magnitude longer in $\Gamma^- \cdot \text{U} \cdot \text{H}_2\text{O}$ clusters and is expected to reflect stabilization of the VB state relative to decay by autodetachment. Autodetachment is also measured as a dissociation channel of the photoexcited $\Gamma^- \cdot \text{U} \cdot \text{H}_2\text{O}$ complexes. Overshoot of the measured autodetachment intensity beyond the negative-time autodetachment signal indicates that absorption of the probe pulse by the long-lived VB anion produces additional autodetachment.

6.8 Supplementary Material

Probe power dependence for 1.58 eV autodetachment dynamics

We note in the manuscript that the similarity between the autodetachment dynamics for 1.58 eV probe energy and 3.18 eV probe energy (Fig. 6.S2) may arise from the absorption of two 1.58 eV probe photons by the VB anion. To test this, we have measured the $\Gamma^- \cdot \text{U} \cdot \text{H}_2\text{O}$ autodetachment dynamics for several 1.58 eV probe powers ranging from 27 $\mu\text{J}/\text{pulse}$ to 105 $\mu\text{J}/\text{pulse}$ to compare to the original 80 $\mu\text{J}/\text{pulse}$ experiment (Fig. 6.S3). We find that, to first order, the autodetachment dynamics at each employed probe power are similar. Below 27 $\mu\text{J}/\text{pulse}$, the signal-to-noise for the measurement becomes prohibitively low. Variations in day-to-day signal intensity and stability preclude analysis of the signal intensity dependence on probe power. Within our experimental capabilities, it appears to not be possible to eliminate or verify two-photon absorption of the 800 nm probe. Future experiments could employ a lower energy probe pulse (e.g. ~ 1.0 eV) to examine this issue further.

Uracil Tautomerization

We briefly comment here on the role of the addition of water on the possible tautomerization of the uracil nucleobase. In our previous work in near-VDE photoexcited $\Gamma^- \cdot \text{U} \cdot \text{H}_2\text{O}$

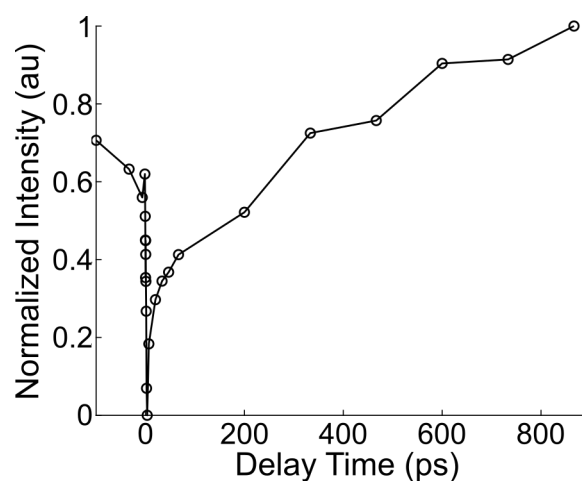


Figure 6.S1: Normalized integrated intensity for autodetachment signal arising from 4.38 eV pump excitation energy and 3.14 eV probe energy for $\Gamma^- \cdot \text{U} \cdot \text{H}_2\text{O}$, excited 20 meV below the cluster VDE. The observed dynamics qualitatively mirror the near-VDE TNI dynamics; the signal depletion occurs in ~ 1 ps with recovery in ~ 5 ps and ~ 200 ps. The increase in intensity at the longest time delays is due to signal contributions from the spectrally adjacent Γ^- feature that grows in strongly at longer delays; see Ch. 5.

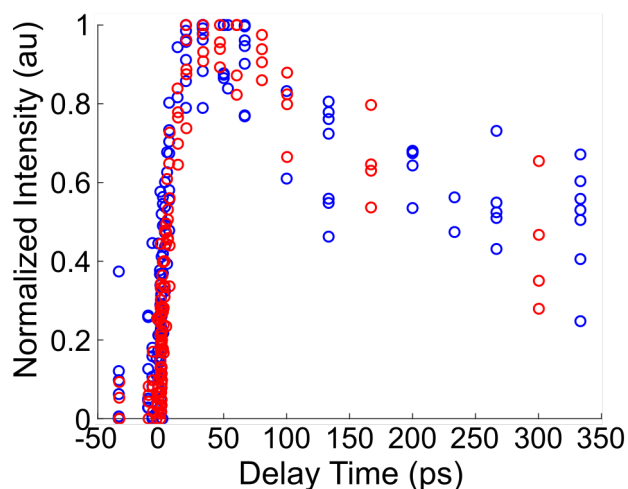


Figure 6.S2: Concatenated normalized integrated intensities for feature A of $\Gamma^- \cdot \text{U} \cdot \text{H}_2\text{O}$ produced at 4.77 eV pump excitation energy and 1.58 eV probe energy (red) and 3.18 eV probe energy (blue). The rise and decay lifetimes for the 1.58 eV probe data are 11.3 ± 2.2 ps and 285 ± 70 ps, respectively. The rise and decay lifetimes for the 3.18 eV probe data are 6.6 ± 2.3 ps and 340 ± 45 ps, respectively.

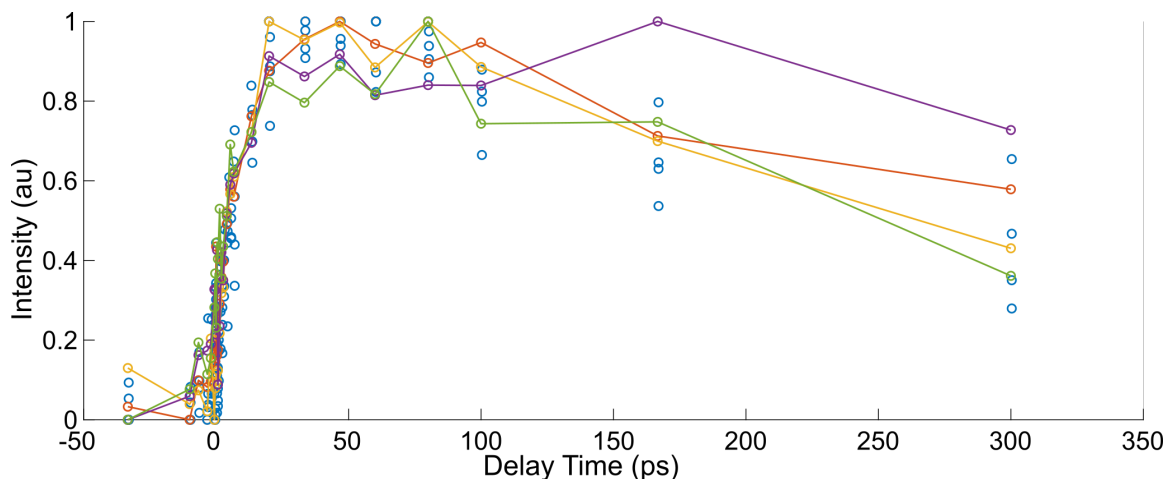


Figure 6.S3: Comparison of $\text{I}^- \cdot \text{U} \cdot \text{H}_2\text{O}$ autodetachment dynamics resulting from 4.77 eV pump and 1.58 eV probe energy for 27 $\mu\text{J}/\text{pulse}$ (green, purple), 50 $\mu\text{J}/\text{pulse}$ (yellow), 80 $\mu\text{J}/\text{pulse}$ (blue), and 105 $\mu\text{J}/\text{pulse}$ (orange).

clusters [32], we observed weak evidence in our TRPE spectra for the slow appearance of features that could potentially arise from two uracil anionic tautomers previously identified with photoelectron spectroscopy by Bowen and co-workers [38]. No such tautomers were observed in near-VDE photoexcitation studies of $\text{I}^- \cdot \text{U}$ [23], which suggested that the presence of water could lower the barrier to tautomerization. In the $\pi - \pi^*$ photoexcitation regime in the current work, we do not observe any additional features or evidence for tautomerization in either $\text{I}^- \cdot \text{U} \cdot \text{H}_2\text{O}$ here or previous $\text{I}^- \cdot \text{U}$ studies [21, 22], which suggests that if the presence of water facilitates tautomerization, it does so only in the TNIs formed in the lower energy photoexcitation regime.

6.9 References

- [1] J. Kohanoff, M. McAllister, G. A. Tribello, and B. Gu, “Interactions between low energy electrons and DNA: a perspective from first-principles simulations”, *J. Phys.: Condens. Matter* **29**, 383001 (2017).
- [2] B. Boudaïffa, P. Cloutier, D. Hunting, M. A. Huels, and L. Sanche, “Resonant formation of DNA strand breaks by low-energy (3 to 20 eV) electrons”, *Science* **287**, 1658–1660 (2000).
- [3] F. Martin, P. D. Burrow, Z. L. Cai, P. Cloutier, D. Hunting, and L. Sanche, “DNA strand breaks induced by 0-4 eV electrons: The role of shape resonances”, *Phys. Rev. Lett.* **93**, 068101 (2004).

- [4] E. Alizadeh and L. Sanche, “Precursors of solvated electrons in radiobiological physics and chemistry”, *Chem. Rev.* **112**, 5578–5602 (2012).
- [5] D. Voet, W. B. Gratzer, R. A. Cox, and P. Doty, “Absorption spectra of nucleotides, polynucleotides, and nucleic acids in the far ultraviolet”, *Biopolymers* **1**, 193–208 (1963).
- [6] T. Gustavsson, Á. Bányász, E. Lazzarotto, D. Markovitsi, G. Scalmani, M. J. Frisch, V. Barone, and R. Improta, “Singlet excited-state behavior of uracil and thymine in aqueous solution: a combined experimental and computational study of 11 uracil derivatives”, *J. Am. Chem. Soc.* **128**, 607–619 (2006).
- [7] Y. He, C. Wu, and W. Kong, “Decay pathways of thymine and methyl-substituted uracil and thymine in the gas phase”, *J. Phys. Chem. A* **107**, 5145–5148 (2003).
- [8] Y. He, C. Wu, and W. Kong, “Photophysics of methyl-substituted uracils and thymines and their water complexes in the gas phase”, *J. Phys. Chem. A* **108**, 943–949 (2004).
- [9] R. Barrios, P. Skurski, and J. Simons, “Mechanism for damage to DNA by low-energy electrons”, *J. Phys. Chem. B* **106**, 7991–7994 (2002).
- [10] G. Hanel, B. Gstir, S. Denifl, P. Scheier, M. Probst, B. Farizon, M. Farizon, E. Illenberger, and T. D. Märk, “Electron attachment to uracil: effective destruction at subexcitation energies”, *Phys. Rev. Lett.* **90**, 188104 (2003).
- [11] J. Berdys, I. Anusiewicz, P. Skurski, and J. Simons, “Damage to model DNA fragments from very low-energy (< 1 eV) electrons”, *J. Am. Chem. Soc.* **126**, 6441–6447 (2004).
- [12] J. Berdys, P. Skurski, and J. Simons, “Damage to model DNA fragments by 0.25–1.0 eV electrons attached to a thymine π^* orbital”, *J. Phys. Chem. B* **108**, 5800–5805 (2004).
- [13] S. Ptasińska, S. Denifl, S. Gohlke, P. Scheier, E. Illenberger, and T. D. Märk, “Decomposition of thymidine by low-energy electrons: Implications for the molecular mechanisms of single-strand breaks in DNA”, *Angew. Chem. Int. Ed.* **45**, 1893–1896 (2006).
- [14] J. Simons, “How do low-energy (0.1–2 eV) electrons cause DNA-strand breaks?”, *Acc. Chem. Res.* **39**, 772–779 (2006).
- [15] H.-Y. Chen, P.-Y. Yang, H.-F. Chen, C.-L. Kao, and L.-W. Liao, “DFT reinvestigation of DNA strand breaks induced by electron attachment”, *J. Phys. Chem. B* **118**, 11137–11144 (2014).
- [16] M. A. Fennimore and S. Matsika, “Electronic resonances of nucleobases using stabilization methods”, *J. Phys. Chem. A* **122**, 4048–4057 (2018).
- [17] J. H. Hendricks, S. A. Lyapustina, H. L. de Clercq, and K. H. Bowen, “The dipole bound-to-covalent anion transformation in uracil”, *J. Chem. Phys.* **108**, 8–11 (1998).
- [18] J. Schiedt, R. Weinkauff, D. M. Neumark, and E. W. Schlag, “Anion spectroscopy of uracil, thymine and the amino-oxo and amino-hydroxy tautomers of cytosine and their water clusters”, *Chem. Phys.* **239**, 511–524 (1998).

- [19] J. Zhao, M. Wang, A. Fu, H. Yang, and Y. Bu, “Hydrated electron transfer to nucleobases in aqueous solutions revealed by ab initio molecular dynamics simulations”, *ChemPhysChem* **16**, 2348–2356 (2015).
- [20] A. Stolow, A. E. Bragg, and D. M. Neumark, “Femtosecond time-resolved photoelectron spectroscopy”, *Chem. Rev.* **104**, 1719–1758 (2004).
- [21] M. A. Yandell, S. B. King, and D. M. Neumark, “Time-resolved radiation chemistry: photoelectron imaging of transient negative ions of nucleobases”, *J. Am. Chem. Soc.* **135**, 2128–2131 (2013).
- [22] S. B. King, M. A. Yandell, and D. M. Neumark, “Time-resolved photoelectron imaging of the iodide-thymine and iodide-uracil binary cluster systems”, *Faraday Discuss.* **163**, 59–72 (2013).
- [23] S. B. King, M. A. Yandell, A. B. Stephansen, and D. M. Neumark, “Time-resolved radiation chemistry: Dynamics of electron attachment to uracil following UV excitation of iodide-uracil complexes”, *J. Chem. Phys.* **141**, 224310 (2014).
- [24] S. B. King, A. B. Stephansen, Y. Yokoi, M. A. Yandell, A. Kunin, T. Takayanagi, and D. M. Neumark, “Electron accommodation dynamics in the DNA base thymine”, *J. Chem. Phys.* **143**, 024312 (2015).
- [25] A. B. Stephansen, S. B. King, Y. Yokoi, Y. Minoshima, W.-L. Li, A. Kunin, T. Takayanagi, and D. M. Neumark, “Dynamics of dipole- and valence bound anions in iodide-adenine binary complexes: A time-resolved photoelectron imaging and quantum mechanical investigation”, *J. Chem. Phys.* **143**, 104308 (2015).
- [26] W.-L. Li, A. Kunin, E. Matthews, N. Yoshikawa, C. E. H. Dessent, and D. M. Neumark, “Photodissociation dynamics of the iodide-uracil (I^-U) complex”, *J. Chem. Phys.* **145**, 044319 (2016).
- [27] A. Kunin and D. M. Neumark, “Time-resolved radiation chemistry: femtosecond photoelectron spectroscopy of electron attachment and photodissociation dynamics in iodide–nucleobase clusters”, *Phys. Chem. Chem. Phys.* **21**, 7239–7255 (2019).
- [28] M. A. Yandell, S. B. King, and D. M. Neumark, “Decay dynamics of nascent acetonitrile and nitromethane dipole-bound anions produced by intracuster charge-transfer”, *J. Chem. Phys.* **140**, 184317 (2014).
- [29] A. Kunin, W.-L. Li, and D. M. Neumark, “Time-resolved photoelectron imaging of iodide-nitromethane ($I^- \cdot CH_3NO_2$) photodissociation dynamics”, *Phys. Chem. Chem. Phys.* **18**, 33226–33232 (2016).
- [30] E. Matthews, R. Cercola, G. Mensa-Bonsu, D. M. Neumark, and C. E. H. Dessent, “Photoexcitation of iodide ion-pyrimidine clusters above the electron detachment threshold: Intracuster electron transfer versus nucleobase-centred excitations”, *J. Chem. Phys.* **148**, 084304 (2018).

- [31] R. Cercola, E. Matthews, and C. E. H. Dessent, “Near-threshold electron transfer in anion-nucleobase clusters: does the identity of the anion matter?”, *Mol. Phys.* **117**, 3001–3010 (2019).
- [32] A. Kunin, W.-L. Li, and D. M. Neumark, “Dynamics of electron attachment and photodissociation in iodide-uracil-water clusters via time-resolved photoelectron imaging”, *J. Chem. Phys.* **149**, 084301 (2018).
- [33] I. Kulakowska, M. Geller, B. Lesyng, and K. L. Wierzchowski, “Dipole moments of 2,4-diketopyrimidines: Part II: Uracil, thymine and their derivatives”, *Biochim. Biophys. Acta, Nucleic Acids Protein Synth.* **361**, 119–130 (1974).
- [34] C. Desfrancois, H. Abdoul-Carime, and J.-P. Schermann, “Ground-state dipole-bound anions”, *Int. J. Mod. Phys. B* **10**, 1339–1395 (1996).
- [35] J. H. Hendricks, S. A. Lyapustina, H. L. de Clercq, J. T. Snodgrass, and K. H. Bowen, “Dipole bound, nucleic acid base anions studied via negative ion photoelectron spectroscopy”, *J. Chem. Phys.* **104**, 7788–7791 (1996).
- [36] S. Carles, F. Lecomte, J. P. Schermann, and C. Desfrancois, “Gas-phase experimental and theoretical studies of adenine, imidazole, pyrrole, and water non-covalent complexes”, *J. Phys. Chem. A* **104**, 10662–10668 (2000).
- [37] M. Hanus, M. Kabelac, J. Rejnek, F. Ryjacek, and P. Hobza, “Correlated ab initio study of nucleic acid bases and their tautomers in the gas phase, in a microhydrated environment, and in aqueous solution. Part 3. Adenine”, *J. Phys. Chem. B* **108**, 2087–2097 (2004).
- [38] R. Bachorz, W. Klopper, M. Gutowski, X. Li, and K. H. Bowen, “Photoelectron spectrum of valence anions of uracil and first-principles calculations of excess electron binding energies”, *J. Chem. Phys.* **129**, 054309 (2008).
- [39] J. Simons, “Propensity rules for vibration-induced electron detachment of anions”, *J. Am. Chem. Soc.* **103**, 3971–3976 (1981).
- [40] P. K. Acharya, R. A. Kendall, and J. Simons, “Vibration-induced electron detachment in molecular anions”, *J. Am. Chem. Soc.* **106**, 3402–3407 (1984).
- [41] F. Mbaiwa, N. Holtgrewe, D. B. Dao, J. Lasinski, and R. Mabbs, “Photoelectron angular distributions as probes of cluster anion structure: $i^- \cdot (H_2O)_2$ and $i^- \cdot (CH_3CN)_2$ ”, *J. Phys. Chem. A* **118**, 7249–7254 (2014).
- [42] B. Baguenard, J. Pinaré, F. Lépine, C. Bordas, and M. Broyer, “Thermionic emission in small carbon cluster anions”, *Chem. Phys. Lett.* **352**, 147–153 (2002).
- [43] C. Desfrancois, H. Abdoul-Carime, and J. P. Schermann, “Electron attachment to isolated nucleic acid bases”, *J. Chem. Phys.* **104**, 7792–7794 (1996).
- [44] O. Dolgounitcheva, V. G. Zakrzewski, and J. V. Ortiz, “Anionic and neutral complexes of uracil and water”, *J. Phys. Chem. A* **103**, 7912–7917 (1999).

- [45] O. Dolgounitcheva, V. G. Zakrzewski, and J. V. Ortiz, “Diffuse-bound and valence-bound anions of cytosine”, *J. Phys. Chem. A* **105**, 8782–8786 (2001).
- [46] R. Bachorz, W. Klopper, and M. Gutowski, “Coupled-cluster and explicitly correlated perturbation-theory calculations of the uracil anion”, *J. Chem. Phys.* **126**, 085101 (2007).
- [47] R. J. Peláez, C. Blondel, C. Delsart, and C. Drag, “Pulsed photodetachment microscopy and the electron affinity of iodine”, *J. Phys. B- At. Mol. Opt.* **42**, 125001 (2009).
- [48] A. Davis, R. Wester, A. E. Bragg, and D. M. Neumark, “Time-resolved photoelectron imaging of the photodissociation of I_2^- ”, *J. Chem. Phys.* **118**, 999–1002 (2003).
- [49] A. E. Bragg, J. R. R. Verlet, A. Kammrath, O. Cheshnovsky, and D. M. Neumark, “Electronic relaxation dynamics of water cluster anions”, *J. Am. Chem. Soc.* **127**, 15283–15295 (2005).
- [50] W. C. Wiley and I. H. McLaren, “Time-of-flight mass spectrometer with improved resolution”, *Rev. Sci. Instrum.* **26**, 1150–1157 (1955).
- [51] A. Eppink and D. H. Parker, “Velocity map imaging of ions and electrons using electrostatic lenses: application in photoelectron and photofragment ion imaging of molecular oxygen”, *Rev. Sci. Instrum.* **68**, 3477–3484 (1997).
- [52] V. Dribinski, A. Ossadtchi, V. Mandelshtam, and H. Reisler, “Reconstruction of Abel-transformable images: the Gaussian basis-set expansion Abel transform method”, *Rev. Sci. Instrum.* **73**, 2634–2642 (2002).
- [53] G. Markovich, R. Giniger, M. Levin, and O. Cheshnovsky, “Photoelectron spectroscopy of iodine anion solvated in water clusters”, *J. Chem. Phys.* **95**, 9416–9419 (1991).
- [54] G. Markovich, S. Pollack, R. Giniger, and O. Cheshnovsky, “Photoelectron spectroscopy of Cl^- , Br^- , and I^- solvated in water clusters”, *J. Chem. Phys.* **101**, 9344–9353 (1994).
- [55] T. Sommerfeld, “Intramolecular electron transfer from dipole-bound to valence orbitals: uracil and 5-chlorouracil”, *J. Phys. Chem. A* **108**, 9150–9154 (2004).
- [56] T. Takayanagi, T. Asakura, and H. Motegi, “Theoretical study on the mechanism of low-energy dissociative electron attachment for uracil”, *J. Phys. Chem. A* **113**, 4795–4801 (2009).
- [57] R. M. Young, M. A. Yandell, and D. M. Neumark, “Dynamics of electron solvation in $I^-(CH_3OH)_n$ clusters ($4 < n < 11$)”, *J. Chem. Phys.* **134**, 124311 (2011).

Chapter 7

Electron Attachment and Photodissociation Dynamics in Iodide-Nucleobase Clusters

And it certainly did seem a little provoking ('almost as if it happened on purpose,' she thought) that, though she managed to pick plenty of beautiful rushes as the boat glided by, there was always a more lovely one that she couldn't reach.

Lewis Carroll

The content and figures of this chapter are adapted from:

A. Kunin and D. M. Neumark, "Time-Resolved Radiation Chemistry: Femtosecond Photoelectron Spectroscopy of Electron Attachment and Photodissociation Dynamics in Iodide-Nucleobase Clusters" *Phys. Chem. Chem. Phys.* **21**, 7239 (2019)

with permission from the PCCP Owner Societies.

7.1 Abstract

Iodide-nucleobase ($I^- \cdot N$) clusters studied by time-resolved photoelectron spectroscopy (TRPES) are an opportune model system for examining radiative damage of DNA induced by low-energy electrons. By initiating charge transfer from iodide to the nucleobase and following the dynamics of the resulting transient negative ions (TNIs) with femtosecond time resolution, TRPES provides a novel window into the chemistry triggered by the attachment of low-energy electrons to nucleobases. In this Perspective, we examine and compare the dynamics of electron attachment, autodetachment, and photodissociation in a variety of $I^- \cdot N$ clusters, including iodide-uracil ($I^- \cdot U$), iodide-thymine ($I^- \cdot T$), iodide-uracil-water ($I^- \cdot U \cdot H_2O$), and iodide-adenine ($I^- \cdot A$), to develop a more unified representation of our understanding of nucleobase TNIs. The experiments probe whether dipole-bound or valence-bound TNIs are formed initially and the subsequent time evolution of these species. We also provide an outlook for forthcoming applications of TRPES to larger iodide-containing complexes to enable the further investigation of microhydration dynamics in nucleobases, as well as electron attachment and photodissociation in more complex nucleic acid constituents.

7.2 Introduction

DNA damage induced by low-energy electron attachment [1] has been a topic of considerable interest in recent years. Electron attachment to nucleobases and the subsequent formation of transient negative ions (TNIs) of the base has been implicated as the initial step in the damage mechanism [2–4]. It is predicted that single and double strand breaks then occur as a result of electron transfer from the base moiety to the sugar-phosphate backbone facilitated by strong electronic coupling [2, 3, 5, 6]. These considerations have motivated many experimental and theoretical studies of the interactions between nucleic acid constituents and low-energy electrons [7].

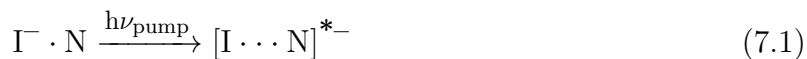
Nucleobases are capable of forming both a dipole-bound (DB) anion [8] in which the excess electron is trapped by the relatively large dipole moment of the base, or a conventional valence-bound (VB) anion [3, 9] by electron attachment to the π^* orbital of the base. Electron scattering experiments have suggested that the DB state is initially formed and may then convert or act as a “doorway” to the formation of a VB anion [10]. These metastable TNIs are then expected to decay, possibly leading to dissociation or fragmentation of the nucleobases, the larger nucleotide, or the DNA backbone structure [11, 12]. Many groups have studied the properties of these nucleobase DB and VB anions experimentally with a variety of techniques, including dissociative electron attachment [10, 13–15] and anion photoelectron spectroscopy [9, 16, 17]. Numerous theoretical studies of these anions have been carried out as well [18–22]. Of interest, however, is not only the electron binding properties and anionic dissociation channels but also the ultrafast time-resolved dynamics and evolution of these TNIs, including interconversion of a DB anion to form a VB anion,

as well as the timescales for autodetachment, internal conversion, and fragmentation.

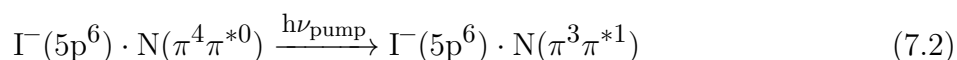
Our group has explored the time-resolved dynamics of electron attachment and transient decay in the nucleobase species uracil [23–26], thymine [27], and adenine [28], as well as the uracil-water moiety [29], using time-resolved photoelectron spectroscopy (TRPES) of iodide-nucleobase ($\text{I}^- \cdot \text{N}$) clusters. We have measured and modelled the process of low-energy electron attachment to the nucleobase and observed the formation, evolution, and decay of both DB and VB anions for these $\text{I}^- \cdot \text{N}$ clusters. In this Perspective, we provide an overview of these results for iodide-uracil ($\text{I}^- \cdot \text{U}$), iodide-thymine ($\text{I}^- \cdot \text{T}$), iodide-adenine ($\text{I}^- \cdot \text{A}$), and iodide-uracil-water ($\text{I}^- \cdot \text{U} \cdot \text{H}_2\text{O}$) clusters, and revisit the analyses of these studies based on the new insights provided by continued work on these clusters over the last five years. We also provide a framework for the continuation of these studies and the application of this TRPES scheme to more complex iodide-containing biomolecule clusters.

Anion photoelectron spectroscopy is an effective tool to probe DB and VB states since these anions are readily distinguished from one another by electron binding energy (eBE) as well as the shape of the photoelectron spectrum [16, 30]. DB anions are formed when an excess electron is bound by the dipole moment of a molecule, creating a weakly bound anion (typically <100 meV eBE) with the excess electron residing in a large, diffuse orbital outside of the molecular framework [8]. A molecular dipole moment of at least $\sim 2 - 2.5$ D is needed to bind the excess electron [31]; all of the canonical nucleobase species examined here have larger dipole moments than this and are thus capable of forming DB anions [32–34]. The neutral core of a DB state undergoes little or no geometry change upon photodetachment [35], yielding a narrow peak in the anion photoelectron spectrum as there is negligible Franck-Condon activity. VB nucleobase anions, on the other hand, are conventional anions in which the excess electron resides in a valence orbital. For these species, the vertical detachment energy (VDE), corresponding to the difference in energy between the anion and the neutral at the equilibrium geometry of the anion, is typically hundreds of meV [9, 17, 36–39]. Moreover, the geometry of VB nucleobase anions is typically distorted relative to the neutral nucleobase in the ring puckering coordinate [18, 19, 27, 28, 40], yielding a broad photoelectron spectrum [41]. Photoelectron spectra from Bowen and co-workers [41] (Fig. 7.1) for the U^- DB anion and the $\text{U}^- \cdot \text{H}_2\text{O}$ VB anion exemplify the binding energy and spectral shape of these two types of negative ions.

This Perspective focuses on the application of TRPES to various $\text{I}^- \cdot \text{N}$ clusters in order to probe the dynamics of electron attachment to nucleobases and the subsequent decay channels. The $\text{I}^- \cdot \text{N}$ complexes have two regimes of UV photoabsorption [42]: the first is near-VDE photoexcitation corresponding to direct optical excitation by an ultraviolet (UV) pump pulse of energy $h\nu_{\text{pump}}$ to initiate charge transfer from the iodide to the nucleobase moiety, labelled N in Eq. 7.1 below, creating a TNI.



Excitations of this nature are clearly interesting as a model for reductive DNA damage by low-energy secondary electron attachment. The second regime of UV photoabsorption, measured to be near 4.8 eV [42], is calculated [26, 42] to encompass a strong base-centered $\pi - \pi^*$ excitation on the nucleobase with the excess electron still remaining with iodide, i.e.:



As discussed in more detail in Section 7.4.2, we believe this $\pi - \pi^*$ excitation is followed by rapid charge transfer from the iodide moiety to fill the hole in the π orbital of the base to create a VB anion. These higher energy excitations are also of interest in the DNA damage mechanism as the rapid, nonradiative photodeactivation pathways of $\pi - \pi^*$ UV photoexcited nucleobases are the core of the remarkable photostability of DNA [43–45]. Other optical transitions in $\Gamma^- \cdot N$ clusters may also contribute to photoabsorption in this region; we explore the dynamics in this high energy photoexcitation regime for $\Gamma^- \cdot U$ and $\Gamma^- \cdot T$ clusters in detail in Section 7.4.2.

The time evolution of the TNI is traced by the probe pulse, which can photodetach the TNI or its photodissociation products at varying time delays. There are numerous energetically accessible decay pathways for the photoexcited $\Gamma^- \cdot N$ clusters, including autodetachment,

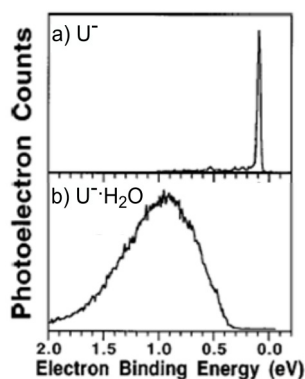
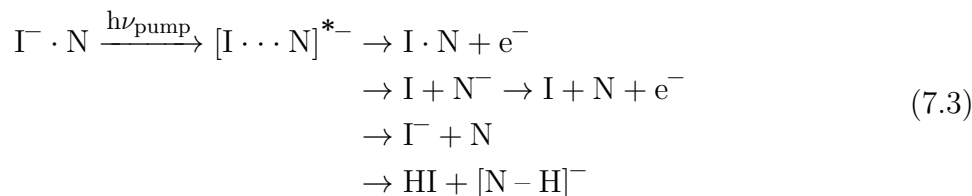


Figure 7.1: Photoelectron spectra of a) the uracil DB anion and b) the $U^- \cdot H_2O$ VB anion. The U^- DB anion exhibits a spectrum with a very narrow peak at very low binding energy, characteristic of DB anions, while the $U^- \cdot H_2O$ VB anion exhibits a broad feature covering higher eBEs. Adapted from Hendricks et al., *J. Chem. Phys.* 108, 1 (1998), with the permission of AIP Publishing.

iodine loss, Γ^- formation, or a chemical reaction to form HI and a deprotonated nucleobase anion $[\text{N-H}]^-$, all of which are listed in Eq. 7.3.



While the 1.58 eV fundamental of Ti:Sapphire ultrafast lasers is sufficiently energetic as a probe to photodetach the nascent TNIs, higher energy UV probe pulses are required to photodetach many of the possible photofragments these complexes can form, including iodide (eBE = 3.059 eV) [46] and deprotonated nucleobase anions [47–49].

In this Perspective, we begin in Section 7.3 with a discussion of the methodologies, both experimental and theoretical, used to understand the dynamics of these $\Gamma^- \cdot \text{N}$ systems. In Section 7.4.1, we examine TRPES studies of the simpler, model system of photoexcited iodide-nitromethane ($\Gamma^- \cdot \text{CH}_3\text{NO}_2$) clusters that provide an illustrative framework for understanding the more complex dynamics of the larger nucleobase species. In Section 7.4.2, we delve into the dynamics of electron attachment and photodissociation in $\Gamma^- \cdot \text{U}$ and $\Gamma^- \cdot \text{T}$ clusters, which have been studied in more detail by TRPES as well as laser photodissociation spectroscopy. In particular, we cover results for $\Gamma^- \cdot \text{U}$ and $\Gamma^- \cdot \text{T}$ clusters following photoexcitation near the cluster VDE as well as photoexcitation in the higher energy regime near the base-centered $\pi-\pi^*$ transition. In Section 7.4.3, we present recent results for electron attachment and photodissociation in photoexcited microhydrated $\Gamma^- \cdot \text{U} \cdot \text{H}_2\text{O}$ clusters, and finally, in Section 7.4.4 we discuss TRPES studies of photoexcited $\Gamma^- \cdot \text{A}$ clusters, which bear some similarities to $\Gamma^- \cdot \text{CH}_3\text{NO}_2$ but pose additional challenges in analysis due to the propensity for tautomerization in gas phase adenine. We conclude with a summary of these systems and the salient information learned thus far as it relates to reductive damage of nucleic acid constituents and iodide-associated clusters in general. We also provide an outlook for the future avenues of this research and the application of TRPES of iodide-containing clusters to advance our understanding of reductive damage pathways in DNA.

7.3 Methodologies

A. Time-resolved photoelectron spectroscopy (TRPES)

A number of reviews dedicated to TRPES are available [50–62], so we only briefly describe the key principles here as they relate to the study of TNIs. Single-photon anion photoelectron spectroscopy (PES), as shown schematically in Fig. 7.2a, involves the preparation of stable

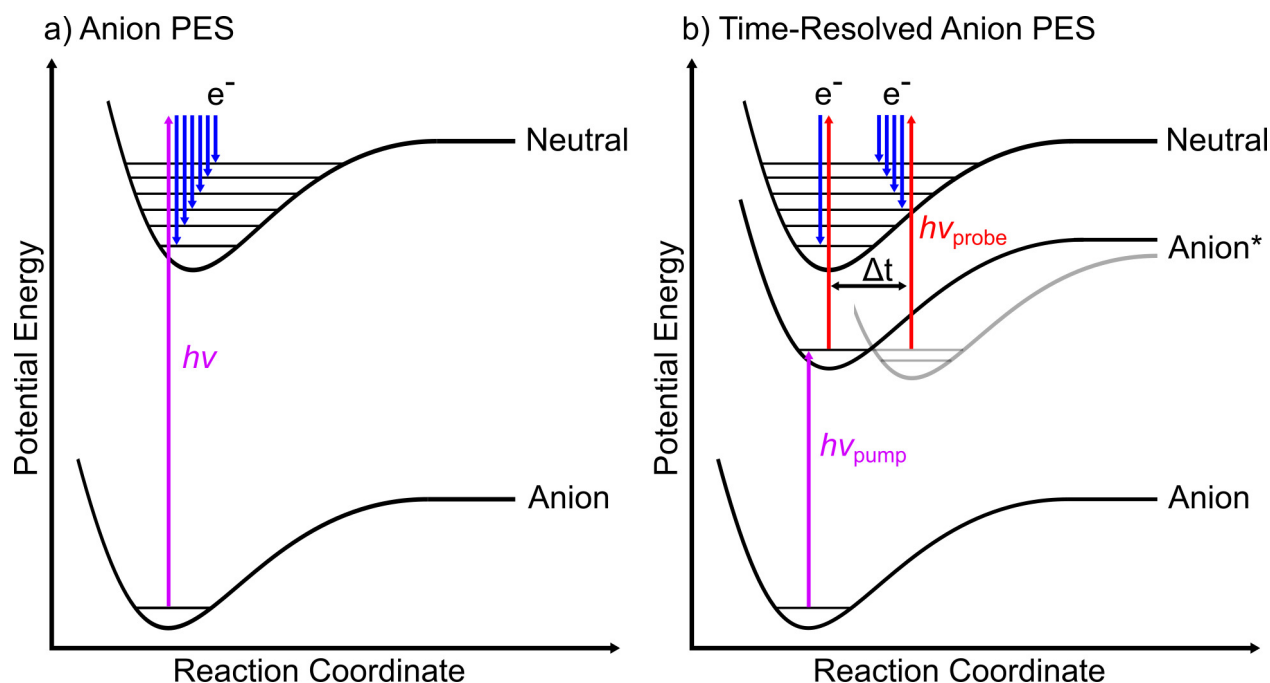


Figure 7.2: Example scheme for a) anion photoelectron spectroscopy and b) time-resolved photoelectron spectroscopy. Anion* is used to indicate the photoexcited state. The blue lines indicate the resultant kinetic energies of the photodetached electrons.

anions that can then be photodetached by an intersecting laser beam if the photon energy ($h\nu$) exceeds the electron binding energy (eBE). The kinetic energy (eKE) distribution of the outgoing photodetached electrons is then measured, and the principle of energy conservation, as shown in Eq. 7.4, may then be used to determine accurate eBEs:

$$\text{eBE} = h\nu - \text{eKE} \quad (7.4)$$

Provided there is sufficient Franck-Condon overlap between the anion and neutral vibrational wavefunctions, photodetachment can occur to any neutral vibrational (and electronic) states within the photon energy range. In spectra that do not show any vibrational structure, the vertical detachment energy (VDE), or the difference in energy between the anion and the neutral at the equilibrium geometry of the anion, is identifiable as the peak or maximum intensity (maximum Franck-Condon overlap) of the photoelectron spectrum, and the width of the spectrum is an indication of the geometry change that occurs upon photodetachment.

In the implementation of femtosecond (fs) anion TRPES used here, Fig. 7.2b, a fs pump pulse photoexcites a ground state $\Gamma^- \cdot N$ anion to prepare an excited TNI, as in Eq. 7.1. A

fs probe pulse then photodetaches the TNI to monitor, as a function of pump-probe delay, the ultrafast time evolution of the transient species. As described in the Introduction, a sufficiently energetic probe pulse can interrogate not only TNIs, but also any dissociation products that may form due to fragmentation of the evolving TNI. Thus, this technique effectively probes the ultrafast chemical dynamics of a TNI from formation through decay.

The experimental apparatus used for the TRPES studies herein, shown in Fig. 7.3, has been described in detail previously [63, 64], and is briefly described here. $I^- \cdot N$ clusters are generated by flowing 375 – 450 kPa of neon or argon buffer gas or 550 kPa of helium buffer gas over a reservoir of methyl iodide. This gas mixture is then passed into a pulsed Even-Lavie valve operating at 500 Hz that contains a cartridge with a solid sample of the nucleobase of interest heated to 205 – 220 °C. For the $I^- \cdot CH_3NO_2$ studies, the cartridge is left empty; an additional reservoir on the gas line is filled with liquid CH_3NO_2 and chilled in an ice water bath. For the $I^- \cdot U \cdot H_2O$ studies, this reservoir is filled with deionized liquid water and heated, along with the connecting gas lines, to approximately 40 °C. In each configuration, the gas mixture is then supersonically expanded into vacuum through a ring filament ionizer to produce cluster anions. The anions are perpendicularly extracted into a Wiley McLaren time-of-flight mass spectrometer [65] and mass-selected to isolate the $I^- \cdot N$ species of interest. These ions are photodetached through their interaction with one or two femtosecond laser pulses. The resultant photoelectrons are analyzed by velocity map imaging [66] on a chevron-stacked position-sensitive microchannel plate detector coupled to a phosphor screen and imaged using a charge-coupled device camera. Basis-set expansion (BASEX) reconstruction techniques [67] are used to reconstruct the 3D eKE distributions.

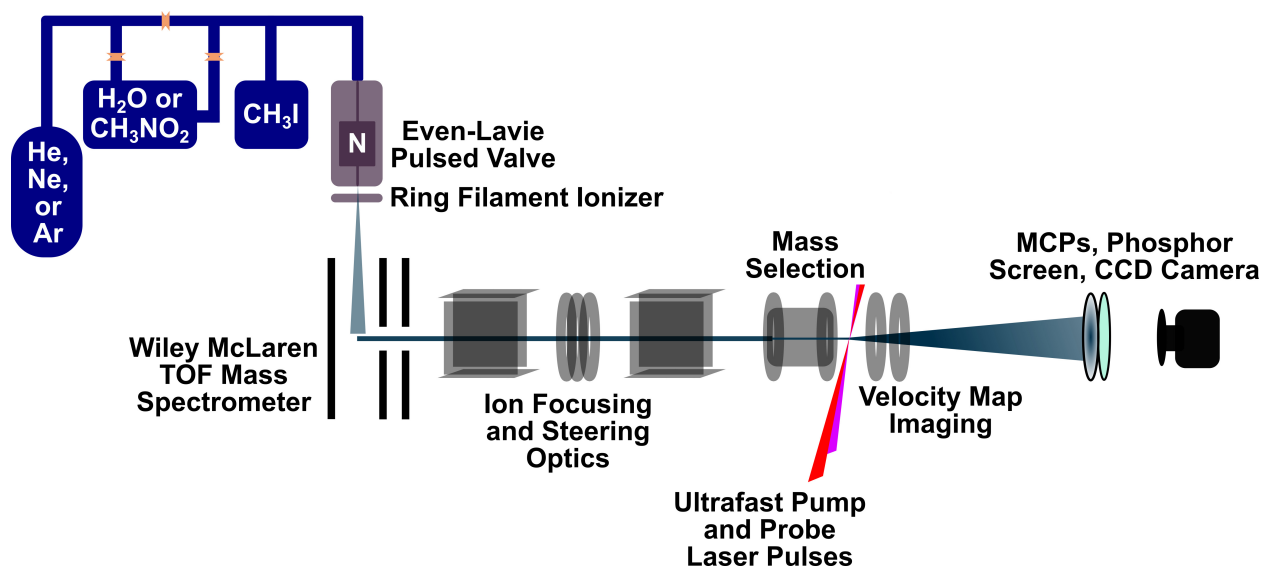


Figure 7.3: Diagram of the TRPES apparatus employed in this work.

Various pump-probe schemes are employed among the studies in this work to excite and photodetach the $\text{I}^- \cdot \text{N}$ clusters. A KMLabs Griffin oscillator and Dragon amplifier are used to generate 1.8 – 1.9 mJ/pulse laser pulses approximately 40 – 45 fs wide centered near 790 nm (1.57 eV) at a repetition rate of 1 kHz. Depending on the desired pump-probe scheme, these pulses are split into a pump arm and a probe arm delayed by a delay stage. In the pump arm, UV light is usually generated by frequency-doubling the output of a LightCon TOPAS-C optical parametric amplifier with a β -barium borate (BBO) crystal. This scheme yields pump pulses between 235 nm – 350 nm of approximately 8 – 13 $\mu\text{J}/\text{pulse}$. The fundamental infrared (IR) of the KMLabs system can be used as the probe beam (1.57 eV, 80 $\mu\text{J}/\text{pulse}$), or the fundamental can be frequency-doubled in a BBO crystal to yield 395 nm pulses (3.14 eV, 65 $\mu\text{J}/\text{pulse}$). Other schemes include recovering the residual fundamental from the TOPAS-C to use as the probe, or recovering residual visible non-frequency-doubled TOPAS-C output to recombine nonlinearly in a BBO crystal with the fundamental pulse to yield UV probe pulses in the range of 340 – 360 nm (~ 10 $\mu\text{J}/\text{pulse}$). We refer the reader to the individual $\text{I}^- \cdot \text{N}$ papers referenced herein for the specific laser scheme details for each study. The cross-correlation measured at the vacuum chamber for the pump and probe laser pulses is typically ~ 150 – 185 fs for UV/IR-type pump/probe schemes and ~ 200 – 220 fs for UV/UV-type pump/probe schemes.

B. Computational Methods

We comment briefly on the various computational methods used to characterize both the ground states and the excited states of $\text{I}^- \cdot \text{N}$ anionic clusters, as these calculations can greatly inform the analysis and interpretation of the measured experimental results. The detailed work described herein was performed using the Gaussian 03 or Gaussian 09 computing packages [68, 69]. The results of these theoretical methods applied to specific $\text{I}^- \cdot \text{N}$ clusters are described further in the corresponding sections that follow.

Theoretical work on the interaction of iodide with a uracil molecule was first performed by Ortiz and co-workers [70], who employed second-order Møller-Plesset theory (MP2) with augmented, correlation-consistent triple- ζ (aug-cc-pVTZ) bases [71] and an augmented Stuttgart pseudopotential (-pp) [72] to calculate the VDE of the $\text{I}^- \cdot \text{U}$ cluster. These calculations found the $\text{I}^- \cdot \text{U}$ cluster VDE to be approximately 4.16 eV, and the cluster structure to be planar with the charge localized on the iodine atom. Since then, Takayanagi and co-workers have employed various density functional theory (DFT) functionals and diffuse basis sets as well as long-range corrected (LC)-DFT to examine several species of interest including anionic uracil, uracil-water, thymine, and adenine, as well as $\text{I}^- \cdot \text{U}$, and $\text{I}^- \cdot \text{T}$ [19–21, 27, 28]. Their calculations have focused on the use of these methods to determine the structure and energetics of these species, the DB to VB anion conversion barrier height and transition state geometry, and simulations of photoelectron spectra.

Our group has carried out calculations at the MP2/aug-cc-pVDZ(-pp) level of theory as

well as the coupled cluster singles and doubles (CCSD)/aug-cc-pVDZ(-pp) level of theory to calculate anion ground state structures and VDEs for each of the $\text{I}^- \cdot \text{N}$ cluster systems examined here to inform our experimental measurements [23, 25–29, 73]. Table 7.1 presents the structure for each ground state anion, as well as the dipole moment of the neutral I·N species at the equilibrium geometry of the anion. In all cases, the I^- binds primarily to the most acidic H atom on the nucleobase. The VDEs of the $\text{I}^- \cdot \text{N}$ species reported in Table 7.1 are those experimentally measured by single-photon PES.

Takayanagi et al. [27] have performed excited state calculations at the time-dependent (TD)-DFT/ ω B97XD/aug-cc-pVDZ(-pp) level of theory for $\text{I}^- \cdot \text{U}$ and $\text{I}^- \cdot \text{T}$, and Dessent et al. [42] at the TD-DFT/B3LYP/6-311++G(2d,2p) and 6-311G(d,p)(-pp) level of theory [74–79] for $\text{I}^- \cdot \text{U}$, $\text{I}^- \cdot \text{T}$, and iodide-cytosine ($\text{I}^- \cdot \text{C}$). These excited state calculations are valuable for the analysis of the $\text{I}^- \cdot \text{N}$ cluster absorption profiles as they elucidate the energetics and character of the various possible transition channels. Our group [26, 29] has performed equation-of-motion (EOM)-CCSD calculations based on $\text{I}^- \cdot \text{U}$ and $\text{I}^- \cdot \text{U} \cdot \text{H}_2\text{O}$ structures optimized at the MP2/aug-cc-pVDZ(-pp) level of theory. Although computationally expensive, these wavefunction-based calculations have proved effective at identifying the DB state for both of these species and are expected to provide among the best possible theoretical results for the nature of the initially formed photoexcited charge transfer states in our TRPES experiments.

One of the decay mechanisms for photoexcited $\text{I}^- \cdot \text{N}$ clusters is internal conversion followed by fragmentation to $\text{I}^- + \text{N}$. To analyze this photodissociation mechanism further, our group has also performed Rice-Ramsperger-Kassel-Marcus (RRKM) calculations to estimate the rate of statistical unimolecular dissociation for these photoexcited species to yield I^- [26, 80]. Variational transition state theory was used to determine the transition state along the barrierless iodide-molecule stretching coordinate potential energy curve. The zero-point energy corrected energy difference between the ground and transition state was then used to calculate the microcanonical reaction rate constant using the Beyer-Swinehart algorithm [81] to calculate the reactant density of states and transition state sum of states. The Stein-Rabinovitch modification [82] was used to treat low-energy iodide-molecule $\text{I}^- \cdot \cdot \cdot \text{N}$ in-plane and out-of-plane modes as hindered internal rotors.

7.4 Electron Attachment and Photodissociation Dynamics in $\text{I}^- \cdot \text{N}$ Clusters

In order to emphasize trends across the range of systems studied here, one-photon and TRPE spectra for each $\text{I}^- \cdot \text{N}$ species are shown in Figs. 7.4 – 7.7. Figs. 7.4a) – e) show one-photon photoelectron spectra for $\text{I}^- \cdot \text{CH}_3\text{NO}_2$, $\text{I}^- \cdot \text{U}$, $\text{I}^- \cdot \text{T}$, $\text{I}^- \cdot \text{U} \cdot \text{H}_2\text{O}$, and $\text{I}^- \cdot \text{A}$, respectively. Figs. 7.5a) – e) show near-VDE photoexcited TRPE spectra for the same five systems along

Table 7.1: A summary of calculated anion ground state structures and neutral dipole moments for the $\Gamma^- \cdot N$ cluster systems examined in this work. The neutral dipole moment (μ) is reported at the geometry of the ground state anion. Reported VDEs are experimentally measured by anion PES, all ± 0.05 eV error. See cited references for specific computational details.

Cluster	$\Gamma^- \cdot \text{CH}_3\text{NO}_2$	$\Gamma^- \cdot \text{A9}$	$\Gamma^- \cdot \text{A3}$
VDE (eV)	3.60 eV	3.96 eV	4.11 eV
Neutral μ (D)	4.62 D	4.0 D [28]	5.6 D [28]
Cluster	$\Gamma^- \cdot \text{T}$	$\Gamma^- \cdot \text{U}$	$\Gamma^- \cdot \text{U} \cdot \text{H}_2\text{O}$
VDE (eV)	4.05 eV	4.11 eV	4.40 eV
Neutral μ (D)	6.23 D [27]	6.48 D [27]	6.93 D [29]

with the time-evolution of TNI production and decay at both early and long delay times. Figs. 7.6a) – d) show the time-evolution of I^- production via photodissociation for select systems and excitation energies, and Figs. 7.7a) and b) show the TRPE spectra and time-dependent signal evolution for $\text{I}^- \cdot \text{U}$ and $\text{I}^- \cdot \text{T}$ photoexcited at excitation energies near ~ 4.7 eV. These results are considered in more detail in the subsections below. For consistency and ease of comparison throughout this work, we refer to the TRPES pump energies employed here relative to the cluster VDE by $h\nu_{\text{pump}} - \text{VDE}$.

A. $\text{I}^- \cdot \text{CH}_3\text{NO}_2$

We begin by first considering the photoexcited $\text{I}^- \cdot \text{CH}_3\text{NO}_2$ binary complex, which serves as an interesting model system for conversion between DB and VB anions. Nitromethane (CH_3NO_2) has a sufficiently large dipole moment, 3.46 D, to bind an electron in a DB state and also supports a conventional valence bound anion, which lies lower in energy and is the ground state of the anion [30, 83, 84]. Both DB and VB anions of CH_3NO_2^- have been measured by photoelectron spectroscopy; the DB anion has a VDE of 8 ± 8 meV, and the VDE of the VB anion is 0.9 – 1 eV [30, 85].

$\text{I}^- \cdot \text{CH}_3\text{NO}_2$ binary complexes have been studied with photofragment action spectroscopy by Dessent and Johnson [83]. This work has identified the $\text{I}^- \cdot \text{CH}_3\text{NO}_2$ cluster VDE as 3.60 ± 0.01 eV and detected evidence for the presence of the $\text{I}^- \cdot \text{CH}_3\text{NO}_2$ DB anion. Our group has performed two sets of TRPES studies of $\text{I}^- \cdot \text{CH}_3\text{NO}_2$ clusters photoexcited near the cluster VDE with two aims: 1.56 eV probe experiments to test for the presence of DB and VB anions of nitromethane [73], and 3.14 eV probe experiments to measure the time-resolved formation of I^- and other photofragments [80].

The single-photon photoelectron spectrum of $\text{I}^- \cdot \text{CH}_3\text{NO}_2$ is shown in Fig. 7.4a. Feature A, the lowest energy and most intense feature, and the location of its maximum, 3.60 eV, should be the cluster VDE; this value matches previous experimental results for $\text{I}^- \cdot \text{CH}_3\text{NO}_2$ [83]. Feature A corresponds to detachment to the lower spin orbit state of the complex $\text{I}(^2\text{P}_{3/2}) \cdot \text{CH}_3\text{NO}_2$, while feature B, appearing near 4.5 eV, corresponds to photodetachment to the upper spin orbit state of the complex $\text{I}(^2\text{P}_{1/2}) \cdot \text{CH}_3\text{NO}_2$, lying approximately 0.94 eV higher in energy [86].

In the first set of time-resolved experiments, $\text{I}^- \cdot \text{CH}_3\text{NO}_2$ clusters are photoexcited at the VDE and probed at 1.56 eV [73]. Fig. 7.5a shows the TRPE spectra for $\text{I}^- \cdot \text{CH}_3\text{NO}_2$ photoexcited at 3.60 eV. The left panel shows a false-color two-dimensional plot of eBE versus pump-probe delay. There is a narrow, short lived feature (A) with a low eBE that is assigned to a DB state, and a broader, longer lived feature (B) assigned to a VB state. The center and right panels of Fig. 7.5a show integrated intensities of feature A (blue) and feature B (red) at short and longer time delays, respectively. A similar layout is used for the

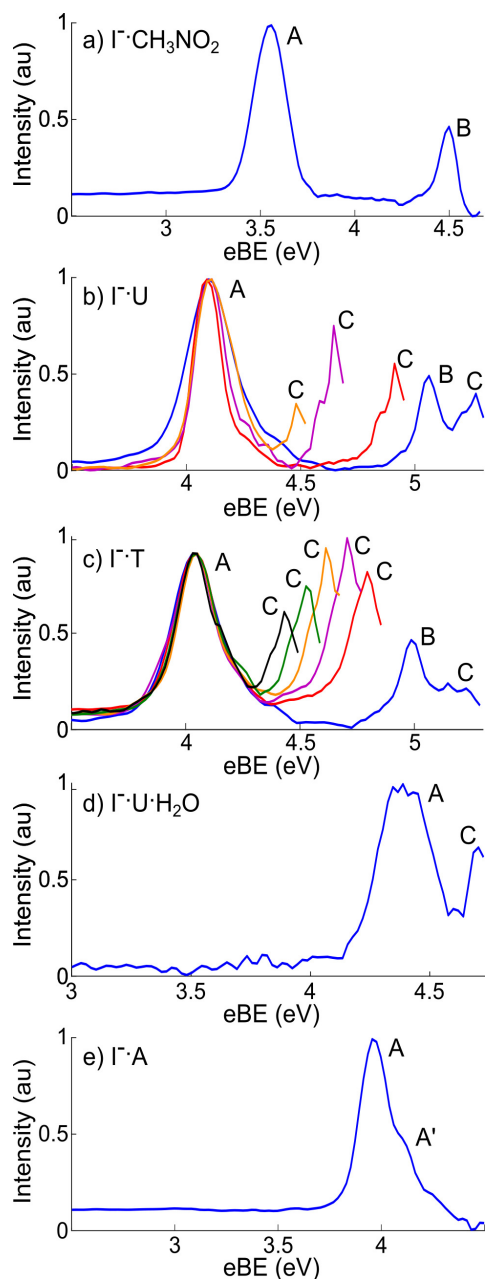


Figure 7.4: Single photon photoelectron spectra for a) $\text{I}^- \cdot \text{CH}_3\text{NO}_2$ with 4.68 eV; b) $\text{I}^- \cdot \text{U}$ with 5.30 eV in blue, 4.92 eV in red, 4.68 eV in purple, and 4.51 eV in orange; c) $\text{I}^- \cdot \text{T}$ with 5.30 eV in blue, 4.87 eV in red, 4.78 eV in purple, 4.68 eV in orange, 4.59 eV in green, and 4.51 eV in black; d) $\text{I}^- \cdot \text{U} \cdot \text{H}_2\text{O}$ with 4.74 eV; and e) $\text{I}^- \cdot \text{A}$ with 4.52 eV. “A” denotes vertical detachment to the lower spin orbit state of the iodine-containing complex ($\text{I}(^2\text{P}_{3/2}) \cdot \text{N}$) (with A’ shoulder for the detachment of two tautomers of adenine), “B” denotes detachment to the upper spin orbit state ($\text{I}(^2\text{P}_{1/2}) \cdot \text{N}$), and “C” denotes autodetachment.

other rows of Fig. 7.5.

The nascent $[\text{I} \cdots \text{CH}_3\text{NO}_2]^-$ DB anion appears within the cross-correlation of the pump and probe laser pulses, <150 fs. The DB anion decays mono-exponentially in 460 ± 60 fs, while the $[\text{I} \cdots \text{CH}_3\text{NO}_2]^-$ VB anion appears in 420 ± 50 fs. This close match-up in lifetimes indicates that the DB anion decays primarily to form the VB anion in a rapid and complete or nearly-complete conversion. The VB state was measured to decay bi-exponentially with time constants of 2 ps and 1300 ps.

Photoelectron signal corresponding to autodetachment was also measured as near ~ 0 eV eKE signal from photoexcited $\text{I}^- \cdot \text{CH}_3\text{NO}_2$ clusters [73]. Autodetachment refers to the spontaneous ejection of an electron following photoexcitation of an anion resonance. If a nascent metastable photoexcited anion lies isoenergetically within a manifold of vibrational levels of the corresponding neutral plus a free electron, then nonadiabatic coupling between the electronic and nuclear degrees of freedom can facilitate the detachment of an electron [35, 87, 88]. In the specific case in which the internal energy of the excited anion (or cluster) is randomized prior to electron ejection, the detached electron typically carries ~ 0 eV electron kinetic energy (eKE) and this statistical process is referred to as thermionic emission [89, 90]. Since the DB state appears to decay solely to the VB anion, it is reasonable to attribute at least one of the bi-exponential decay constants of the VB anion to autodetachment.

To further characterize the decay dynamics of the $[\text{I} \cdots \text{CH}_3\text{NO}_2]^-$ VB anion, a second experiment with 3.56 eV pump energy (-40 meV) and 3.14 eV probe energy was performed [80]. This pump-probe scheme enables detection of photodissociation channels that yield I^- (eBE = 3.059 eV) [46] or the nitromethide anion CH_2NO_2^- (VDE = 2.635 ± 0.010 eV) [80, 91], both of which can be photodetached with the higher energy 3.14 eV probe pulse. I^- was measured as the major photofragmentation channel with a mono-exponential rise time of 21 ± 1 ps, shown in Fig. 7.6a. This finding suggests that the shorter time constant for VB anion decay (2 ps) corresponds to back-electron transfer to re-form $\text{I}^- \cdot \text{CH}_3\text{NO}_2$, followed by internal conversion (IC) to the $\text{I}^- \cdot \text{CH}_3\text{NO}_2$ anion ground state and, finally, dissociation to yield I^- .

Given the relatively long I^- rise time compared to the approximately 2 ps short decay time of the $[\text{I} \cdots \text{CH}_3\text{NO}_2]^-$ VB anion, RRKM calculations were performed to analyze the statistical dissociation of $\text{I}^- \cdot \text{CH}_3\text{NO}_2$ complexes to yield I^- [80]. These RRKM calculations yielded dissociation rates of approximately 300 – 400 fs, depending on the treatment of internal rotations in the $\text{I}^- \cdot \text{CH}_3\text{NO}_2$ complex. This calculated lifetime is quite fast and is unlikely to be a realistic physical timescale for intramolecular vibrational energy redistribution (IVR) and subsequent dissociation in a cluster, and indicates that there exists some dynamical bottleneck in the formation of I^- from $\text{I}^- \cdot \text{CH}_3\text{NO}_2$.

The $[\text{I} \cdots \text{CH}_3\text{NO}_2]^-$ DB anion is expected to geometrically resemble the neutral iodine-

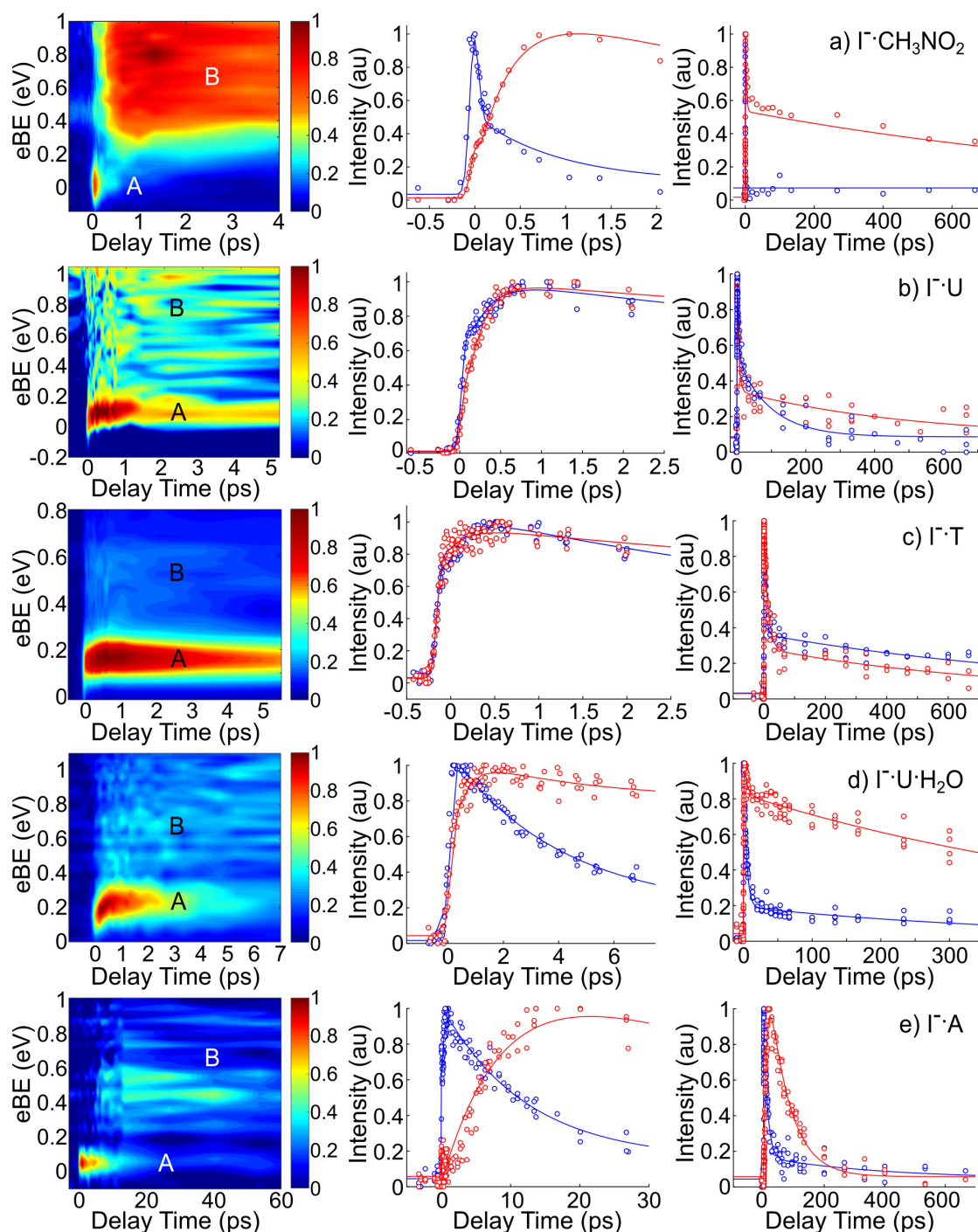
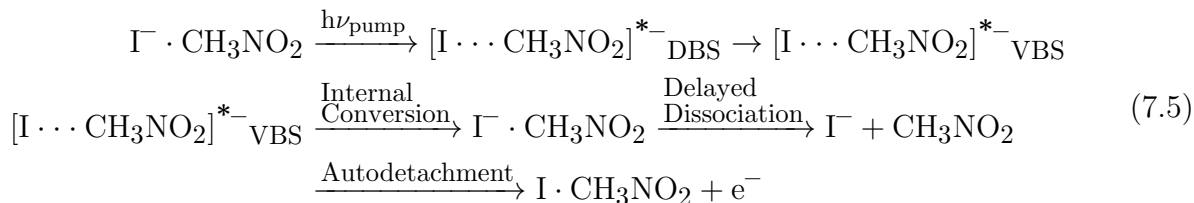


Figure 7.5: TRPE spectra and DB anion (feature A, blue) and VB anion (feature B, red) integrated intensities at both early times and long delay times for a) $\text{I}^- \cdot \text{CH}_3\text{NO}_2$ photoexcited at +0 meV; b) $\text{I}^- \cdot \text{U}$ photoexcited at +30 meV; c) $\text{I}^- \cdot \text{T}$ photoexcited at +20 meV; d) $\text{I}^- \cdot \text{U} \cdot \text{H}_2\text{O}$ photoexcited at -20 meV; and e) $\text{I}^- \cdot \text{A}$ photoexcited at -60 meV.

nitromethane species as the electron resides largely outside the molecular framework, while the $[\text{I} \cdots \text{CH}_3\text{NO}_2]^-$ VB anion is expected to more closely resemble the puckered CH_3NO_2^- geometry in which the $-\text{NO}_2$ is out of the plane of the molecule [73, 85]. During the DB to VB anion transition, it can therefore be expected that the $-\text{NO}_2$ vibrational modes become vibrationally excited as the VB anion is formed. We therefore suggest that a dynamical bottleneck arises in $\text{I}^- \cdot \text{CH}_3\text{NO}_2$ from inefficient energy flow from these high frequency $-\text{NO}_2$ vibrational modes to the relatively low frequency ($<100 \text{ cm}^{-1}$) $\text{I} \cdots \text{CH}_3\text{NO}_2$ modes that will ultimately yield I^- dissociation. Hase and co-workers [92, 93] and Brauman and co-workers [94] have theoretically examined a number of $\text{X}^- + \text{CH}_3\text{Y} \rightarrow \text{CH}_3\text{X} + \text{Y}^-$ gas phase $\text{S}_{\text{N}}2$ reactions for X and Y as halogens or molecular species and have shown that energy transfer between high energy and low energy vibrational modes may be inefficient and lead to non-statistical dynamics [95, 96]. Thus, IVR within the $\text{I}^- \cdot \text{CH}_3\text{NO}_2$ complex reformed from the VB anion can act as the rate-limiting step in the dissociation of these complexes. We therefore conclude that the fast bi-exponential decay of the VB anion is IC to the ground state followed by delayed I^- evaporation, and the long-time VB anion decay (1300 ps) is by autodetachment. The proposed scheme for the photoinduced dynamics of $\text{I}^- \cdot \text{CH}_3\text{NO}_2$ are summarized by Eq. 7.5:



The rapid and complete DB anion to VB anion conversion following near-VDE photoexcitation of $\text{I}^- \cdot \text{CH}_3\text{NO}_2$, in addition to the observed non-statistical decay to yield I^- , provides insight into the energetics of the TNI partial conversion process and also the possible interactions between the iodine atom and the CH_3NO_2 moiety. We take these observed $\text{I}^- \cdot \text{CH}_3\text{NO}_2$ dynamics into consideration to help inform the studies of the $\text{I}^- \cdot \text{N}$ clusters in the discussion that follows.

B. $\text{I}^- \cdot \text{Uracil}$ and $\text{I}^- \cdot \text{Thymine}$ Binary Complexes

The pyrimidine bases uracil and thymine both have dipole moments of approximately 4.15 D, so each can support a DB anion [34]. Photoelectron spectroscopy has previously found both the uracil and thymine DB anions to have eBEs of approximately 90 meV and 70 meV, respectively [16]. No photoelectron spectrum has been recorded for the VB anion of either uracil or thymine, but Rydberg electron transfer experiments [37] as well as theoretical calculations [36, 97] predict that both the DB anion as well as the VB anion for both

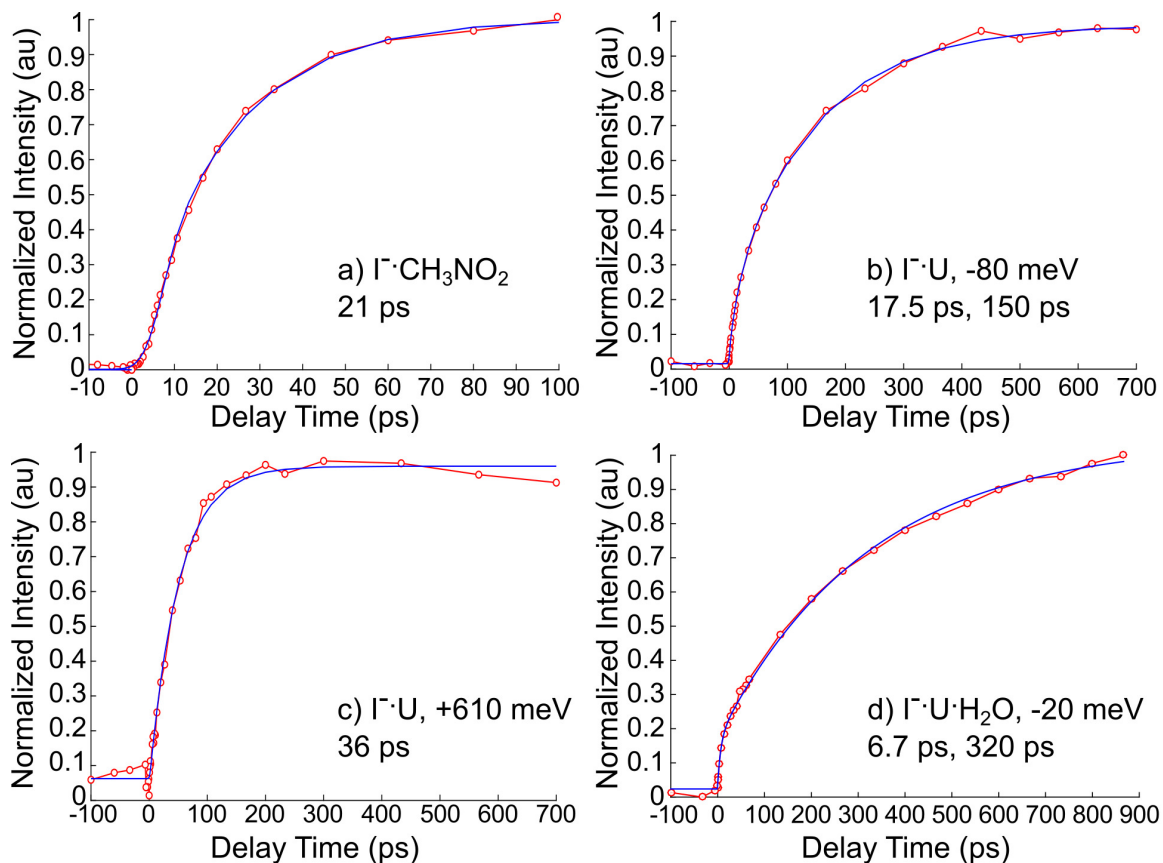


Figure 7.6: Iodide rise times for a) $\text{I}^- \cdot \text{CH}_3\text{NO}_2$, b) $\text{I}^- \cdot \text{U}$ photoexcited -80 meV below the VDE, c) $\text{I}^- \cdot \text{U}$ photoexcited at $+610$ meV (4.72 eV), and d) $\text{I}^- \cdot \text{U} \cdot \text{H}_2\text{O}$ near-VDE pump.

nucleobases exist, at least as TNIs, with VB anion VDEs of approximately 500 meV. For both uracil and thymine, the DB anion is the anionic ground state [41, 98], with a predicted barrier of $36 - 155$ meV for conversion to form the VB anion, depending on the level of theory [27]. However, bare thymine has been calculated to have a $\sim 10 - 20$ meV higher conversion barrier for DB to VB anion conversion than bare uracil at each calculation method and basis set combination employed [27].

The time-resolved dynamics of $\text{I}^- \cdot \text{U}$ and $\text{I}^- \cdot \text{T}$ clusters have been explored at photoexcitation energies near the VDE [25, 27] as well as in the higher energy ($\sim 4.6 - 4.9$ eV) excitation regime [23, 24, 26]. Laser photodissociation spectroscopy experiments by the Dessent group, in combination with theoretical results, complement the analysis of the time-resolved work described in more detail here [26, 42]. In this section, we consider the dynamics for $\text{I}^- \cdot \text{U}$ and $\text{I}^- \cdot \text{T}$ in these two photoexcitation regions both at early delay times to examine the dynamics of TNI formation and at longer delay times to probe the various autodetachment and dissociation channels.

One-photon photoelectron spectra at multiple photon energies are reproduced for $\Gamma^- \cdot \text{U}$ and $\Gamma^- \cdot \text{T}$ in Fig. 7.4b and 7.4c, respectively. Feature A corresponds to direct detachment to the $\text{I}(\text{}^2\text{P}_{3/2}) \cdot \text{N}$ neutral complex, yielding VDEs of 4.11 ± 0.05 eV [23, 24] and 4.05 eV ± 0.05 eV [24] for $\Gamma^- \cdot \text{U}$ and $\Gamma^- \cdot \text{T}$, respectively. Feature B, seen only at the highest photon energies, arises from photodetachment to the upper iodine spin-orbit state. Feature C, which corresponds to ~ 0 eV eKE photoelectron signal from autodetachment, is also present at each detachment energy. Two interesting trends can be seen in this autodetachment signal. At all photon energies, there is somewhat stronger autodetachment signal from $\Gamma^- \cdot \text{T}$ than $\Gamma^- \cdot \text{U}$ relative to peak A, the direct detachment feature. Moreover, the intensity of the autodetachment signal appears to reach a maximum near 4.7 – 4.8 eV photon energy, and declines at energies above and below this region. We explore these trends and the origin of the autodetachment signal in more detail below with the assistance of laser photodissociation spectroscopy, excited state calculations, and the time-resolved results.

Laser photodissociation spectroscopy has been carried out on $\Gamma^- \cdot \text{U}$ and $\Gamma^- \cdot \text{T}$ by Dessent et al [26, 42]; the photodepletion (photoabsorption, including dissociation and detachment) profiles for $\Gamma^- \cdot \text{U}$ and $\Gamma^- \cdot \text{T}$ from 3.6 to 5.3 eV are reproduced here in Fig. 7.8a and 7.8b, respectively (black dots, with the red lines indicating five-point adjacent averages). Two regimes of UV photoabsorption are measured: the first excited state in the vicinity of the VDE, centered at approximately 4 eV for both clusters, and the second centered around 4.8 eV. The photofragment yields of Γ^- for $\Gamma^- \cdot \text{U}$ and $\Gamma^- \cdot \text{T}$ are shown in Figs. 7.8c and 7.8d, respectively.

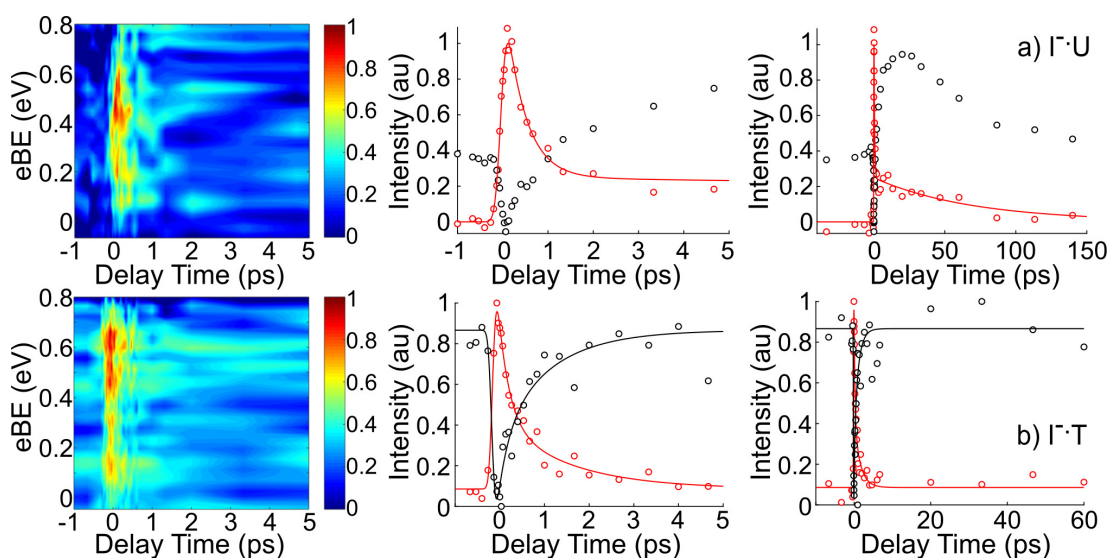


Figure 7.7: TRPE spectra and VB anion (red) and autodetachment (black) integrated intensities at both early times and long delay times for a) $\Gamma^- \cdot \text{U}$ photoexcited at 4.69 eV; b) $\Gamma^- \cdot \text{T}$ photoexcited at 4.69 eV.

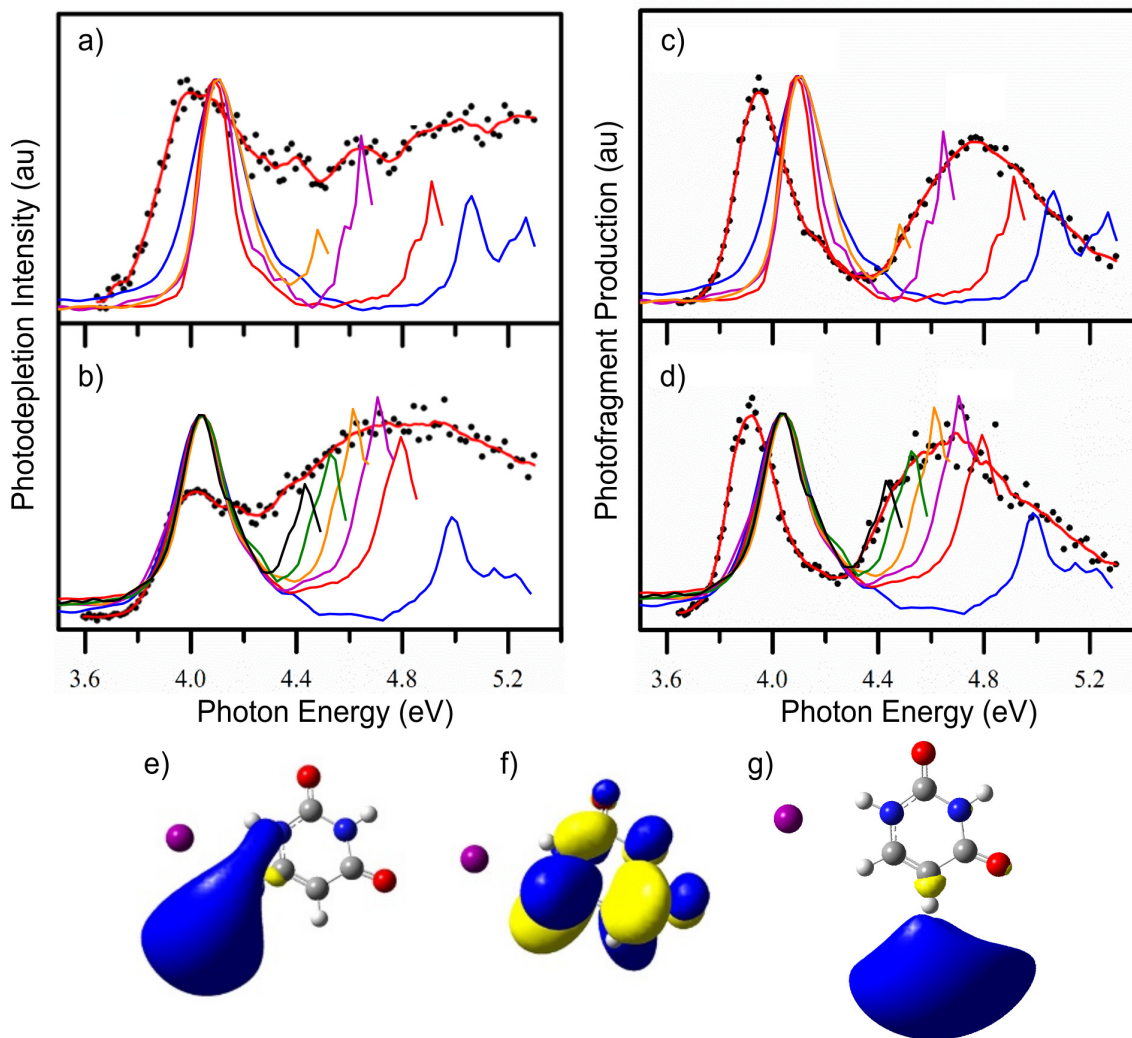


Figure 7.8: An overlay of the one color photoelectron spectra from Fig. 7.4b) for $I^- \cdot U$ and Fig. 7.4c) for $I^- \cdot T$ with the laser photodissociation spectroscopy results from Ref. [42]. a) Photodepletion (absorption) for $I^- \cdot U$ clusters photoexcited between 3.6 and 5.3 eV and b) for $I^- \cdot T$ clusters. c) Formation of I^- from photoexcited $I^- \cdot U$ clusters and d) formation of I^- from photoexcited $I^- \cdot T$ clusters. Photoelectron spectra are normalized to match the photodissociation data (black dots). e) EOM-CCSD/aug-cc-pVDZ(-pp) calculated image of the $I^- \cdot U$ DB orbital and f) for the π^* orbital and g) for the σ^* orbital for transitions localized near 4.7 eV. Laser photodissociation spectroscopy results are reproduced from Matthews et al., J. Chem. Phys. 148, 084304 (2018), with the permission of AIP Publishing.

I^- and $[\text{N-H}]^-$, the deprotonated nucleobase anion, were measured as the photofragments for both clusters, with I^- appearing as the overwhelmingly dominant species [42]. Both photofragments form in two distinct bands of photoexcitation: one centered near the VDE of each cluster, and one centered near 4.8 eV.

For ease of comparison of results, in Fig. 7.8 we overlay these laser photodissociation results with the respective $\text{I}^- \cdot \text{U}$ and $\text{I}^- \cdot \text{T}$ one color photoelectron spectra from Figs. 7.4b and 7.4c. The near-VDE photoabsorption and photofragmentation bands appear at lower energies than the VDE photodetachment bands; this has been observed previously and is due to the fact that photodetachment is not possible below the VDE, but photoabsorption and formation of the DB anion is possible and has been measured at pump energies below the VDE, as described in more detail in this section [25–27, 42]. More interestingly, the autodetachment feature present in the one color spectra for both $\text{I}^- \cdot \text{U}$ and $\text{I}^- \cdot \text{T}$ appears to track closely with the higher energy photoabsorption and I^- photofragmentation bands; we consider this finding and the dynamics resulting from high energy photoexcitation in more detail in Section 7.4.2.

Excited state calculations have been performed at the TD-DFT/B3LYP level for $\text{I}^- \cdot \text{U}$ and $\text{I}^- \cdot \text{T}$ [42], and at the EOM-CCSD/aug-cc-pVDZ(-pp) level for $\text{I}^- \cdot \text{U}$ [26] to examine the nature of photoexcitation in each of the two energy regimes in more detail. The EOM-CCSD results find three transitions with prominent oscillator strength in the energy region near the VDE corresponding to excitation from an iodide (5p) orbital to form a DB state of the complex (Fig. 7.8e). By far, the strongest transition near 4.8 eV was calculated to be a base-centered $\pi - \pi^*$ excitation (Fig. 7.8f), with two less intense channels (approximately 10x less oscillator strength) near 4.7 eV corresponding to excitation from an iodide (5p) orbital to a σ^* state of the complex (Fig. 7.8g). The TD-DFT calculations for both $\text{I}^- \cdot \text{U}$ and $\text{I}^- \cdot \text{T}$ also find base centered $\pi - \pi^*$ excitation to be the most prominent excitation channel, with four less intense $\text{I}(5p) \rightarrow \sigma^*$ transitions in $\text{I}^- \cdot \text{U}$ in the energy region near the $\pi - \pi^*$ excitation, and two such transitions in $\text{I}^- \cdot \text{T}$ (2-3x less oscillator strength in $\text{I}^- \cdot \text{U}$, 3-18x less in $\text{I}^- \cdot \text{T}$). No evidence is found in either set of excited state calculations for channels with significant oscillator strength corresponding to $\text{I}(5p) \rightarrow \pi^*$ charge transfer, i.e. direct optical excitation to form the VB anion, presumably reflecting near-zero spatial overlap between these initial and final states. Thus, we may expect that photoexcitation near the VDE most likely yields direct optical excitation from iodide to form the DB anion instantaneously, while photoexcitation at higher pump energies will most likely yield dynamics with the largest contribution from base-centered $\pi - \pi^*$ excitation, although $\text{I}(5p) \rightarrow \sigma^*$ type charge transfer may also be active to a lesser extent. We now turn our attention to the time-resolved results of photoexcitation of $\text{I}^- \cdot \text{U}$ and $\text{I}^- \cdot \text{T}$ clusters in each of these two pump energy regimes.

1. Early time dynamics from near-VDE excitation of $I^- \cdot U$ and $I^- \cdot T$

TRPES studies of $I^- \cdot U$ clusters were carried out at pump excitation energies from -110 meV to $+100$ meV relative to the VDE [25], and are shown at $+30$ meV in Fig. 7.5b. At each of these excitation energies, both the DB anion (feature A, blue) and the VB anion (feature B, red) of $I^- \cdot U$ were observed. The DB anion rise time decreases from approximately 250 fs to ≤ 150 fs as the pump energy is increased from -110 meV to $+100$ meV, while the VB anion rise time remains near 250 fs over this pump energy range.

The TRPES studies of $I^- \cdot T$ employed pump energies ranging from -120 meV to $+90$ meV in an analogous fashion to the $I^- \cdot U$ studies, and are shown for $+20$ meV in Fig. 7.5c. Both the DB anion and the VB anion of $I^- \cdot T$ were observed each at pump energy. The DB anion appears in approximately 230 fs, exhibiting no dependence on the pump excitation energy. The VB anion forms in approximately 300 fs, with clear energy dependence only revealed at the lowest pump energy used, -120 meV, which yielded a VB anion rise time over 1 ps.

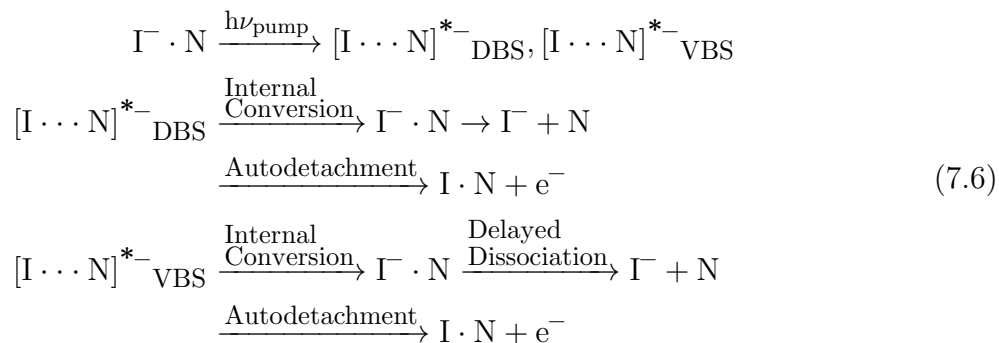
The findings for $I^- \cdot U$ and $I^- \cdot T$ that the DB rise time is faster or the same as that for the VB anion indicate that the DB state is formed first, followed by appearance of VB signal. The calculations in Section 7.4.2 show that there is no direct excitation of the VB state near the VDE, so we propose that the DB anion is created by photoexcitation and the VB signal results from DB to VB anion conversion. However, the observation that the DB signal remains while the VB signal grows in suggests that at most only partial DB to VB anion conversion occurs subsequent to photoexcitation. In contrast to $I^- \cdot CH_3NO_2$, the DB anion is the anionic ground state for uracil and thymine [41, 98], and the barrier for conversion to form the VB anion is calculated to lie approximately $\sim 36 - 155$ meV higher in energy [18, 20, 21, 27], depending on the level of theory. As a result, it is reasonable that the dynamics of DB to VB anion conversion differ from the complete conversion in $I^- \cdot CH_3NO_2$.

Note that while the $I^- \cdot CH_3NO_2$ TRPE spectrum shows a cross-correlation limited rise time for the DB anion, the $I^- \cdot U$ and $I^- \cdot T$ DB anions (and those of other $I^- \cdot N$ clusters presented here) exhibit finite rise times. This rise time may originate from an increase in the photodetachment cross section as a result of iodine-nucleobase motion following the vertical formation of the TNI [27]. The DB orbital calculated for $I^- \cdot U$ in Fig. 7.8e appears to avoid the iodine atom; iodine is calculated to sit within the region where the DB orbital for bare uracil has been calculated to exist [22]. We have previously proposed that following initial photoexcitation, the iodine atom moves in such a way as to decrease the repulsive interaction between the diffuse DB orbital and the iodine atom [25, 27]. This increased localization of the DB orbital is expected to increase the photodetachment cross section for the DB anion at early times, manifesting in a finite rise time for the DB anion [27].

2. Long time dynamics of near-VDE excited $\Gamma^- \cdot \text{U}$ and $\Gamma^- \cdot \text{T}$ clusters

The DB and VB TNI signals for $\Gamma^- \cdot \text{U}$ and $\Gamma^- \cdot \text{T}$ clusters decay bi-exponentially, with each set of lifetimes generally decreasing with increasing pump excitation energy in the near-VDE regime. For $\Gamma^- \cdot \text{U}$ photoexcited at +30 meV (Fig. 7.5b), the DB anion bi-exponential decay constants are 5.0 ps and 500 ps, while the VB anion undergoes bi-exponential decay in 5.6 ps and 80 ps [25]. $\Gamma^- \cdot \text{T}$ photoexcited at +20 meV (Fig. 7.5c) similarly exhibits DB anion decay in 5.2 ps and 1100 ps, and VB anion decay in 13.1 ps and 530 ps [27].

Two decay pathways have been measured in our TRPES work on near-VDE photoexcited $\Gamma^- \cdot \text{U}$ clusters: autodetachment and bi-exponential re-formation of Γ^- . Autodetachment has been measured in TRPES of $\Gamma^- \cdot \text{U}$ and $\Gamma^- \cdot \text{T}$ at all near-VDE photoexcitation energies as near 0 eV eKE signal with initial depletion dynamics followed by intensity recovery at longer times, although the dynamics for ~ 0 eV signal are challenging to extract here with certainty. TRPES of $\Gamma^- \cdot \text{U}$ clusters photoexcited at 4.03 eV (-80 meV) and probed at 3.61 eV finds bi-exponential formation of Γ^- in 17.5 ± 1.6 ps and 150 ± 10 ps as the only major photodissociation pathway; this Γ^- rise signal is shown in Fig. 7.6b, and is attributed to internal conversion followed by fragmentation. The overall decay mechanisms for the DB and VB anions are given by Eq. 7.6.



To assign the bi-exponential Γ^- rise dynamics in near-VDE photoexcited $\Gamma^- \cdot \text{U}$, we compare the dynamics here to the mechanism of Γ^- reformation in $\Gamma^- \cdot \text{CH}_3\text{NO}_2$. There, we observed complete DB to VB anion conversion and concluded that the fast decay component of the VB anion may be decay by IC to the $\Gamma^- \cdot \text{CH}_3\text{NO}_2$ ground state followed by dissociation to yield Γ^- at a delay due to a dynamical bottleneck. Thus, for $\Gamma^- \cdot \text{U}$ clusters we may expect, since both TNIs are present as the DB to VB anion conversion is only partially complete, that each TNI has a fast decay process of IC to the electronic $\Gamma^- \cdot \text{U}$ ground state followed by evaporation of Γ^- to ultimately yield bi-exponential Γ^- rise rather than the solely mono-exponential rise observed in $\Gamma^- \cdot \text{CH}_3\text{NO}_2$ clusters. Given that the fast Γ^- rise time of 17.5 ps from $\Gamma^- \cdot \text{U}$ is a few ps longer than both the DB anion and VB anion fast decay lifetimes, it is possible for $\Gamma^- \cdot \text{U}$ clusters that the fast Γ^- appearance arises from IC of the DB anion, and

the slow I^- appearance of 150 ps originates from IC and delayed ejection of I^- from the VB anion.

We expect that the long time decays of each TNI for both species are from autodetachment, or rather, more specifically, by thermionic emission considering the ~ 100 ps – 1 ns long decay lifetimes of each TNI. Such a statistical mechanism is congruent with the decrease in the long time constants with increasing pump energy as measured here. The DB anion of $I^- \cdot U$ clusters, for example, exhibits a decrease in the long time constant from 2000 ps to 30 ps in the range of pump excitation from -110 meV to $+100$ meV [25]. Laser photodissociation spectra find $[U-H]^-$ (neutral electron affinity = 3.481 eV) [47] as an additional minor dissociation product from $I^- \cdot U$ clusters, but due to its minor abundance and molecular cross section, we did not observe this channel in our TRPES studies.

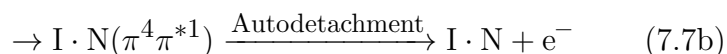
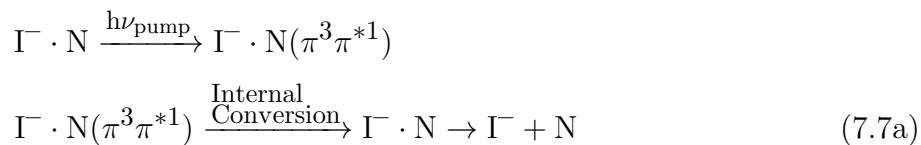
3. Dynamics of $I^- \cdot U$ and $I^- \cdot T$ excited at higher energy

TRPES studies for $I^- \cdot U$ and $I^- \cdot T$ were also conducted at pump excitation energies from 4.6 eV – 4.9 eV [23, 24]. TRPE spectra for $I^- \cdot U$ and $I^- \cdot T$ photoexcited at 4.69 eV and probed at 1.57 eV are shown in Figs. 7.7a and 7.7b, respectively. In this energy regime, no evidence for the existence of a DB state was measured for either cluster. Both species exhibit VB anion signal (red integrated intensity) with a cross-correlation limited rise (≤ 150 fs), as well as time-dependent signal at $\sim 0 - 0.08$ eV eKE corresponding to autodetachment (black integrated intensity). At this excitation energy, the $I^- \cdot U$ VB anion decays bi-exponentially in 620 fs and 52 ps, while the $I^- \cdot T$ VB anion undergoes mono-exponential decay [27] in ~ 610 fs. The lifetimes for the $I^- \cdot U$ VB anion bi-exponential decay were found to decrease somewhat with increasing pump energy, while the $I^- \cdot T$ VB anion mono-exponential decay did not exhibit excitation energy dependence in this high energy pump regime. The autodetachment signal for both clusters was measured to exhibit non-zero autodetachment intensity at negative times, prompt depletion at $t=0$ fs, and recovery to the initial intensity, although the signal in $I^- \cdot U$ clusters was found to exceed its initial intensity. As seen in the integrated intensities in Fig. 7.7b, in $I^- \cdot T$ clusters, the VB anion prompt appearance and decay time constant mirrors the time constants for the autodetachment dynamics [24].

TRPES of $I^- \cdot U$ at 4.72 eV pump energy with 3.15 eV probe energy finds mono-exponential appearance of I^- in 36 ± 3 ps as the major photodissociation channel (Fig. 7.6c), as well as TRPES signal arising from autodetachment. The 3.15 eV probe study also measured autodetachment depletion and recovery but without any long-time overshoot of the initial intensity, although these dynamics are noisier due to the very close energetic overlap of the $\sim 0 - 0.08$ eV eKE autodetachment signal with I^- photodetachment (~ 0.09 eV eKE). An analogous high energy probe study has not yet been performed for $I^- \cdot T$ clusters, but the laser photodissociation spectroscopy results confirm that I^- is produced from both sets of photoexcited clusters. We now consider the assignment of the origin of the iodide signal as well as the autodetachment signal from both $I^- \cdot U$ and $I^- \cdot T$ clusters.

For both $\Gamma^- \cdot \text{U}$ and $\Gamma^- \cdot \text{T}$ clusters, the VB anion appearance and fast decay dynamics in Fig. 7.7 match closely with the autodetachment depletion and recovery signal. It is also striking from the overlay of the one-color photoelectron spectra with the laser photodissociation results for Γ^- formation in Figs. 7.8c and 7.8d that the autodetachment signal tracks closely with the Γ^- photofragment production. Thus, it appears that Γ^- formation, autodetachment, and the VB anion share one common dynamical origin that is similar in nature between both sets of clusters.

Given that the excited state calculations for both $\Gamma^- \cdot \text{U}$ and $\Gamma^- \cdot \text{T}$ clusters find strong oscillator strength for a base-centered $\pi - \pi^*$ excitation as a result of photoexcitation in this energy regime, we can begin by considering the possible ensuing relaxation and decay channels from an optical excitation of this nature. Specifically, two possibilities following $\pi - \pi^*$ excitation that exist are IC to the $\Gamma^- \cdot \text{N}$ ground state to yield cluster dissociation to produce Γ^- , as in Eq. 7.7a, and charge transfer from iodide to the base moiety to fill the hole in the π orbital, essentially creating a VB anion that may then undergo autodetachment (Eq. 7.7b).



We previously considered the possibility of formation of the VB anion in this excitation regime by charge transfer from iodide, but thought it unlikely given the <150 fs appearance of the VB anion and the lack of orbital overlap between the $\text{I}(5p)$ and π^* VB orbitals [26]. However, the calculated result that the $\pi - \pi^*$ optical excitation is expected to dominate in this UV absorption region and the experimental result that the presence of autodetachment (and therefore the VB anion) tracks closely with the envelope of Γ^- formation are compelling evidence that $\pi - \pi^*$ excitation is the origin of the observed dynamics. The calculated results described at the beginning of Section 7.4.2 find some evidence that a $\text{I}(5p) \rightarrow \sigma^*$ photoexcitation channel is active, and such a σ^* state may potentially couple more effectively with the VB state to facilitate its rapid formation. If the existence of a σ^* state is real and resembles that in Fig. 7.8g, photodetachment from this state would likely yield a narrow spectral profile given that this excited anion geometry is likely not significantly distorted from the neutral. However, the TRPES results find no evidence for the presence of another charged intermediate state. Moreover, it is clear from the time-resolved results for $\Gamma^- \cdot \text{T}$ that the VB anion decays solely by autodetachment, and therefore does not produce the Γ^- signal measured by laser photodissociation spectroscopy. It thus seems unlikely that $\text{I}(5p) \rightarrow \sigma^*$ photoexcitation is the source of the observed dynamics here.

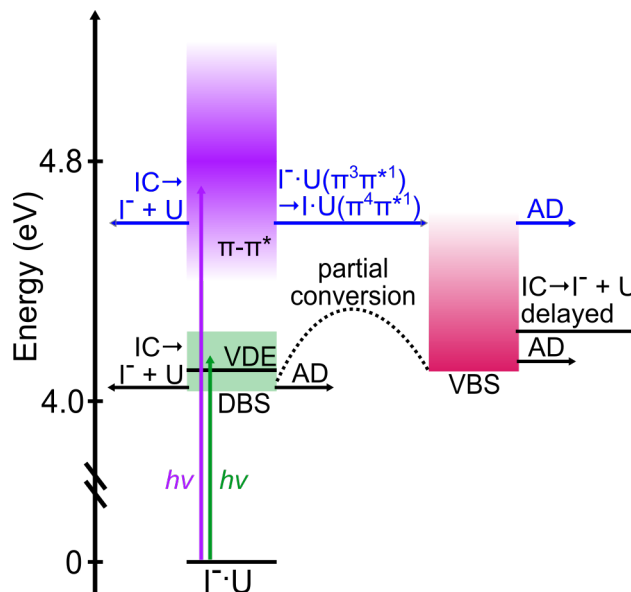


Figure 7.9: Diagram of the approximate energies and ranges for the various excited states of $\text{I}^- \cdot \text{U}$ accessed in this work, as well as the proposed pathways resulting from near-VDE photoexcitation (green photon, black arrows) and higher energy photoexcitation (purple photon, blue arrows). DBS and VBS denote the DB and VB states, respectively.

It has also been previously suggested [25] that in the TRPES experiments, the pump pulse ejects the excess electron from the I^- moiety that is then captured by the nucleobase to form the VB anion in a two-step scattering type mechanism. This interpretation was offered before observation and characterization of the I^- channel. However, it now seems more likely that both autodetachment and I^- production originate from one common mechanism, rather than a combination of a scattering mechanism to create a VB anion that decays by autodetachment and a $\pi - \pi^*$ excited state that relaxes by IC to produce I^- . Therefore, it appears that the strongest possibility for VB anion formation in this photoexcitation regime for both $\text{I}^- \cdot \text{U}$ and $\text{I}^- \cdot \text{T}$ is base-centered $\pi - \pi^*$ excitation followed by prompt charge transfer from the iodide.

We can expect then that a mechanism as in Eq. 7.7a, or IC of the photoexcited state followed by cluster dissociation, is the origin of the I^- formation measured in this UV region. Thus, we conclude that in both $\text{I}^- \cdot \text{U}$ and $\text{I}^- \cdot \text{T}$, photoexcitation from $\sim 4.6 \text{ eV} - 4.8 \text{ eV}$ creates a $\pi - \pi^*$ excited state, some fraction of which may decay by IC to the $\text{I}^- \cdot \text{N}$ ground state followed by dissociation to produce I^- (Eq. 7.7a), and another fraction of which may have charge transfer within the cross-correlation of the pump and probe laser pulses from the iodide moiety to produce a VB anion that then decays by autodetachment (Eq. 7.7b). Fig. 7.9 shows the approximate energies and ranges for the excited states of $\text{I}^- \cdot \text{U}$ and summarizes these proposed pathways (blue arrows) resulting from higher energy photoexcitation of $\text{I}^- \cdot \text{U}$.

Additionally, Fig. 7.9 shows the near-VDE photoexcitation pathways (black arrows) of $\text{I}^- \cdot \text{U}$ as described in the earlier subsections of Section 7.4.2.

While this overall excitation and decay mechanism for the higher energy excitation regime is appealing, it is challenging to explain the rapid rate of charge transfer from iodide to the π orbital to form the VB anion in <150 fs given the lack of orbital overlap. Additionally, $\text{I}^- \cdot \text{U}$ exhibits long-lived dynamics that are not present in $\text{I}^- \cdot \text{T}$, and it is unclear why the $\text{I}^- \cdot \text{U}$ VB anion exhibits both fast and slow decay by autodetachment, although we have put forth such mechanistic explanations previously [23–25, 27]. A more extensive theoretical investigation into the nature and energetics of the photoexcited states accessible in this pump energy region may be needed to fully explain the mechanism of the VB anion formation as well as these differences exhibited here in the long-time dynamics of $\text{I}^- \cdot \text{U}$ compared to $\text{I}^- \cdot \text{T}$.

C. $\text{I}^- \cdot \text{Uracil} \cdot \text{H}_2\text{O}$

Microhydration of $\text{I}^- \cdot \text{U}$ clusters, the step-wise addition of individual water molecules, provides insight into the role of water and solvation on the dynamics of electron attachment and photodissociation in these clusters. Anion photoelectron spectroscopy shows an increase in the electron affinity of pyrimidine nucleobases with the successive addition of water molecules [17], and resonantly enhanced multiphoton ionization (REMPI) experiments find an increase in IC and photostability and decrease in excited state lifetimes with the addition of water to uracil and thymine [99, 100]. Previous $\text{U}^- \cdot \text{H}_2\text{O}$ photoelectron spectra only show evidence for the VB anion [17, 41], and suggest that the VB anion may be preferentially stabilized over the DB anion due to the interaction energy with water being higher with the increased density of the excess electron in the VB anion [20, 101]. We have recently investigated the dynamics of electron attachment and photodissociation in TRPES experiments on near-VDE photoexcited $\text{I}^- \cdot \text{U} \cdot \text{H}_2\text{O}$ clusters [29].

Single photon PES of $\text{I}^- \cdot \text{U} \cdot \text{H}_2\text{O}$ finds the cluster VDE to be $4.40 \text{ eV} \pm 0.05 \text{ eV}$ (Fig. 7.4d, peak A), in agreement with the calculated VDEs for a variety of $\text{I}^- \cdot \text{U} \cdot \text{H}_2\text{O}$ conformers [29]. EOM-CCSD/aug-cc-pVDZ(-pp) excited state calculations carried out by our group on $\text{I}^- \cdot \text{U} \cdot \text{H}_2\text{O}$ clusters, analogous to those results presented for $\text{I}^- \cdot \text{U}$ above, also find three low-energy photoexcitation channels with considerable oscillator strength corresponding to excitation of the excess iodine ($5p$) electron to a cluster DB orbital. No photodepletion experiments have been carried out for this cluster, but if the same energetic offset for $\text{I}^- \cdot \text{U}$ is employed for $\text{I}^- \cdot \text{U} \cdot \text{H}_2\text{O}$, these three channels lie in the vicinity of the $\text{I}^- \cdot \text{U} \cdot \text{H}_2\text{O}$ VDE. Thus, we may expect that in $\text{I}^- \cdot \text{U} \cdot \text{H}_2\text{O}$, pump excitation directly yields the DB anion as in $\text{I}^- \cdot \text{U}$.

TRPES of $\text{I}^- \cdot \text{U} \cdot \text{H}_2\text{O}$ clusters photoexcited at 4.38 eV , 20 meV below the VDE, show cross-correlation limited appearance of the DB anion, followed by appearance of the VB anion in $400 \pm 140 \text{ fs}$ (Fig. 7.5d). The binding energy range for each of these features is notably $\sim 0.2 \text{ eV}$ higher in maximum eBE for each TNI than the corresponding TNIs of $\text{I}^- \cdot \text{U}$

clusters, indicating that association of water with the $\Gamma^- \cdot \text{U}$ cluster serves to energetically stabilize both the DB and VB anion.

The greatest accord in lifetimes between $\Gamma^- \cdot \text{U} \cdot \text{H}_2\text{O}$ (-20 meV) and $\Gamma^- \cdot \text{U}$ was found to be for $\Gamma^- \cdot \text{U}$ ($+30$ meV) [29]. The fast appearance of the DB anion is similar in both clusters, but the appearance of the VB anion in 400 fs is somewhat delayed compared to the approximately 220 fs VB anion rise in $\Gamma^- \cdot \text{U}$. This finite VB anion rise time may reflect partial DB to VB anion conversion, as has been suggested for $\Gamma^- \cdot \text{U}$ clusters [25, 29]. The DB to VB anion conversion barrier for $\text{U}^- \cdot \text{H}_2\text{O}$ has been calculated by Takayanagi and co-workers to vary from approximately 18.6 – 130 meV depending on the specific binding site of H_2O around uracil [20]. They have calculated the barrier to water-binding-site isomerization to be approximately 40 – 200 meV as well, and suggest that the water molecule may rearrange to a binding site that will lower the DB to VB conversion barrier. This water binding site rearrangement could delay the VB anion formation by approximately 100 – 200 fs, yielding the somewhat delayed VB formation in $\Gamma^- \cdot \text{U} \cdot \text{H}_2\text{O}$ relative to $\Gamma^- \cdot \text{U}$, and therefore a more prominent DB to VB anion conversion, as seen in the $\Gamma^- \cdot \text{U} \cdot \text{H}_2\text{O}$ DB anion decay and VB anion rise in Fig. 7.5d compared to the TNIs of $\Gamma^- \cdot \text{U}$ in Fig. 7.5b.

Both TNIs of $\Gamma^- \cdot \text{U} \cdot \text{H}_2\text{O}$ decay bi-exponentially in approximately 5 ps and 500 ps, and autodetachment is observed as a decay channel [29]. The $\Gamma^- \cdot \text{U} \cdot \text{H}_2\text{O}$ DB anion fast and slow decay and the VB anion fast decay are quite similar to the $\Gamma^- \cdot \text{U}$ ($+30$ meV) results, but the long-time decay component of the VB anion is considerably longer in $\Gamma^- \cdot \text{U} \cdot \text{H}_2\text{O}$ (650 ps) than that of $\Gamma^- \cdot \text{U}$ (80 ps). This may arise from the preferential stabilization of the VB anion over the DB anion upon the addition of water [20, 101], effectively stabilizing the $\Gamma^- \cdot \text{U} \cdot \text{H}_2\text{O}$ VB anion relative to autodetachment at longer times.

TRPES of $\Gamma^- \cdot \text{U} \cdot \text{H}_2\text{O}$ with -20 meV pump excitation energy and a probe energy of 3.14 eV finds bi-exponential rise of Γ^- with time constants of 6.7 ± 3.8 ps and 320 ± 30 ps (Fig. 7.6d). Given the relatively similar bi-exponential DB and VB anion decay and similar Γ^- bi-exponential rise in near-VDE excited $\Gamma^- \cdot \text{U}$ and $\Gamma^- \cdot \text{U} \cdot \text{H}_2\text{O}$ clusters, these results indicate there is likely a congruent mechanism in both cluster systems for TNI decay to yield bi-exponential formation of the Γ^- . For both $\Gamma^- \cdot \text{U}$ and $\Gamma^- \cdot \text{U} \cdot \text{H}_2\text{O}$ clusters, we can thus expect that the Γ^- fast rise originates from IC of the DB anion to the anion ground state followed by evaporation of Γ^- , and the Γ^- slow rise from delayed ejection of Γ^- from VB anion IC and dissociation, as in Eq. 7.6. However, these 3.14 eV probe experiments are not able to photodetach some possible photofragments such as $\Gamma^- \cdot \text{H}_2\text{O}$ (VDE = 3.51 eV) [102, 103], which could also act as an intermediate in the re-formation of Γ^- . TRPES experiments for $\Gamma^- \cdot \text{U} \cdot \text{H}_2\text{O}$ with near-VDE pump and >3.6 eV probe pulses to probe the possible appearance of $\Gamma^- \cdot \text{H}_2\text{O}$ are currently underway in our laboratory, as well as $\pi-\pi^*$ pump excitation energy TRPES studies for $\Gamma^- \cdot \text{U} \cdot \text{H}_2\text{O}$.

D. Γ^- -Adenine

Adenine, a purine nucleobase, is also expected to be capable of supporting an excess electron in a DB state, although adenine anions have been less extensively studied than those of uracil or thymine. The biological adenine tautomer, A9, has a molecular dipole moment of 2.5 – 2.8 D [32, 33], which is large enough to support a DB state [31, 104, 105]. The A9 VB anion, however, has been calculated to be adiabatically unbound and only weakly vertically bound, if at all [28, 106, 107]. However, some higher-lying non-canonical tautomers of adenine such as the A3 tautomer have been calculated to support a VB anion with a VDE of 0.686 eV [28]. Anion photoelectron spectroscopy studies by Bowen and co-workers have measured various gas phase anions of adenine [108, 109], but neither DB nor VB anions of A9 were detected in these studies. Here, we present TRPES studies of the dynamics of TNI formation in near-VDE photoexcited Γ^- -A complexes [28].

The single photon photoelectron spectrum of Γ^- -A, Fig. 7.4e, shows vertical detachment of the Γ^- -A9 complex at 3.96 eV, feature A, in agreement with CCSD/aug-cc-pVDZ(-pp) calculations for the cluster VDE [28]. A shoulder, feature A', is observed near 4.1 eV in the one color spectrum; we discuss possible origins for this shoulder below. TRPES studies for Γ^- -A clusters were conducted with pump photon energies from -110 meV to +10 meV relative to the Γ^- -A9 VDE. At each of these excitation energies, both DB and VB anions were measured; the TRPES results for -60 meV photoexcitation are presented in Fig. 7.5e. At each pump excitation energy, a DB state is observed with a rise time of approximately 250 fs. At (and below) -60 meV photoexcitation, the DB anion decays mono-exponentially with a decay lifetime of approximately 11 ps, but at pump energies ≥ -20 meV, the DB anion decays bi-exponentially in approximately 4 ps and 100 – 1000 ps. The VB anion, with a VDE of ~ 0.5 eV, appears in approximately 5 – 10 ps at each photoexcitation energy, with mono-exponential decay in approximately 60 – 100 ps. The close match-up of lifetimes of the DB anion fast decay and the VB anion rise time at all excitation energies is commensurate with the DB anion to VB anion conversion previously observed in photoexcited Γ^- -CH₃NO₂ complexes. However, the observed VDE of ~ 0.5 eV for the VB anion lies well above the calculated values for the A9 tautomer, which range from 0.03 eV – 0.135 eV [28, 107].

To assign these differing Γ^- -A TNI dynamics at each pump excitation energy, it is important to consider the propensity of adenine to form low-lying non-canonical tautomers upon heating in the thermal desorption cluster source. CCSD/aug-cc-pVDZ(-pp) calculations have calculated the Γ^- -A3 VDE to be 4.15 eV [28], which is in close agreement with the 4.11 eV A' shoulder feature observed in the one color photoelectron spectra in Fig. 7.4e. The low-lying A3 tautomer has a dipole moment of 4.7 D [33], and thus it may contribute to the DB anion signal measured here. The A3 tautomer has also been calculated to have a VB anion with a positive adiabatic electron affinity [107], for which the VDE has been calculated to be 0.686 eV [28]. Thus, it appears that both Γ^- -A9 and Γ^- -A3 tautomers contribute to the measured time-resolved signal, and it is necessary to distinguish the contributions of each to

the observed dynamics.

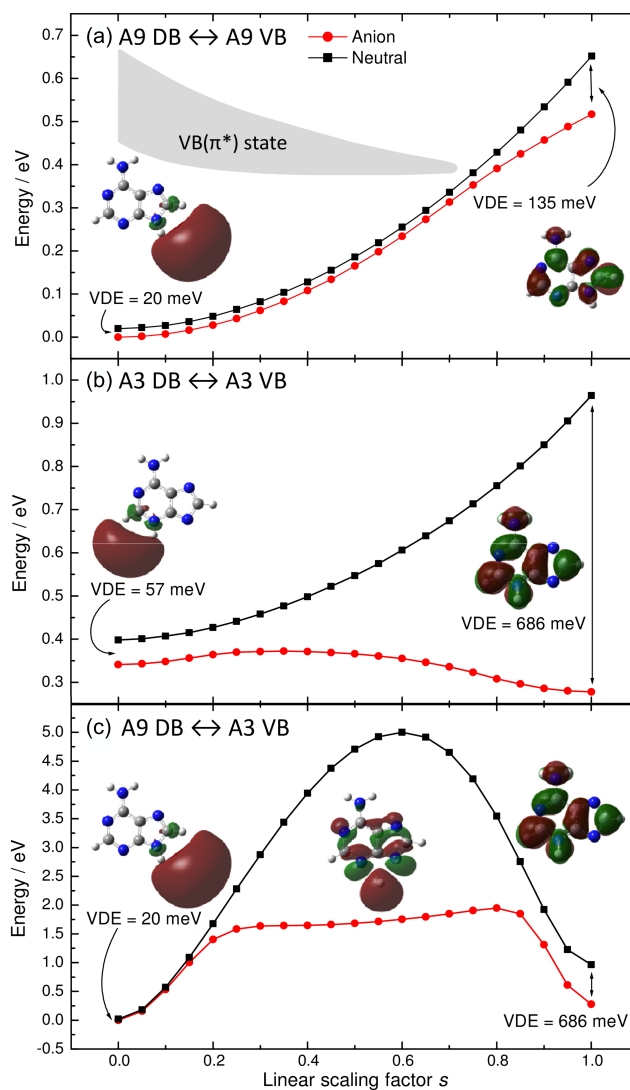
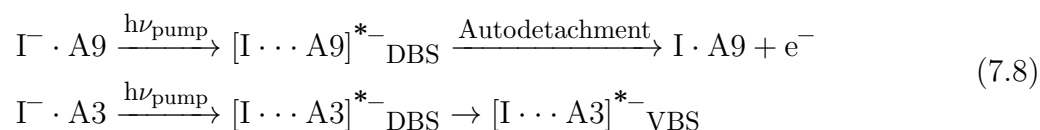


Figure 7.10: Calculated potential energy surfaces corresponding to a DB to VB anion transition within the a) A9 and b) A3 tautomers of adenine and c) between the A9 DB anion to form the A3 VB anion. The linear scaling factor s refers to the linear interpolated geometries between the equilibrium DB anion ($s=0$) and the equilibrium VB anion ($s=1$). Calculated at the CAM-B3LYP/6-311++G(2d,p) level of theory, see Ref. [28] for additional computational details.

The energetic landscape for the DB to VB anion interconversion has been calculated by Takayanagi and co-workers for the A9 and A3 tautomers, as well as interconversion from the A9 DB anion to form the A3 VB anion [28]. The calculated potential energy surfaces for these DB to VB anion transitions in and among A9 and A3 are presented in Fig. 7.10. It

can be seen that the conversion in A9 has a high barrier and is nearly ~ 0.5 eV endothermic, while the A3 tautomer DB to VB anion conversion is exothermic with a very modest barrier. Thus, the A3 tautomer is expected to have an energetic landscape similar to CH_3NO_2 , for which the VB anion is the ground state and the conversion from the DB anion to the VB anion is exothermic and nearly barrierless. Based on the previously discussed calculated results that indicate an A9 VB anion is not expected to be bound and this calculated ~ 0.5 eV barrier to A9 TNI partial conversion, the similar energetic landscape between CH_3NO_2 and the A3 tautomer would suggest that the A3 tautomer is likely to be the species that undergoes the DB anion to VB anion conversion measured by TRPES. However, the bi-exponential DB anion decay dynamics measured here likely contain both tautomers, and it may be expected that the A9 tautomer, unable energetically to form the VB anion, will undergo autodetachment and give rise to the long-time decay component of the DB anion measured here. These dynamics are summarized in Eq. 7.8:



Given the similarities between the A3 tautomer and CH_3NO_2 , it is interesting that the VB anion of near-VDE photoexcited $\Gamma \cdot \text{CH}_3\text{NO}_2$ complexes exhibits bi-exponential decay in 2 ps (from internal conversion) and 1200 ps while that of $\Gamma \cdot \text{A3}$ exhibits mono-exponential decay in $\sim 60 - 100$ ps. Although higher energy probe TRPES studies on $\Gamma \cdot \text{A}$ have not been performed, this $\sim 60 - 100$ ps timescale may result from cluster internal conversion to dissociate to yield Γ rather than decay by autodetachment or H-atom loss as previously suggested [28], although contributions from all of these channels are possible. We note that as a result of the presence of low-lying non-canonical tautomers upon heating, further TRPES studies for $\Gamma \cdot \text{A}$, iodide-cytosine ($\Gamma \cdot \text{C}$) and iodide-guanine ($\Gamma \cdot \text{G}$) have not been performed.

7.5 Summary and Outlook

TRPES of $\Gamma \cdot \text{N}$ clusters has revealed the ultrafast formation and conversion of nucleobase TNIs thought to be important in reductive damage pathways in DNA. Following photoexcitation in the vicinity of the cluster VDE, the DB anion is found in some cases, as in $\Gamma \cdot \text{A3}$, to act as a doorway to the exothermic formation of the conventional VB anion. In other cases, as in $\Gamma \cdot \text{U}$ and $\Gamma \cdot \text{T}$, the DB anion is the ground state and a greater energetic barrier to TNI interconversion appears to yield only partial conversion. These TNIs are both susceptible to autodetachment, but also appear to participate in cluster photodissociation in 10s of ps by internal conversion to the ground state to eventually re-form Γ . Base-centered $\pi - \pi^*$ photoexcitation also appears to lead to cluster decay by internal conversion followed by dissociation to form Γ , and may also coincide with VB anion formation by intracuster

charge transfer following $\pi - \pi^*$ excitation with subsequent decay by autodetachment. However, more theoretical work is needed to fully understand the dynamics resulting from $\pi - \pi^*$ photoexcitation in these anionic clusters.

Ongoing work in our laboratory is aimed at the continued microhydration of $I^- \cdot N$ clusters. Microsolvation is expected to eventually stabilize the VB anion and fully suppress the DB anion, and it remains to be seen how many water molecules must be added before this transition occurs. Theoretical calculations have suggested that $U^-(H_2O)_2$ may support a DB state [20, 101], but the DB and VB states of larger nucleobase-water clusters have not been examined. The stepwise addition of individual water molecules building up to a solvation shell will also allow for comparison between gas-phase dynamics of nucleobases and those recorded in bulk solution. In this regard, TRPES experiments in our group [110] and elsewhere [111, 112] on the dynamics of nucleic acid constituents in liquid water microjets are of particular interest.

The future implementation of a new cluster source, such as one based on electrospray ionization [62], will enable TRPES of nucleobases commonly prone to tautomerization upon heating, such as cytosine and guanine, in addition to the study of larger biomolecules such as nucleosides and nucleotides. Dessent et al. have recently measured distinct photoabsorption and photofragmentation profiles in $I^- \cdot C$ clusters in which there is relatively flat and intense I^- production across the entire region above the VDE [42]. Electrospray ionization could thus similarly be used to generate clusters of iodide-uridine or iodide-uridine-monophosphate, among others, with the ultimate goal of inducing electron attachment and monitoring not only the initial site of electron attachment and the TNI dynamics, but also probing photofragment formation to measure the identities and timescales for formation of photodissociation products in these larger nucleic acid constituents.

7.6 References

- [1] B. Boudaïffa, P. Cloutier, D. Hunting, M. A. Huels, and L. Sanche, "Resonant formation of DNA strand breaks by low-energy (3 to 20 eV) electrons", *Science* **287**, 1658–1660 (2000).
- [2] R. Barrios, P. Skurski, and J. Simons, "Mechanism for damage to DNA by low-energy electrons", *J. Phys. Chem. B* **106**, 7991–7994 (2002).
- [3] J. Simons, "How do low-energy (0.1-2 eV) electrons cause DNA-strand breaks?", *Acc. Chem. Res.* **39**, 772–779 (2006).
- [4] H.-Y. Chen, P.-Y. Yang, H.-F. Chen, C.-L. Kao, and L.-W. Liao, "DFT reinvestigation of DNA strand breaks induced by electron attachment", *J. Phys. Chem. B* **118**, 11137–11144 (2014).

- [5] J. Berdys, I. Anusiewicz, P. Skurski, and J. Simons, “Damage to model DNA fragments from very low-energy (< 1 eV) electrons”, *J. Am. Chem. Soc.* **126**, 6441–6447 (2004).
- [6] J. Berdys, P. Skurski, and J. Simons, “Damage to model DNA fragments by 0.25-1.0 eV electrons attached to a thymine π^* orbital”, *J. Phys. Chem. B* **108**, 5800–5805 (2004).
- [7] E. Alizadeh, F. Ferreira da Silva, F. Zappa, A. Mauracher, M. Probst, S. Denifl, A. Bacher, T. D. Märk, P. Limão-Vieira, and P. Scheier, “Dissociative electron attachment to nitromethane”, *Int. J. Mass Spectrom.* **271**, 15–21 (2008).
- [8] C. Desfrancois, H. Abdoul-Carime, and J.-P. Schermann, “Ground-state dipole-bound anions”, *Int. J. Mod. Phys. B* **10**, 1339–1395 (1996).
- [9] R. Bachorz, W. Klopper, M. Gutowski, X. Li, and K. H. Bowen, “Photoelectron spectrum of valence anions of uracil and first-principles calculations of excess electron binding energies”, *J. Chem. Phys.* **129**, 054309 (2008).
- [10] P. D. Burrow, G. A. Gallup, A. M. Scheer, S. Denifl, S. Ptasińska, T. D. Märk, and P. Scheier, “Vibrational Feshbach resonances in uracil and thymine”, *J. Chem. Phys.* **124**, 124310 (2006).
- [11] G. Hanel, B. Gstir, S. Denifl, P. Scheier, M. Probst, B. Farizon, M. Farizon, E. Illenberger, and T. D. Märk, “Electron attachment to uracil: effective destruction at subexcitation energies”, *Phys. Rev. Lett.* **90**, 188104 (2003).
- [12] S. Ptasińska, S. Denifl, S. Gohlke, P. Scheier, E. Illenberger, and T. D. Märk, “Decomposition of thymidine by low-energy electrons: Implications for the molecular mechanisms of single-strand breaks in DNA”, *Angew. Chem. Int. Ed.* **45**, 1893–1896 (2006).
- [13] S. Denifl, S. Ptasińska, G. Hanel, B. Gstir, M. Probst, P. Scheier, and T. D. Märk, “Electron attachment to gas-phase uracil”, *J. Chem. Phys.* **120**, 6557–6565 (2004).
- [14] G. A. Gallup and I. I. Fabrikant, “Vibrational Feshbach resonances in dissociative electron attachment to uracil”, *Phys. Rev. A* **83**, 012706 (2011).
- [15] S. Denifl, P. Sulzer, F. Zappa, S. Moser, B. Kraeutler, O. Echt, D. K. Bohme, T. D. Märk, and P. Scheier, “Isotope effects in dissociative electron attachment to the dna base thymine”, *Int. J. Mass Spectrom.* **277**, 296–299 (2008).
- [16] J. H. Hendricks, S. A. Lyapustina, H. L. de Clercq, J. T. Snodgrass, and K. H. Bowen, “Dipole bound, nucleic acid base anions studied via negative ion photoelectron spectroscopy”, *J. Chem. Phys.* **104**, 7788–7791 (1996).
- [17] J. Schiedt, R. Weinkauff, D. M. Neumark, and E. W. Schlag, “Anion spectroscopy of uracil, thymine and the amino-oxo and amino-hydroxy tautomers of cytosine and their water clusters”, *Chem. Phys.* **239**, 511–524 (1998).
- [18] T. Sommerfeld, “Intramolecular electron transfer from dipole-bound to valence orbitals: uracil and 5-chlorouracil”, *J. Phys. Chem. A* **108**, 9150–9154 (2004).

- [19] T. Takayanagi, T. Asakura, and H. Motegi, “Theoretical study on the mechanism of low-energy dissociative electron attachment for uracil”, *J. Phys. Chem. A* **113**, 4795–4801 (2009).
- [20] H. Motegi and T. Takayanagi, “Theoretical study on the transformation mechanism between dipole-bound and valence-bound anion states of small uracil-water clusters and their photoelectron spectra”, *J. Mol. Struct.-THEOCHEM* **907**, 85–92 (2009).
- [21] Y. Yokoi, K. Kano, Y. Minoshima, and T. Takayanagi, “Application of long-range corrected density-functional theory to excess electron attachment to biomolecules”, *Comput. Theor. Chem.* **1046**, 99–106 (2014).
- [22] J. D. Gu, J. Leszczynski, and H. F. Schaefer, “Interactions of electrons with bare and hydrated biomolecules: from nucleic acid bases to DNA segments”, *Chem. Rev.* **112**, 5603–5640 (2012).
- [23] M. A. Yandell, S. B. King, and D. M. Neumark, “Time-resolved radiation chemistry: photoelectron imaging of transient negative ions of nucleobases”, *J. Am. Chem. Soc.* **135**, 2128–2131 (2013).
- [24] S. B. King, M. A. Yandell, and D. M. Neumark, “Time-resolved photoelectron imaging of the iodide-thymine and iodide-uracil binary cluster systems”, *Faraday Discuss.* **163**, 59–72 (2013).
- [25] S. B. King, M. A. Yandell, A. B. Stephansen, and D. M. Neumark, “Time-resolved radiation chemistry: Dynamics of electron attachment to uracil following UV excitation of iodide-uracil complexes”, *J. Chem. Phys.* **141**, 224310 (2014).
- [26] W.-L. Li, A. Kunin, E. Matthews, N. Yoshikawa, C. E. H. Dessent, and D. M. Neumark, “Photodissociation dynamics of the iodide-uracil (I^-U) complex”, *J. Chem. Phys.* **145**, 044319 (2016).
- [27] S. B. King, A. B. Stephansen, Y. Yokoi, M. A. Yandell, A. Kunin, T. Takayanagi, and D. M. Neumark, “Electron accommodation dynamics in the DNA base thymine”, *J. Chem. Phys.* **143**, 024312 (2015).
- [28] A. B. Stephansen, S. B. King, Y. Yokoi, Y. Minoshima, W.-L. Li, A. Kunin, T. Takayanagi, and D. M. Neumark, “Dynamics of dipole- and valence bound anions in iodide-adenine binary complexes: A time-resolved photoelectron imaging and quantum mechanical investigation”, *J. Chem. Phys.* **143**, 104308 (2015).
- [29] A. Kunin, W.-L. Li, and D. M. Neumark, “Dynamics of electron attachment and photodissociation in iodide-uracil-water clusters via time-resolved photoelectron imaging”, *J. Chem. Phys.* **149**, 084301 (2018).
- [30] R. N. Compton, H. S. Carman, C. Desfrancois, H. Abdoul-Carime, J. P. Schermann, J. H. Hendricks, S. A. Lyapustina, and K. H. Bowen, “On the binding of electrons to nitromethane - dipole and valence bound anions”, *J. Chem. Phys.* **105**, 3472–3478 (1996).

- [31] O. H. Crawford, “Negative ions of polar molecules”, *Mol. Phys.* **20**, 585–591 (1971).
- [32] S. Carles, F. Lecomte, J. P. Schermann, and C. Desfrancois, “Gas-phase experimental and theoretical studies of adenine, imidazole, pyrrole, and water non-covalent complexes”, *J. Phys. Chem. A* **104**, 10662–10668 (2000).
- [33] M. Hanus, M. Kabelac, J. Rejnek, F. Ryjacek, and P. Hobza, “Correlated ab initio study of nucleic acid bases and their tautomers in the gas phase, in a microhydrated environment, and in aqueous solution. Part 3. Adenine”, *J. Phys. Chem. B* **108**, 2087–2097 (2004).
- [34] I. Kulakowska, M. Geller, B. Lesyng, and K. L. Wierzchowski, “Dipole moments of 2,4-diketopyrimidines: Part II: Uracil, thymine and their derivatives”, *Biochim. Biophys. Acta, Nucleic Acids Protein Synth.* **361**, 119–130 (1974).
- [35] J. Simons, “Molecular anions”, *J. Phys. Chem. A* **112**, 6401–6511 (2008).
- [36] R. Bachorz, W. Klopper, and M. Gutowski, “Coupled-cluster and explicitly correlated perturbation-theory calculations of the uracil anion”, *J. Chem. Phys.* **126**, 085101 (2007).
- [37] C. Desfrancois, H. Abdoul-Carime, and J. P. Schermann, “Electron attachment to isolated nucleic acid bases”, *J. Chem. Phys.* **104**, 7792–7794 (1996).
- [38] O. Dolgounitcheva, V. G. Zakrzewski, and J. V. Ortiz, “Anionic and neutral complexes of uracil and water”, *J. Phys. Chem. A* **103**, 7912–7917 (1999).
- [39] O. Dolgounitcheva, V. G. Zakrzewski, and J. V. Ortiz, “Diffuse-bound and valence-bound anions of cytosine”, *J. Phys. Chem. A* **105**, 8782–8786 (2001).
- [40] D. Svozil, T. Frigato, Z. Havlas, and P. Jungwirth, “Ab initio electronic structure of thymine anions”, *Phys. Chem. Chem. Phys.* **7**, 840–845 (2005).
- [41] J. H. Hendricks, S. A. Lyapustina, H. L. de Clercq, and K. H. Bowen, “The dipole bound-to-covalent anion transformation in uracil”, *J. Chem. Phys.* **108**, 8–11 (1998).
- [42] E. Matthews, R. Cercola, G. Mensa-Bonsu, D. M. Neumark, and C. E. H. Dessent, “Photoexcitation of iodide ion-pyrimidine clusters above the electron detachment threshold: Intracuster electron transfer versus nucleobase-centred excitations”, *J. Chem. Phys.* **148**, 084304 (2018).
- [43] R. Improta, F. Santoro, and L. Blancafort, “Quantum mechanical studies on the photophysics and the photochemistry of nucleic acids and nucleobases”, *Chem. Rev.* **116**, 3540–3593 (2016).
- [44] K. Kleinermands, D. Nachtigallova, and M. S. de Vries, “Excited state dynamics of DNA bases”, *Int. Rev. Phys. Chem.* **32**, 308–342 (2013).
- [45] C. T. Middleton, K. de La Harpe, C. Su, Y. K. Law, C. E. Crespo-Hernández, and B. Kohler, “DNA excited-state dynamics: From single bases to the double helix”, *Annu. Rev. Phys. Chem.* **60**, 217–239 (2009).

- [46] R. J. Peláez, C. Blondel, C. Delsart, and C. Drag, “Pulsed photodetachment microscopy and the electron affinity of iodine”, *J. Phys. B- At. Mol. Opt.* **42**, 125001 (2009).
- [47] H.-T. Liu, C.-G. Ning, D.-L. Huang, and L.-S. Wang, “Vibrational spectroscopy of the dehydrogenated uracil radical by autodetachment of dipole-bound excited states of cold anions”, *Angew. Chem. Int. Ed.* **53**, 2464–2468 (2014).
- [48] B. F. Parsons, S. M. Sheehan, T. A. Yen, D. M. Neumark, N. Wehres, and R. Weinkauf, “Anion photoelectron imaging of deprotonated thymine and cytosine”, *Phys. Chem. Chem. Phys.* **9**, 3291–3297 (2007).
- [49] H. Xie and Z. Cao, “Electron attachment to the DNA bases adenine and guanine and dehydrogenation of their anionic derivatives: density functional study”, *Int. J. Quantum Chem.* **107**, 1261–1269 (2006).
- [50] C. C. Hayden and A. Stolow, “Non-adiabatic dynamics studied by femtosecond time-resolved photoelectron spectroscopy”, in *Photoionization and photodetachment*, Vol. Volume 10, Advanced Series in Physical Chemistry (WORLD SCIENTIFIC, 2000), pp. 91–126.
- [51] D. M. Neumark, “Time-resolved photoelectron spectroscopy of molecules and clusters”, *Annu. Rev. Phys. Chem.* **52**, 255–277 (2001).
- [52] T. Suzuki and B. J. Whitaker, “Non-adiabatic effects in chemistry revealed by time-resolved charged-particle imaging”, *Int. Rev. Phys. Chem.* **20**, 313–356 (2001).
- [53] A. Stolow, “Femtosecond time-resolved photoelectron spectroscopy of polyatomic molecules”, *Annu. Rev. Phys. Chem.* **54**, 89–119 (2003).
- [54] A. Stolow, “Time-resolved photoelectron spectroscopy: Non-adiabatic dynamics in polyatomic molecules”, *Int. Rev. Phys. Chem.* **22**, 377–405 (2003).
- [55] A. Stolow, A. E. Bragg, and D. M. Neumark, “Femtosecond time-resolved photoelectron spectroscopy”, *Chem. Rev.* **104**, 1719–1758 (2004).
- [56] T. Suzuki, “Time-resolved photoelectron spectroscopy and imaging”, in *Modern trends in chemical reaction dynamics*, Vol. Volume 14, Advanced Series in Physical Chemistry (WORLD SCIENTIFIC, 2004), pp. 529–578.
- [57] M. Wollenhaupt, V. Engel, and T. Baumert, “Femtosecond laser photoelectron spectroscopy on atoms and small molecules: prototype studies in quantum control”, *Annu. Rev. Phys. Chem.* **56**, 25–56 (2004).
- [58] T. Suzuki, “Femtosecond time-resolved photoelectron imaging”, *Annu. Rev. Phys. Chem.* **57**, 555–592 (2006).
- [59] J. R. R. Verlet, “Femtosecond spectroscopy of cluster anions: insights into condensed-phase phenomena from the gas-phase”, *Chem. Soc. Rev.* **37**, 505–517 (2008).
- [60] A. Stolow and J. G. Underwood, *Time-resolved photoelectron spectroscopy of nonadiabatic dynamics in polyatomic molecules*, edited by S. A. Rice, Vol. 139 (2008).

- [61] V. G. Stavros and J. R. R. Verlet, “Gas-phase femtosecond particle spectroscopy: a bottom-up approach to nucleotide dynamics”, *Annu. Rev. Phys. Chem.* **67**, 211–232 (2016).
- [62] C. S. Anstöter, J. N. Bull, and J. R. R. Verlet, “Ultrafast dynamics of temporary anions probed through the prism of photodetachment”, *Int. Rev. Phys. Chem.* **35**, 509–538 (2016).
- [63] A. Davis, R. Wester, A. E. Bragg, and D. M. Neumark, “Time-resolved photoelectron imaging of the photodissociation of I_2^- ”, *J. Chem. Phys.* **118**, 999–1002 (2003).
- [64] A. E. Bragg, J. R. R. Verlet, A. Kammrath, O. Cheshnovsky, and D. M. Neumark, “Electronic relaxation dynamics of water cluster anions”, *J. Am. Chem. Soc.* **127**, 15283–15295 (2005).
- [65] W. C. Wiley and I. H. McLaren, “Time-of-flight mass spectrometer with improved resolution”, *Rev. Sci. Instrum.* **26**, 1150–1157 (1955).
- [66] A. Eppink and D. H. Parker, “Velocity map imaging of ions and electrons using electrostatic lenses: application in photoelectron and photofragment ion imaging of molecular oxygen”, *Rev. Sci. Instrum.* **68**, 3477–3484 (1997).
- [67] V. Dribinski, A. Ossadtchi, V. Mandelshtam, and H. Reisler, “Reconstruction of Abel-transformable images: the Gaussian basis-set expansion Abel transform method”, *Rev. Sci. Instrum.* **73**, 2634–2642 (2002).
- [68] M. J. Frisch, G. W. Trucks, H. B. Schlegel, G. E. Scuseria, M. A. Robb, J. R. Cheeseman, J. A. Montgomery Jr., T. Vreven, K. N. Kudin, J. C. Burant, J. M. Millam, S. S. Iyengar, J. Tomasi, V. Barone, B. Mennucci, M. Cossi, G. Scalmani, N. Rega, G. A. Petersson, H. Nakatsuji, M. Hada, M. Ehara, K. Toyota, R. Fukuda, J. Hasegawa, M. Ishida, T. Nakajima, Y. Honda, O. Kitao, H. Nakai, M. Klene, X. Li, J. E. Knox, H. P. Hratchian, J. B. Cross, V. Bakken, C. Adamo, J. Jaramillo, R. Gomperts, R. E. Stratmann, O. Yazyev, A. J. Austin, R. Cammi, C. Pomelli, J. W. Ochterski, P. Y. Ayala, K. Morokuma, G. A. Voth, P. Salvador, J. J. Dannenberg, V. G. Zakrzewski, S. Dapprich, A. D. Daniels, M. C. Strain, O. Farkas, D. K. Malick, A. D. Rabuck, K. Raghavachari, J. B. Foresman, J. V. Ortiz, Q. Cui, A. G. Baboul, S. Clifford, J. Cioslowski, B. B. Stefanov, G. Liu, A. Liashenko, P. Piskorz, I. Komaromi, R. L. Martin, D. J. Fox, T. Keith, M. A. Al-Laham, C. Y. Peng, A. Nanayakkara, M. Challacombe, P. M. W. Gill, B. Johnson, W. Chen, M. W. Wong, C. Gonzalez, and J. A. Pople, *Gaussian 03*, 2004.
- [69] M. J. Frisch, G. W. Trucks, H. B. Schlegel, G. E. Scuseria, M. A. Robb, J. R. Cheeseman, G. Scalmani, V. Barone, B. Mennucci, G. A. Petersson, H. Nakatsuji, M. Caricato, X. Li, H. P. Hratchian, A. F. Izmaylov, J. Bloino, G. Zheng, J. L. Sonnenberg, M. Hada, M. Ehara, K. Toyota, R. Fukuda, J. Hasegawa, M. Ishida, T. Nakajima, Y. Honda, O. Kitao, H. Nakai, T. Vreven, J. A. Montgomery Jr., J. E. Peralta, F. Ogliaro, M. J. Bearpark, J. Heyd, E. N. Brothers, K. N. Kudin, V. N. Staroverov, R.

- Kobayashi, J. Normand, K. Raghavachari, A. P. Rendell, J. C. Burant, S. S. Iyengar, J. Tomasi, M. Cossi, N. Rega, N. J. Millam, M. Klene, J. E. Knox, J. B. Cross, V. Bakken, C. Adamo, J. Jaramillo, R. Gomperts, R. E. Stratmann, O. Yazyev, A. J. Austin, R. Cammi, C. Pomelli, J. W. Ochterski, R. L. Martin, K. Morokuma, V. G. Zakrzewski, G. A. Voth, P. Salvador, J. J. Dannenberg, S. Dapprich, A. D. Daniels, Ö. Farkas, J. B. Foresman, J. V. Ortiz, J. Cioslowski, and D. J. Fox, *Gaussian 09, Revision C.01*, 2009.
- [70] F. Martin, P. D. Burrow, Z. L. Cai, P. Cloutier, D. Hunting, and L. Sanche, “DNA strand breaks induced by 0-4 eV electrons: The role of shape resonances”, *Phys. Rev. Lett.* **93**, 068101 (2004).
- [71] T. H. Dunning, “Gaussian basis sets for use in correlated molecular calculations. I. The atoms boron through neon and hydrogen”, *J. Chem. Phys.* **90**, 1007–1023 (1989).
- [72] K. A. Peterson, B. C. Shepler, D. Figgen, and H. Stoll, “On the spectroscopic and thermochemical properties of ClO, BrO, IO, and their anions”, *J. Phys. Chem. A* **110**, 13887 (2006).
- [73] M. A. Yandell, S. B. King, and D. M. Neumark, “Decay dynamics of nascent acetonitrile and nitromethane dipole-bound anions produced by intracluster charge-transfer”, *J. Chem. Phys.* **140**, 184317 (2014).
- [74] A. D. McLean and G. S. Chandler, “Contracted Gaussian basis sets for molecular calculations. I. Second row atoms, Z=11-18”, *J. Chem. Phys.* **72**, 5639–5648 (1980).
- [75] A. Bergner, M. Dolg, W. Küchle, H. Stoll, and H. Preuß, “Ab initio energy-adjusted pseudopotentials for elements of groups 13-17”, *Mol. Phys.* **80**, 1431–1441 (1993).
- [76] R. Krishnan, J. S. Binkley, R. Seeger, and J. A. Pople, “Self-consistent molecular orbital methods. XX. a basis set for correlated wave functions”, *J. Chem. Phys.* **72**, 650–654 (1980).
- [77] A. D. Becke, “Density-functional thermochemistry. III. The role of exact exchange”, *J. Chem. Phys.* **98**, 5648–5652 (1993).
- [78] T. Clark, J. Chandrasekhar, G. W. Spitznagel, and P. V. R. Schleyer, “Efficient diffuse function-augmented basis sets for anion calculations. III. The 3-21+G basis set for first-row elements, Li-F”, *J. Comp. Chem.* **4**, 294–301 (1983).
- [79] M. J. Frisch, J. A. Pople, and J. S. Binkley, “Self-consistent molecular orbital methods 25. Supplementary functions for Gaussian basis sets”, *J. Chem. Phys.* **80**, 3265–3269 (1984).
- [80] A. Kunin, W.-L. Li, and D. M. Neumark, “Time-resolved photoelectron imaging of iodide-nitromethane ($\Gamma \cdot \text{CH}_3\text{NO}_2$) photodissociation dynamics”, *Phys. Chem. Chem. Phys.* **18**, 33226–33232 (2016).
- [81] T. Beyer and D. F. Swinehart, “Number of multiply-restricted partitions”, *Commun. ACM* **16**, 379–379 (1973).

- [82] S. E. Stein and B. S. Rabinovitch, “Accurate evaluation of internal energy level sums and densities including anharmonic oscillators and hindered rotors”, *J. Chem. Phys.* **58**, 2438–2445 (1973).
- [83] C. E. H. Dessent, J. Kim, and M. A. Johnson, “Spectroscopic observation of vibrational Feshbach resonances in near-threshold photoexcitation of $X^- \cdot \text{CH}_3\text{NO}_2$ ($X^- = \text{I}^-$ and Br^-)”, *Faraday Discuss.* **115**, 395–406 (2000).
- [84] F. Lecomte, S. Carles, C. Desfrancois, and M. A. Johnson, “Dipole bound and valence state coupling in argon-solvated nitromethane anions”, *J. Chem. Phys.* **113**, 10973–10977 (2000).
- [85] C. L. Adams, H. Schneider, K. M. Ervin, and J. M. Weber, “Low-energy photoelectron imaging spectroscopy of nitromethane anions: electron affinity, vibrational features, anisotropies, and the dipole-bound state”, *J. Chem. Phys.* **130**, 074307 (2009).
- [86] J. E. Sansonetti and W. C. Martin, “Handbook of basic atomic spectroscopic data”, *J. Phys. Chem. Ref. Data* **34**, 1559–2259 (2005).
- [87] J. Simons, “Propensity rules for vibration-induced electron detachment of anions”, *J. Am. Chem. Soc.* **103**, 3971–3976 (1981).
- [88] P. K. Acharya, R. A. Kendall, and J. Simons, “Vibration-induced electron detachment in molecular anions”, *J. Am. Chem. Soc.* **106**, 3402–3407 (1984).
- [89] E. E. B. Campbell and R. D. Levine, “Delayed ionization and fragmentation en route to thermionic emission: statistics and dynamics”, *Annu. Rev. Phys. Chem.* **51**, 65–98 (2000).
- [90] J. U. Andersen, E. Bonderup, and K. Hansen, “Thermionic emission from clusters”, *J. Phys. B: At., Mol. Opt. Phys.* **35**, R1 (2002).
- [91] R. B. Metz, D. R. Cyr, and D. M. Neumark, “Study of the 2B_1 and 2A_2 states of CH_2NO_2 via ultraviolet photoelectron spectroscopy of the CH_2NO_2^- anion”, *J. Phys. Chem.* **95**, 2900–2907 (1991).
- [92] W. L. Hase, “Simulations of gas-phase chemical reactions: applications to SN_2 nucleophilic substitution”, *Science* **266**, 998–1002 (1994).
- [93] J. Xie, R. Otto, J. Mikosch, J. Zhang, R. Wester, and W. L. Hase, “Identification of atomic-level mechanisms for gas-phase $X^- + \text{CH}_3\text{Y}$ SN_2 reactions by combined experiments and simulations”, *Acc. Chem. Res.* **47**, 2960–2969 (2014).
- [94] M. L. Chabinye, S. L. Craig, C. K. Regan, and J. I. Brauman, “Gas-phase ionic reactions: dynamics and mechanism of nucleophilic displacements”, *Science* **279**, 1882 (1998).
- [95] H. Wang, G. H. Peslherbe, and W. L. Hase, “Trajectory studies of SN_2 nucleophilic substitution. 4. Intramolecular and unimolecular dynamics of the $\text{I}^- \cdots \text{CH}_3\text{Br}$ and $\text{ClCH}_3 \cdots \text{Br}^-$ complexes”, *J. Am. Chem. Soc.* **116**, 9644–9651 (1994).

- [96] G. H. Peslherbe, H. Wang, and W. L. Hase, “Unimolecular dynamics of $\text{Cl}^- \cdots \text{CH}_3\text{Cl}$ intermolecular complexes formed by $\text{Cl}^- + \text{CH}_3\text{Cl}$ association”, *J. Chem. Phys.* **102**, 5626–5635 (1995).
- [97] K. Mazurkiewicz, R. Bachorz, M. Gutowski, and J. Rak, “On the unusual stability of valence anions of thymine based on very rare tautomers: A computational study”, *J. Phys. Chem. B* **110**, 24696–24707 (2006).
- [98] N. A. Oyler and L. Adamowicz, “Electron attachment to uracil: theoretical ab initio study”, *J. Phys. Chem.* **97**, 11122–11123 (1993).
- [99] Y. He, C. Wu, and W. Kong, “Decay pathways of thymine and methyl-substituted uracil and thymine in the gas phase”, *J. Phys. Chem. A* **107**, 5145–5148 (2003).
- [100] Y. He, C. Wu, and W. Kong, “Photophysics of methyl-substituted uracils and thymines and their water complexes in the gas phase”, *J. Phys. Chem. A* **108**, 943–949 (2004).
- [101] C. A. Morgado, K. Y. Pichugin, and L. Adamowicz, “Stabilization of an excess electron on uracil by water. Ab initio study”, *Phys. Chem. Chem. Phys.* **6**, 2758–2762 (2004).
- [102] G. Markovich, R. Giniger, M. Levin, and O. Cheshnovsky, “Photoelectron spectroscopy of iodine anion solvated in water clusters”, *J. Chem. Phys.* **95**, 9416–9419 (1991).
- [103] G. Markovich, S. Pollack, R. Giniger, and O. Cheshnovsky, “Photoelectron spectroscopy of Cl^- , Br^- , and I^- solvated in water clusters”, *J. Chem. Phys.* **101**, 9344–9353 (1994).
- [104] G. L. Gutsev and L. Adamowicz, “Relationship between the dipole-moments and the electron-affinities for some polar organic-molecules”, *Chem. Phys. Lett.* **235**, 377–381 (1995).
- [105] G. L. Gutsev and L. Adamowicz, “Electronic and geometrical structure of dipole-bound anions formed by polar-molecules”, *J. Phys. Chem.* **99**, 13412–13421 (1995).
- [106] D. Roca-Sanjuán, M. Merchan, L. Serrano-Andres, and M. Rubio, “Ab initio determination of the electron affinities of DNA and RNA nucleobases”, *J. Chem. Phys.* **129**, 095104 (2008).
- [107] E. D. Raczyńska, M. Makowski, K. Zientara-Rytter, K. Kolczyńska, T. M. Stepniewski, and M. Hallmann, “Quantum-chemical studies on the favored and rare tautomers of neutral and redox adenine”, *J. Phys. Chem. A* **117**, 1548–1559 (2013).
- [108] M. Haranczyk, M. Gutowski, X. Li, and K. H. Bowen, “Bound anionic states of adenine”, *Proc. Natl. Acad. Sci. U.S.A.* **104**, 4804–4807 (2007).
- [109] X. Li, K. H. Bowen, M. Haranczyk, R. Bachorz, K. Mazurkiewicz, J. Rak, and M. Gutowski, “Photoelectron spectroscopy of adiabatically bound valence anions of rare tautomers of the nucleic acid bases”, *J. Chem. Phys.* **127**, 174309 (2007).

- [110] H. L. Williams, B. A. Erickson, and D. M. Neumark, “Time-resolved photoelectron spectroscopy of adenosine and adenosine monophosphate photodeactivation dynamics in water microjets”, *J. Chem. Phys.* **148**, 194303 (2018).
- [111] F. Buchner, H. H. Ritze, J. Lahl, and A. Lübcke, “Time-resolved photoelectron spectroscopy of adenine and adenosine in aqueous solution”, *Phys. Chem. Chem. Phys.* **15**, 11402–11408 (2013).
- [112] F. Buchner, A. Nakayama, S. Yamazaki, H. H. Ritze, and A. Lübcke, “Excited-state relaxation of hydrated thymine and thymidine measured by liquid-jet photoelectron spectroscopy: experiment and simulation”, *J. Am. Chem. Soc.* **137**, 2931–2938 (2015).

Chapter 8

Femtosecond Time-Resolved Photoelectron Spectroscopy of Molecular Anions

“It’s no use going back to
yesterday, because I was a
different person then.”

Lewis Carroll

The content and figures of this chapter are adapted with permission from:

A. Kunin and D. M. Neumark, “Femtosecond Time-Resolved Photoelectron Spectroscopy of Molecular Anions” In *Physical Chemistry of Cold Gas-Phase Functional Molecules and Clusters*, edited by Ebata, T. and Fujii, M. Springer Nature Singapore Pte Ltd. pp 307–335 (2019).

8.1 Abstract

Femtosecond time-resolved photoelectron spectroscopy (TRPES) is a powerful technique to probe the ultrafast excited state dynamics of molecules. TRPES applied to gas-phase molecular anions and clusters is capable of probing not only excited state formation and relaxation, but also electron accommodation dynamics upon injection of an excess electron into a solvent or molecule. We review the basics of TRPES as it applies to molecular anions and several applications including the study of electron solvation dynamics in clusters and excited state relaxation in several biomolecules. We then explore in detail the dynamics of electron attachment and photodissociation in iodide-nucleobase clusters studied by TRPES as a model system for examining radiative damage of DNA induced by low-energy electrons. By initiating charge transfer from iodide to the nucleobase and following the dynamics of the resulting transient negative ions with femtosecond time resolution, TRPES provides a novel window into the chemistry triggered by the attachment of low-energy electrons to nucleobases.

8.2 Introduction

Anions are ubiquitous in nature and are important in many biological processes and chemical phenomena. Anionic clusters, which are gas-phase size-selected aggregates of atoms or molecules with one or more excess electrons, can readily be mass-selected and hence are particularly useful model systems to study the evolution of electronic and vibrational structure as a function of size for many systems, including carbon clusters [1, 2], metal and semiconductor clusters [3–6], and solute-solvent clusters [7–9]. One can also investigate electron accommodation or solvation dynamics in an isolated environment [10, 11], thus gaining new insights into the energetics and mechanism of electron solvation in water and other solvents [12]. Anionic clusters can also model charge transfer processes such as charge-transfer-to-solvent (CTTS) transitions with the use of an anionic dopant that, upon photoexcitation, injects the excess electron into the solvent [12, 13]. Modeling electron transfer and attachment dynamics is especially relevant for the study of a number of biological processes such as single- and double-strand DNA damage induced by low-energy electron attachment [14], or dynamics in electron transport chains found in photosynthesis and cellular respiration processes [15].

Femtosecond (fs) time-resolved photoelectron spectroscopy (TRPES) is a powerful technique to probe the excited states and ultrafast relaxation or dissociation dynamics in molecules and clusters [16–18]. In anions, this pump-probe technique creates an excited state upon pump excitation of a ground state anion; the probe pulse photodetaches the excess electron and the resulting time-evolving photoelectron energy and angular distribution follows the resulting relaxation or decay dynamics. Negative ions are particularly well-suited to study with TRPES as the excess electron binding energy is typically within the range of energies

that can be easily generated by traditional Ti:sapphire ultrafast lasers.

The basic principles and several applications of TRPES have been thoroughly reviewed [11, 15–28], so we focus here on only the key concepts as they relate to the study of anions. Single-photon anion photoelectron spectroscopy (PES) [29–35], shown schematically in Fig. 8.1a, employs a laser beam of photon energy $h\nu$ to photodetach the excess electron of a prepared, stable anion. Only if the photon energy exceeds the electron binding energy (eBE) of the electron to the anion can the excess electron be detached. The kinetic energy (eKE) distribution of the outgoing photodetached electrons is measured, and the principle of energy conservation, as shown in Eq. 8.1, may then be used to determine accurate eBEs:

$$\text{eBE} = h\nu - \text{eKE} \quad (8.1)$$

For a one-electron transition, photodetachment can occur to any neutral vibrational (and electronic) states within the photon energy range, provided there is sufficient Franck-Condon overlap between the anion and neutral vibrational wavefunctions. Identification of the transition between the anion and neutral vibrational ground states yields the electron

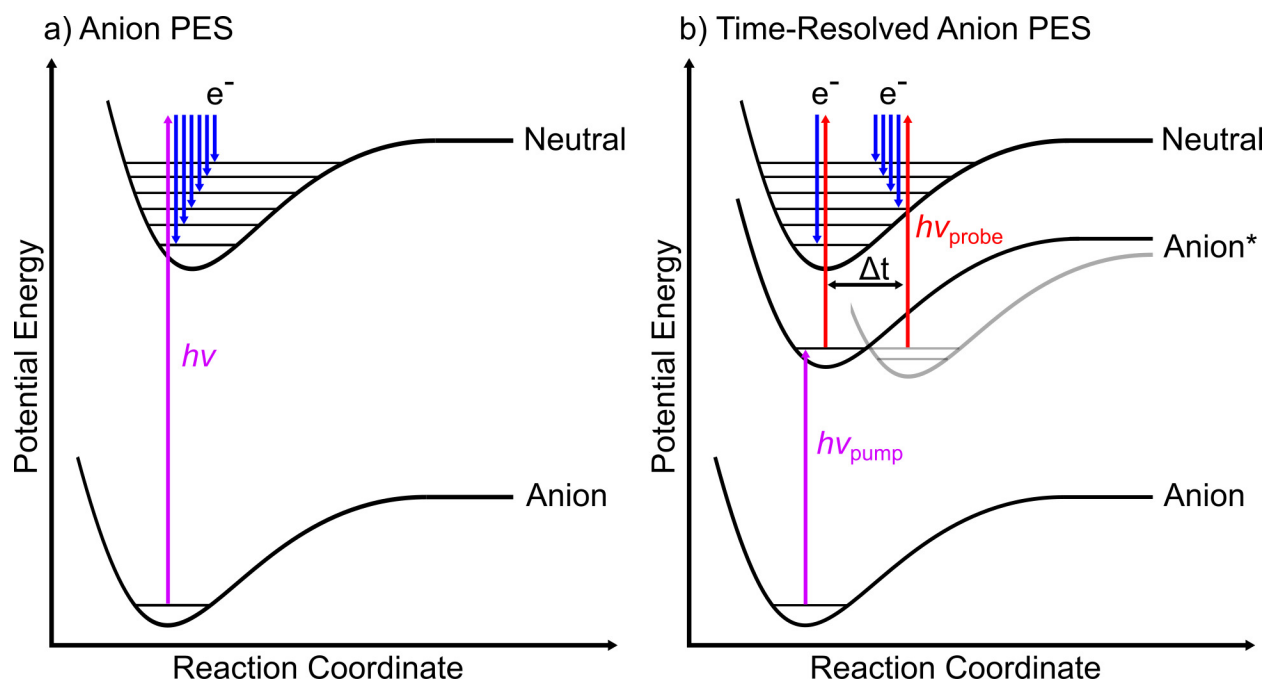


Figure 8.1: Example scheme for a) anion PES and b) TRPES. Anion* indicates the photoexcited state. The blue lines indicate the resultant kinetic energies of the photodetached electrons. Reproduced from Ch. 7 for clarity.

affinity (EA). The vertical detachment energy (VDE) corresponds to the difference in energy between the anion and the neutral at the equilibrium geometry of the anion. In spectra that do not show any vibrational structure, the VDE is identifiable as the peak or maximum intensity (maximum Franck-Condon overlap) of the photoelectron spectrum, and the width of the spectrum is an indication of the geometry change that occurs upon photodetachment.

Fig. 8.1b shows a schematic diagram for fs anion TRPES. A fs pump pulse is used to generate an electronically excited anion, which can decay by multiple mechanisms including dissociation, internal conversion, or autodetachment. A time-delayed fs probe pulse photodetaches this transient negative ion (TNI) to monitor its temporal evolution, enabling characterization of these various pathways. A sufficiently energetic probe pulse can interrogate not only TNIs, but also any anionic dissociation products that may form due to fragmentation, as well its radiationless transitions to other excited states or the anion ground state. The ability to follow ground state dynamics is a notable advantage of anion TRPES as compared to neutral TRPES, in which ionization from the ground state is often not energetically feasible. Thus, anion TRPES can offer a complete picture of the relaxation and dissociation dynamics subsequent to electronic excitation.

Anion TRPES has been previously applied to study size-dependent electron solvation dynamics or CTTS dynamics with an iodide dopant atom in a cluster of solvent molecules or atoms [12, 36]. Size-dependent relaxation dynamics have also been probed for carbon clusters [37, 38] and transition metal clusters [39–45] with anion TRPES. TRPES has also been applied to probe fundamental dynamics of long-range interactions involved in excess electron binding, such as non-valence bound anionic states [46–48] and multiply-charged anions (MCAs) [49–52]. In recent years, electronic resonances and electron accommodation dynamics in many biologically-relevant species have been of great interest [53–57].

In this chapter, Section 8.3 provides a brief description of select past studies to illustrate the nature of the information that is uniquely gained by the versatile application of TRPES to anionic clusters. Section 8.4 delves into the specific work that has been done in the Neumark group on the dynamics of TNI formation and decay in iodide-nucleobase ($I^- \cdot N$) clusters as a model system for the reductive damage of DNA. Section 8.5 covers the experimental and computational methodologies specific to the study of $I^- \cdot N$ complexes, and Section 8.6 examines the results of these TRPES studies of iodide-uracil ($I^- \cdot U$) and iodide-thymine ($I^- \cdot T$) clusters, as well as the simpler, model system of photoexcited iodide-nitromethane ($I^- \cdot CH_3NO_2$) clusters that provide an illustrative framework for understanding the more complex dynamics of the larger nucleobase species. We conclude with a summary and outlook for future applications of anion TRPES of iodide-containing clusters to advance our understanding of reductive damage pathways in DNA.

8.3 A Brief Overview of Past Anion TRPES Studies

Several TRPES studies by the Neumark and Zewail groups have been directed at probing relaxation dynamics in size-selected anionic clusters A_n^- and iodide-associated $I^- \cdot A_n$ clusters, including carbon clusters [37, 38, 58, 59], oxygen and solvated oxygen species [60–63], mercury [45, 64–67], and I_2^- and $I_2^- \cdot A_n$ [68–82], among others [83, 84]. Others have worked to theoretically simulate the TRPE spectra of I_2^- and $I_2^- \cdot Y$ complexes to aid and improve the dynamical analysis of these studies [85–88], and the I_2^- studies have also been extended by Sanov [89, 90] to probe the photodissociation dynamics of I_2Br^- and IBr^- anions. TRPES has also been used by the Eberhardt and Ganteför groups to explore dynamics of metal thermalization in transition metal A_n^- clusters [39–44, 91, 92] and desorption in metals with anionic adsorbates [93–98]. These transition metal cluster studies are able to probe the metal band structure and relaxation processes on a molecular level. Much of this work has been previously reviewed [11].

TRPES has been employed by Johnson [99], Neumark [100–104], and Zewail [36] to study size-selected $(H_2O)_n^-$ and $(D_2O)_n^-$ water clusters to probe the time-resolved dynamics of solvated electrons. These studies probed the excited state lifetimes of electronically excited water clusters as a model for the relaxation of the bulk solvated electron. The relaxation mechanism is expected to be initial relaxation along the excited state surface, internal conversion (IC), and finally ground state relaxation, but the timescales for each step are a matter of debate [12]. Transient absorption studies of hydrated electrons have measured a rapid, initial ~ 50 fs lifetime that has been ascribed either to relaxation along the excited state surface (“adiabatic” model) [105, 106] or IC (“nonadiabatic” model) [107] as the fastest observable step. TRPES of $(H_2O)_n^-$ clusters by Neumark and co-workers [101, 103, 108] measured abrupt appearance and decay of an excited state feature with concomitant dynamics for ground state depletion and recovery, which is indicative of decay by IC. A dramatic decrease in excited state lifetime was observed with increasing cluster size, with sub-100 fs IC of the excited state in the largest clusters studied ($n = 70 - 200$) [103]. Thus, this rapid timescale for IC strongly supports the nonadiabatic model for hydrated electron relaxation. This nonadiabatic mechanism is also more recently supported by TRPES studies of hydrated electrons in liquid micro-jets by Neumark [109, 110] and Suzuki [111].

TRPES of $I^- \cdot (H_2O)_n$ and $I^- \cdot (D_2O)_n$ clusters [112–114] allow one to study the injection of an excess electron into a solvent network as in a CTTS transition since a UV pump pulse can be used to promote charge transfer from the iodide to the solvent moiety (S_n), as in Eq. 8.2:



TRPES of $\text{I}^{\cdot-}(\text{H}_2\text{O})_n$ most notably exhibited a strong shift to higher VDEs of the excited state feature after 1 – 2 ps, and greater magnitude shifting was observed in larger clusters. When compared to the VDEs measured for different isomers of $(\text{H}_2\text{O})_n^-$ clusters, this shift suggests that the water cluster relaxation proceeds in a few ps via isomerization from an initially surface bound excess electron to one that may be in a more tightly bound configuration [112–116].

Other S_n^- and $\text{I}^{\cdot-}\text{S}_n$ solvent clusters have also been investigated in time-resolved experiments by Neumark and Zewail, including those of methanol and various iodide-alcohol complexes [117–120], ammonia [121, 122], acetonitrile $(\text{CH}_3\text{CN})_n^-$ [123, 124], and tetrahydrofuran $(\text{C}_4\text{H}_8\text{O})$ [125, 126]. Many of these solvents are proposed to share some similarities with the proposed relaxation schemes for water, although differences in hydrogen bonding and solvent molecule packing result in different sites or cavities that the excess electron can occupy. Additionally, the presence of different vibrational modes in these solvents compared to those of water affects the IC and solvent motion-driven relaxation pathways. These studies have been previously reviewed in considerable detail [11, 12].

Anion TRPES has also been employed to analyze the properties and dynamics of several non-traditional valence anions. While conventional anions have the excess electron occupying a valence orbital, nonvalence bound anions, in which there is a long-range attraction between the molecular core and the excess electron, are also important species [127]. These anions can be dipole-bound or multipole-bound if the neutral species possesses a sufficiently large dipole or multipole moment, as discussed in considerable detail in the later portions of this chapter. More recently, Verlet and co-workers have reported observation of correlation-bound states (CBSs) of the para-toluquinone trimer cluster anion $(\text{pTQ})_3^-$ [47], and the iodide-hexafluorobenzene cluster $(\text{I}^{\cdot-}\cdot\text{C}_6\text{F}_6)$ using TRPES [48]. Such CBSs have been described by calculations to be nonvalence bound states that arise from correlation forces between the excess electron and the molecular valence electrons [128–133]. With TRPES, the pump pulse is used to either excite the species to a π^* excited state that appears to internally convert to a transient CBS in <60 fs, as in the case of $(\text{pTQ})_3^-$, or the pump pulse may generate the CBS directly via UV initiated charge transfer from iodide, as in $\text{I}^{\cdot-}\cdot\text{C}_6\text{F}_6$, and the probe pulse follows the evolution and decay of this metastable state.

Repulsive long-range interactions in the form of the repulsive Coulomb barrier (RCB) are fundamental in dictating the characteristics and stability of multiply charged anions (MCAs), as shown by Wang [33] and others [52]. For multiply charged anions with negative EA, the RCB can support (meta)stable gas-phase A^{n-} MCAs because although the energy of the excess electron may lie above the $\text{A}^{(n-1)-} + e^-$ energetic asymptote, the RCB imposes an energetic barrier such that this electron must be photoexcited well above the EA to be detached. TRPES has been used by Kappes [49–51, 134, 135] and Verlet [136–138] to probe the properties and decay dynamics of the resonant states that are bound by the

RCB in a number of MCA fluorophores and chromophores. These time-resolved studies are able to determine the lifetimes for excited state IC, intersystem crossing, and tunneling autodetachment.

We close this section with a brief discussion of the more recent applications of TRPES to study a number of electron-driven processes prominent in biological systems. Electron transport chains (ETCs), for example, are key for energy extraction in photosynthesis and cellular respiration, and quinones are often found as electron acceptors in ETCs [15]. TRPES has been used by Verlet to probe numerous anionic quinone derivatives [54, 139–142] including coenzyme Q₀ [143, 144] and vitamin K3 [145], in a bottom-up approach to understanding the role of this structural motif in ETCs. Chemical substitutions in this class of quinones were used with TRPES to probe, for example, the effects of conjugation or various nearby electron donating groups on the timescales and mechanisms of excited state IC. Important biological chromophores have also been studied with anion TRPES in the Verlet and Zewail groups, including stilbene [146], the anionic fluorescent chromophore of green fluorescent protein (GFP) [55, 147–149] and the timescales for twisting in the trans-to-cis isomerization process of the photoactive yellow protein chromophore [53].

Mechanisms of excited state relaxation and dissociation in DNA and its constituents are naturally of significant interest [150]. To this end, Verlet and co-workers have employed anion TRPES to study the excited state dynamics of isolated deprotonated DNA nucleotides [27, 56, 151]. These studies used UV pump energies near the nucleobase $\pi - \pi^*$ transitions and probed the unique relaxation pathways and timescales for each nucleotide, deprotonated at the phosphate group, to model the non-radiative relaxation processes of DNA. Neumark and co-workers have examined dynamics in a number of iodide-nucleobase clusters, including iodide-uracil ($\text{I}^- \cdot \text{U}$) [152–155], iodide-thymine ($\text{I}^- \cdot \text{T}$) [153, 156], iodide-uracil-water [157], iodide-adenine [158], and the related system iodide-nitromethane ($\text{I}^- \cdot \text{CH}_3\text{NO}_2$) [46, 159], to elucidate the role of low-energy electron attachment to nucleobases in the mechanism of reductive damage of DNA. In the sections that follow, we cover in detail the ultrafast dynamics of electron attachment and photodissociation in photoexcited $\text{I}^- \cdot \text{CH}_3\text{NO}_2$, $\text{I}^- \cdot \text{U}$, and $\text{I}^- \cdot \text{T}$ clusters. This work is described in more detail elsewhere [57].

8.4 Electron Attachment and Photodissociation Dynamics in $\text{I}^- \cdot \text{N}$ Clusters

Low-energy electron attachment to DNA has been shown to induce damage such as single and double strand breaks, and the mechanism of this damage has been a topic of considerable interest in recent years [14]. The initial site of attachment has been implicated to be the DNA nucleobases, and upon attachment a TNI of the base is expected to form [160–162]. It is predicted that electron transfer from the base moiety to the sugar-phosphate backbone,

facilitated by strong electronic coupling [160, 161, 163, 164], then leads to dissociation or fragmentation. These considerations have motivated many experimental and theoretical studies of the interactions between nucleic acid constituents and low-energy electrons [165].

A conventional valence-bound (VB) anion can be formed by electron attachment to the π^* orbital of the nucleobase [161, 166], but an excess electron can also be bound by the fairly large dipolar moment of the base to form a dipole-bound (DB) anion [167]. A molecular dipole moment (μ) of at least $\sim 2 - 2.5$ D is needed to bind the excess electron [168]; all of the canonical nucleobase species examined here have larger dipole moments than this and are thus capable of forming DB anions [169–171]. Electron scattering experiments have suggested that the DB state is initially formed and may then convert or act as a “doorway” to the formation of a VB anion [172]. The decay of these metastable states is then expected to lead to dissociation or fragmentation of the nucleobases, the larger nucleotide, or the DNA backbone structure [173, 174]. To better understand the role of these nucleobase DB and VB anions in DNA damage, many laboratories have probed these anions with a variety of experimental techniques, including dissociative electron attachment [172, 175–177] and anion PES [166, 178, 179]. Numerous theoretical studies of these anions have been carried out as well [180–184]. Anion TRPES is uniquely able to probe the ultrafast time-resolved dynamics and evolution of these TNIs, including interconversion of a DB anion to form a VB anion, as well as the timescales for autodetachment, IC, and fragmentation.

As demonstrated by Bowen and co-workers [178, 185], DB and VB anions can be easily distinguished from one another in photoelectron spectra by both their energetics and spectral shape. DB anions are weakly bound (typically < 100 meV eBE), with the excess electron residing in a large, diffuse orbital outside of the molecular framework [167]. Due to this diffuse nature, the neutral core of a DB state undergoes little or no geometry change upon photodetachment [127], yielding a narrow peak in the anion photoelectron spectrum. VB nucleobase anions typically have VDEs of hundreds of meV [166, 179, 186–189], and the geometry of VB nucleobase anions is typically distorted relative to the neutral nucleobase in the ring puckering coordinate [156, 158, 180, 181, 190], yielding a broad photoelectron spectrum [191]. Photoelectron spectra from Bowen [191], shown in Fig. 8.2 for the U^- DB anion and the $U^- \cdot H_2O$ VB anion, exemplify the binding energy and spectral shape of these two types of negative ions.

In studies of electron attachment dynamics to nucleobases and related species, the nucleobase of interest, N, is clustered with iodide. A UV pump pulse of energy $h\nu_{\text{pump}}$ can be absorbed by the $I^- \cdot N$ complex to initiate charge transfer from the iodide to the nucleobase moiety, thereby creating a TNI:



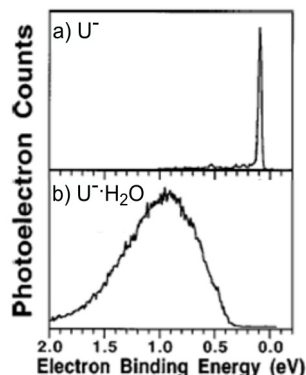
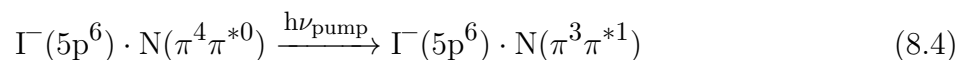


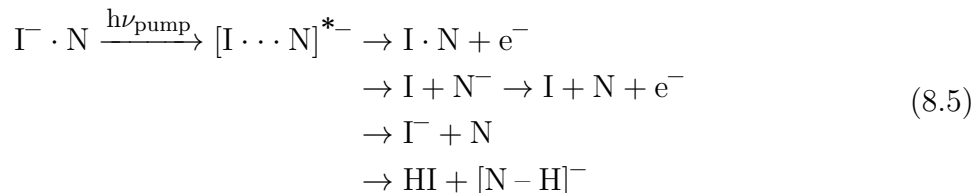
Figure 8.2: Photoelectron spectra of a) the U^- DB anion and b) the $\text{U}^- \cdot \text{H}_2\text{O}$ VB anion. The U^- DB anion exhibits a very narrow peak at very low binding energy, characteristic of DB anions, while the $\text{U}^- \cdot \text{H}_2\text{O}$ anion exhibits a broad feature covering higher eBEs. Adapted with permission from Ref. [191].

This excitation can be carried out near the VDE of the $\text{I}^- \cdot \text{N}$ complex. Excitations of this nature are clearly interesting as a model for reductive DNA damage by low-energy secondary electron attachment. These complexes also exhibit a second regime of UV photoabsorption near 4.8 eV [192], which is calculated [155, 192] to encompass a strong base-centered $\pi - \pi^*$ excitation on the nucleobase with the excess electron still remaining with iodide, i.e.:



Excitation in this UV range is also of interest in the DNA damage mechanism as the rapid, nonradiative photodeactivation pathways of $\pi - \pi^*$ UV photoexcited nucleobases are the core of the remarkable photostability of DNA [193–195]. We believe this $\pi - \pi^*$ excitation is followed by rapid charge transfer from the iodide moiety to fill the hole in the π orbital of the base to create a VB anion, as discussed in more detail in Section 8.6.2 and elsewhere [57].

Photoexcited $\text{I}^- \cdot \text{N}$ clusters can decay by a number of pathways listed in Eq. 8.5, including autodetachment, iodine loss, I^- formation, or a chemical reaction to form HI and a deprotonated nucleobase anion $[\text{N-H}]^-$.



The $\Gamma^- \cdot \text{N}$ TRPES studies here have employed both the 1.58 eV Ti:sapphire fundamental as well as higher energy UV probe pulses to photodetach the nascent TNIs and the possible photofragments these complexes can form, including iodide (eBE = 3.059 eV) [196], as described in more detail in the following sections.

8.5 Methodologies for $\Gamma^- \cdot \text{N}$ Clusters

Fig. 8.3 shows the anion TRPES experimental apparatus used by the Neumark group, which has been described in more detail previously [81, 102]. $\Gamma^- \cdot \text{N}$ clusters are generated by flowing 375 – 450 kPa of neon or argon buffer gas over a reservoir of methyl iodide. This gas mixture passes into a pulsed Even-Lavie valve operating at 500 Hz that contains a cartridge with a solid sample of the nucleobase of interest heated to 205 °C. For the $\Gamma^- \cdot \text{CH}_3\text{NO}_2$ studies, the cartridge is left empty, and instead an additional reservoir on the gas line is filled with liquid CH_3NO_2 and chilled in an ice water bath. In each configuration, the gas mixture is then supersonically expanded into vacuum through a ring filament ionizer to produce cluster anions. The anions are perpendicularly extracted into a Wiley McLaren time-of-flight mass spectrometer [197] and mass-selected to isolate the $\Gamma^- \cdot \text{N}$ species of interest. These ions are photodetached through their interaction with fs pump and probe laser pulses as described below. A velocity map imaging [198] spectrometer focuses the resultant photoelectrons onto a chevron-stacked position-sensitive microchannel plate detector coupled to a phosphor screen which is imaged using a charge-coupled device camera. The 3D eKE distributions are reconstructed using Basis-set expansion (BASEX) methods [199].

Various pump-probe laser schemes are employed among the studies in this work. A KMLabs Griffin oscillator and Dragon amplifier are used to generate 1 kHz, 40 fs pulses centered near 790 nm (1.57 eV) with 1.8 mJ/pulse. The output of the KMLabs system is split into a pump arm and a probe arm delayed by a delay stage. In the pump arm, 1 mJ/pulse of the 1.57 eV light is used to pump a LightCon TOPAS-C optical parametric amplifier. UV light is generated by frequency-doubling the TOPAS-C output with a β -barium borate (BBO) crystal to yield pump pulses between 235 nm – 350 nm of approximately 8 – 13 $\mu\text{J}/\text{pulse}$. Pump pulses near 266 nm ($\sim 5 - 12 \mu\text{J}/\text{pulse}$) can also be generated by frequency tripling the 1.57 eV fundamental infrared (IR) of the KMLabs system. The fundamental can also be used as the probe beam (1.57 eV, 80 $\mu\text{J}/\text{pulse}$), or frequency-doubled in a BBO crystal to yield 395 nm pulses (3.14 eV, 65 $\mu\text{J}/\text{pulse}$). The residual visible non-frequency-doubled

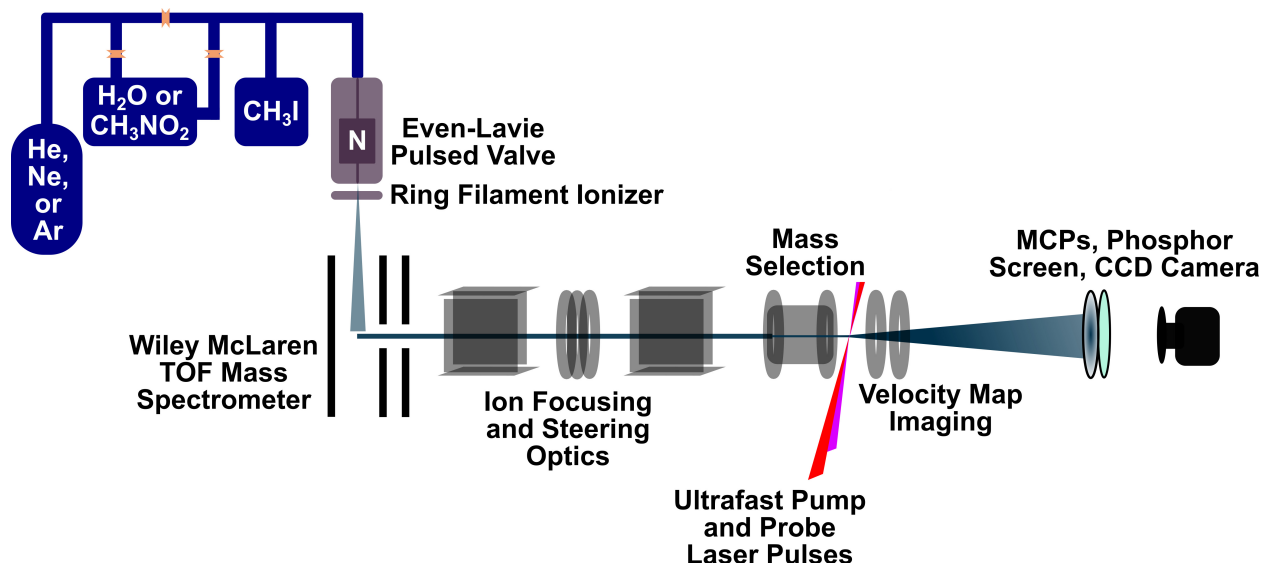


Figure 8.3: Diagram of the TRPES apparatus employed by Neumark and co-workers, reproduced from Ch. 7 for clarity.

TOPAS-C output can also be recovered and recombined nonlinearly in a BBO crystal with the fundamental pulse to yield a UV probe pulse of 344 nm (8 μ J/pulse). Cross-correlations measured outside the vacuum chamber for the pump and probe laser pulses are <150 fs for UV/IR-type pump/probe schemes and $\sim 150 - 200$ fs for UV/UV-type pump/probe schemes.

8.6 $\text{I}^- \cdot \text{CH}_3\text{NO}_2$, $\text{I}^- \cdot \text{U}$, and $\text{I}^- \cdot \text{T}$ clusters

Fig. 8.4 presents the calculated structures [200] for ground state $\text{I}^- \cdot \text{CH}_3\text{NO}_2$, $\text{I}^- \cdot \text{U}$, and $\text{I}^- \cdot \text{T}$ at the MP2/aug-cc-pVDZ(-pp) level of theory. Table 8.1 presents the calculated dipole moments of the neutral I-N species at the equilibrium geometry of the anion, as well as the experimentally measured VDEs of the $\text{I}^- \cdot \text{N}$ species. To facilitate comparison between the three different systems studied here, one-photon and TRPE spectra for each species are shown in Figs. 8.5 – 8.8. Figs. 8.5a) – c) show one-photon photoelectron spectra for $\text{I}^- \cdot \text{CH}_3\text{NO}_2$, $\text{I}^- \cdot \text{U}$, and $\text{I}^- \cdot \text{T}$, respectively. Figs. 8.6a) – c) show near-VDE photoexcited TRPE spectra for each of these systems along with the time-evolution of TNI production and decay at both early and long delay times. Figs. 8.7a) – c) show the time-evolution of I^- production via photodissociation for $\text{I}^- \cdot \text{CH}_3\text{NO}_2$ and $\text{I}^- \cdot \text{U}$, and Figs. 8.8a) and b) show the TRPE spectra and time-dependent signal evolution for $\text{I}^- \cdot \text{U}$ and $\text{I}^- \cdot \text{T}$ photoexcited at excitation energies near ~ 4.7 eV. These results are considered in more detail in the subsections below. For consistency and ease of comparison throughout this work, TRPES pump energies are given as $h\nu_{\text{pump}} - \text{VDE}$, i.e. they are referenced to the VDE of the cluster.

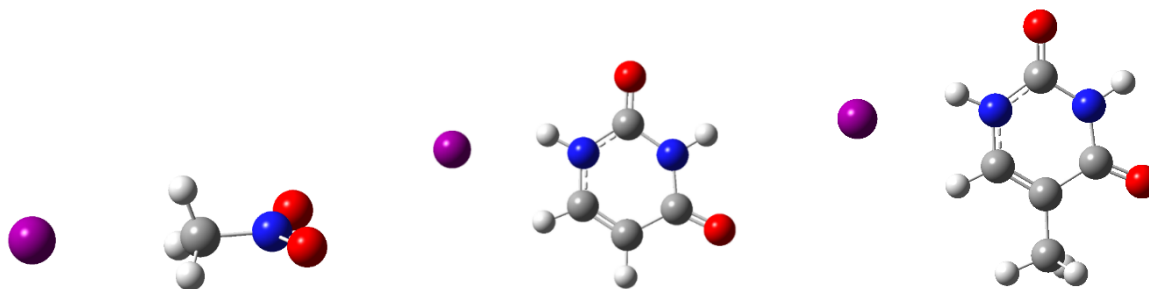


Figure 8.4: Calculated structures for $\text{I}^- \cdot \text{CH}_3\text{NO}_2$ (left), $\text{I}^- \cdot \text{U}$ (center), and $\text{I}^- \cdot \text{T}$ (right). See Ref. [46] for computational details for $\text{I}^- \cdot \text{CH}_3\text{NO}_2$, and Ref. [156] for computational details for $\text{I}^- \cdot \text{U}$ and $\text{I}^- \cdot \text{T}$.

$\text{I}^- \cdot \text{CH}_3\text{NO}_2$

We first apply TRPES to the dynamics of the photoexcited $\text{I}^- \cdot \text{CH}_3\text{NO}_2$ binary complex, which serves as an interesting model system for conversion between DB and VB anions and helps inform studies of the more complex uracil and thymine systems. Nitromethane (CH_3NO_2 , $\mu=3.46$ D) supports both a DB anion as well as a VB anion; the VB anion lies lower in energy and is the ground state of the anion [185, 201, 202]. Both DB and VB anions of CH_3NO_2^- have been previously measured by single-photon PES; the DB anion has a VDE of 8 ± 8 meV, and the VB anion has a VDE of $0.9 - 1$ eV [185, 203].

Photofragment action spectroscopy has been used by Dessent et al to probe $\text{I}^- \cdot \text{CH}_3\text{NO}_2$ binary complexes, which measured the $\text{I}^- \cdot \text{CH}_3\text{NO}_2$ cluster VDE as 3.60 ± 0.01 eV and detected evidence for the presence of the $\text{I}^- \cdot \text{CH}_3\text{NO}_2$ DB anion [201]. Our group has performed two sets of TRPES studies of near-VDE photoexcited $\text{I}^- \cdot \text{CH}_3\text{NO}_2$ clusters at two probe energies: 1.56 eV probe experiments to examine the presence and time-resolved dynamics of DB and VB anions of nitromethane [46], and 3.14 eV probe experiments to measure the time-resolved formation of I^- and other photofragments [159].

Table 8.1: Neutral dipole moments (μ) and VDEs for the $\text{I}^- \cdot \text{N}$ cluster systems examined in this work. Neutral dipole moment is calculated at the ground state anion geometry. Reported VDEs are experimentally measured by single-photon anion PES, all ± 0.05 eV error. See Ref. [156] for computational details for $\text{I}^- \cdot \text{U}$ and $\text{I}^- \cdot \text{T}$.

Cluster	$\text{I}^- \cdot \text{CH}_3\text{NO}_2$	$\text{I}^- \cdot \text{U}$	$\text{I}^- \cdot \text{T}$
VDE (eV)	3.60 eV	4.11 eV	4.05 eV
Neutral μ (D)	4.62 D	6.48 D	6.23 D

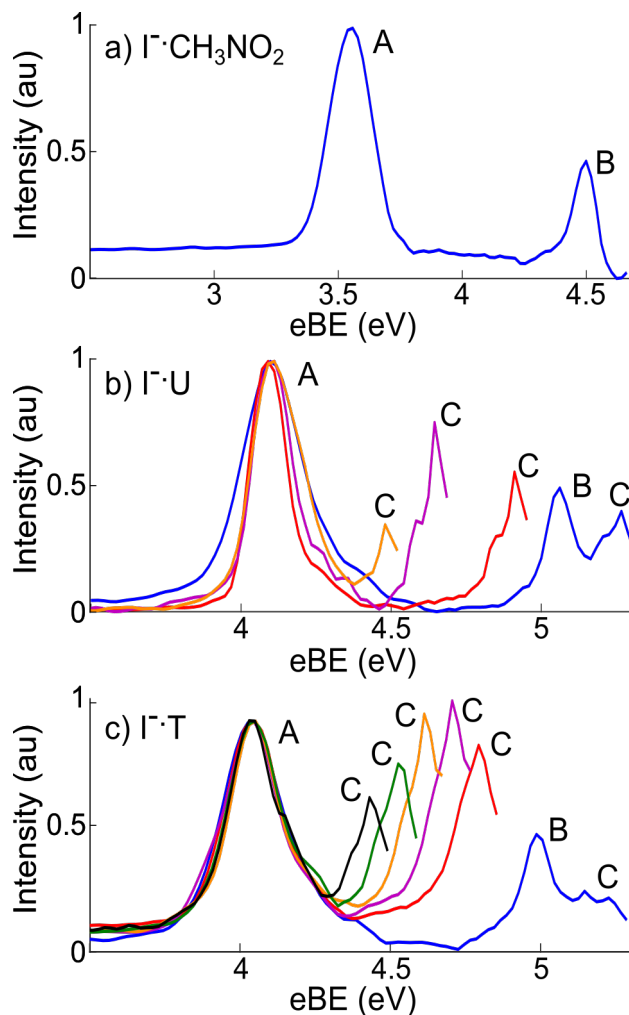


Figure 8.5: Single-photon PE spectra for a) $\text{I}^- \cdot \text{CH}_3\text{NO}_2$ with 4.68 eV; b) $\text{I}^- \cdot \text{U}$ with 5.30 eV in blue, 4.92 eV in red, 4.68 eV in purple, and 4.51 eV in orange; and c) $\text{I}^- \cdot \text{T}$ with 5.30 eV in blue, 4.87 eV in red, 4.78 eV in purple, 4.68 eV in orange, 4.59 eV in green, and 4.51 eV in black. “A” denotes vertical detachment to the lower spin orbit state of the iodine-containing complex ($\text{I}(^2\text{P}_{3/2}) \cdot \text{N}$), “B” denotes detachment to the upper spin orbit state ($\text{I}(^2\text{P}_{1/2}) \cdot \text{N}$), and “C” denotes autodetachment.

Fig. 8.5a shows the single-photon photoelectron spectrum of $\text{I}^- \cdot \text{CH}_3\text{NO}_2$. Feature A, centered at 3.60 eV, corresponds to the cluster VDE, and matches previous experimental results for $\text{I}^- \cdot \text{CH}_3\text{NO}_2$ [201]. This feature corresponds to detachment to the lower spin orbit state of the complex $\text{I}(^2\text{P}_{3/2}) \cdot \text{CH}_3\text{NO}_2$ while feature B, appearing near 4.5 eV, corresponds to photodetachment to the upper spin orbit state of the complex $\text{I}(^2\text{P}_{1/2}) \cdot \text{CH}_3\text{NO}_2$, lying approximately 0.94 eV higher in energy [204].

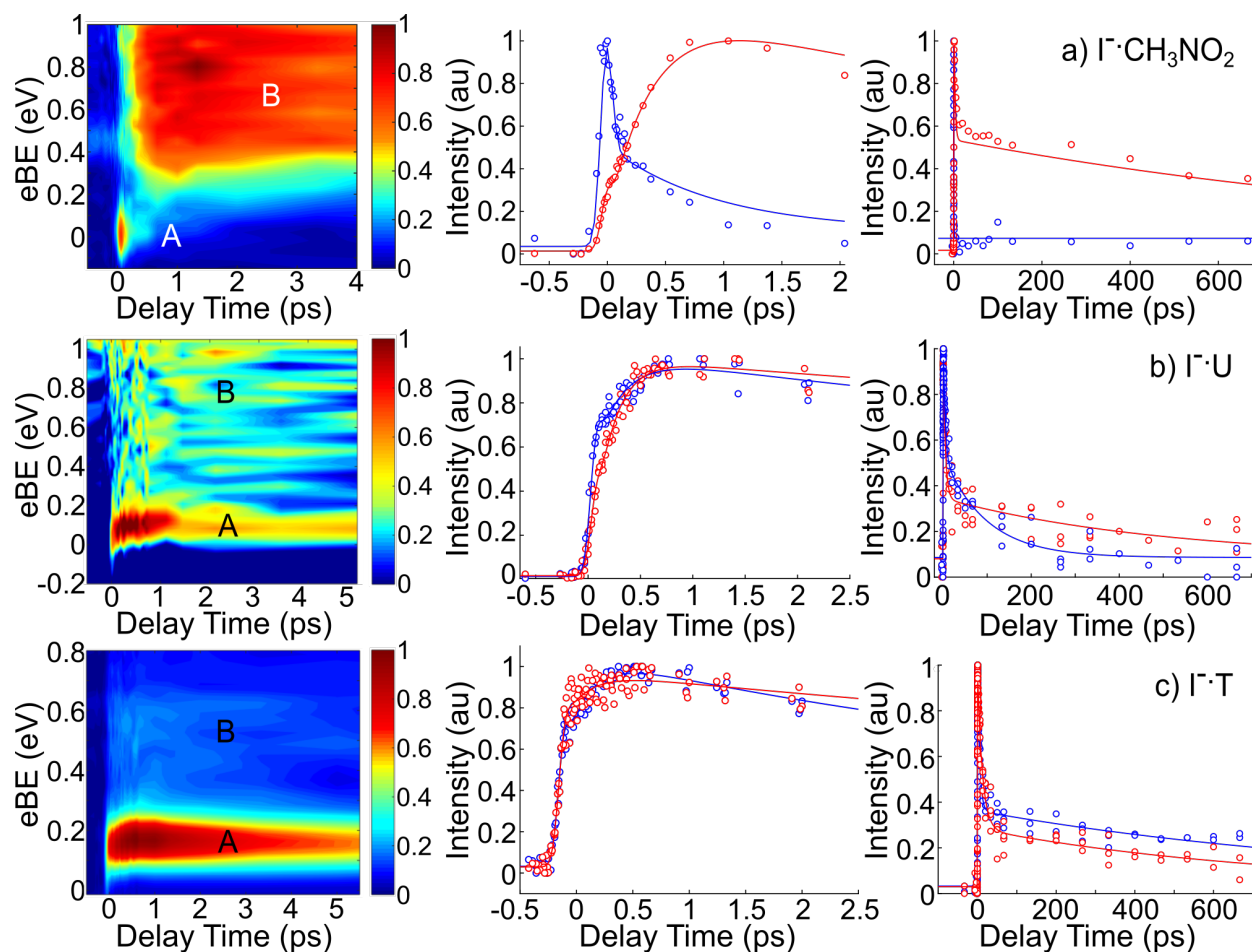


Figure 8.6: TRPE spectra (left) and integrated intensities at both early times and long delay times (right) for the DB anion (feature A, blue) and VB anion (feature B, red) for a) $\text{I}^{\cdot-}\text{CH}_3\text{NO}_2$ photoexcited at +0 meV; b) $\text{I}^{\cdot-}\text{U}$ photoexcited at +30 meV; and c) $\text{I}^{\cdot-}\text{T}$ photoexcited at +20 meV.

TRPE spectra for $\text{I}^{\cdot-}\text{CH}_3\text{NO}_2$ photoexcited at 3.60 eV (at the cluster VDE) and probed at 1.56 eV are shown in Fig. 8.6a. The left panel shows a false-color contour plot of eBE as a function of pump-probe delay. Feature A is a narrow, short-lived, low eBE feature that is assigned to a DB state, while feature B is broader and longer-lived, assigned to a VB state. The center and right panels of Fig. 8.6a present integrated intensities of feature A (blue) and feature B (red) at short and longer time delays, respectively. A similar layout is used for the other rows of Fig. 8.6. The nascent $[\text{I}^{\cdot-}\text{CH}_3\text{NO}_2]^-$ DB anion appears within the cross-correlation of the pump and probe laser pulses, <150 fs, and decays mono-exponentially in 460 ± 60 fs, while the $[\text{I}^{\cdot-}\text{CH}_3\text{NO}_2]^-$ VB anion appears in 420 ± 50 fs [46]. These congruent lifetimes indicate that the DB anion decays primarily to form the VB anion in a rapid and complete or nearly-complete conversion. The VB state was found to decay bi-exponentially

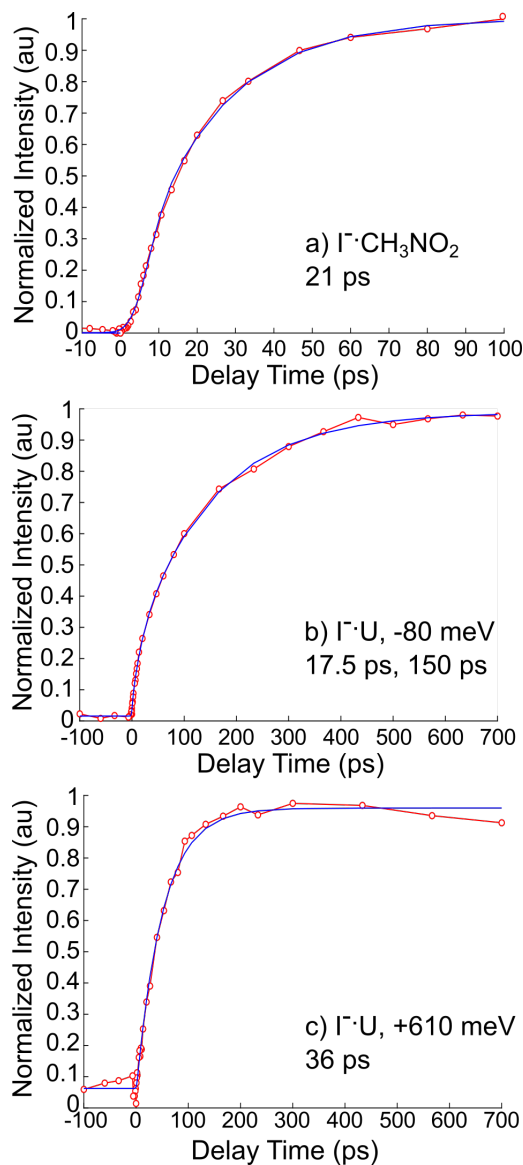


Figure 8.7: Iodide integrated intensities for a) $\text{I}^- \cdot \text{CH}_3\text{NO}_2$, b) $\text{I}^- \cdot \text{U}$ photoexcited -80 meV below the VDE, and c) $\text{I}^- \cdot \text{U}$ photoexcited at +610 meV (4.72 eV).

with time constants of 2 ps and 1300 ps.

A second TRPES study with 3.56 eV pump energy (-40 meV) and 3.14 eV probe energy was performed to characterize the decay dynamics of the $[\text{I} \cdot \cdot \text{CH}_3\text{NO}_2]^-$ VB anion [159]. This probe energy is high enough to detect photodissociation products such as I^- (eBE = 3.059 eV) [196] and the nitromethide anion CH_2NO_2^- (VDE = 2.635 ± 0.010 eV) [159, 205]. I^- is measured as the major photofragmentation channel with a mono-exponential rise

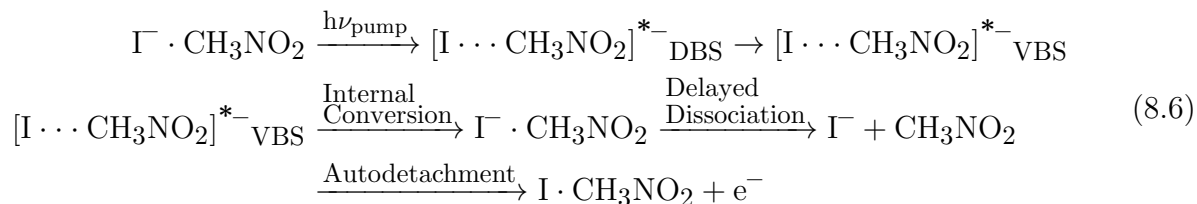
time of 21 ± 1 ps, shown in Fig. 8.7a. This finding suggests that the 2 ps VB anion decay lifetime corresponds to back-electron transfer to re-form $\Gamma^- \cdot \text{CH}_3\text{NO}_2$, followed by IC to the $\Gamma^- \cdot \text{CH}_3\text{NO}_2$ anion ground state and, finally, dissociation to yield Γ^- in 21 ps.

Rice-Ramsperger-Kassel-Marcus (RRKM) calculations were performed to analyze the statistical unimolecular dissociation of $\Gamma^- \cdot \text{CH}_3\text{NO}_2$ complexes to determine if the 21 ps Γ^- formation from 2 ps VB anion decay is a statistical process [159, 206, 207]. These RRKM calculations yield dissociation rates of only 300 – 400 fs, and this rapid lifetime is unlikely to be a realistic physical timescale for intramolecular vibrational energy redistribution (IVR) and subsequent dissociation in a cluster. This result indicates that there exists a dynamical bottleneck in the formation of Γ^- from $\Gamma^- \cdot \text{CH}_3\text{NO}_2$.

We have suggested that such a bottleneck arises in $\Gamma^- \cdot \text{CH}_3\text{NO}_2$ from inefficient energy flow from high frequency $-\text{NO}_2$ vibrational modes in the VB anion to the relatively low frequency ($<100 \text{ cm}^{-1}$) $\text{I} \cdot \cdot \text{CH}_3\text{NO}_2$ modes that ultimately yield Γ^- dissociation [159]. The $[\text{I} \cdot \cdot \text{CH}_3\text{NO}_2]^-$ DB anion should geometrically resemble neutral $\text{I} \cdot \text{CH}_3\text{NO}_2$, while the $[\text{I} \cdot \cdot \text{CH}_3\text{NO}_2]^-$ VB anion is expected to more closely resemble the puckered CH_3NO_2^- geometry in which the $-\text{NO}_2$ is out of the plane of the molecule [46, 203]. Hence, during the DB to VB anion transition, the $-\text{NO}_2$ vibrational modes become vibrationally excited. Previous theoretical work of gas phase $\text{S}_{\text{N}}2$ -type reactions has shown that energy transfer between high energy and low energy vibrational modes in a binary complex may be inefficient and lead to non-statistical dynamics [208–212]. Thus, IVR within the reformed $\Gamma^- \cdot \text{CH}_3\text{NO}_2$ complex can act as the rate-limiting step in cluster dissociation and cause the delayed Γ^- rise observed here.

Autodetachment from photoexcited $\Gamma^- \cdot \text{CH}_3\text{NO}_2$ clusters was also measured as near ~ 0 eV eKE photoelectron signal [46]. Autodetachment, the spontaneous ejection of an electron following photoexcitation of an anion resonance, can occur if the resonance lies isoenergetically within a manifold of vibrational levels of the corresponding neutral plus a free electron. The ejection is thus facilitated by nonadiabatic coupling between the electronic and nuclear degrees of freedom in the system [127, 213, 214]. If the internal energy of the excited anion (or cluster) is randomized prior to electron ejection, the detached electron typically carries ~ 0 eV eKE and this statistical process is referred to as thermionic emission [215, 216]. We expect, then, that the long 1300 ps VB anion decay corresponds to autodetachment.

To summarize these photoexcited $\Gamma^- \cdot \text{CH}_3\text{NO}_2$ decay dynamics, we conclude that the 2 ps decay of the VB anion is IC to the ground state followed by delayed Γ^- evaporation, and the long, 1300 ps VB anion decay is by autodetachment, as in Eq. 8.6:



These measured dynamics for near-VDE photoexcited $\Gamma \cdot \text{CH}_3\text{NO}_2$ complexes provide insight into the dynamics and energetics of the TNIs and also the possible interactions between the iodine atom and the CH_3NO_2 moiety. We consider these results in the discussion of the $\Gamma \cdot \text{U}$ and $\Gamma \cdot \text{T}$ studies in the following sections.

$\Gamma \cdot \text{Uracil}$ and $\Gamma \cdot \text{Thymine}$ Binary Complexes

The pyrimidine bases uracil and thymine each have a sufficiently large dipole moment to support a DB anion ($\mu \sim 4.15$ D) [169]. Single-photon PES measured by Bowen [178] finds the uracil and thymine DB anions to have eBEs of approximately 90 meV and 70 meV, respectively. No VB anions of either base have been detected in previous PES studies, but Rydberg electron transfer experiments [187] and theoretical calculations [186, 217] predict that both the DB anion and the VB anion for both uracil and thymine exist, at least as metastable TNIs, with VB anion VDEs of approximately 500 meV. For both nucleobases, the DB anion is the anionic ground state [191, 218], with a calculated barrier of 36 – 155 meV for conversion to form the VB anion, depending on the level of theory used [156]. However, bare thymine is calculated to have a $\sim 10 - 20$ meV higher conversion barrier for DB to VB anion conversion than bare uracil at each level of theory employed.

TRPES has been used to study the time-resolved dynamics of $\Gamma \cdot \text{U}$ and $\Gamma \cdot \text{T}$ clusters at photoexcitation energies near the VDE [154, 156] as well as in the higher energy ($\sim 4.6 - 4.9$ eV) excitation regime [152, 153, 155]. Here, we first briefly cover single-photon PES results as well as laser photodissociation spectroscopy experiments on $\Gamma \cdot \text{U}$ and $\Gamma \cdot \text{T}$ by the Dessent group and excited state calculations to provide context for the discussion of the time-resolved work [155, 192].

Single photon PE spectra collected at multiple photon energies for $\Gamma \cdot \text{U}$ and $\Gamma \cdot \text{T}$ are overlaid and reproduced in Fig. 8.5b and 8.5c, respectively [152, 153]. Feature A corresponds to direct detachment to the $\text{I}(^2\text{P}_{3/2}) \cdot \text{N}$ neutral complex, yielding a VDE of 4.11 ± 0.05 eV for $\Gamma \cdot \text{U}$ and $4.05 \text{ eV} \pm 0.05 \text{ eV}$ for $\Gamma \cdot \text{T}$. Feature B, seen only at the highest photon energies, arises from photodetachment to the upper iodine spin-orbit state. Feature C is present at each detachment energy at ~ 0 eV eKE and corresponds to autodetachment. Interestingly, we note that the intensity of the autodetachment signal appears to reach a maximum near 4.7 – 4.8 eV photon energy, and declines at energies above and below this region.

Laser photodissociation spectroscopy has been carried out on $\Gamma\cdot\text{U}$ and $\Gamma\cdot\text{T}$ by Dessent et al [155, 192] for $\Gamma\cdot\text{U}$ and $\Gamma\cdot\text{T}$ clusters to measure their photoabsorption profiles as well as photofragment formation as a function of pump energy. Figs. 8.9a and 8.9b show the photodepletion (photoabsorption, including dissociation and detachment) profiles for $\Gamma\cdot\text{U}$ and $\Gamma\cdot\text{T}$, respectively, from 3.6 to 5.3 eV. Two regimes of UV photoabsorption are measured: the first excited state near the VDE, approximately 4 eV for both clusters, and the second centered around 4.8 eV. The photofragmentation results find Γ^- and $[\text{N-H}]^-$, the deprotonated nucleobase anion, as photofragments for both clusters, with Γ^- appearing as the overwhelmingly dominant species [192]. Figs. 8.9c and 8.9d present the photofragment yields of Γ^- for $\Gamma\cdot\text{U}$ and $\Gamma\cdot\text{T}$, respectively. Both photofragments are also found to form in two distinct bands of photoexcitation: one centered near the VDE of each cluster, and one centered near 4.8 eV.

In Fig. 8.9 we also overlay these laser photodissociation results with the respective $\Gamma\cdot\text{U}$ and $\Gamma\cdot\text{T}$ one color photoelectron spectra from Figs. 8.5b and 8.5c. The VDE photodetachment features appear at energies slightly above the first photoabsorption and photofragmentation bands; this occurs because photodetachment is not possible below the VDE, but photoabsorption and formation of the DB anion is possible and has been measured at pump energies below the VDE, as described in more detail below [154–156, 192]. Note that the single-photon PES autodetachment feature for both $\Gamma\cdot\text{U}$ and $\Gamma\cdot\text{T}$ appears to track closely with the higher energy photoabsorption and Γ^- photofragmentation bands; we discuss this and the dynamics resulting from high energy photoexcitation in more detail in Section 8.6.

To examine the nature of the photoexcitation in each of the two measured energy regimes, excited state calculations have been performed at the TD-DFT/B3LYP level for $\Gamma\cdot\text{U}$ and $\Gamma\cdot\text{T}$ [192], and at the EOM-CCSD/aug-cc-pVDZ(-pp) level for $\Gamma\cdot\text{U}$ [155]. Near the $\Gamma\cdot\text{U}$ VDE, the EOM-CCSD calculation finds three optical transitions with prominent oscillator strength corresponding to excitation from an iodide (5p) orbital to form a DB state of the complex (Fig. 8.9e). Both sets of excited state calculations find by far the strongest transition near 4.8 eV to be a base-centered $\pi-\pi^*$ excitation (Fig. 8.9f). Much weaker transitions near 4.7 eV, corresponding to excitation from an iodide (5p) orbital to a σ^* state of the complex (Fig. 8.9g), are also found; the oscillator strength is lower by a factor ranging from two to 18 depending on cluster and method. No evidence is found for channels with significant oscillator strength corresponding to $\text{I}(5p)\rightarrow\pi^*$ charge transfer, i.e. direct optical excitation to form the VB anion, presumably reflecting near-zero spatial overlap between these initial and final states. Thus, we expect that near-VDE photoexcitation likely yields direct optical excitation from iodide to form the DB anion instantaneously, while photoexcitation at higher pump energies will likely yield dynamics with the largest contribution from base-centered $\pi-\pi^*$ excitation. We now turn our attention to the time-resolved results of photoexcited $\Gamma\cdot\text{U}$ and $\Gamma\cdot\text{T}$ clusters in each of these two pump energy regimes.

Early time dynamics from near-VDE excitation of $\Gamma^- \cdot \text{U}$ and $\Gamma^- \cdot \text{T}$

TRPES studies of $\Gamma^- \cdot \text{U}$ and $\Gamma^- \cdot \text{T}$ clusters were carried out at pump excitation energies from $\sim \pm 100$ meV relative to the VDE [154, 156], and are shown in Figs. 8.6b and 8.6c for $\Gamma^- \cdot \text{U}$ at +30 meV and $\Gamma^- \cdot \text{T}$ at +20 meV, respectively. At each of these excitation energies, both the DB anion (feature A, blue) and the VB anion (feature B, red) of each cluster are observed. In $\Gamma^- \cdot \text{U}$, the DB anion rise time decreases from approximately 250 fs to ≤ 150 fs as the pump energy is increased, while the VB anion rise time remains near 250 fs over this pump energy range. In $\Gamma^- \cdot \text{T}$, the DB anion appears in approximately 230 fs, exhibiting no dependence on the pump excitation energy, and the VB anion forms in approximately 300 fs.

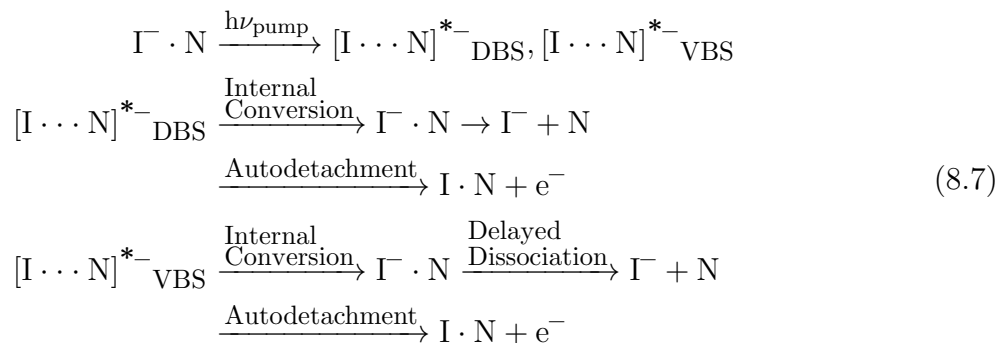
These results indicate that while the DB state is formed first and followed in appearance by the VB anion, because the DB signal remains while the VB signal grows in, both $\Gamma^- \cdot \text{U}$ and $\Gamma^- \cdot \text{T}$ seem to exhibit at most only partial DB to VB anion conversion. The excited state calculations in Section 8.6 show that there is direct optical excitation to form a DB state but no optical transition to form the VB state, indicating that the origin of the VB signal is expected to be from DB to VB anion conversion. Given that the DB anion is the anionic ground state for uracil and thymine [191, 218] and there is expected to be an uphill barrier of $\sim 36 - 155$ meV for conversion [156], it is reasonable that only partial DB to VB anion conversion occurs, in comparison for example to the rapid and complete DB to VB anion conversion in $\Gamma^- \cdot \text{CH}_3\text{NO}_2$.

Long time dynamics of near-VDE excited $\Gamma^- \cdot \text{U}$ and $\Gamma^- \cdot \text{T}$ clusters

The DB and VB anions of near-VDE photoexcited $\Gamma^- \cdot \text{U}$ and $\Gamma^- \cdot \text{T}$ clusters decay bi-exponentially, with each set of lifetimes generally decreasing with increasing pump excitation energy. For $\Gamma^- \cdot \text{U}$ photoexcited at +30 meV (Fig. 8.6b), the DB anion decay constants are 5.0 ps and 500 ps, while the VB anion decays in 5.6 ps and 80 ps [154]. $\Gamma^- \cdot \text{T}$ photoexcited at +20 meV (Fig. 8.6c) similarly exhibits DB anion decay in 5.2 ps and 1100 ps, and VB anion decay in 13.1 ps and 530 ps [156].

TRPES of near-VDE photoexcited $\Gamma^- \cdot \text{U}$ clusters finds two decay pathways: autodetachment and bi-exponential re-formation of Γ^- [154, 155]. TRPES of $\Gamma^- \cdot \text{U}$ clusters photoexcited at 4.03 eV (-80 meV) and probed at 3.61 eV measures bi-exponential formation of Γ^- in 17.5 ± 1.6 ps and 150 ± 10 ps as the only major photodissociation pathway; this Γ^- rise signal is shown in Fig. 8.7b. These bi-exponential Γ^- rise dynamics can be assigned in light of the mechanism of Γ^- reformation in $\Gamma^- \cdot \text{CH}_3\text{NO}_2$ (Eq. 8.6). For $\Gamma^- \cdot \text{U}$ clusters, since both TNIs are present as the DB to VB anion conversion is only partially complete, we expect that each TNI has a fast decay process of IC to the electronic $\Gamma^- \cdot \text{U}$ ground state followed by evaporation of Γ^- to ultimately yield bi-exponential Γ^- rise. We attribute the fast Γ^- appearance to IC of the DB anion, and the slow Γ^- appearance of 150 ps to IC and delayed ejection of Γ^-

from the VB anion, as the VB anion decay may also have a dynamical bottleneck similar to that observed in $\Gamma^- \cdot \text{CH}_3\text{NO}_2$. The overall decay mechanisms for the DB and VB anions are summarized in Eq. 8.7.



The long time decays of each TNI for both species are likely by autodetachment, or rather, more specifically, by thermionic emission considering the ~ 100 ps – 1 ns long decay lifetimes and measured decrease in the long time constants with increasing pump energy. Laser photodissociation spectra found $[\text{U-H}]^-$ (neutral electron affinity = 3.481 eV) [219] as an additional minor dissociation product from $\Gamma^- \cdot \text{U}$ clusters; this channel was not measured by TRPES, most likely due to its low abundance and broad photoelectron spectral profile [155, 220].

Dynamics of $\Gamma^- \cdot \text{U}$ and $\Gamma^- \cdot \text{T}$ excited at higher energy

TRPE spectra of $\Gamma^- \cdot \text{U}$ and $\Gamma^- \cdot \text{T}$ photoexcited at 4.69 eV and probed at 1.57 eV are shown in Figs. 8.8a and 8.8b, respectively [152, 153]. No evidence for the existence of a DB state is measured for either cluster in this pump energy regime, but both species exhibit VB anion signal (red integrated intensity) with a cross-correlation limited rise (≤ 150 fs), as well as ~ 0 eV eKE signal corresponding to autodetachment (black integrated intensity). The $\Gamma^- \cdot \text{U}$ VB anion decays bi-exponentially in 620 fs and 52 ps, while the $\Gamma^- \cdot \text{T}$ VB anion undergoes mono-exponential decay [156] in ~ 610 fs. The autodetachment signal for both clusters exhibits non-zero autodetachment intensity at negative times (i.e. pump only), prompt depletion at $t=0$ fs, and recovery to the initial intensity, although in $\Gamma^- \cdot \text{U}$ clusters the signal is found to exceed its initial intensity. The $\Gamma^- \cdot \text{T}$ VB anion prompt appearance and decay dynamics mirror that of the autodetachment signal, as seen in the integrated intensities in Fig. 8.8b [153].

Experiments on $\Gamma^- \cdot \text{U}$ at pump and probe energies of 4.72 eV and 3.15 eV, respectively, find formation of Γ^- be the dominant photodissociation channel; mono-exponential appearance of Γ^- occurs in 36 ± 3 ps (Fig. 8.7c). An analogous high energy probe study has not yet been performed for $\Gamma^- \cdot \text{T}$ clusters, but the laser photodissociation spectroscopy results confirm that

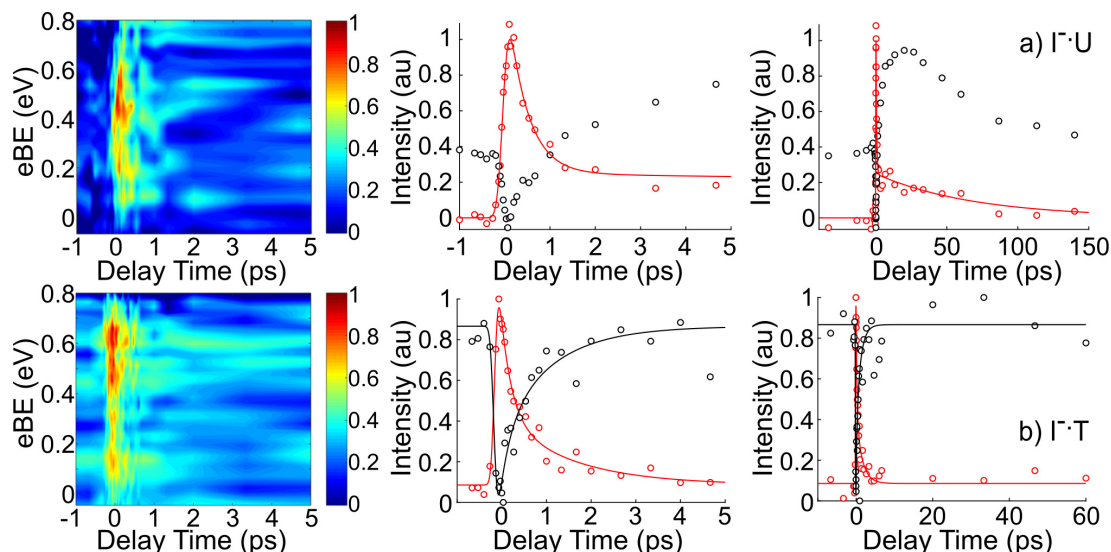
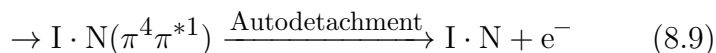
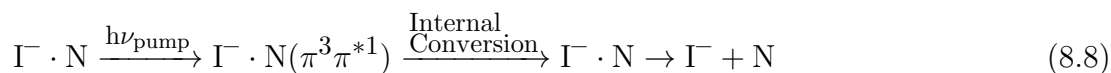


Figure 8.8: TRPE spectra (left) and integrated intensities at both early times and long delay times (right) for the VB anion (red) and autodetachment (black) features for a) $\text{I}^- \cdot \text{U}$ photoexcited at 4.69 eV; b) $\text{I}^- \cdot \text{T}$ photoexcited at 4.69 eV. Reproduced from Ch. 7 for ease of comparison.

I^- is the major photofragment produced from both sets of photoexcited clusters [192]. It is apparent in Fig. 8.8 that, for both $\text{I}^- \cdot \text{U}$ and $\text{I}^- \cdot \text{T}$ clusters, the VB anion appearance and fast decay dynamics match closely with the autodetachment depletion and recovery. It is also striking from the overlay of the single-photon PE spectra with the I^- photofragment formation results in Figs. 8.9c and 8.9d that the autodetachment signal tracks closely with the I^- photofragment production. Thus, it appears that I^- formation, autodetachment, and the VB anion share one common dynamical origin that is similar in nature for both clusters.

Given that one dynamical process is expected to give rise to all three of these features and that the excited state calculations for both $\text{I}^- \cdot \text{U}$ and $\text{I}^- \cdot \text{T}$ clusters find very strong oscillator strength for a base-centered $\pi - \pi^*$ excitation in this energy regime, it is likely that the pump pulse creates a $\pi - \pi^*$ excited state that is responsible for the observed dynamics [57]. Two possible channels following $\pi - \pi^*$ excitation are IC to the $\text{I}^- \cdot \text{N}$ ground state to yield cluster dissociation to produce I^- , as in Eq. 8.8, and charge transfer from iodide to the base moiety to fill the hole in the π orbital, essentially creating a VB anion that may then undergo autodetachment (Eq. 8.9).



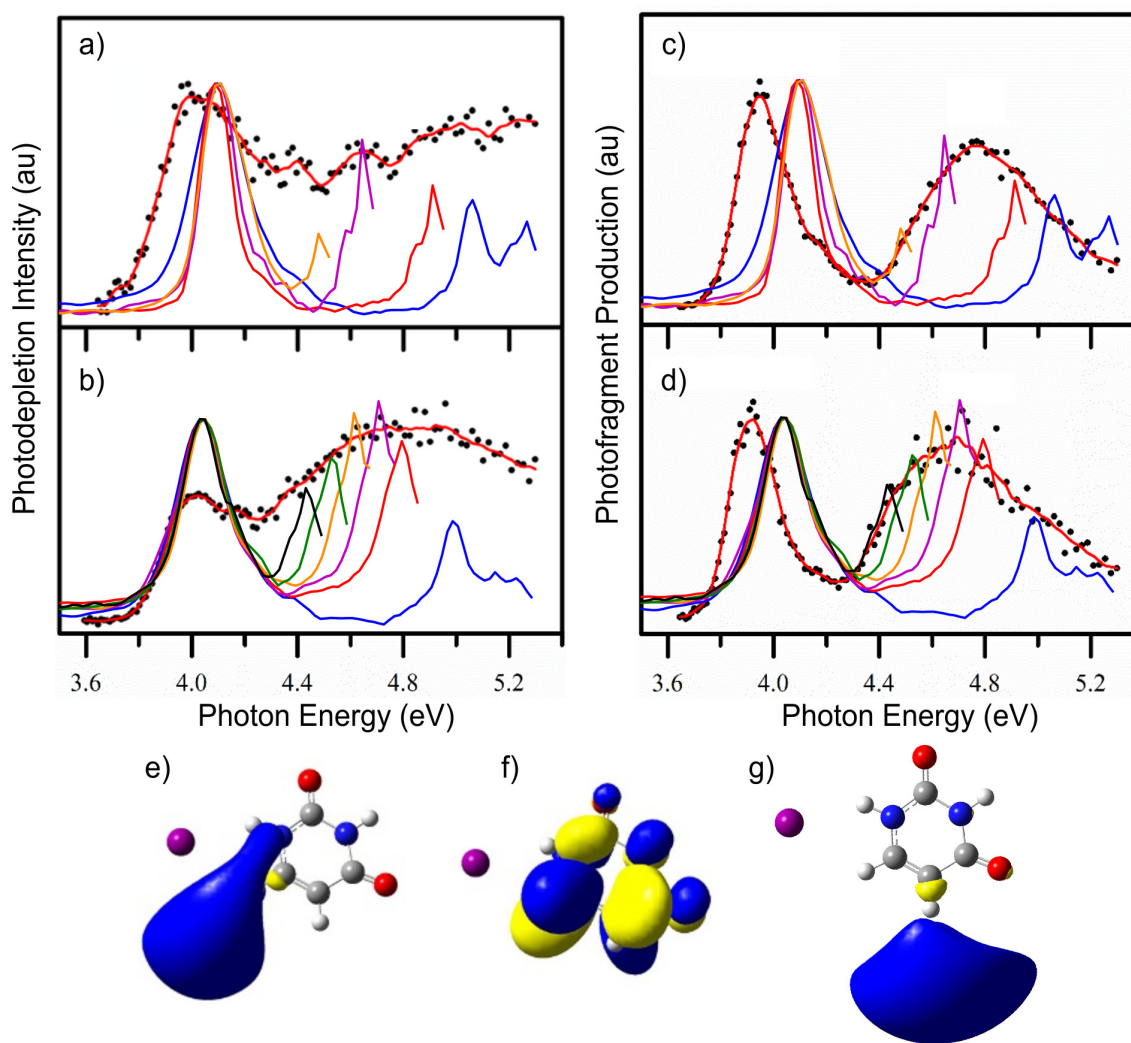


Figure 8.9: Overlay of the single-photon PE spectra from Fig. 8.5b) for I⁻·U and Fig. 8.5c) for I⁻·T with the laser photodissociation spectroscopy results from Ref. [192]. a) Photodepletion (absorption) for I⁻·U clusters photoexcited between 3.6 and 5.3 eV and b) for I⁻·T clusters. c) I⁻ formation from photoexcited I⁻·U clusters and d) I⁻ formation from photoexcited I⁻·T clusters. Photoelectron spectra are normalized to match the photodissociation data (black dots). e) EOM-CCSD/aug-cc-pVDZ(-pp) calculated image of the I⁻·U DB orbital and f) for the π* orbital and g) for the σ* orbital for transitions localized near 4.7 eV. Reproduced from Ch. 7 for ease of comparison.

We have thus previously proposed that in both $\Gamma^- \cdot \text{U}$ and $\Gamma^- \cdot \text{T}$, photoexcitation from ~ 4.6 eV – 4.8 eV creates a $\pi - \pi^*$ excited state, some fraction of which may decay by IC to the $\Gamma^- \cdot \text{N}$ ground state followed by dissociation to produce Γ^- (Eq. 8.8), and another fraction of which may have charge transfer within the cross-correlation of the pump and probe laser pulses from the iodide moiety to produce a VB anion that then decays by autodetachment (Eq. 8.9) [57]. These proposed pathways are summarized for the approximate energies and ranges of the excited states of $\Gamma^- \cdot \text{U}$ in Fig. 8.10. This figure also shows the $\Gamma^- \cdot \text{U}$ near-VDE photoexcitation dynamics as described in the earlier subsections of Section 8.6.

Some portions of this $\pi - \pi^*$ photoexcitation mechanism are not fully explained and would benefit considerably from a more extensive theoretical investigation into the nature and energetics of the photoexcited states accessible in this pump energy region. For example, it is challenging to explain the rapid rate of charge transfer from iodide to the π orbital and instantaneous VB anion formation given the lack of overlap between these two orbitals. Additionally, $\Gamma^- \cdot \text{U}$ exhibits long-lived dynamics that are not present in $\Gamma^- \cdot \text{T}$, and it is unclear why the $\Gamma^- \cdot \text{U}$ VB anion exhibits both fast and slow decay by autodetachment, although we have put forth such mechanistic explanations previously [152–154, 156].

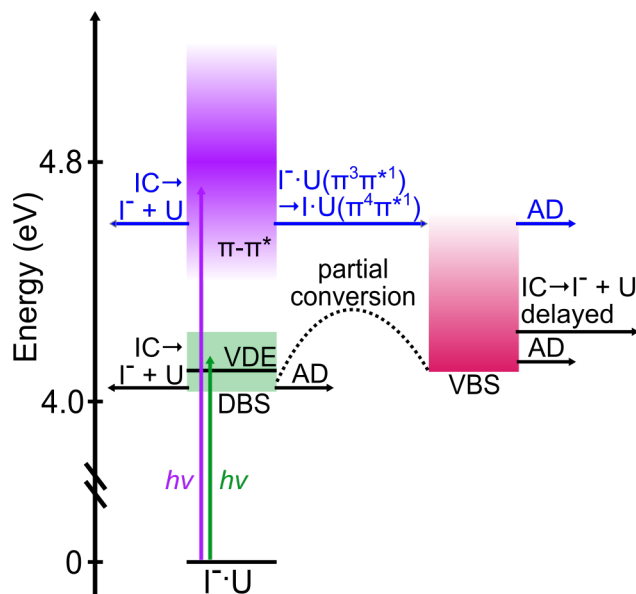


Figure 8.10: Diagram of the proposed $\Gamma^- \cdot \text{U}$ dynamical pathways resulting from near-VDE photoexcitation (green photon, black arrows) and higher energy photoexcitation (purple photon, blue arrows). DBS and VBS denote the DB and VB states, respectively. Reproduced from Ch. 7 for ease of comparison.

8.7 Summary and Outlook

The application of TRPES to molecular anions and clusters has proven to be an opportune method to explore the nature of fundamental ultrafast interactions of solvents and molecules with excess electrons. This versatile technique has been applied to a number of different solvent systems, multiply charged species, and biomolecular anions to uncover relaxation mechanisms and ultrafast charge accommodation dynamics. Specifically, TRPES of $\text{I}^- \cdot \text{N}$ clusters has revealed the ultrafast formation and conversion of nucleobase TNIs thought to be important in reductive damage pathways in DNA.

There are many promising future directions for work of this kind, including microhydration of $\text{I}^- \cdot \text{N}$ clusters, specifically $\text{I}^- \cdot \text{U} \cdot \text{H}_2\text{O}$ complexes [157]. The stepwise addition of individual water molecules building up to a solvation shell will allow for comparison between gas-phase dynamics of nucleobases and those recorded in bulk solution. In this regard, TRPES experiments in our group [221] and elsewhere [222, 223] on the dynamics of nucleic acid constituents in liquid water microjets are of particular interest. The future implementation of a new cluster source to our apparatus, such as one based on electrospray ionization [15], will enable TRPES studies of larger biomolecules such as nucleosides and nucleotides, with the ultimate goal of inducing electron attachment and monitoring not only the initial site of electron attachment and the TNI dynamics, but also probing photofragment formation to measure the identities and timescales for formation of photodissociation products in these larger nucleic acid constituents.

8.8 References

- [1] S. H. Yang, C. L. Pettiette, J. Conceicao, O. Cheshnovsky, and R. E. Smalley, “UPS of buckminsterfullerene and other large clusters of carbon”, *Chem. Phys. Lett.* **139**, 233–238 (1987).
- [2] S. Yang, K. J. Taylor, M. J. Craycraft, J. Conceicao, C. L. Pettiette, O. Cheshnovsky, and R. E. Smalley, “UPS of 2–30-atom carbon clusters: chains and rings”, *Chem. Phys. Lett.* **144**, 431–436 (1988).
- [3] G. Ganteför, M. Gausa, K.-H. Meiwes-Broer, and H. O. Lutz, “Ultraviolet photodetachment spectroscopy on jet-cooled metal-cluster anions”, *Faraday Discuss. Chem. Soc.* **86**, 197–208 (1988).
- [4] J. Ho, K. M. Ervin, and W. C. Lineberger, “Photoelectron spectroscopy of metal cluster anions: Cu_n^- , Ag_n^- and Au_n^- ”, *J. Chem. Phys.* **93**, 6987–7002 (1990).
- [5] D. Y. Zubarev, B. B. Averkiev, H.-J. Zhai, L.-S. Wang, and A. I. Boldyrev, “Aromaticity and antiaromaticity in transition-metal systems”, *Phys. Chem. Chem. Phys.* **10**, 257–267 (2008).

- [6] L.-M. Wang and L.-S. Wang, “Probing the electronic properties and structural evolution of anionic gold clusters in the gas phase”, *Nanoscale* **4**, 4038–4053 (2012).
- [7] H. Haberland and K. H. Bowen, “Solvated electron clusters”, in *Clusters of atoms and molecules*, edited by H. Haberland (Springer-Verlag, Heidelberg, 1993).
- [8] W. H. Robertson and M. A. Johnson, “Molecular aspects of halide ion hydration: the cluster approach”, *Annu. Rev. Phys. Chem.* **54**, 173–213 (2003).
- [9] J. V. Coe, S. M. Williams, and K. H. Bowen, “Photoelectron spectra of hydrated electron clusters vs. cluster size: connecting to bulk”, *Int. Rev. Phys. Chem.* **27**, 27–51 (2008).
- [10] A. Sanov and W. Carl Lineberger, “Dynamics of cluster anions: a detailed look at condensed-phase interactions”, *PhysChemComm* **5**, 165–177 (2002).
- [11] J. R. R. Verlet, “Femtosecond spectroscopy of cluster anions: insights into condensed-phase phenomena from the gas-phase”, *Chem. Soc. Rev.* **37**, 505–517 (2008).
- [12] R. M. Young and D. M. Neumark, “Dynamics of solvated electrons in clusters”, *Chem. Rev.* **112**, 5553–5577 (2012).
- [13] A. V. Davis, M. T. Zanni, C. Frischkorn, and D. M. Neumark, “Time-resolved dynamics of charge transfer to solvent states in solvated iodide clusters”, *J. Electron Spectrosc. Relat. Phenom.* **108**, 203–211 (2000).
- [14] B. Boudaïffa, P. Cloutier, D. Hunting, M. A. Huels, and L. Sanche, “Resonant formation of DNA strand breaks by low-energy (3 to 20 eV) electrons”, *Science* **287**, 1658–1660 (2000).
- [15] C. S. Anstöter, J. N. Bull, and J. R. R. Verlet, “Ultrafast dynamics of temporary anions probed through the prism of photodetachment”, *Int. Rev. Phys. Chem.* **35**, 509–538 (2016).
- [16] A. Stolow, A. E. Bragg, and D. M. Neumark, “Femtosecond time-resolved photoelectron spectroscopy”, *Chem. Rev.* **104**, 1719–1758 (2004).
- [17] H. H. Fielding and G. A. Worth, “Using time-resolved photoelectron spectroscopy to unravel the electronic relaxation dynamics of photoexcited molecules”, *Chem. Soc. Rev.* **47**, 309–321 (2018).
- [18] T. Suzuki, “Femtosecond time-resolved photoelectron imaging”, *Annu. Rev. Phys. Chem.* **57**, 555–592 (2006).
- [19] C. C. Hayden and A. Stolow, “Non-adiabatic dynamics studied by femtosecond time-resolved photoelectron spectroscopy”, in *Photoionization and photodetachment*, Vol. Volume 10, Advanced Series in Physical Chemistry (WORLD SCIENTIFIC, 2000), pp. 91–126.
- [20] D. M. Neumark, “Time-resolved photoelectron spectroscopy of molecules and clusters”, *Annu. Rev. Phys. Chem.* **52**, 255–277 (2001).

- [21] T. Suzuki and B. J. Whitaker, “Non-adiabatic effects in chemistry revealed by time-resolved charged-particle imaging”, *Int. Rev. Phys. Chem.* **20**, 313–356 (2001).
- [22] A. Stolow, “Femtosecond time-resolved photoelectron spectroscopy of polyatomic molecules”, *Annu. Rev. Phys. Chem.* **54**, 89–119 (2003).
- [23] A. Stolow, “Time-resolved photoelectron spectroscopy: Non-adiabatic dynamics in polyatomic molecules”, *Int. Rev. Phys. Chem.* **22**, 377–405 (2003).
- [24] T. Suzuki, “Time-resolved photoelectron spectroscopy and imaging”, in *Modern trends in chemical reaction dynamics*, Vol. Volume 14, Advanced Series in Physical Chemistry (WORLD SCIENTIFIC, 2004), pp. 529–578.
- [25] M. Wollenhaupt, V. Engel, and T. Baumert, “Femtosecond laser photoelectron spectroscopy on atoms and small molecules: prototype studies in quantum control”, *Annu. Rev. Phys. Chem.* **56**, 25–56 (2004).
- [26] A. Stolow and J. G. Underwood, *Time-resolved photoelectron spectroscopy of nonadiabatic dynamics in polyatomic molecules*, edited by S. A. Rice, Vol. 139 (2008).
- [27] V. G. Stavros and J. R. R. Verlet, “Gas-phase femtosecond particle spectroscopy: a bottom-up approach to nucleotide dynamics”, *Annu. Rev. Phys. Chem.* **67**, 211–232 (2016).
- [28] R. Spesyvtsev, J. G. Underwood, and H. H. Fielding, “Time-resolved photoelectron spectroscopy for excited state dynamics”, in *Ultrafast phenomena in molecular sciences: femtosecond physics and chemistry*, edited by R. de Nalda and L. Bañares (Springer International Publishing, Cham, 2014), pp. 99–117.
- [29] R. R. Corderman and W. C. Lineberger, “Negative ion spectroscopy”, *Annu. Rev. Phys. Chem.* **30**, 347–378 (1979).
- [30] L. A. Posey, M. J. Deluca, and M. A. Johnson, “Demonstration of a pulsed photoelectron spectrometer on mass-selected negative ions: O^- , O_2^- , and O_4^- ”, *Chem. Phys. Lett.* **131**, 170–174 (1986).
- [31] O. Cheshnovsky, S. H. Yang, C. L. Pettiette, M. J. Craycraft, and R. E. Smalley, “Magnetic time-of-flight photoelectron spectrometer for mass-selected negative cluster ions”, *Rev. Sci. Instrum.* **58**, 2131–2137 (1987).
- [32] S. Arnold, J. Coe, J. Eaton, C. Freidhoff, L. Kidder, G. Lee, M. Manaa, K. McHugh, D. Patel-Misra, H. Sarkas, J. Snodgrass, and K. Bowen, “Photodetachment spectroscopy of negative cluster ions”, in *The chemical physics of atomic and molecular clusters*, edited by G. Scholes (North-Holland Amsterdam, 1990), pp. 467–490.
- [33] X.-B. Wang and L.-S. Wang, “Photoelectron spectroscopy of multiply charged anions”, *Annu. Rev. Phys. Chem.* **60**, 105–126 (2009).
- [34] W. C. Lineberger, “Once upon anion: a tale of photodetachment”, *Annu. Rev. Phys. Chem.* **64**, 21–36 (2013).

- [35] L.-S. Wang, “Photoelectron spectroscopy of size-selected boron clusters: from planar structures to borophenes and borospherenes”, *Int. Rev. Phys. Chem.* **35**, 69–142 (2016).
- [36] D. H. Paik, I. R. Lee, D.-S. Yang, J. S. Baskin, and A. H. Zewail, “Electrons in finite-sized water cavities: hydration dynamics observed in real time”, *Science* **306**, 672 (2004).
- [37] C. Frischkorn, A. E. Bragg, A. V. Davis, R. Wester, and D. M. Neumark, “Electronic relaxation dynamics of carbon cluster anions: excitation of the $\check{C}^2\pi_g \leftarrow \check{X}^2\pi_u$ transition in C_6^- ”, *J. Chem. Phys.* **115**, 11185–11192 (2001).
- [38] A. E. Bragg, R. Wester, A. V. Davis, A. Kammrath, and D. M. Neumark, “Excited-state detachment dynamics and rotational coherences of C_2^- via time-resolved photoelectron imaging”, *Chem. Phys. Lett.* **376**, 767–775 (2003).
- [39] N. Pontius, P. S. Bechthold, M. Neeb, and W. Eberhardt, “Ultrafast hot-electron dynamics observed in Pt_3^- using time-resolved photoelectron spectroscopy”, *Phys. Rev. Lett.* **84**, 1132–1135 (2000).
- [40] N. Pontius, G. Lüttgens, P. S. Bechthold, M. Neeb, and W. Eberhardt, “Size-dependent hot-electron dynamics in small Pd_n^- clusters”, *J. Chem. Phys.* **115**, 10479–10483 (2001).
- [41] M. Niemietz, P. Gerhardt, G. Ganteför, and Y. Dok Kim, “Relaxation dynamics of the Au_3^- and Au_6^- cluster anions”, *Chem. Phys. Lett.* **380**, 99–104 (2003).
- [42] N. Pontius, M. Neeb, W. Eberhardt, G. Lüttgens, and P. S. Bechthold, “Ultrafast relaxation dynamics of optically excited electrons in Ni_3^- ”, *Phys. Rev. B* **67**, 035425 (2003).
- [43] J. Stanzel, F. Burmeister, M. Neeb, W. Eberhardt, R. Mitrić, C. Bürgel, and V. Bonačić-Koutecký, “Size-dependent dynamics in excited states of gold clusters: from oscillatory motion to photoinduced melting”, *J. Chem. Phys.* **127**, 164312 (2007).
- [44] M. Niemietz, M. Engelke, Y. D. Kim, and G. Ganteför, “Electronic relaxation in Ag nanoclusters studied with time-resolved photoelectron spectroscopy”, *Phys. Rev. B* **75**, 085438 (2007).
- [45] G. B. Griffin, O. T. Ehrler, A. Kammrath, R. M. Young, O. Cheshnovsky, and D. M. Neumark, “Auger recombination and excited state relaxation dynamics in Hg_n^- ($n=9-20$) anion clusters”, *J. Chem. Phys.* **130**, 231103 (2009).
- [46] M. A. Yandell, S. B. King, and D. M. Neumark, “Decay dynamics of nascent acetonitrile and nitromethane dipole-bound anions produced by intracuster charge-transfer”, *J. Chem. Phys.* **140**, 184317 (2014).
- [47] J. N. Bull and J. R. R. Verlet, “Observation and ultrafast dynamics of a nonvalence correlation-bound state of an anion”, *Sci. Adv.* **3**, e1603106 (2017).

- [48] J. P. Rogers, C. S. Anstöter, and J. R. R. Verlet, “Ultrafast dynamics of low-energy electron attachment via a non-valence correlation-bound state”, *Nat. Chem.* **10**, 341 (2018).
- [49] O. T. Ehrler, J.-P. Yang, A. B. Sugiharto, A. N. Unterreiner, and M. M. Kappes, “Excited state dynamics of metastable phthalocyanine-tetrasulfonate tetra-anions probed by pump/probe photoelectron spectroscopy”, *J. Chem. Phys.* **127**, 184301 (2007).
- [50] P. D. Dau, H.-T. Liu, J.-P. Yang, M.-O. Winghart, T. J. A. Wolf, A.-N. Unterreiner, P. Weis, Y.-R. Miao, C.-G. Ning, M. M. Kappes, and L.-S. Wang, “Resonant tunneling through the repulsive Coulomb barrier of a quadruply charged molecular anion”, *Phys. Rev. A* **85**, 064503 (2012).
- [51] M.-O. Winghart, J.-P. Yang, M. Kühn, A.-N. Unterreiner, T. J. A. Wolf, P. D. Dau, H.-T. Liu, D.-L. Huang, W. Klopfer, L.-S. Wang, and M. M. Kappes, “Electron tunneling from electronically excited states of isolated bisdisulizole-derived trianion chromophores following UV absorption”, *Phys. Chem. Chem. Phys.* **15**, 6726–6736 (2013).
- [52] J. R. R. Verlet, D. A. Horke, and A. S. Chatterley, “Excited states of multiply-charged anions probed by photoelectron imaging: riding the repulsive Coulomb barrier”, *Phys. Chem. Chem. Phys.* **16**, 15043–15052 (2014).
- [53] I. R. Lee, W. Lee, and A. H. Zewail, “Primary steps of the photoactive yellow protein: isolated chromophore dynamics and protein directed function”, *Proc. Natl. Acad. Sci. U.S.A.* **103**, 258 (2006).
- [54] D. A. Horke, Q. Li, L. Blancafort, and J. R. R. Verlet, “Ultrafast above-threshold dynamics of the radical anion of a prototypical quinone electron-acceptor”, *Nat. Chem.* **5**, 711 (2013).
- [55] C. R. S. Mooney, D. A. Horke, A. S. Chatterley, A. Simperler, H. H. Fielding, and J. R. R. Verlet, “Taking the green fluorescence out of the protein: dynamics of the isolated GFP chromophore anion”, *Chem. Sci.* **4**, 921–927 (2013).
- [56] A. S. Chatterley, C. W. West, V. G. Stavros, and J. R. R. Verlet, “Time-resolved photoelectron imaging of the isolated deprotonated nucleotides”, *Chem. Sci.* **5**, 3963–3975 (2014).
- [57] A. Kunin and D. M. Neumark, “Time-resolved radiation chemistry: femtosecond photoelectron spectroscopy of electron attachment and photodissociation dynamics in iodide–nucleobase clusters”, *Phys. Chem. Chem. Phys.* **21**, 7239–7255 (2019).
- [58] A. E. Bragg, J. R. R. Verlet, A. Kammrath, and D. M. Neumark, “C₆[−] electronic relaxation dynamics probed via time-resolved photoelectron imaging”, *J. Chem. Phys.* **121**, 3515–3526 (2004).
- [59] O. T. Ehrler, J. P. Yang, C. Hättig, A. N. Unterreiner, H. Hippler, and M. M. Kappes, “Femtosecond pump/probe photoelectron spectroscopy of isolated C₆₀ negative ions”, *J. Chem. Phys.* **125**, 074312 (2006).

- [60] D. H. Paik, T. M. Bernhardt, N. J. Kim, and A. H. Zewail, “Femtochemistry of mass-selected negative-ion clusters of dioxygen: charge-transfer and solvation dynamics”, *J. Chem. Phys.* **115**, 612–616 (2001).
- [61] D. H. Paik, N. J. Kim, and A. H. Zewail, “Femtosecond dynamics of solvated oxygen anions. I. Bifurcated electron transfer dynamics probed by photoelectron spectroscopy”, *J. Chem. Phys.* **118**, 6923–6929 (2003).
- [62] N. J. Kim, D. H. Paik, and A. H. Zewail, “Femtosecond dynamics of solvated oxygen anions. II. Nature of dissociation and caging in finite-sized clusters”, *J. Chem. Phys.* **118**, 6930–6940 (2003).
- [63] D. H. Paik, J. S. Baskin, N. J. Kim, and A. H. Zewail, “Ultrafast vectorial and scalar dynamics of ionic clusters: azobenzene solvated by oxygen”, *J. Chem. Phys.* **125**, 133408 (2006).
- [64] J. R. R. Verlet, A. E. Bragg, A. Kammrath, O. Cheshnovsky, and D. M. Neumark, “Time-resolved relaxation dynamics of Hg_n^- ($11 \leq n \leq 16$, $n=18$) clusters following intraband excitation at 1.5 eV”, *J. Chem. Phys.* **121**, 10015–10025 (2004).
- [65] A. E. Bragg, J. R. R. Verlet, A. Kammrath, O. Cheshnovsky, and D. M. Neumark, “Time-resolved intraband electronic relaxation dynamics of Hg_n^- clusters ($n=7-13,15,18$) excited at 1.0 eV”, *J. Chem. Phys.* **122**, 054314 (2005).
- [66] G. B. Griffin, A. Kammrath, O. T. Ehrler, R. M. Young, O. Cheshnovsky, and D. M. Neumark, “Auger recombination dynamics in Hg_{13}^- clusters”, *Chem. Phys.* **350**, 69–74 (2008).
- [67] R. M. Young, G. B. Griffin, O. T. Ehrler, A. Kammrath, A. E. Bragg, J. R. R. Verlet, O. Cheshnovsky, and D. M. Neumark, “Charge carrier dynamics in semiconducting mercury cluster anions”, *Phys. Scr.* **80**, 048102 (2009).
- [68] B. J. Greenblatt, M. T. Zanni, and D. M. Neumark, “Photodissociation dynamics of the I_2^- anion using femtosecond photoelectron spectroscopy”, *Chem. Phys. Lett.* **258**, 523–529 (1996).
- [69] B. J. Greenblatt, M. T. Zanni, and D. M. Neumark, “Time-resolved photodissociation of $\text{I}_2^-(\text{Ar})_n$ clusters studied with anion femtosecond photoelectron spectroscopy”, *Science* **276**, 1675 (1997).
- [70] B. J. Greenblatt, M. T. Zanni, and D. M. Neumark, “Time-resolved studies of dynamics in molecular and cluster anions”, *Faraday Discuss.* **108**, 101–113 (1997).
- [71] M. T. Zanni, T. R. Taylor, B. J. Greenblatt, B. Soep, and D. M. Neumark, “Characterization of the I_2^- anion ground state using conventional and femtosecond photoelectron spectroscopy”, *J. Chem. Phys.* **107**, 7613–7619 (1997).
- [72] M. T. Zanni, B. J. Greenblatt, and D. M. Neumark, “Solvent effects on the vibrational frequency of I_2^- in size-selected $\text{I}_2^-(\text{Ar})_n$ and $\text{I}_2^-(\text{CO}_2)_n$ clusters”, *J. Chem. Phys.* **109**, 9648–9651 (1998).

- [73] B. J. Greenblatt, M. T. Zanni, and D. M. Neumark, “Femtosecond photoelectron spectroscopy of $I_2^-(Ar)_n$ clusters ($n=6,9,12,16,20$)”, *J. Chem. Phys.* **111**, 10566–10577 (1999).
- [74] B. J. Greenblatt, M. T. Zanni, and D. M. Neumark, “Femtosecond photoelectron spectroscopy of $I_2^-(CO_2)_n$ clusters ($n=4, 6, 9, 12, 14, 16$)”, *J. Chem. Phys.* **112**, 601–612 (1999).
- [75] M. T. Zanni, V. S. Batista, B. J. Greenblatt, W. H. Miller, and D. M. Neumark, “Femtosecond photoelectron spectroscopy of the I_2^- anion: characterization of the $\tilde{a}^2\pi_{g,1/2}$ excited state”, *J. Chem. Phys.* **110**, 3748–3755 (1999).
- [76] A. V. Davis, M. T. Zanni, C. Frischkorn, M. Elhanine, and D. M. Neumark, “Femtosecond stimulated emission pumping: dynamics of vibrational energy loss in excited $I_2^-(CO_2)_4$ clusters”, *J. Electron Spectrosc. Relat. Phenom.* **112**, 221–230 (2000).
- [77] M. T. Zanni, A. V. Davis, C. Frischkorn, M. Elhanine, and D. M. Neumark, “Femtosecond stimulated emission pumping: characterization of the I_2^- ground state”, *J. Chem. Phys.* **112**, 8847–8854 (2000).
- [78] A. V. Davis, R. Wester, A. E. Bragg, and D. M. Neumark, “Vibrational relaxation in clusters: energy transfer in $I_2^-(CO_2)_4$ excited by femtosecond stimulated emission pumping”, *J. Chem. Phys.* **117**, 4282–4292 (2002).
- [79] R. Wester, A. V. Davis, A. E. Bragg, and D. M. Neumark, “Cluster calorimetry by femtosecond stimulated emission pumping: excitation and evaporative cooling of $I_2^-(CO_2)_n$ ”, *Phys. Rev. A* **65**, 051201 (2002).
- [80] A. V. Davis, R. Wester, A. E. Bragg, and D. M. Neumark, “Vibrational relaxation in $I_2^-(Ar)_n$ ($n=1,2,6,9$) and $I_2^-(CO_2)_n$ ($n=1,4,5$) clusters excited by femtosecond stimulated emission pumping”, *J. Chem. Phys.* **119**, 2020–2031 (2003).
- [81] A. V. Davis, R. Wester, A. E. Bragg, and D. M. Neumark, “Time-resolved photoelectron imaging of the photodissociation of I_2^- ”, *J. Chem. Phys.* **118**, 999–1002 (2003).
- [82] R. Wester, A. E. Bragg, A. V. Davis, and D. M. Neumark, “Time-resolved study of the symmetric SN2 reaction $I^- + CH_3I$ ”, *J. Chem. Phys.* **119**, 10032–10039 (2003).
- [83] M. T. Zanni, B. J. Greenblatt, A. V. Davis, and D. M. Neumark, “Photodissociation of gas phase I_3^- using femtosecond photoelectron spectroscopy”, *J. Chem. Phys.* **111**, 2991–3003 (1999).
- [84] M. T. Zanni, C. Frischkorn, A. V. Davis, and D. M. Neumark, “Dynamics of the charge-transfer-to-solvent states in $I^-(Xe)_n$ clusters”, *J. Phys. Chem. A* **104**, 2527–2530 (2000).
- [85] J. Faeder and R. Parson, “Ultrafast reaction dynamics in cluster ions: simulation of the transient photoelectron spectrum of $I_2^-Ar_n$ photodissociation”, *J. Chem. Phys.* **108**, 3909–3914 (1998).

- [86] V. S. Batista, M. T. Zanni, B. J. Greenblatt, D. M. Neumark, and W. H. Miller, “Femtosecond photoelectron spectroscopy of the I_2^- anion: a semiclassical molecular dynamics simulation method”, *J. Chem. Phys.* **110**, 3736–3747 (1999).
- [87] N. Yu, C. J. Margulis, and D. F. Coker, “Ultrafast nonadiabatic dynamics: quasiclassical calculation of the transient photoelectron spectrum of $I_2^-(CO_2)_8$ ”, *J. Chem. Phys.* **120**, 3657–3664 (2004).
- [88] X.-Y. Miao, L. Wang, L. Yao, and H.-S. Song, “Theoretical study of the femtosecond-resolved photoelectron spectrum of the i_2^- anion”, *Chem. Phys. Lett.* **433**, 28–31 (2006).
- [89] R. Mabbs, K. Pichugin, E. Surber, and A. Sanov, “Time-resolved electron detachment imaging of the I^- channel in I_2Br^- photodissociation”, *J. Chem. Phys.* **121**, 265–272 (2004).
- [90] R. Mabbs, K. Pichugin, and A. Sanov, “Time-resolved imaging of the reaction coordinate”, *J. Chem. Phys.* **122**, 174305 (2005).
- [91] P. Gerhardt, M. Niemietz, Y. Dok Kim, and G. Ganteför, “Fast electron dynamics in small aluminum clusters: non-magic behavior of a magic cluster”, *Chem. Phys. Lett.* **382**, 454–459 (2003).
- [92] J. Heinzelmann, P. Kruppa, S. Proch, Y. D. Kim, and G. Ganteför, “Electronic relaxation in lead clusters: an indicator of non-metallic behavior”, *Chem. Phys. Lett.* **603**, 1–6 (2014).
- [93] G. Lüttgens, N. Pontius, P. S. Bechthold, M. Neeb, and W. Eberhardt, “Photon-induced thermal desorption of CO from small metal-carbonyl clusters”, *Phys. Rev. Lett.* **88**, 076102 (2002).
- [94] Y. D. Kim, M. Niemietz, P. Gerhardt, F. v. Gynz-Rekowski, and G. Ganteför, “Relaxation dynamics of magic clusters”, *Phys. Rev. B* **70**, 035421 (2004).
- [95] M. Niemietz, M. Engelke, Y. D. Kim, and G. Ganteför, “Photodesorption of O_2 from Ag_2^- : a time-resolved study of Ag_2O_2 ”, *Appl. Phys. A* **87**, 615–619 (2007).
- [96] K. Koyasu, M. Niemietz, M. Götz, and G. Ganteför, “Time-resolved study of the photodissociation of Au_2O^- ”, *Chem. Phys. Lett.* **450**, 96–100 (2007).
- [97] M. Niemietz, K. Koyasu, G. Ganteför, and Y. D. Kim, “Dynamics of O_2 photodesorption from metal clusters: a significant difference from bulk behaviour”, *Chem. Phys. Lett.* **438**, 263–267 (2007).
- [98] K. Koyasu, W. Westhäuser, M. Niemietz, J. Heinen, and G. Ganteför, “ O_2 photodesorption from AuO_2^- and $Au_2O_2^-$ ”, *Appl. Phys. A* **96**, 679–684 (2009).
- [99] J. M. Weber, J. Kim, E. A. Woronowicz, G. H. Weddle, I. Becker, O. Cheshnovsky, and M. A. Johnson, “Observation of resonant two-photon photodetachment of water cluster anions via femtosecond photoelectron spectroscopy”, *Chem. Phys. Lett.* **339**, 337–342 (2001).

- [100] A. E. Bragg, J. R. R. Verlet, A. Kammrath, O. Cheshnovsky, and D. M. Neumark, “Hydrated electron dynamics: from clusters to bulk”, *Science* **306**, 669 (2004).
- [101] J. R. R. Verlet, A. E. Bragg, A. Kammrath, O. Cheshnovsky, and D. M. Neumark, “Observation of large water-cluster anions with surface-bound excess electrons”, *Science* **307**, 93 (2005).
- [102] A. E. Bragg, J. R. R. Verlet, A. Kammrath, O. Cheshnovsky, and D. M. Neumark, “Electronic relaxation dynamics of water cluster anions”, *J. Am. Chem. Soc.* **127**, 15283–15295 (2005).
- [103] G. B. Griffin, R. M. Young, O. T. Ehrler, and D. M. Neumark, “Electronic relaxation dynamics in large anionic water clusters: $(\text{H}_2\text{O})_n^-$ and $(\text{D}_2\text{O})_n^-$ ($n=25-200$)”, *J. Chem. Phys.* **131**, 194302 (2009).
- [104] R. M. Young, M. A. Yandell, S. B. King, and D. M. Neumark, “Thermal effects on energetics and dynamics in water cluster anions $(\text{H}_2\text{O})_n^-$ ”, *J. Chem. Phys.* **136**, 094304 (2012).
- [105] B. J. Schwartz and P. J. Rossky, “Aqueous solvation dynamics with a quantum mechanical solute: computer simulation studies of the photoexcited hydrated electron”, *J. Chem. Phys.* **101**, 6902–6916 (1994).
- [106] B. J. Schwartz and P. J. Rossky, “Pump-probe spectroscopy of the hydrated electron: a quantum molecular dynamics simulation”, *J. Chem. Phys.* **101**, 6917–6926 (1994).
- [107] Y. Kimura, J. C. Alfano, P. K. Walkout, and P. F. Barbara, “Ultrafast transient absorption spectroscopy of the solvated electron in water”, *J. Phys. Chem.* **98**, 3450–3458 (1994).
- [108] A. Kammrath, J. R. R. Verlet, G. B. Griffin, and D. M. Neumark, “Photoelectron spectroscopy of large $(\text{water})_n^-$ ($n=50-200$) clusters at 4.7 eV”, *J. Chem. Phys.* **125**, 076101 (2006).
- [109] M. H. Elkins, H. L. Williams, A. T. Shreve, and D. M. Neumark, “Relaxation mechanism of the hydrated electron”, *Science* **342**, 1496–1499 (2013).
- [110] M. H. Elkins, H. L. Williams, and D. M. Neumark, “Isotope effect on hydrated electron relaxation dynamics studied with time-resolved liquid jet photoelectron spectroscopy”, *J. Chem. Phys.* **144**, 184503 (2016).
- [111] S. Karashima, Y.-i. Yamamoto, and T. Suzuki, “Resolving nonadiabatic dynamics of hydrated electrons using ultrafast photoemission anisotropy”, *Phys. Rev. Lett.* **116**, 137601 (2016).
- [112] L. Lehr, M. T. Zanni, C. Frischkorn, R. Weinkauff, and D. M. Neumark, “Electron solvation in finite systems: femtosecond dynamics of iodide· $(\text{water})_n$ anion clusters”, *Science* **284**, 635 (1999).

- [113] A. Kammrath, J. R. R. Verlet, A. E. Bragg, G. B. Griffin, and D. M. Neumark, “Dynamics of charge-transfer-to-solvent precursor states in $\text{I}^-(\text{water})_n$ ($n=3-10$) clusters studied with photoelectron imaging”, *J. Phys. Chem. A* **109**, 11475–11483 (2005).
- [114] J. R. R. Verlet, A. Kammrath, G. B. Griffin, and D. M. Neumark, “Electron solvation in water clusters following charge transfer from iodide”, *J. Chem. Phys.* **123**, 231102 (2005).
- [115] L. Turi, W.-S. Sheu, and P. J. Rossky, “Characterization of excess electrons in water-cluster anions by quantum simulations”, *Science* **309**, 914–917 (2005).
- [116] Á. Madarász, P. J. Rossky, and L. Turi, “Interior- and surface-bound excess electron states in large water cluster anions”, *J. Chem. Phys.* **130**, 124319 (2009).
- [117] A. Kammrath, J. R. R. Verlet, G. B. Griffin, and D. M. Neumark, “Photoelectron imaging of large anionic methanol clusters: $(\text{MeOH})_n^-$ ($n=70-460$)”, *J. Chem. Phys.* **125**, 171102 (2006).
- [118] A. Kammrath, G. B. Griffin, J. R. R. Verlet, R. M. Young, and D. M. Neumark, “Time-resolved photoelectron imaging of large anionic methanol clusters: $(\text{MeOH})_n^-$ ($n=145-535$)”, *J. Chem. Phys.* **126**, 244306 (2007).
- [119] R. M. Young, M. A. Yandell, and D. M. Neumark, “Dynamics of electron solvation in $\text{I}^-(\text{CH}_3\text{OH})_n$ clusters ($4 < n < 11$)”, *J. Chem. Phys.* **134**, 124311 (2011).
- [120] M. A. Yandell, R. M. Young, S. B. King, and D. M. Neumark, “Effects of excitation energy on the autodetachment lifetimes of small iodide-doped ROH clusters ($\text{R}=\text{H}^-, \text{CH}_3^-, \text{CH}_3\text{CH}_2^-$)”, *J. Phys. Chem. A* **116**, 2750–2757 (2012).
- [121] C. Frischkorn, M. T. Zanni, A. V. Davis, and D. M. Neumark, “Electron solvation dynamics in $\text{I}^-(\text{NH}_3)$ clusters”, *Faraday Discuss.* **115**, 49–62 (2000).
- [122] I. R. Lee, W. Lee, and A. H. Zewail, “Dynamics of electrons in ammonia cages: the discovery system of solvation”, *ChemPhysChem* **9**, 83–88 (2008).
- [123] O. T. Ehrler, G. B. Griffin, R. M. Young, and D. M. Neumark, “Photoinduced electron transfer and solvation in iodide-doped acetonitrile clusters”, *J. Phys. Chem. B* **113**, 4031–4037 (2009).
- [124] R. M. Young, G. B. Griffin, A. Kammrath, O. T. Ehrler, and D. M. Neumark, “Time-resolved dynamics in acetonitrile cluster anions $(\text{CH}_3\text{CN})_n^-$ ”, *Chem. Phys. Lett.* **485**, 59–63 (2010).
- [125] R. M. Young, M. A. Yandell, M. Niemeyer, and D. M. Neumark, “Photoelectron imaging of tetrahydrofuran cluster anions $(\text{THF})_n^-$ ($1 \leq n \leq 100$)”, *J. Chem. Phys.* **133**, 154312 (2010).
- [126] R. M. Young, R. J. Azar, M. A. Yandell, S. B. King, M. Head-Gordon, and D. M. Neumark, “Iodide solvation in tetrahydrofuran clusters: $\text{I}^-(\text{THF})_n$ ($1 \leq n \leq 30$)”, *Mol. Phys.* **110**, 1787–1799 (2012).

- [127] J. Simons, “Molecular anions”, *J. Phys. Chem. A* **112**, 6401–6511 (2008).
- [128] V. G. Bezchastnov, V. P. Vysotskiy, and L. S. Cederbaum, “Anions of xenon clusters bound by long-range electron correlations”, *Phys. Rev. Lett.* **107**, 133401 (2011).
- [129] V. K. Voora, L. S. Cederbaum, and K. D. Jordan, “Existence of a correlation bound s-type anion state of C_{60} ”, *J. Phys. Chem. Lett.* **4**, 849–853 (2013).
- [130] S. Klaiman, E. V. Gromov, and L. S. Cederbaum, “Extreme correlation effects in the elusive bound spectrum of C_{60}^- ”, *J. Phys. Chem. Lett.* **4**, 3319–3324 (2013).
- [131] V. K. Voora and K. D. Jordan, “Nonvalence correlation-bound anion state of C_6F_6 : doorway to low-energy electron capture”, *J. Phys. Chem. A* **118**, 7201–7205 (2014).
- [132] S. Klaiman, E. V. Gromov, and L. S. Cederbaum, “All for one and one for all: accommodating an extra electron in C_{60} ”, *Phys. Chem. Chem. Phys.* **16**, 13287–13293 (2014).
- [133] V. K. Voora and K. D. Jordan, “Nonvalence correlation-bound anion states of polycyclic aromatic hydrocarbons”, *J. Phys. Chem. Lett.* **6**, 3994–3997 (2015).
- [134] M.-O. Winghart, J.-P. Yang, M. Vonderach, A.-N. Unterreiner, D.-L. Huang, L.-S. Wang, S. Kruppa, C. Riehn, and M. M. Kappes, “Time-resolved photoelectron spectroscopy of a dinuclear Pt(II) complex: tunneling autodetachment from both singlet and triplet excited states of a molecular dianion”, *J. Chem. Phys.* **144**, 054305 (2016).
- [135] C. Rensing, O. T. Ehrler, J.-P. Yang, A.-N. Unterreiner, and M. M. Kappes, “Photodissociation dynamics of $IrBr_6^{2-}$ dianions by time-resolved photoelectron spectroscopy”, *J. Chem. Phys.* **130**, 234306 (2009).
- [136] D. A. Horke, A. S. Chatterley, and J. R. R. Verlet, “Femtosecond photoelectron imaging of aligned polyanions: probing molecular dynamics through the electron–anion Coulomb repulsion”, *J. Phys. Chem. Lett.* **3**, 834–838 (2012).
- [137] D. A. Horke, A. S. Chatterley, and J. R. R. Verlet, “Effect of internal energy on the repulsive Coulomb barrier of polyanions”, *Phys. Rev. Lett.* **108**, 083003 (2012).
- [138] A. S. Chatterley, D. A. Horke, and J. R. R. Verlet, “On the intrinsic photophysics of indigo: a time-resolved photoelectron spectroscopy study of the indigo carmine dianion”, *Phys. Chem. Chem. Phys.* **14**, 16155–16161 (2012).
- [139] G. M. Roberts, J. Lecointre, D. A. Horke, and J. R. R. Verlet, “Spectroscopy and dynamics of the 7,7,8,8-tetracyanoquinodimethane radical anion”, *Phys. Chem. Chem. Phys.* **12**, 6226–6232 (2010).
- [140] J. Lecointre, G. M. Roberts, D. A. Horke, and J. R. R. Verlet, “Ultrafast relaxation dynamics observed through time-resolved photoelectron angular distributions”, *J. Phys. Chem. A* **114**, 11216–11224 (2010).
- [141] D. A. Horke, G. M. Roberts, and J. R. R. Verlet, “Excited states in electron-transfer reaction products: ultrafast relaxation dynamics of an isolated acceptor radical anion”, *J. Phys. Chem. A* **115**, 8369–8374 (2011).

- [142] D. A. Horke and J. R. R. Verlet, “Time-resolved photoelectron imaging of the chloranil radical anion: ultrafast relaxation of electronically excited electron acceptor states”, *Phys. Chem. Chem. Phys.* **13**, 19546–19552 (2011).
- [143] J. N. Bull, C. W. West, and J. R. R. Verlet, “Anion resonances and above-threshold dynamics of coenzyme Q₀”, *Phys. Chem. Chem. Phys.* **17**, 16125–16135 (2015).
- [144] J. N. Bull, C. W. West, and J. R. R. Verlet, “Ultrafast dynamics of formation and autodetachment of a dipole-bound state in an open-shell π -stacked dimer anion”, *Chem. Sci.* **7**, 5352–5361 (2016).
- [145] J. N. Bull, C. W. West, and J. R. R. Verlet, “On the formation of anions: frequency-, angle-, and time-resolved photoelectron imaging of the menadione radical anion”, *Chem. Sci.* **6**, 1578–1589 (2015).
- [146] I. R. Lee, L. Bañares, and A. H. Zewail, “Direct observation of the primary bond-twisting dynamics of stilbene anion radical”, *J. Am. Chem. Soc.* **130**, 6708–6709 (2008).
- [147] D. A. Horke and J. R. R. Verlet, “Photoelectron spectroscopy of the model GFP chromophore anion”, *Phys. Chem. Chem. Phys.* **14**, 8511–8515 (2012).
- [148] C. W. West, A. S. Hudson, S. L. Cobb, and J. R. R. Verlet, “Communication: autodetachment versus internal conversion from the S₁ state of the isolated GFP chromophore anion”, *J. Chem. Phys.* **139**, 071104 (2013).
- [149] C. W. West, J. N. Bull, A. S. Hudson, S. L. Cobb, and J. R. R. Verlet, “Excited state dynamics of the isolated green fluorescent protein chromophore anion following UV excitation”, *J. Phys. Chem. B* **119**, 3982–3987 (2015).
- [150] S. Ullrich, T. Schultz, M. Z. Zgierski, and A. Stolow, “Direct observation of electronic relaxation dynamics in adenine via time-resolved photoelectron spectroscopy”, *J. Am. Chem. Soc.* **126**, 2262–2263 (2004).
- [151] A. S. Chatterley, C. W. West, G. M. Roberts, V. G. Stavros, and J. R. R. Verlet, “Mapping the ultrafast dynamics of adenine onto its nucleotide and oligonucleotides by time-resolved photoelectron imaging”, *J. Phys. Chem. Lett.* **5**, 843–848 (2014).
- [152] M. A. Yandell, S. B. King, and D. M. Neumark, “Time-resolved radiation chemistry: photoelectron imaging of transient negative ions of nucleobases”, *J. Am. Chem. Soc.* **135**, 2128–2131 (2013).
- [153] S. B. King, M. A. Yandell, and D. M. Neumark, “Time-resolved photoelectron imaging of the iodide-thymine and iodide-uracil binary cluster systems”, *Faraday Discuss.* **163**, 59–72 (2013).
- [154] S. B. King, M. A. Yandell, A. B. Stephansen, and D. M. Neumark, “Time-resolved radiation chemistry: Dynamics of electron attachment to uracil following UV excitation of iodide-uracil complexes”, *J. Chem. Phys.* **141**, 224310 (2014).

- [155] W.-L. Li, A. Kunin, E. Matthews, N. Yoshikawa, C. E. H. Dessent, and D. M. Neumark, “Photodissociation dynamics of the iodide-uracil (I^-U) complex”, *J. Chem. Phys.* **145**, 044319 (2016).
- [156] S. B. King, A. B. Stephansen, Y. Yokoi, M. A. Yandell, A. Kunin, T. Takayanagi, and D. M. Neumark, “Electron accommodation dynamics in the DNA base thymine”, *J. Chem. Phys.* **143**, 024312 (2015).
- [157] A. Kunin, W.-L. Li, and D. M. Neumark, “Dynamics of electron attachment and photodissociation in iodide-uracil-water clusters via time-resolved photoelectron imaging”, *J. Chem. Phys.* **149**, 084301 (2018).
- [158] A. B. Stephansen, S. B. King, Y. Yokoi, Y. Minoshima, W.-L. Li, A. Kunin, T. Takayanagi, and D. M. Neumark, “Dynamics of dipole- and valence bound anions in iodide-adenine binary complexes: A time-resolved photoelectron imaging and quantum mechanical investigation”, *J. Chem. Phys.* **143**, 104308 (2015).
- [159] A. Kunin, W.-L. Li, and D. M. Neumark, “Time-resolved photoelectron imaging of iodide-nitromethane ($I^- \cdot CH_3NO_2$) photodissociation dynamics”, *Phys. Chem. Chem. Phys.* **18**, 33226–33232 (2016).
- [160] R. Barrios, P. Skurski, and J. Simons, “Mechanism for damage to DNA by low-energy electrons”, *J. Phys. Chem. B* **106**, 7991–7994 (2002).
- [161] J. Simons, “How do low-energy (0.1-2 eV) electrons cause DNA-strand breaks?”, *Acc. Chem. Res.* **39**, 772–779 (2006).
- [162] H.-Y. Chen, P.-Y. Yang, H.-F. Chen, C.-L. Kao, and L.-W. Liao, “DFT reinvestigation of DNA strand breaks induced by electron attachment”, *J. Phys. Chem. B* **118**, 11137–11144 (2014).
- [163] J. Berdys, I. Anusiewicz, P. Skurski, and J. Simons, “Damage to model DNA fragments from very low-energy (< 1 eV) electrons”, *J. Am. Chem. Soc.* **126**, 6441–6447 (2004).
- [164] J. Berdys, P. Skurski, and J. Simons, “Damage to model DNA fragments by 0.25-1.0 eV electrons attached to a thymine π^* orbital”, *J. Phys. Chem. B* **108**, 5800–5805 (2004).
- [165] E. Alizadeh, F. Ferreira da Silva, F. Zappa, A. Mauracher, M. Probst, S. Denifl, A. Bacher, T. D. Märk, P. Limão-Vieira, and P. Scheier, “Dissociative electron attachment to nitromethane”, *Int. J. Mass Spectrom.* **271**, 15–21 (2008).
- [166] R. Bachorz, W. Klopper, M. Gutowski, X. Li, and K. H. Bowen, “Photoelectron spectrum of valence anions of uracil and first-principles calculations of excess electron binding energies”, *J. Chem. Phys.* **129**, 054309 (2008).
- [167] C. Desfrancois, H. Abdoul-Carime, and J.-P. Schermann, “Ground-state dipole-bound anions”, *Int. J. Mod. Phys. B* **10**, 1339–1395 (1996).
- [168] O. H. Crawford, “Negative ions of polar molecules”, *Mol. Phys.* **20**, 585–591 (1971).

- [169] I. Kulakowska, M. Geller, B. Lesyng, and K. L. Wierzchowski, “Dipole moments of 2,4-diketopyrimidines: Part II: Uracil, thymine and their derivatives”, *Biochim. Biophys. Acta, Nucleic Acids Protein Synth.* **361**, 119–130 (1974).
- [170] S. Carles, F. Lecomte, J. P. Schermann, and C. Desfrancois, “Gas-phase experimental and theoretical studies of adenine, imidazole, pyrrole, and water non-covalent complexes”, *J. Phys. Chem. A* **104**, 10662–10668 (2000).
- [171] M. Hanus, M. Kabelac, J. Rejnek, F. Ryjacek, and P. Hobza, “Correlated ab initio study of nucleic acid bases and their tautomers in the gas phase, in a microhydrated environment, and in aqueous solution. Part 3. Adenine”, *J. Phys. Chem. B* **108**, 2087–2097 (2004).
- [172] P. D. Burrow, G. A. Gallup, A. M. Scheer, S. Denifl, S. Ptasińska, T. D. Märk, and P. Scheier, “Vibrational Feshbach resonances in uracil and thymine”, *J. Chem. Phys.* **124**, 124310 (2006).
- [173] G. Hanel, B. Gstir, S. Denifl, P. Scheier, M. Probst, B. Farizon, M. Farizon, E. Illenberger, and T. D. Märk, “Electron attachment to uracil: effective destruction at subexcitation energies”, *Phys. Rev. Lett.* **90**, 188104 (2003).
- [174] S. Ptasińska, S. Denifl, S. Gohlke, P. Scheier, E. Illenberger, and T. D. Märk, “Decomposition of thymidine by low-energy electrons: Implications for the molecular mechanisms of single-strand breaks in DNA”, *Angew. Chem. Int. Ed.* **45**, 1893–1896 (2006).
- [175] S. Denifl, S. Ptasińska, G. Hanel, B. Gstir, M. Probst, P. Scheier, and T. D. Märk, “Electron attachment to gas-phase uracil”, *J. Chem. Phys.* **120**, 6557–6565 (2004).
- [176] S. Denifl, P. Sulzer, F. Zappa, S. Moser, B. Kraeutler, O. Echt, D. K. Bohme, T. D. Märk, and P. Scheier, “Isotope effects in dissociative electron attachment to the dna base thymine”, *Int. J. Mass Spectrom.* **277**, 296–299 (2008).
- [177] G. A. Gallup and I. I. Fabrikant, “Vibrational Feshbach resonances in dissociative electron attachment to uracil”, *Phys. Rev. A* **83**, 012706 (2011).
- [178] J. H. Hendricks, S. A. Lyapustina, H. L. de Clercq, J. T. Snodgrass, and K. H. Bowen, “Dipole bound, nucleic acid base anions studied via negative ion photoelectron spectroscopy”, *J. Chem. Phys.* **104**, 7788–7791 (1996).
- [179] J. Schiedt, R. Weinkauff, D. M. Neumark, and E. W. Schlag, “Anion spectroscopy of uracil, thymine and the amino-oxo and amino-hydroxy tautomers of cytosine and their water clusters”, *Chem. Phys.* **239**, 511–524 (1998).
- [180] T. Sommerfeld, “Intramolecular electron transfer from dipole-bound to valence orbitals: uracil and 5-chlorouracil”, *J. Phys. Chem. A* **108**, 9150–9154 (2004).
- [181] T. Takayanagi, T. Asakura, and H. Motegi, “Theoretical study on the mechanism of low-energy dissociative electron attachment for uracil”, *J. Phys. Chem. A* **113**, 4795–4801 (2009).

- [182] H. Motegi and T. Takayanagi, “Theoretical study on the transformation mechanism between dipole-bound and valence-bound anion states of small uracil-water clusters and their photoelectron spectra”, *J. Mol. Struct.-THEOCHEM* **907**, 85–92 (2009).
- [183] Y. Yokoi, K. Kano, Y. Minoshima, and T. Takayanagi, “Application of long-range corrected density-functional theory to excess electron attachment to biomolecules”, *Comput. Theor. Chem.* **1046**, 99–106 (2014).
- [184] J. D. Gu, J. Leszczynski, and H. F. Schaefer, “Interactions of electrons with bare and hydrated biomolecules: from nucleic acid bases to DNA segments”, *Chem. Rev.* **112**, 5603–5640 (2012).
- [185] R. N. Compton, H. S. Carman, C. Desfrancois, H. Abdoul-Carime, J. P. Schermann, J. H. Hendricks, S. A. Lyapustina, and K. H. Bowen, “On the binding of electrons to nitromethane - dipole and valence bound anions”, *J. Chem. Phys.* **105**, 3472–3478 (1996).
- [186] R. Bachorz, W. Klopper, and M. Gutowski, “Coupled-cluster and explicitly correlated perturbation-theory calculations of the uracil anion”, *J. Chem. Phys.* **126**, 085101 (2007).
- [187] C. Desfrancois, H. Abdoul-Carime, and J. P. Schermann, “Electron attachment to isolated nucleic acid bases”, *J. Chem. Phys.* **104**, 7792–7794 (1996).
- [188] O. Dolgounitcheva, V. G. Zakrzewski, and J. V. Ortiz, “Anionic and neutral complexes of uracil and water”, *J. Phys. Chem. A* **103**, 7912–7917 (1999).
- [189] O. Dolgounitcheva, V. G. Zakrzewski, and J. V. Ortiz, “Diffuse-bound and valence-bound anions of cytosine”, *J. Phys. Chem. A* **105**, 8782–8786 (2001).
- [190] D. Svozil, T. Frigato, Z. Havlas, and P. Jungwirth, “Ab initio electronic structure of thymine anions”, *Phys. Chem. Chem. Phys.* **7**, 840–845 (2005).
- [191] J. H. Hendricks, S. A. Lyapustina, H. L. de Clercq, and K. H. Bowen, “The dipole bound-to-covalent anion transformation in uracil”, *J. Chem. Phys.* **108**, 8–11 (1998).
- [192] E. Matthews, R. Cercola, G. Mensa-Bonsu, D. M. Neumark, and C. E. H. Dessent, “Photoexcitation of iodide ion-pyrimidine clusters above the electron detachment threshold: Intracuster electron transfer versus nucleobase-centred excitations”, *J. Chem. Phys.* **148**, 084304 (2018).
- [193] C. T. Middleton, K. de La Harpe, C. Su, Y. K. Law, C. E. Crespo-Hernández, and B. Kohler, “DNA excited-state dynamics: From single bases to the double helix”, *Annu. Rev. Phys. Chem.* **60**, 217–239 (2009).
- [194] K. Kleinermanns, D. Nachtigallova, and M. S. de Vries, “Excited state dynamics of DNA bases”, *Int. Rev. Phys. Chem.* **32**, 308–342 (2013).
- [195] R. Improta, F. Santoro, and L. Blancafort, “Quantum mechanical studies on the photophysics and the photochemistry of nucleic acids and nucleobases”, *Chem. Rev.* **116**, 3540–3593 (2016).

- [196] R. J. Peláez, C. Blondel, C. Delsart, and C. Drag, “Pulsed photodetachment microscopy and the electron affinity of iodine”, *J. Phys. B- At. Mol. Opt.* **42**, 125001 (2009).
- [197] W. C. Wiley and I. H. McLaren, “Time-of-flight mass spectrometer with improved resolution”, *Rev. Sci. Instrum.* **26**, 1150–1157 (1955).
- [198] A. Eppink and D. H. Parker, “Velocity map imaging of ions and electrons using electrostatic lenses: application in photoelectron and photofragment ion imaging of molecular oxygen”, *Rev. Sci. Instrum.* **68**, 3477–3484 (1997).
- [199] V. Dribinski, A. Ossadtchi, V. Mandelshtam, and H. Reisler, “Reconstruction of Abel-transformable images: the Gaussian basis-set expansion Abel transform method”, *Rev. Sci. Instrum.* **73**, 2634–2642 (2002).
- [200] M. J. Frisch, G. W. Trucks, H. B. Schlegel, G. E. Scuseria, M. A. Robb, J. R. Cheeseman, G. Scalmani, V. Barone, B. Mennucci, G. A. Petersson, H. Nakatsuji, M. Caricato, X. Li, H. P. Hratchian, A. F. Izmaylov, J. Bloino, G. Zheng, J. L. Sonnenberg, M. Hada, M. Ehara, K. Toyota, R. Fukuda, J. Hasegawa, M. Ishida, T. Nakajima, Y. Honda, O. Kitao, H. Nakai, T. Vreven, J. A. Montgomery Jr., J. E. Peralta, F. Ogliaro, M. J. Bearpark, J. Heyd, E. N. Brothers, K. N. Kudin, V. N. Staroverov, R. Kobayashi, J. Normand, K. Raghavachari, A. P. Rendell, J. C. Burant, S. S. Iyengar, J. Tomasi, M. Cossi, N. Rega, N. J. Millam, M. Klene, J. E. Knox, J. B. Cross, V. Bakken, C. Adamo, J. Jaramillo, R. Gomperts, R. E. Stratmann, O. Yazyev, A. J. Austin, R. Cammi, C. Pomelli, J. W. Ochterski, R. L. Martin, K. Morokuma, V. G. Zakrzewski, G. A. Voth, P. Salvador, J. J. Dannenberg, S. Dapprich, A. D. Daniels, Ö. Farkas, J. B. Foresman, J. V. Ortiz, J. Cioslowski, and D. J. Fox, *Gaussian 09, Revision C.01*, 2009.
- [201] C. E. H. Dessent, J. Kim, and M. A. Johnson, “Spectroscopic observation of vibrational Feshbach resonances in near-threshold photoexcitation of $X^- \cdot \text{CH}_3\text{NO}_2$ ($X^- = \text{I}^-$ and Br^-)”, *Faraday Discuss.* **115**, 395–406 (2000).
- [202] F. Lecomte, S. Carles, C. Desfrancois, and M. A. Johnson, “Dipole bound and valence state coupling in argon-solvated nitromethane anions”, *J. Chem. Phys.* **113**, 10973–10977 (2000).
- [203] C. L. Adams, H. Schneider, K. M. Ervin, and J. M. Weber, “Low-energy photoelectron imaging spectroscopy of nitromethane anions: electron affinity, vibrational features, anisotropies, and the dipole-bound state”, *J. Chem. Phys.* **130**, 074307 (2009).
- [204] J. E. Sansonetti and W. C. Martin, “Handbook of basic atomic spectroscopic data”, *J. Phys. Chem. Ref. Data* **34**, 1559–2259 (2005).
- [205] R. B. Metz, D. R. Cyr, and D. M. Neumark, “Study of the ${}^2\text{B}_1$ and ${}^2\text{A}_2$ states of CH_2NO_2 via ultraviolet photoelectron spectroscopy of the CH_2NO_2^- anion”, *J. Phys. Chem.* **95**, 2900–2907 (1991).

- [206] T. Beyer and D. F. Swinehart, “Number of multiply-restricted partitions”, *Commun. ACM* **16**, 379–379 (1973).
- [207] S. E. Stein and B. S. Rabinovitch, “Accurate evaluation of internal energy level sums and densities including anharmonic oscillators and hindered rotors”, *J. Chem. Phys.* **58**, 2438–2445 (1973).
- [208] W. L. Hase, “Simulations of gas-phase chemical reactions: applications to SN2 nucleophilic substitution”, *Science* **266**, 998–1002 (1994).
- [209] H. Wang, G. H. Peslherbe, and W. L. Hase, “Trajectory studies of SN2 nucleophilic substitution. 4. Intramolecular and unimolecular dynamics of the $\text{I}^- \cdots \text{CH}_3\text{Br}$ and $\text{ClCH}_3 \cdots \text{Br}^-$ complexes”, *J. Am. Chem. Soc.* **116**, 9644–9651 (1994).
- [210] G. H. Peslherbe, H. Wang, and W. L. Hase, “Unimolecular dynamics of $\text{Cl}^- \cdots \text{CH}_3\text{Cl}$ intermolecular complexes formed by $\text{Cl}^- + \text{CH}_3\text{Cl}$ association”, *J. Chem. Phys.* **102**, 5626–5635 (1995).
- [211] M. L. Chabinye, S. L. Craig, C. K. Regan, and J. I. Brauman, “Gas-phase ionic reactions: dynamics and mechanism of nucleophilic displacements”, *Science* **279**, 1882 (1998).
- [212] J. Xie, R. Otto, J. Mikosch, J. Zhang, R. Wester, and W. L. Hase, “Identification of atomic-level mechanisms for gas-phase $\text{X}^- + \text{CH}_3\text{Y}$ SN2 reactions by combined experiments and simulations”, *Acc. Chem. Res.* **47**, 2960–2969 (2014).
- [213] J. Simons, “Propensity rules for vibration-induced electron detachment of anions”, *J. Am. Chem. Soc.* **103**, 3971–3976 (1981).
- [214] P. K. Acharya, R. A. Kendall, and J. Simons, “Vibration-induced electron detachment in molecular anions”, *J. Am. Chem. Soc.* **106**, 3402–3407 (1984).
- [215] E. E. B. Campbell and R. D. Levine, “Delayed ionization and fragmentation en route to thermionic emission: statistics and dynamics”, *Annu. Rev. Phys. Chem.* **51**, 65–98 (2000).
- [216] J. U. Andersen, E. Bonderup, and K. Hansen, “Thermionic emission from clusters”, *J. Phys. B: At., Mol. Opt. Phys.* **35**, R1 (2002).
- [217] K. Mazurkiewicz, R. Bachorz, M. Gutowski, and J. Rak, “On the unusual stability of valence anions of thymine based on very rare tautomers: A computational study”, *J. Phys. Chem. B* **110**, 24696–24707 (2006).
- [218] N. A. Oyler and L. Adamowicz, “Electron attachment to uracil: theoretical ab initio study”, *J. Phys. Chem.* **97**, 11122–11123 (1993).
- [219] H.-T. Liu, C.-G. Ning, D.-L. Huang, and L.-S. Wang, “Vibrational spectroscopy of the dehydrogenated uracil radical by autodetachment of dipole-bound excited states of cold anions”, *Angew. Chem. Int. Ed.* **53**, 2464–2468 (2014).

- [220] B. F. Parsons, S. M. Sheehan, T. A. Yen, D. M. Neumark, N. Wehres, and R. Weinkauf, “Anion photoelectron imaging of deprotonated thymine and cytosine”, *Phys. Chem. Chem. Phys.* **9**, 3291–3297 (2007).
- [221] H. L. Williams, B. A. Erickson, and D. M. Neumark, “Time-resolved photoelectron spectroscopy of adenosine and adenosine monophosphate photodeactivation dynamics in water microjets”, *J. Chem. Phys.* **148**, 194303 (2018).
- [222] F. Buchner, H. H. Ritze, J. Lahl, and A. Lübcke, “Time-resolved photoelectron spectroscopy of adenine and adenosine in aqueous solution”, *Phys. Chem. Chem. Phys.* **15**, 11402–11408 (2013).
- [223] F. Buchner, A. Nakayama, S. Yamazaki, H. H. Ritze, and A. Lübcke, “Excited-state relaxation of hydrated thymine and thymidine measured by liquid-jet photoelectron spectroscopy: experiment and simulation”, *J. Am. Chem. Soc.* **137**, 2931–2938 (2015).

Chapter 9

Experimental Developments Towards TRPES of Larger Biomolecular Anions

For, you see, so many out-of-the-way things had happened lately, that Alice had begun to think that very few things indeed were really impossible.

Lewis Carroll

9.1 Overview

While nucleobases are expected to be initial sites for electron attachment and TNI formation [1–6], naturally the dissociation mechanisms and channels active in larger nucleic acid systems are of significant interest. In this chapter we describe experimental modifications that were made in an attempt to reconfigure the cluster source of the experiment to produce larger gas-phase biomolecular anions such as nucleosides and nucleotides. The existing thermal desorption cluster source was modified to produce gas-phase anions by laser desorption. Despite a variety of attempted configurations, ultimately this approach was unsuccessful in producing high repetition rate biomolecular anions and clusters with enough stability for TRPES experiments and the original design was reinstated. For this reason, we focus here on the overall design and approach rather than provide detailed machine diagrams and specific measurements. We also provide an outlook for the future production of large, biomolecular anions through the construction of an electrospray ionization cluster source. With such a source, iodide-nucleotide anions or oligonucleotide clusters, for example, could be probed with TRPES to reveal the complex mechanisms of attachment and photodissociation as well as competition between fragmentation and autodetachment decay pathways.

9.2 Larger Nucleic Acid Constituents

The extension of TRPES to iodide-associated clusters of nucleosides and nucleotides presents a powerful model system for more advanced studies of reductive DNA damage and fragmentation patterns in nucleic acid constituents. The uridine nucleoside (Ur), for example, has been calculated [7] at the DFT/B3LYP/LANL2DZ level of theory here to have an asymptotic dissociation energy of 0.6 eV for dissociation into $[\text{Ur-H}]^-$ and the ribose sugar unit. At the DFT/B3LYP/6-311+G* level of theory, both the uridine ring and the ribose sugar adopt a more “puckered” geometry as seen in Fig. 9.1. Previous single-photon PES studies of laser desorbed uridine anions have suggested that the excess negative charge is mostly associated with the nucleobase moiety and that uridine preferentially forms a stable VB anion rather than a DB anion [8]. The VDE of Ur^- was measured to be approximately 1.39 eV. The binding of iodide to the cluster is calculated (Fig. 9.2) to produce a slightly different configuration as compared to the calculated ground state structure of $\text{I}^- \cdot \text{U}$ due to the presence of the ribose moiety. The iodide-uridine ($\text{I}^- \cdot \text{Ur}$) cluster VDE is calculated to be 4.47 eV at the DFT/ ω B97XD/LANL2DZ level of theory. $\text{I}^- \cdot \text{Ur}$ clusters have been calculated to have an energy of 1.12 eV for dissociation to iodide and neutral uridine.

The current cluster source in the experimental apparatus described in Ch. 2 relies on the inherent vapor pressure of the species of interest. Liquid CH_3I provides a volatile source of I^- to produce iodide-associated clusters. Other species examined are volatile liquids, such as CH_3NO_2 , or are solids that may be thermally desorbed at temperatures ≤ 240 °C to produce gas phase population. Nucleobases such as uracil and thymine are sufficiently

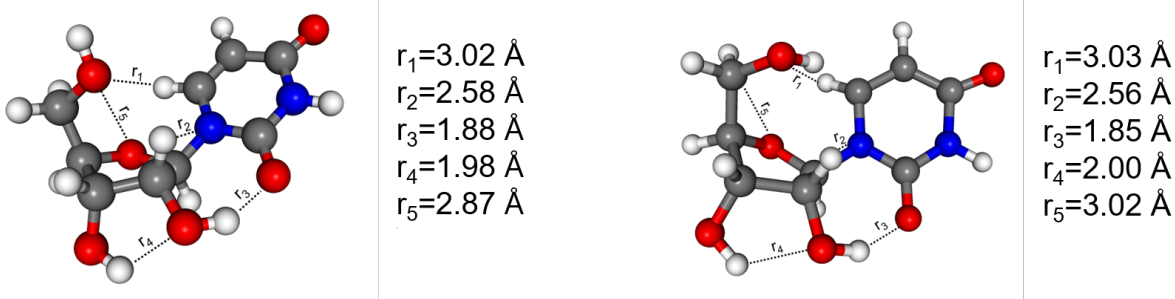


Figure 9.1: B3LYP/6-311+G* calculated structures for the uridine neutral (left) and anion (right) with selected distances as marked.

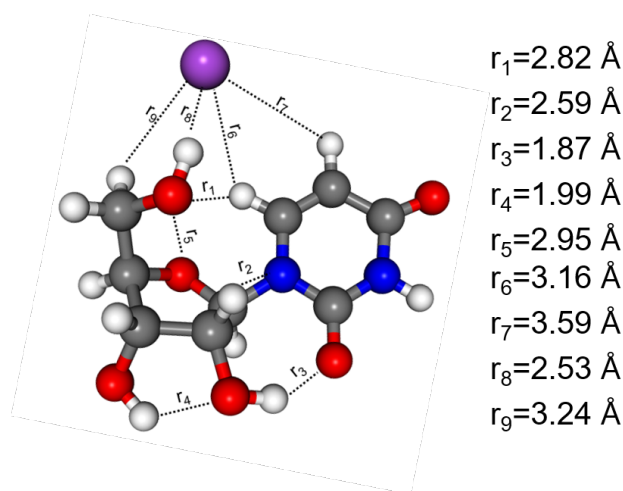


Figure 9.2: ω B97XD/LANL2DZ calculated structure for the iodide-uridine anion ground state structure with selected distances as marked.

volatile when heated to $\sim 205 - 235$ °C to produce $\text{I}^- \cdot \text{N}$ clusters and do not decompose at these temperatures. However, some nucleobases such as adenine, guanine, and cytosine are known to produce non-canonical tautomers when heated which poses a significant challenge for the interpretation of TRPE spectra [9]. Larger nucleic acid constituents, such as nucleosides, have relatively low melting points (Table 9.1) and heating of the solid results in dissociation of the relatively low energy glycosidic bond between the nucleobase and sugar moieties.

To promote larger nucleic acid constituents into the gas phase as anions and anionic clusters, two general techniques have been employed: laser desorption (ablation) [8, 10, 11], and electrospray ionization [12–17]. Each technique presents unique inherent advantages and disadvantages. Electrospray ionization (ESI), for example, which involves solvating the species of interest in solution and aspirating the solution into vacuum through a charged

Table 9.1: Experimentally determined melting points (MPs) of the canonical DNA and RNA nucleobases and nucleosides. All values from ChemSpider.

Nucleobase	MP (°C)	Nucleoside	MP (°C)
Uracil	330 – 335	Uridine	167
Thymine	317	Thymidine	186
Adenine	360	Adenosine	235
Cytosine	320 – 325	Cytidine	215
Guanine	360	Guanosine	250

capillary [18], requires the addition of multiple vacuum chambers, pumps, differential pumping regions, and an ion trap to create pulsed packets of ions from the continuous ESI source (see Section 9.4 for more details) [19, 20]. ESI also has a tendency to produce multiply charged clusters and deprotonated clusters, the latter of which is particularly challenging to distinguish within the energy resolution of the current Wiley-McLaren configuration [21]. Finally, the internal temperature of the produced clusters tends to be relatively high, which could lead to the formation of non-canonical biological tautomers [17] or internally excited species. Laser desorption or ablation cluster sources are known to exhibit instability, but have been employed to generate gas-phase nucleoside and nucleotide anions for photoelectron spectroscopy in previous work [8, 10, 11]. For these reasons, and past success in our laboratory with laser ablation-produced cluster anions for photoelectron spectroscopy [22], a laser desorption cluster source was constructed.

9.3 Laser Desorption Cluster Source

In the development of this cluster source design, several factors are important to be able to implement the new source into the existing experimental apparatus.¹ First, TRPES requires, in general, long signal averaging times, particularly for the study of anions and anionic clusters for which the molecule number density is many orders of magnitude smaller than that typical for a neutral gas jet. The KMLabs laser system in its current implementation operates at a repetition rate of 1 kHz. Most laser desorption cluster sources, however, operate typically at $\sim 10 - 20$ Hz. To enable time-resolved studies with realistic data collection times while maintaining reasonable shot-to-shot cluster stability, our laser desorption cluster source was designed to operate at 200 Hz. We note that although a 1 kHz repetition rate laser ablation cluster source for the production of gas-phase guanine was reported in 2003 [23], time-resolved studies for laser ablation-produced biological anions have never been reported.

¹ The original laser desorption design and many of the attempts described herein were a combined effort with Dr. Wei-li Li whose work was instrumental in this effort.

An overall view of the design within the “SRC” chamber region and the basic cluster source design is shown in Fig. 9.3. In the left panel, the existing Wiley-McLaren plates enclosed within the “0D” differential pumping region are shown. A 50 mm diameter window was cut and installed on the left-side door to the chamber (and a small hole through the left 0D plate) to allow the laser light from the ablation laser (see below for details) to pass into the chamber between the Wiley-McLaren repeller and extractor plates. The Even-Lavie valve, which was previously mounted directly above the Wiley-McLaren repeller and extractor plates was remounted in the right side of the chamber. A custom copper block was constructed to mount and interface between the Even-Lavie valve, the solid sample of interest (target), two stepper motors for rotation and translation of the target, and interchangeable channels for growth of the ablated gas sample and for supersonic expansion. The laser light was passed through the expansion channel to strike the target, and the ablated gas mixture was supersonically expanded collinearly with the laser light into the Wiley-McLaren. The square Wiley-McLaren plates were rotated 90° to re-wire the high voltage electrical connections to the top of the chamber where the Even-Lavie valve originally sat.

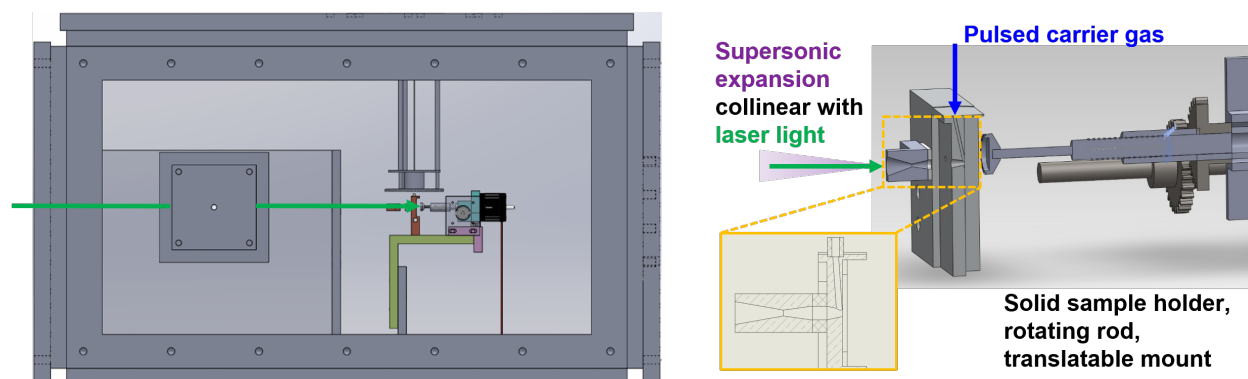


Figure 9.3: Interior of the SRC and 0D vacuum regions (left) and cross-section of the ablation cluster source design (right). The green arrow represents the ablation laser light.

Our initial attempts focused primarily on the generation of $\text{I}^- \cdot \text{Ur}$ clusters, although uracil, other nucleobases and nucleosides, and a variety of metals were also explored. Lower repetition rate laser ablation sources have employed, in general, two types of “targets”: 1) a graphite rod with the solid sample of interest (e.g. solid uridine) rubbed onto the exterior of the rod [8], and 2) hand-pressed or hydraulic-pressed pellets of graphite mixed with the solid sample of interest [22]. For maximum sample longevity, we ultimately opted for a design with hand-pressed or hydraulic-pressed pellets of uridine mixed in a variety of ratios with a variety of different malleable metals including graphite, indium, lead, bismuth, and neat uridine. Early designs featured a 1 cm diameter target that was later increased to 2.5 cm diameter to increase the usable area of the target. Targets were hand-pressed up to 3 T (1 cm targets) or hydraulic-pressed (Across International MP24A) at a variety of pressures up to 24 T in a 25 mm cylindrical die. Targets with a higher proportion of metal were generally

much less fragile than neat nucleosides or nucleobases, and targets pressed to a thickness of at least 0.25 cm were the most robust. Targets were secured to a tapped aluminum target holder (for mounting to the rotation motor) with either Krazy Glue or Torr Seal epoxy. Some examples of 25 mm hydraulic press targets following laser irradiation are shown in Fig. 9.4.



Figure 9.4: Homemade pressed uridine targets after irradiation. Clockwise from top right: neat uridine pressed by 20 T, 1:1 by volume indium:uridine pressed by 12 T, 1:1 by volume carbon:uridine pressed by 20 T, 2:3 by volume carbon:uridine pressed by 12 T.

Regardless of the target composition, each laser pulse must hit a fresh spot on the solid target for effective ablation and minimum formation of pits on the surface. For this reason, stepper motors were employed to rotate and translate the solid target (Automation Direct SureStep STP-DRV-4850). To produce collisionally cooled, iodide-associated clusters, a gas expansion of 400 – 1100 kPa of argon or helium gas seeded with CH_3I was passed in front of the target to entrain the ablated gas molecules and then supersonically expanded into the existing Wiley-McLaren design. The pulsed carrier gas was delivered by the Even-Lavie valve which was unmounted and re-wired to sit comfortably inside the chamber by the solid target. The best results were obtained when the Even-Lavie valve fired approximately 250 μs before the arrival of the laser pulse at the target. The Wiley-McLaren plates were then pulsed $\sim 450 \mu\text{s}$ after the valve. The valve was mounted with a close but not overly tight fit to the copper block interface between the pulsed valve, the solid target, and the cluster growth and supersonic expansion channels. The block was constructed of copper for maximum heat dissipation as the ablation source was found to heat up considerably, particularly with higher laser power. The gas was flowed into an angled gas channel to force the gas to meet the face of the target and expand from the target face to the trumpet-shaped nozzle, as seen in the inset in Fig. 9.3. The expansion nozzle was also constructed of copper, and a variety of nozzle lengths, inner diameters, and opening sizes were explored. An interchangeable “growth channel” constructed of either aluminum or teflon was tested to adjust the size of

the interaction region for the ablated molecules and the backing gas. At the exit of the supersonic expansion channel, the Even-Lavie ionizer was eventually mounted to attempt to improve the production of anions from the desorption source. The ~ 1 cm ionizer body opening also helped to collimate the molecular beam entering the Wiley-McLaren. Overall, the ionizer was not found to improve the anion cluster signal. If placed too close to the Wiley-McLaren, the adjacent electric fields were found to produce erratic behavior in the cluster source.

For desorption, a Litron Lasers Ltd. Nano TRL 0-200 Nd:YAG laser operating at 200 Hz was employed. In this scheme, the KMLabs femtosecond laser system reference trigger remained the “master” trigger for the experimental apparatus, but was cut to 200 Hz instead of 500 Hz by the DEI PDG-2510 pulse box. The Litron laser was therefore externally triggered by the KMLabs laser, with an optimal delay between the lamp trigger and Q-switch trigger of ~ 535 μ s. When operating at 532 nm, the laser produced a 15-20 ns pulse. Unfortunately, the high laser repetition rate was found to degrade the laser flashlamps quickly, and if running for 8 – 10 hours per day, required laser maintenance as much as every 1 – 2 weeks. The laser produced ≤ 80 mJ/pulse at 1064 nm or ≤ 45 mJ/pulse at 532. With an external 5 mm thick KDP crystal cut for SHG of 532 nm, (Eksma Optics KDP-401) up to 2 – 3 mJ/pulse of 266 nm light could also be obtained. We explored the effectiveness of laser ablation with each of these wavelengths for a wide range of powers. A focusing lens was used to focus the laser down at the target to < 1 mm, and a variety of focal lengths and focal spot choices (e.g. in front of target, at target, behind target) were tested.

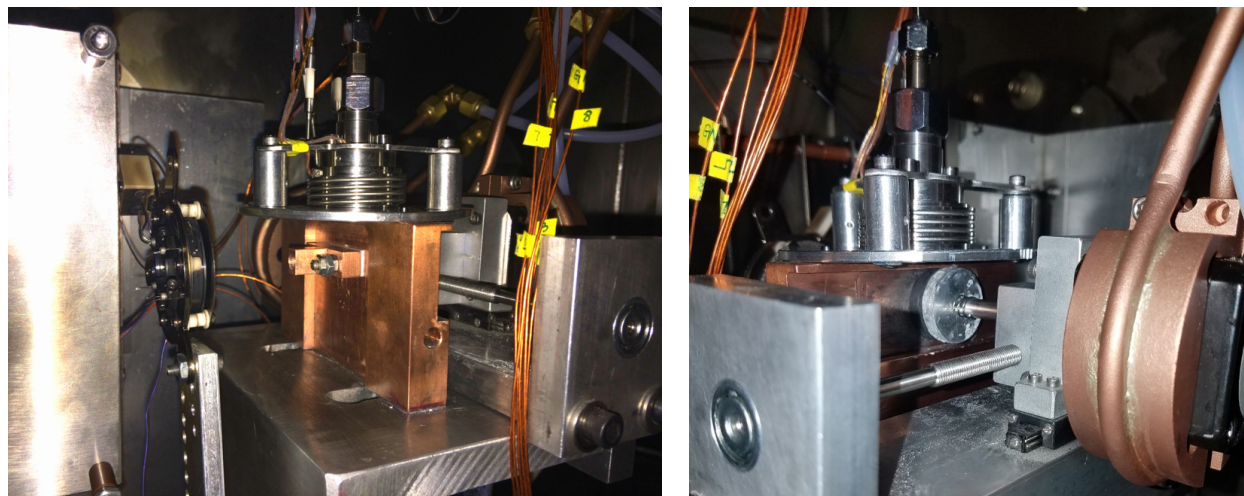


Figure 9.5: Images of front (left) and rear (right) of the constructed laser ablation cluster source.

As shown in Fig. 9.3 and Fig. 9.5, the apparatus sat to the right of the Wiley-McLaren plates (left) with the copper block on an aluminum mount with fully adjustable translation

relative to the Wiley-McLaren plates and adjustable height. In general, the ion signal was found to be the best with the expansion nozzle placed as close as possible to the Wiley-McLaren plates. To accommodate this, the differential pumping enclosure between the SRC and OD regions of the chamber was eventually removed. The target was spring-load mounted to the rotation motor (shown, right). For thicker targets for which the spring could become overly tight, a spacer was needed to push back the mount for the motor slightly, otherwise too much friction between the target face and the copper block would destroy the target. The target and rotation motor were translated along a threaded rod controlled by a second step motor (not shown) mounted to the mounting block. Each motor was encased in a custom copper cooling block cut to fit the motor and connected externally from the vacuum chamber to a chilled water supply.

Mass spectra confirmed the formation of $\text{I}^- \cdot \text{Ur}$ in the cluster source with reasonable signal intensity, as shown in Fig. 9.6. However, the cluster signal exhibited considerable shot-to-shot intensity fluctuations and instability and was not able to persist for more than 10s of minutes. In the following subsection we outline some of the expected underlying reasons for the instability in the cluster source and the attempts made to mitigate them.

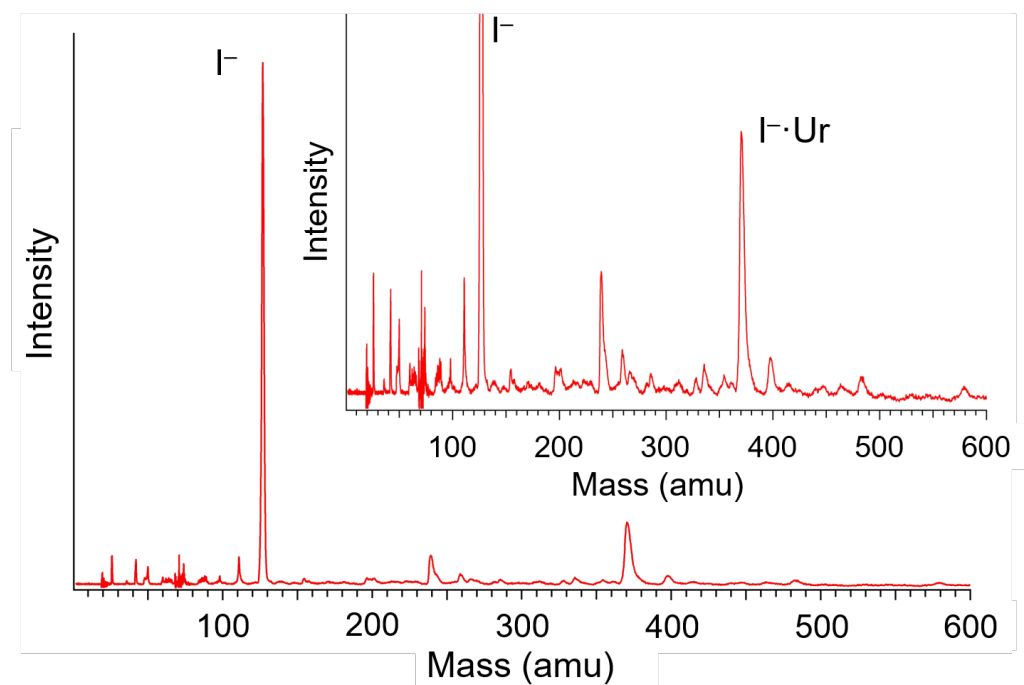


Figure 9.6: Mass spectrum of desorbed $\text{I}^- \cdot \text{Ur}$. This spectrum was collected from a 1:4 by volume bismuth:uridine target pressed to 5 T and irradiated with 532 nm at ~ 20 mJ/pulse entrained by He carrier gas seeded with CH_3I . The smaller peak between I^- and $\text{I}^- \cdot \text{Ur}$ corresponds to either Ur^- (244 amu) or $\text{I}^- \cdot [\text{U-H}]$ (238 amu).

Challenges

A variety of challenges were encountered with the production of stable nucleoside anions from the desorption cluster source. The underlying mechanism of laser desorption and laser ablation techniques remains an active area of research today (e.g. for matrix-assisted laser desorption/ionization (MALDI) [24]), but some known difficulties with stable laser ablation, particularly at higher repetition rates, have been previously reported [23]. In particular, the characteristics of the employed laser have been shown to be very important, including the laser wavelength, pulse duration, and power. The target composition is also of significant importance, particularly for metals employed as binding agents as the various thermodynamic, topological, and optical properties of a given target can render it more susceptible to clogging or target deformation.

Clogging of the growth channel in the cluster source was found to be a major problem. For targets of neat uridine, targets had a tendency to melt upon contact with the laser and after $\sim 1 - 2$ hours would fully clog the expansion channel. Temporarily increasing the laser power, for example, to melt the clog was found to be unsuccessful and once clogged the apparatus must be vented and sonicated clean. For targets with metal binders, debris formation and condensation inside the growth channel was also problematic and would also cause clogging within an hour. As observed by others [23], ablation will exfoliate the surface of the target and can cause μm -sized particulates to build up in the narrow growth and expansion channels. In particular, low melting point binder metals with high conductivity (e.g. indium), which are typically the most convenient for custom-pressing pellets, may lead to subsurface boiling in the target which also produces small particulate matter. For this reason it was important to maintain the highest backing gas pressure possible so as to sufficiently sweep particulate from the growth channel to prevent build-up. Build-up of particle deposits, however, was often found to be inevitable regardless of the diameter or length of the interchangeable growth channel. An overly long growth channel was also found to decrease signal intensity because the temporal spread of the ion packet into the Wiley-McLaren increased, producing weak ion packets. It is possible that a “leak valve” scheme to produce continuous rather than pulsed backing gas would be more effective to prevent clogging. Running the Even-Lavie valve at a higher repetition rate than the ablation source or using the longest possible pulse width both were found to produce higher ion signal intensity but significantly decreased signal stability.

Debris from the ablated target was also found to settle on the laser inlet window due to the configuration in which the gas was expanded collinearly with the incoming laser beam. Neutral particles undeflected by the Wiley-McLaren would settle on the window within a few hours. While the laser maintained a clear path, the particulate on the window would eventually heat up from the laser and, if severe enough, would shatter the window to the vacuum chamber even for a window several mm thick. It has been suggested² that VHS

² Private communication, Michael Zürich, August 28, 2017.

cassette tape film could be applied to the window in the interior of the vacuum chamber to prevent particle build-up on the window but still allow 532 nm light to effectively pass through, but this was ultimately not tested here.

Target deformation and depletion was also found to be a considerable problem in conjunction with clogging. Neat uridine targets were particularly fragile and would often crack or shatter upon loading into the apparatus. Once melted, clogging would become inevitable. Uridine-binder metal mixes generally remained more structurally intact, especially those with a higher percentage of metal. However, mixed targets were found to quickly deplete the full amount of uridine in the target and leave behind only the remaining metal, particularly with high laser powers. For pure metal targets (e.g. graphite), $\sim 8 - 10$ mJ/pulse of laser power at 532 nm was able to produce excellent cluster signal, while as much as $20 - 25$ mJ/pulse was required to produce uridine anion signal. We note also that these required laser powers are, in general, rather high compared to those employed in other laser ablation sources [8, 22, 23]. To combat problems with target depletion, other laser ablation designs have incorporated the use of multiple loaded targets staggered along the translation rod, so that once one target is depleted, a new one may be translated into place without the need to break vacuum.

Regardless of target composition and laser focusing characteristics, the laser would etch a spiral into the rotating and translating target surface as seen in Fig. 9.4. Previous work has reported the development of these grooves or threads in the surface would ultimately lead to strong signal attenuation [23]. Mounting the laser focusing lens to a stepper motor and dithering the laser focus asynchronously to the target motion to prevent any regular pattern from forming on the target surface may help remedy this problem.

A re-designed “SEVI-style” laser ablation apparatus modeled after the cluster source design in use on the Slow Electron Velocity-map Imaging apparatus in the Neumark group [22] was also tested in our system with relatively little success. Briefly, in this design, the expanding, ablated gas does not travel collinear to the laser but instead the backing gas is passed orthogonally along the face of the target surface in the direction of the desired cluster expansion. The valve was remounted and the cluster source rotated to accommodate this design. The laser needed to now be steered through the chamber to the target, which required either four optics mounted in the vacuum chamber, or a new window cut into the vacuum chamber and new table to re-mount the ablation laser. Unfortunately, the SRC vacuum chamber region is pumped by diffusion pumps that aspirate oil into the chamber. With high laser power, oil is quickly burned to the surface of the optics, permanently destroying them and leaving behind little laser power, so tight beam enclosures around the mirrors were constructed. Regardless, the SEVI-style design was ultimately found to not be more effective than the original design.

Other designs to promote involatile species to the gas phase to create anions have been

suggested, including laser-induced thermal desorption. In such a design, dissolved uridine may be evaporated and plated onto a thin sheet or foil to increase the surface area and irradiated by a laser from the back side of the foil [25]. Many variations on sample preparation and mixing were also attempted, including a MALDI-type approach with dissolved uridine targets, and “hot-pressing” targets in which the uridine was gently melted and mixed with a metal binder to produce a uniform solid target when cooled slightly and pressed into a pellet. Neither of these target preparation approaches were as effective as the regular hydraulic pressing.

9.4 Outlook

Despite some disadvantages associated with ESI outlined in Section 9.2, ESI has been shown to be an extremely powerful source for generating gas-phase ions of a biological nature [18]. Dessent and co-workers have employed ESI to successfully generate a variety of gas-phase iodide-associated nucleobase clusters [15–17], although we note that differences in the internal energy of the clusters generated by our thermal desorption cluster source and their ESI source have been observed and may result in the presence of different nucleobase tautomers [9, 17]. Verlet and co-workers have demonstrated the efficacy of an ESI source for the production of deprotonated nucleotide anions [12–14], among other biomolecules [26], with enough intensity and stability for TRPES studies. Therefore, future experimental upgrades to our apparatus are focused on the implementation of an ESI source to enable a variety of TRPES experiments aimed at probing the dynamics of iodide-nucleosides and -nucleotides or even larger oligonucleotide species.

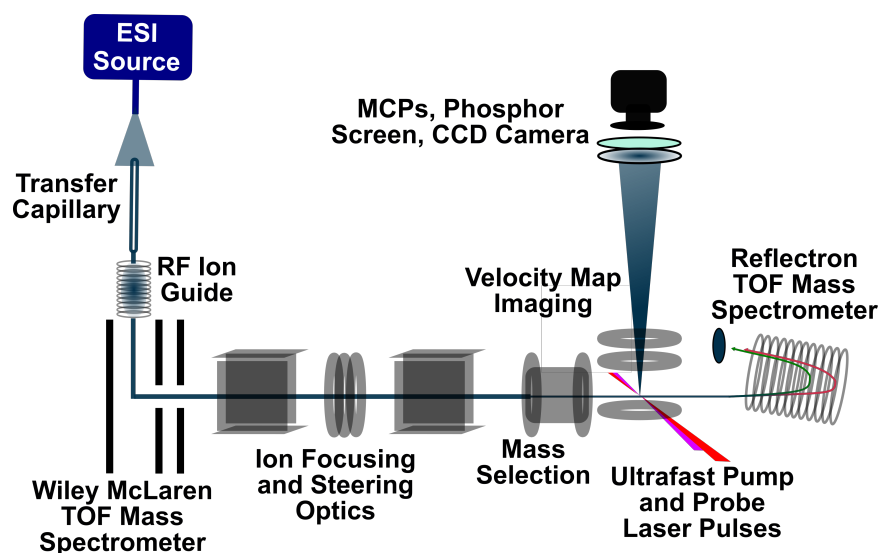


Figure 9.7: Proposed experimental apparatus update with ESI source and radio frequency (RF) ion trap, orthogonal VMI detector and in-line reflectron TOF mass spectrometer.

To facilitate analysis of the increasingly complex photoelectron spectra expected for these larger molecules, the re-installation of a reflectron mass spectrometer [27] previously employed in our apparatus [21, 28] will allow for the identity of the photofragments to be measured independent of the photoelectron spectra. An example schematic of this proposed design is shown in Fig. 9.7. Such a design will relax the necessity for high energy, high power UV probe pulses $\geq 3.5 - 4$ eV, which are challenging to generate given our existing laser implementation, to identify the presence of anionic photofragments with binding energies > 3 eV. In addition, mass spectrometry provides information for the relative abundance of various fragments relative to one another or relative to the parent species, which is typically not possible to reliably extract from photoelectron spectroscopy. The combination of these two experimental upgrades to our existing apparatus is expected to enable a new regime in the study of the ultrafast dynamics of biomolecular anions and DNA damage.

9.5 References

- [1] R. Barrios, P. Skurski, and J. Simons, “Mechanism for damage to DNA by low-energy electrons”, *J. Phys. Chem. B* **106**, 7991–7994 (2002).
- [2] F. Martin, P. D. Burrow, Z. L. Cai, P. Cloutier, D. Hunting, and L. Sanche, “DNA strand breaks induced by 0-4 eV electrons: The role of shape resonances”, *Phys. Rev. Lett.* **93**, 068101 (2004).
- [3] J. Berdys, I. Anusiewicz, P. Skurski, and J. Simons, “Damage to model DNA fragments from very low-energy (< 1 eV) electrons”, *J. Am. Chem. Soc.* **126**, 6441–6447 (2004).
- [4] S. Ptasińska, S. Denifl, S. Gohlke, P. Scheier, E. Illenberger, and T. D. Märk, “Decomposition of thymidine by low-energy electrons: Implications for the molecular mechanisms of single-strand breaks in DNA”, *Angew. Chem. Int. Ed.* **45**, 1893–1896 (2006).
- [5] J. Simons, “How do low-energy (0.1-2 eV) electrons cause DNA-strand breaks?”, *Acc. Chem. Res.* **39**, 772–779 (2006).
- [6] H.-Y. Chen, P.-Y. Yang, H.-F. Chen, C.-L. Kao, and L.-W. Liao, “DFT reinvestigation of DNA strand breaks induced by electron attachment”, *J. Phys. Chem. B* **118**, 11137–11144 (2014).
- [7] M. J. Frisch, G. W. Trucks, H. B. Schlegel, G. E. Scuseria, M. A. Robb, J. R. Cheeseman, G. Scalmani, V. Barone, B. Mennucci, G. A. Petersson, H. Nakatsuji, M. Caricato, X. Li, H. P. Hratchian, A. F. Izmaylov, J. Bloino, G. Zheng, J. L. Sonnenberg, M. Hada, M. Ehara, K. Toyota, R. Fukuda, J. Hasegawa, M. Ishida, T. Nakajima, Y. Honda, O. Kitao, H. Nakai, T. Vreven, J. A. Montgomery Jr., J. E. Peralta, F. Ogliaro, M. J. Bearpark, J. Heyd, E. N. Brothers, K. N. Kudin, V. N. Staroverov, R. Kobayashi, J. Normand, K. Raghavachari, A. P. Rendell, J. C. Burant, S. S. Iyengar, J. Tomasi, M. Cossi, N. Rega, N. J. Millam, M. Klene, J. E. Knox, J. B. Cross, V.

- Bakken, C. Adamo, J. Jaramillo, R. Gomperts, R. E. Stratmann, O. Yazyev, A. J. Austin, R. Cammi, C. Pomelli, J. W. Ochterski, R. L. Martin, K. Morokuma, V. G. Zakrzewski, G. A. Voth, P. Salvador, J. J. Dannenberg, S. Dapprich, A. D. Daniels, Ö. Farkas, J. B. Foresman, J. V. Ortiz, J. Cioslowski, and D. J. Fox, *Gaussian 09, Revision C.01*, 2009.
- [8] S. T. Stokes, X. Li, A. Grubisic, Y. J. Ko, and K. H. Bowen, “Intrinsic electrophilic properties of nucleosides: photoelectron spectroscopy of their parent anions”, *J. Chem. Phys.* **127**, 084321 (2007).
- [9] A. B. Stephansen, S. B. King, Y. Yokoi, Y. Minoshima, W.-L. Li, A. Kunin, T. Takayanagi, and D. M. Neumark, “Dynamics of dipole- and valence bound anions in iodide-adenine binary complexes: A time-resolved photoelectron imaging and quantum mechanical investigation”, *J. Chem. Phys.* **143**, 104308 (2015).
- [10] S. T. Stokes, A. Grubisic, X. Li, Y. J. Ko, and K. H. Bowen, “Photoelectron spectroscopy of the parent anions of the nucleotides, adenosine-5'-monophosphate and 2'-deoxyadenosine-5'-monophosphate”, *J. Chem. Phys.* **128**, 044314 (2008).
- [11] X. Li, H. Wang, and K. H. Bowen, “Photoelectron spectroscopic study of the hydrated nucleoside anions: uridine⁻ (H₂O)_{n=0-2}, cytidine⁻ (H₂O)_{n=0-2}, and thymidine⁻ (H₂O)_{n=0,1}”, *J. Chem. Phys.* **133**, 144304 (2010).
- [12] A. S. Chatterley, C. W. West, G. M. Roberts, V. G. Stavros, and J. R. R. Verlet, “Mapping the ultrafast dynamics of adenine onto its nucleotide and oligonucleotides by time-resolved photoelectron imaging”, *J. Phys. Chem. Lett.* **5**, 843–848 (2014).
- [13] A. S. Chatterley, C. W. West, V. G. Stavros, and J. R. R. Verlet, “Time-resolved photoelectron imaging of the isolated deprotonated nucleotides”, *Chem. Sci.* **5**, 3963–3975 (2014).
- [14] V. G. Stavros and J. R. R. Verlet, “Gas-phase femtosecond particle spectroscopy: a bottom-up approach to nucleotide dynamics”, *Annu. Rev. Phys. Chem.* **67**, 211–232 (2016).
- [15] W.-L. Li, A. Kunin, E. Matthews, N. Yoshikawa, C. E. H. Dessent, and D. M. Neumark, “Photodissociation dynamics of the iodide-uracil (I⁻U) complex”, *J. Chem. Phys.* **145**, 044319 (2016).
- [16] E. Matthews, R. Cercola, G. Mensa-Bonsu, D. M. Neumark, and C. E. H. Dessent, “Photoexcitation of iodide ion-pyrimidine clusters above the electron detachment threshold: Intracuster electron transfer versus nucleobase-centred excitations”, *J. Chem. Phys.* **148**, 084304 (2018).
- [17] R. Cercola, E. Matthews, and C. E. H. Dessent, “Near-threshold electron transfer in anion-nucleobase clusters: does the identity of the anion matter?”, *Mol. Phys.* **117**, 3001–3010 (2019).
- [18] J. B. Fenn, “Electrospray wings for molecular elephants (Nobel lecture)”, *Angew. Chem. Int. Ed.* **42**, 3871–3894 (2003).

- [19] J. Lecointre, G. M. Roberts, D. A. Horke, and J. R. R. Verlet, “Ultrafast relaxation dynamics observed through time-resolved photoelectron angular distributions”, *J. Phys. Chem. A* **114**, 11216–11224 (2010).
- [20] D. A. Horke and J. R. R. Verlet, “Time-resolved photoelectron imaging of the chloranil radical anion: ultrafast relaxation of electronically excited electron acceptor states”, *Phys. Chem. Chem. Phys.* **13**, 19546–19552 (2011).
- [21] B. J. Greenblatt, “Femtosecond photoelectron spectroscopy: a new tool for the study of anion dynamics”, PhD thesis (University of California, Berkeley, 1999).
- [22] C. Hock, J. B. Kim, M. L. Weichman, T. I. Yacovitch, and D. M. Neumark, “Slow photoelectron velocity-map imaging spectroscopy of cold negative ions”, *J. Chem. Phys.* **137**, 244201 (2012).
- [23] M. Smits, C. A. de Lange, S. Ullrich, T. Schultz, M. Schmitt, J. G. Underwood, J. P. Shaffer, D. M. Rayner, and A. Stolow, “Stable kilohertz rate molecular beam laser ablation sources”, *Rev. Sci. Instrum.* **74**, 4812–4817 (2003).
- [24] I.-C. Lu, C. Lee, Y.-T. Lee, and C.-K. Ni, “Ionization mechanism of matrix-assisted laser desorption/ionization”, *Annu. Rev. Anal. Chem.* **8**, 21–39 (2015).
- [25] E. P. Månsson, S. D. Camillis, M. C. Castrovilli, M. Galli, M. Nisoli, F. Calegari, and J. B. Greenwood, “Ultrafast dynamics in the DNA building blocks thymidine and thymine initiated by ionizing radiation”, *Phys. Chem. Chem. Phys.* **19**, 19815–19821 (2017).
- [26] C. S. Anstöter, J. N. Bull, and J. R. R. Verlet, “Ultrafast dynamics of temporary anions probed through the prism of photodetachment”, *Int. Rev. Phys. Chem.* **35**, 509–538 (2016).
- [27] B. Mamyrin, “Time-of-flight mass spectrometry (concepts, achievements, and prospects)”, *Int. J. Mass Spectrom.* **206**, 251–266 (2001).
- [28] M. T. Zanni, “Photodissociation and charge transfer dynamics of negative ions studied with femtosecond photoelectron spectroscopy”, PhD thesis (University of California, Berkeley, 1999).

Appendix A

Publications from Graduate Work

[8] A. Kunin, V. S. McGraw, K. G. Lunny, and D. M. Neumark, “Time-resolved dynamics in iodide-uracil-water clusters upon excitation of the nucleobase”, *J. Chem. Phys.* **151**, 154304 (2019)

[7] A. Kunin and D. M. Neumark, “Femtosecond time-resolved photoelectron spectroscopy of molecular anions”. In *Physical Chemistry of Cold Gas Phase Functional Molecules and Clusters*, edited by Ebata, T.; Fujii, M. (Springer Nature Singapore Pte Ltd.) pp 307–335 (2019)

[6] A. Kunin and D. M. Neumark, “Time-Resolved Radiation Chemistry: Femtosecond Photoelectron Spectroscopy of Electron Attachment and Photodissociation Dynamics in Iodide-Nucleobase Clusters”, *Phys. Chem. Chem. Phys.* **21**, 7239 (2019)

[5] A. Kunin, W.-L. Li, and D. M. Neumark, “Dynamics of electron attachment and photodissociation in iodide-uracil-water clusters via time-resolved photoelectron imaging”, *J. Chem. Phys.* **149**, 084301 (2018)

[4] A. Kunin, W.-L. Li, and D. M. Neumark, “Time-resolved photoelectron imaging of the iodide-nitromethane (I^- - CH_3NO_2) photodissociation dynamics”, *Phys. Chem. Chem. Phys.* **18**, 33226 (2016)

[3] W.-L. Li, A. Kunin, E. Matthews, N. Yoshikawa, C. E. H. Dessent, and D. M. Neumark, “Photodissociation dynamics of the iodide-uracil (I^- -U) complex”, *J. Chem. Phys.* **145**, 044319 (2016)

[2] A. B. Stephansen, S. B. King, Y. Yokoi, Y. Minoshima, W.-L. Li, A. Kunin, T. Takayanagi, and D. M. Neumark, “Dynamics of dipole- and valence bound anions in iodide-adenine binary complexes: A time-resolved photoelectron imaging and quantum mechanical investigation”, *J. Chem. Phys.* **143**, 104308 (2015)

- [1] S. B. King, A. B. Stephansen, Y. Yokoi, M. Yandell, A. Kunin, T. Takayanagi, and D. M. Neumark, “Electron accommodation dynamics in the DNA base thymine”, *J. Chem. Phys.* **143**, 024312 (2015)